HYGROTHERMAL EFFECTS ON STRENGTH OF MECHANICAL JOINTS PREPARED FROM GLASS EPOXY COMPOSITE LAMINATES

Thesis

Submitted for the partial fulfillment of the Degree

of

Doctor of Philosophy

By

Kulwinder Singh
(Registration No.: 901508003)

Under the guidance of

Dr. Jaswinder Singh Saini
Associate Professor
Department of Mechanical Engineering,
Thapar Institute of Engineering &
Technology (Deemed to be University),
Patiala

Dr. Haripada Bhunia
Professor & Head
Department of Chemical Engineering,
Thapar Institute of Engineering &
Technology (Deemed to be University),
Patiala

THAPAR INSTITUTE
OF ENGINEERING & TECHNOLOGY
(Deemed to be University)

Patiala-147004, Punjab (India)
www.thapar.edu

April 2019

Dedicated

To

my father

Late. Mr. Ajmer Singh

Certificate

This is to certify that the thesis entitled **"Hygrothermal effects on strength of mechanical joints prepared from glass epoxy composite laminates"** being submitted by Mr. Kulwinder Singh to Department of Mechanical Engineering, Thapar Institute of Engineering & Technology (Deemed to be University), Patiala for the award of degree of **Doctor of Philosophy**, is a record of bonafide research work carried out by him under our guidance and supervision and has fulfilled the requirements for the submission of this thesis, which to our knowledge has reached the requisite standard.

The results embodied in the thesis have not been submitted in part or full to any other University or Institute for the award of any degree or diploma.

29/4/19

(Jaswinder Singh Saini)
Associate Professor
Department of Mechanical Engineering,
Thapar Institute of Engineering &
Technology (Deemed to be University),
Patiala

29/4/19

(Haripada Bhunia)
Professor & Head
Department of Chemical Engineering
Thapar Institute of Engineering &
Technology (Deemed to be Universit
Patiala

Acknowledgments

I would like to thank most sincerely my supervisors, Associate Prof. Jaswinder Singh Saini, Department of Mechanical Engineering and Prof. Haripada Bhunia, Department of Chemical Engineering, Thapar Institute of Engineering & Technology (Deemed to be University), for providing me such a valuable research opportunity and for their countless guidance, knowledge and motivation during the course of my research. I learned a lot from them over the course of this Ph.D. work. Their goal-oriented style of work, passion towards research, work ethics, has been very inspiring for me. Their daily practice of following up on recent scientific literature is something that I also tried to adopt and greatly benefitted. I really appreciate their unconditional support and encouragement towards doing high-caliber research. It has been a great honor to work under their guidance.

I am extremely thankful to Prof. Prakash Gopalan, Director, Thapar Institute of Engineering & Technology (Deemed to be University), Prof. R. Siddique, Dean of Research & Sponsored Projects, Thapar Institute of Engineering & Technology (Deemed to be University) and Dr. T. P. S. Malik, Head, Department of Mechanical Engineering, Thapar Institute of Engineering & Technology (Deemed to be University) for extending the opportunity to undertake this doctoral research.

I would like to profoundly thank my doctoral committee members, Dr. T. K. Bera and Dr. R. K. Duvedi, Department of Mechanical Engineering and Prof. R. Mehta, Department of Chemical Engineering, Thapar Institute of Engineering & Technology (Deemed to be University) for their immense help and guiding me towards the right direction. I am grateful to Prof. P. K. Bajpai for his expert advice in various stages of my research work and also during writing of my thesis. My heartful thanks to the staff members of the Department of Mechanical Engineering, Thapar Institute of Engineering & Technology (Deemed to be University) for their valuable contribution, spiritual and moral support.

My special thanks to thank Dr. Manjeet Singh, former research fellow Thapar Institute of Engineering and Technology, who patiently and in a very dedicated way offered undivided attention and advice.

My endless thanks go to my research colleagues, Mr. Jaspreet Singh, Mr. Piyush Gupta, Mr. Paramdeep Singh, Mr. Vishwas Grover, Mr. Ankit Sharma, Mr. Dev Kumar Mandal, Mr. Deepak Tiwari, and Mr. Mohit Kumar, for their valuable contribution, spiritual and moral support at various stages of my work.

My deepest gratitude goes to my beloved parents, Mr. Ajmer Singh, Mrs. Chhinder Pal Kaur, my father in law, Mr. Major Singh and my mother in law, Mrs. Paramjeet Kaur, my brother Mr. Parminder Singh, my brother in law Mr. Simratpal Singh, and Mr. Kuldeep Singh who have always supported me through highs and lows of life. They have touched my life in many ways. My last word is reserved for my love, Mrs. Gagandeep Kaur, for her true companionship.

I would like to gratefully acknowledge the financial support from Thapar Institute of Engineering & Technology (Deemed to be University), during my research work.

Finally, I wish to thank the 'ALMIGHTY' God for his sufficiency.

Kulwinder Singh

Abstract

The climatic conditions of the earth are rapidly changing, and every year, an increase in CO_2 content is reported in the earth's environment. On the other hand, development in the technology and growth in population has increased the consumption of natural resources of our planet. To tackle these problems, scientists and the industry are focused on alternative light-weight materials, which can improve the efficiency of the vehicles and also reduce the overall emissions in the environment. Therefore, the demand of the light-weight and high strength materials brought forth the composite materials. To manufacture and transport a big structure of a composite involves joining of the composite to composite or composite to metals and alloys. Adhesive joints being permanent may damage the primary components made of composites while opening the joints for maintenance. However, the mechanical joints facilitate easy assembly and disassembly when required and thus preferred over adhesive joints. The mechanical joints seem to be simple, but they are much more than that because of stress concentration due to drilled holes. Improper design of a joint may lead to a failure of the whole structure. Fiber reinforced plastics (FRPs) used in marine and aerospace structures are generally exposed to high level of humidity and temperature. Consequently, the durability and performance of the structures made of FRPs have become a primary concern for composite designers. The main objective of the present work is to improve the durability and performance of mechanical joints made of glass fiber reinforced plastic (GFRP) composites. The metal insert was used at the pin-hole interface to improve the performance of the single pinned joint. Addition of nanoclay into the epoxy further enhanced the performance of the pinned joints made of glass fiber reinforced composite material. The geometric parameters, *i.e.*, edge distance to hole diameter (E/D) ratio and width to hole diameter (W/D) ratio were varied from 2 to 5 and 3 to 6, respectively. Metal inserts reduced the stress concentration around the hole and redistributed stresses at the pin/hole interface, which eventually increased the ultimate failure load of the joint. The use of nanoclay and metal inserts certainly improved the load-bearing capacity of the pinned joint.

The physics of the pinned joint is relatively simple when compared to the bolted joint as there are no out-of-plane compressive forces present in case of pinned joint. Knowing the

contribution of the nanoclay into the pinned joint, the study was extended to analyze the performance of single and double lap bolted joints. Bolted joints were prepared from woven glass fiber reinforced laminates with the addition of nanoclay contents. Different geometric parameters, *i.e.*, edge distance to hole diameter (E/D) ratio and width to hole diameter (W/D) ratio were varied over the range of 2 to 5. Different levels of torque, *i.e.*, 0, 3 and 5 Nm were considered to analyze the effect of bolt torque on the failure behavior of the joint. Failure load of the bolted joint increased with the increase in E/D and W/D ratios. Increasing bolt torque has shown an increase in the failure load and stiffness of the bolted joint. Both the bolt torque and the nanoclay contributed to the performance of the bolted joint.

To investigate the performance of the bolted joint exposed to aging environments, two different types of aging environments, *i.e.*, hygrothermal aging (moisture, and temperature), and accelerated aging (ultraviolet radiation, moisture, and temperature), were considered. For hygrothermal aging, three different temperatures, *i.e.*, 25, 50, and 75°C along with three different duration of exposure, *i.e.*, 1, 2 and 3 weeks were considered. A full factorial design of experiment was conducted on important control factors, *i.e.*, water temperature, exposure time, bolt torque, and material variation. Exposure to hygrothermal conditions degraded the material significantly and the water temperature was found to be the most significant factor. The specimens under combined attack of elevated temperature (50, and 75°C), and moisture for 3 weeks experienced a significant degradation. For accelerated aging, a maximum of 500 hours cyclical ultraviolet exposure was given to the specimens as per ASTM D1544. A full factorial design of experiment was conducted on control factors (aging time, bolt torque, and material variation) using response surface methodology. It was found that the strength of the joints prepared with and without the nanoclay content decreased with the increase in the duration of aging. However, the joints prepared with nanoclay content demonstrated higher failure loads.

Progressive damage analysis along with Hashin failure criteria was performed to predict failure loads and failure modes in mechanical joints, numerically. A good agreement was obtained between the numerical predictions and the experimental findings.
Figure 1 shows the schematic of overall thesis work.

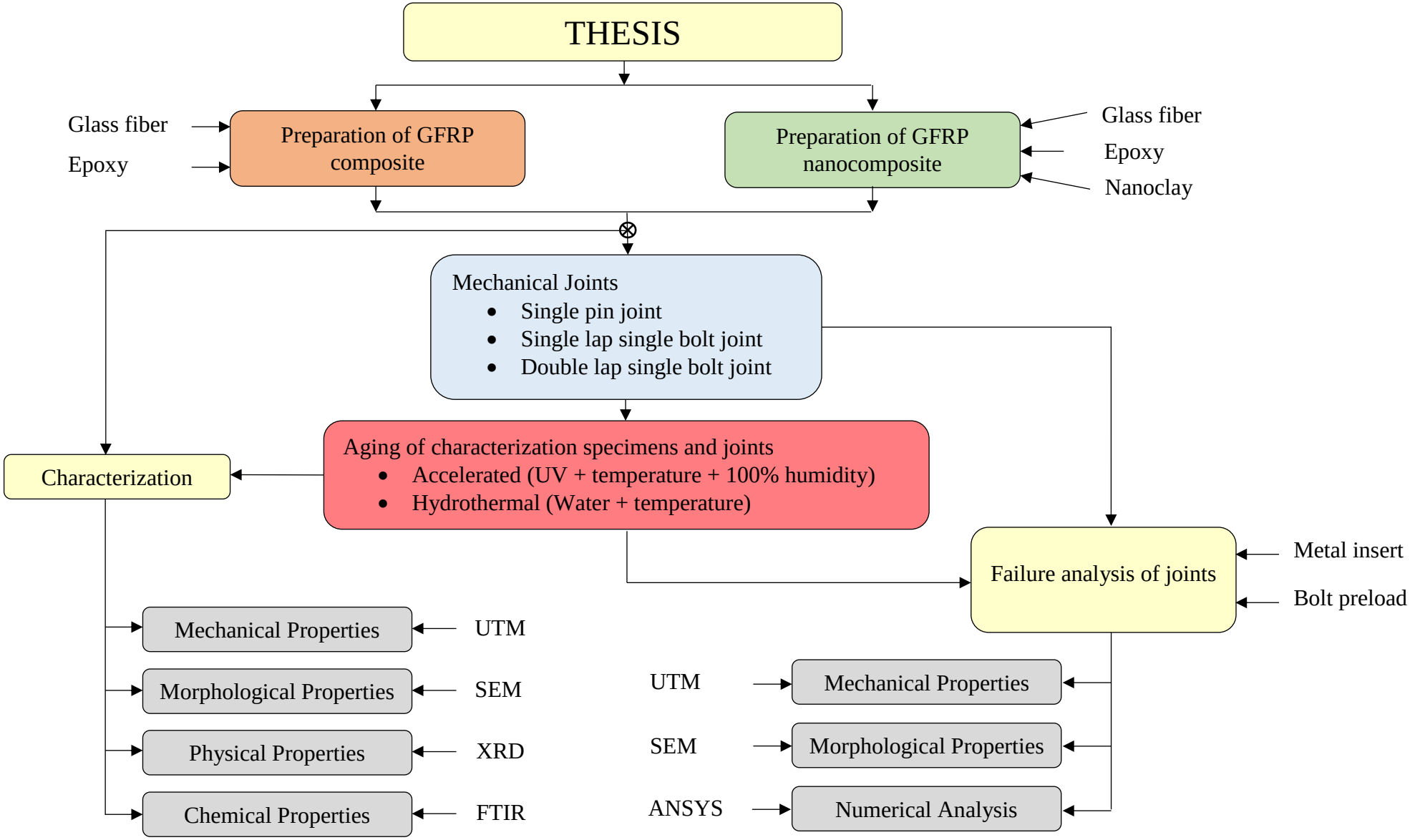

Fig. 1. Schematic of overall research work

Table of Contents

Certificate.....Error! Bookmark not defined.

Acknowledgments .....**i**

Abstract.....**iv**

Table of Contents .....**vii**

List of Figures.....**xi**

List of Tables .....**xviii**

List of Symbols .....**xx**

List of Abbreviations .....**xxi**

Chapter 1 Introduction.....**1**

1.1 Constituents of FRPs 2

1.1.1 Fiber..... 2

1.1.2 Matrix 4

1.2 Manufacturing Techniques 5

1.2.1 Compression molding..... 6

1.2.2 Bag molding 7

1.2.3 Pultrusion process..... 7

1.2.4 Filament winding..... 7

1.2.5 Resin transfer molding 7

1.3 Applications of Composite Materials 8

1.3.1 Aircraft and military..... 8

1.3.2 Space 8

1.3.3 Infrastructure 8

1.3.4 Automotive..... 8

1.3.5 Marines..... 9

1.3.6 Sports..... 9

1.4 Joining of Composite Materials..... 9

1.4.1 Adhesive joints..... 10

1.4.2 Mechanical joints 10

1.5 Design of Mechanical Joints 10
1.5.1 Pin joints 11
1.5.2 Bolted joint 11
1.5.3 Failure modes 11
1.6 Strength Parameters 13
1.7 Aging Effects on Polymer Matrix Composites 13
1.8 Improvements in Performance of FRPs 14
1.8.1 Nanofillers 14
1.8.2 Fiber surface treatments 14
1.9 Motivation and Objectives of the Present Work 15
1.10 Thesis Overview 16
Chapter 2 Literature Review 18
2.1 Effect of Different Parameters on the Strength of Mechanical Joints 18
2.2 Aging Environment Effects on PMCs and FRPs 30
2.3 Conclusion from the Literature Review 38
Chapter 3 Materials, Methods, and Testing 40
3.1 Materials 40
3.1.1 Resin 40
3.1.2 Glass fiber 41
3.1.3 Nanoclay 41
3.1.4 Fastener 41
3.1.5 Metal insert 42
3.2 Methods 42
3.2.1 Manufacturing methods 42
3.2.2 Aging methods 43
3.2.3 Characterization methods 44
3.2.4 ASTM standards 45
3.3 Composite Laminate Preparation and Testing 47
3.3.1 Optimization of curing parameters 48
3.3.2 Estimation of appropriate wt.% of nanoclay 53
3.3.3 Mechanical properties of the laminate 55

3.4 Closure 56
Chapter 4 Performance Analysis of Single Hole Pin Joint 57
4.1 Pin Joint Configurations 57
4.2 Joint Testing 59
4.3 Numerical Analysis 61
4.4 Results and Discussion 62
4.4.1 Unidirectional fiber reinforced composite 62
4.4.2 Bidirectional fiber reinforced composite 72
4.5 Closure 85
Chapter 5 Performance Analysis of Single Hole Bolted Joint 86
5.1 Single Lap Joint 86
5.2 Experimental Results 87
5.2.1 Effect of torque in the bolted joint 92
5.2.2 Regression analysis 94
5.3 Numerical Analysis 95
5.3.1 Characteristic curve method 96
5.3.2 Loads and boundary conditions 98
5.4 Closure 102
Chapter 6 Aging of Bolted Joints 103
6.1 Joint Configurations 103
6.2 Aging 105
6.2.1 Hygrothermal aging 105
6.2.2 Accelerated aging 105
6.3 Joint Testing 106
6.4 Results and Discussion 106
6.4.1 Hygrothermal aging 107
6.4.2 Accelerated aging 121
6.5 Numerical Analysis of the Bolted Joint 139
6.5.1 Loads and boundary conditions 140
6.6 Closure 144
Chapter 7 Conclusions and Recommendations for Future Work 146

7.1 Conclusions 146
7.2 Recommendations for Future Work 150
References 151
List of Publications 160

List of Figures

Figure No.	Title	Page No.
Figure 1	Schematic of overall thesis work	vi
Figure 1.1	Classification of different types of fibers [9] (a) Unidirectional continuous fiber, (b) Bidirectional continuous fiber, (c) Multidirectional continuous fiber, (d) Unidirectional discontinuous fiber, (e) Random discontinuous fiber	3
Figure 1.2	Compression-molding process [9]	6
Figure 1.3	Basic failure modes (a) net-tension, (b) shear-out, and (c) bearing [48]	12
Figure 2.1	Finite element model of the pin-loaded plate: (a) FE mesh adopted with multilayered shell elements (16 nodes per element, 16 + 16 GPs per layer) ranging between 250 and 330; (b) material axes (1,2) specifiable for each layer within the element; (c) finer mesh around the fastener hole [48]	21
Figure 2.2	Finite element model with boundary conditions [91]	27
Figure 2.3	FE mesh, loading and boundary condition of bolted joints (a) global mesh and boundary condition (b) local mesh of protruding head joint and (c) local mesh of countersink joint [54]	28
Figure 3.1	Tensile test specimen as per ASTM D3039	46
Figure 3.2	Compressive test specimen as per ASTM D695	46
Figure 3.3	Shear test specimen as per ASTM D5379	47
Figure 3.4	Bolt joint test specimen as per ASTM D5961	47
Figure 3.5	Membership functions for tensile and compressive strength of the composite laminates	50
Figure 3.6	S/N ratio plots of the combined response of the tensile and the compressive strength of the laminates cured at different levels of pressure, temperature, and duration	52

Figure 3.7	Effect of nanoclay wt.% on the tensile strength of the composite laminate	54
Figure 3.8	FESEM micrograph of epoxy modified with 3 wt.% of nanoclay	54
Figure 4.1	Geometry of the specimen without metal insert	58
Figure 4.2	Geometry of the metal insert	58
Figure 4.3	Geometry of the specimen with metal insert	59
Figure 4.4	Metal inserts in composite specimens made of (a) unidirectional fiber (b) bidirectional fiber	59
Figure 4.5	Test setup to analyze the load bearing response of pinned joints (a) Universal Testing Machine and (b) Specimen held in UTM jaws	60
Figure 4.6	Load vs displacement graphs from the UTM tensile test for specimens with and without the metal inserts: (a) W/D = 3 (without insert), (b) W/D = 3 (with insert), (c) W/D = 4 (without insert), (d) W/D = 4 (with insert), (e) W/D = 5 (without insert), (f) W/D = 5 (with insert), (g) W/D = 6 (without insert), (h) W/D = 6 (with insert)	63
Figure 4.7	Ultimate failure load for the specimen. (a) without metal inserts (b) with metal inserts	65
Figure 4.8	Failure modes of specimens with and without inserts, geometric parameters (a) E/D=2, W/D=3; E/D=3, W/D=3; E/D=4, W/D=3; E/D=5, W/D=3 and (b) E/D=2, W/D=6; E/D=3, W/D=6; E/D=4, W/D=6; E/D = 5, W/D=6	67
Figure 4.9	Generated mesh for a particular specimen	68
Figure 4.10	Tensile load applied on the hole boundary	68
Figure 4.11	Progressive damage status under tensile load at different stages for E/D = 2 and W/D = 3 in the outer layer	69
Figure 4.12	Progressive damage status under tensile load at different stages for E/D = 5 and W/D = 6 in the middle layer	70

Figure 4.13	Failure loads for different specimen from numerical analysis (a) First failure load without insert, (b) First failure load with insert, (c) Last failure load without insert, (d) Last failure load with insert	71
Figure 4.14	Comparison of experimental and numerical results (a) W/D = 3, (b) W/D = 4, (c) W/D = 5, (d) W/D = 6	72
Figure 4.15	Load vs displacement plots for different specimens, with and without metal insert prepared without nanoclay, tested under tensile load for (a) W/D = 3 (without insert), (b) W/D = 3 (with insert), (c) W/D = 4 (without insert), (d) W/D = 4 (with insert), (e) W/D = 5 (without insert), (f) W/D = 5 (with insert), (g) W/D = 6 (without insert), and (h) W/D = 6 (with insert)	74
Figure 4.16	Load vs displacement plots for different specimens, with and without metal insert prepared with 3 wt.% of nanoclay, tested under tensile load for (a) W/D = 3 (without insert), (b) W/D = 3 (with insert), (c) W/D = 4 (without insert), (d) W/D = 4 (with insert), (e) W/D = 5 (without insert), (f) W/D = 5 (with insert), (g) W/D = 6 (without insert), and (h) W/D = 6 (with insert)	75
Figure 4.17	Actual images of the selected failed specimen for E/D = 3 and W/D = 3 (a) neat without metal insert, (b) neat with metal insert (c) clay without metal insert, (d) clay with metal insert	78
Figure 4.18	Actual images of the selected failed specimen for E/D = 5 and W/D = 5 (a) neat without metal insert, (b) neat with metal insert (c) clay without metal insert (d) clay with metal insert	78
Figure 4.19	Ultimate failure loads for joints prepared from glass fiber, neat epoxy and (a) without metal insert (b) with metal insert	79

Figure 4.20	Ultimate failure loads for joints prepared from glass fiber, epoxy modified with nanoclay and (a) without metal insert (b) with metal insert	80
Figure 4.21	Refined mesh around the pin-hole of a particular specimen	81
Figure 4.22	Bearing load applied on the hole boundary of a particular specimen	81
Figure 4.23	Net-Tension failure mode status for E/D = 5 and W/D = 3 with metal insert at (a) 20%, (b) 40%, (c) 60%, (d) 80%, (e) 100% of applied load	82
Figure 4.24	Shear-out failure mode status for E/D = 2 and W/D = 3 without metal insert at (a) 20%, (b) 40%, (c) 60%, (d) 80%, (e) 100% of applied load	82
Figure 4.25	Bearing failure mode status for E/D = 5 and W/D = 6 without metal insert at (a) 20%, (b) 40%, (c) 60%, (d) 80%, (e) at 100% of applied load	83
Figure 4.26	Experimental and numerical failure loads compared for a selected joint configuration with metal insert (a) without nanoclay and (b) with nanoclay	84
Figure 5.1	Geometry of single lap joint	86
Figure 5.2	Tensile testing of the single lap joint on universal testing machine (UTM)	88
Figure 5.3	Load vs displacement plots for the joints without nanoclay with 0 Nm torque at (a) W/D = 2, (b) W/D = 3, (c) W/D = 4, (d) W/D = 5	89
Figure 5.4	Load vs displacement plots for the joints with nanoclay with 0 Nm torque at (a) W/D = 2, (b) W/D = 3, (c) W/D = 4, (d) W/D = 5	90
Figure 5.5	Actual images of the specimens depicting the failure modes of the joints made of composite using (a) neat epoxy, and (b) epoxy modified with nanoclay	91

Figure 5.6	Maximum failure loads for the joints with different E/D and W/D ratios made of composite using (a) neat epoxy, and (b) epoxy modified with nanoclay	92
Figure 5.7	Effect of torque on the failure load of the joint with E/D = 4 and W/D = 4 with neat epoxy, and (b) epoxy modified with nanoclay	93
Figure 5.8	Maximum failure loads for the joints with E/D = 4 and W/D = 4 at different torque settings	94
Figure 5.9	Residual plots for the failure load	95
Figure 5.10	Description of the characteristic curve [68]	96
Figure 5.11	Loads, boundary conditions and contacts set up in the numerical analysis of the joint	98
Figure 5.12	Complete mesh of the single lap joint	99
Figure 5.13	Refined mesh around the hole in the composite joint	99
Figure 5.14	Damage status of the composite joint for (a) W/D = 2 and E/D = 2, (b) W/D = 5 and E/D = 5	101
Figure 5.15	Maximum failure loads for the joints with E/D = 4 and W/D = 4 at different torque settings	101
Figure 6.1	(a) Specimen and (b) fixture schematic design	104
Figure 6.2	Experimental setup for joint testing	106
Figure 6.3	Tensile strength retention of composite laminates aged under different temperatures (a) 25°C, (b) 50°C, and (c) 75°C	108
Figure 6.4	Load vs. displacement graphs for neat composite joints aged at different temperatures and durations	110
Figure 6.5	Load vs. displacement graphs for nanocomposite joints aged at different temperatures and durations	111
Figure 6.6	Ultimate failure load of unaged joints	113
Figure 6.7	Ultimate failure loads for aged joints made of neat epoxy aged at (a) 25°C, (b) 50°C, (c) 75°C, and epoxy with nanoclay aged at (d) 25°C, (e) 50° C, (f) 75°C	114

Figure 6.8	Ultimate failure loads for aged joints made of (a) neat, and (b) nanocomposite specimens	115
Figure 6.9	Actual images of the selected failed joint specimens (a) Neat unaged with 0 Nm, (b) Neat unaged with 2 Nm, (c) Neat unaged with 4 Nm, (d) Neat aged at 75°C for 3 weeks with 0 Nm, (e) Neat aged at 75°C for 3 weeks with 2 Nm, (f) Neat aged at 75°C for 3 weeks with 4 Nm, (g) Nanocomposite unaged with 0 Nm, (h) Nanocomposite unaged with 2 Nm, (i) Nanocomposite unaged with 4 Nm, (j) Nanocomposite aged at 75°C for 3 weeks with 0 Nm, (k) Nanocomposite aged at 75°C for 3 weeks with 2 Nm, (l) Nanocomposite aged at 75°C for 3 weeks with 4 Nm	117
Figure 6.10	SEM images of fractured specimens made of neat composite (a), (b) unaged, (c), (d) aged at 75°C for 3 weeks and nanocomposite (e), (f) unaged, (g), (h) aged at 75°C for 3 weeks	119
Figure 6.11	Residual plots for the failure load (F_L)	121
Figure 6.12	FTIR spectra for unaged and aged composite specimens	122
Figure 6.13	Mechanical properties of the unaged and aged composites (a) Tensile strength, (b) Compressive strength, (c) Shear strength	123
Figure 6.14	Strength retention in the unaged and aged composites (a) Tensile strength, (b) Compressive strength, (c) Shear strength	124
Figure 6.15	Load vs. displacement plots for unaged and aged joints made with neat epoxy	127
Figure 6.16	Load vs. displacement plots for unaged and aged joints made with epoxy modified with nanoclay	128
Figure 6.17	Ultimate failure loads for joints made of neat and nanocomposite laminates	129

Figure 6.18	Comparison of ultimate failure loads for joint configurations aged for 500 hours	130
Figure 6.19	Actual images of the tested specimen prepared from neat epoxy	131
Figure 6.20	SEM micrographs of neat composite (a) unaged, (b) aged for 250 hours, (c) aged for 500 hours, and nanocomposite (d) unaged, (e) aged for 250 hours, (f) aged for 500 hours	133
Figure 6.21	Surface plots for failure load of joints made of (a) neat epoxy, and (b) epoxy modified with nanoclay	138
Figure 6.22	Loads, boundary conditions and contacts set up in the numerical analysis of the joint	140
Figure 6.23	Complete mesh of the double lap joint	141
Figure 6.24	Refined mesh around the hole in the composite joint	141
Figure 6.25	Damage progress in bolted joint with E/D = 5, W/D = 6, and a bolt torque of 2 Nm	142
Figure 6.26	Comparison of experimental and numerical results (a) neat unaged, (b) nanocomposite unaged, (c) neat aged for 500 hours, and (d) nanocomposite aged for 500 hours	144

List of Tables

Table No.	Title	Page No.
Table 3.1	Physical properties of the epoxy resin	40
Table 3.2	Processing properties of the epoxy resin	40
Table 3.3	Mechanical properties of the epoxy resin (L-12 + K-12 + K-13)	40
Table 3.4	Physical and mechanical properties of the glass fabric	41
Table 3.5	Typical properties of the nanoclay	41
Table 3.6	Mechanical properties of the fastener	41
Table 3.7	Physical properties of the mild steel material	42
Table 3.8	Chemical composition of the mild steel material	42
Table 3.9	Factors and levels considered in compression molding process	49
Table 3.10	Tensile and compressive strength of the laminates cured at different levels of pressure, temperature, and duration	49
Table 3.11	Experimental run, normalized values, area and signal-to-noise ratio	51
Table 3.12	Response for signal-to-noise ratios	51
Table 3.13	Analysis of variance for SN ratios	53
Table 3.14	d-spacing of nanoclay and nanocomposites of different wt.% of nanoclay	53
Table 3.15	Mechanical properties of composite laminate prepared from bidirectional glass fiber with and wiythout the addition of nanoclay content	55
Table 3.16	Mechanical properties of laminates prepared with unidirectional glass fiber and neat epoxy [96]	56
Table 4.1	Various values of E/D and W/D ratios	58
Table 4.2	Ultimate failure loads for various levels of E/D and W/D ratios	64
Table 4.3	Failure modes for various levels of E/D and W/D ratios	66

Table 4.4	Ultimate failure load for different joint configurations tested under tensile load	76
Table 4.5	Failure modes for different joint configurations tested under tensile load	77
Table 5.1	Geometry of the specimens tested under tensile load	87
Table 5.2	Failure modes observed for different joint configurations	90
Table 5.3	Analysis of variance	94
Table 5.4	Failure loads obtained from numerical analysis of the joint for different levels of geometric parameters	100
Table 6.1	Different factors and their levels for the design of experiment	105
Table 6.2	Aging effect on different mechanical properties of the composite laminate	109
Table 6.3	Ultimate failure loads for the joints aged at different levels of temperature and time and tested using different torque levels	112
Table 6.4	Analysis of variance	120
Table 6.5	Aging effect on different mechanical properties of the composite laminate	122
Table 6.6	Factors and levels considered for the performance analysis of the joint	126
Table 6.7	Design of experiment	126
Table 6.8	Failure loads for different joint configurations	134
Table 6.9	Analysis of variance	135
Table 6.10	Confirmation test for selected joint configurations	136
Table 6.11	Failure loads predicted through numerical analysis	143

List of Symbols

D	Diameter of the hole
E	Distance from the free edge of specimen
E_1	Longitudinal tensile modulus
E_2	Transverse tensile modulus
F_{opt}	Optimum value of force
G_{12}	Shear modulus
P_{max}	Maximum load
R_{oc}	Characteristic length in compression
R_{ot}	Characteristic length in tension
S	Shear failure strength
S/N ratio	Signal to noise ratio
SS_d	Sum of the squared deviations
SS_e	Sum of the squared error
SS_T	Total Sum of the squared deviation
t	Thickness of the specimen
W	Width of the specimen
wt.%	Weight percentage
X_t	Longitudinal tensile strength
X_c	Longitudinal compressive strength
Y_t	Transverse tensile strength
Y_c	Transverse compressive failure strength
ν_{12}	Poisson ratio
θ	Failure angle
σ_1	Maximum principal stress
σ_2	Minimum principal stress
σ_6	Maximum shear stress

List of Abbreviations

ANOVA	Analysis of variance
B	Bearing
DGEBA	Di glycidyl ether of bisphenol-A
DOE	Design of experiment
DF	Degree of freedom
FEM	Finite element method
FI	Failure Index
FRC	Fiber reinforced composite
FRCs	Fiber reinforced composites
FRP	Fiber reinforced polymer
FRPs	Fiber reinforced polymers
GFRP	Glass fiber reinforced polymers
gsm	Gram per m^2
NT	Net tension
OA	Orthogonal array
S	Shear-out
SEM	Scanning electron microscopy
UTM	Universal testing machine
XRD	X-Ray Diffraction

Chapter 1
Introduction

Natural resources and the climatic conditions of the earth has become the primary concern for today's world [1]. Big automobile companies are shifting from gasoline to electric vehicles [2]. Traditional heavy metals are being replaced by lightweight materials to increase the efficiency of vehicles [3]. Therefore, composite materials having a high strength to weight ratio are getting massive attention from the researchers and the industries. Due to the high strength to weight ratio compared to conventional metal materials, fiber reinforced composite (FRC) materials have shown large applications in aircraft, automobiles [3], space [4], submarines [5], and civil structures [6]. In terms of its construction, fiber reinforced plastic (FRP) consists fibers of high modulus and strength bonded to a matrix. While being different in physical and chemical nature; the fiber and the matrix produce a good fusion of mechanical properties [7]. The idea behind using fiber reinforcement is that many materials exhibit more strength in fiber form as compared to the bulk form. This phenomenon was given by Griffith [8]. In composites, fibers are the main load-carrying members, which are kept in desired orientation and location by the surrounding matrix. The matrix also protects the fiber from environmental damages [9]. Glass fiber and carbon fiber composites are two primary examples of this type of FRPs. Other fibers, such as aluminum oxide, boron, and silicon carbide have very specific applications. Polymers, ceramics, and metals are the various choices for the matrix materials [9].

Traditional metals, such as steel and aluminum alloys, are categorized as isotropic materials whereas the fiber reinforced composites are known as orthotropic materials [7]. For example, tensile strength and modulus of the unidirectional fiber reinforced composites is maximum and minimum along the longitudinal and transverse directions, respectively. The coefficient of thermal expansion for many FRPs is lower than of metals. Therefore, composite structures exhibit good dimensional stability over a wide range of temperature [9].

Another advantage of the FRPs is its non-corroding behavior [10]. However, FRPs may get affected by the moisture or chemicals present in the environment [11-15], which may

result in dimensional changes or internal stresses set up in the material. Exposure to high temperature and ultraviolet rays can also affect the performance of the FRPs [16-20]. Therefore the composite surface must be protected to avoid such situations.

1.1 Constituents of FRPs

The fiber and the matrix, are the primary constituents in FRP materials. Fiber provides strength and matrix keeps all of the fibers well in place and protect them from the environmental effects (moisture, chemicals). Another function of the matrix is to transfer forces between the fibers [9]. Coupling agents [21], fillers [22], and coatings [23] are also used as a fractional part of the FRPs. Coatings and coupling agents are applied on the fiber surfaces to improve their wettability with the matrix as well as to enhance the fiber-matrix interfacial bonding [21]. Use of these agents and fillers promotes better load transfer between the fibers and the matrix and vice versa. Fillers are being used to increase the strength of the FRPs [22, 24-29] and to reduce the effect of hygrothermal environmental conditions [12, 30].

1.1.1 Fiber

The fiber reinforced in the composite material acting as primary load carrying member provides high strength and modulus to the FRP composites.

1.1.1.1 Fiber materials

(i) Glass fibers mainly consists of silica (silicon dioxide) and metallic-oxide-modifying elements. E-glass (named behind its electrical properties) is most widely used as reinforcements for composites. S-glass fiber has approximately 30% higher tensile strength and 20% higher modulus than E-glass. From an economic point of view, S-glass is expensive than E-glass, so E-glass is preferred in many cases over S-glass [31].

(ii) Graphite (99% carbon) or carbon (95% carbon) fibers are most widely used as advanced fibers. Aramid polymer fibers, under the trade name Kevlar 29 were developed to be used in radial tires and are still being used for this purpose. Kevlar has excellent ductility, impact resistance and toughness compared to glass and graphite fibers [31].

(iii) Boron fibers consist of boron coating on a substrate of tungsten or carbon, and its diameter is of range 0.05 to 0.2 mm, which is the largest among all advanced fibers.

Boron fibers which are mostly used in aerospace structures have much higher stiffness and strength. Higher cost of boron fiber is the principal reason of its limited use in specific applications [31].

(iv) Silicon carbide (SiC) fibers have excellent strength retention and oxidation resistance at high temperatures [31].

(v) Jute, hemp, flax, remi, coconut fiber (coir), banana fiber (abaca), and sisal are the natural fibers grown in different parts of the world as agricultural plants. Common applications of these natural fibers are carpet backing, ropes, and bags [9].

1.1.1.2 Different types of fibers

Comparing the length of the fibers, continuous, and discontinuous fibers are the two main classifications of the fibers. The continuous fibers offer high modulus and strength in the direction of the fiber and thus offers directional tailoring to the load carrying capacity of the fiber-reinforced composite. Whereas, discontinuous fibers offer isotropic features to the resultant composite material. However, the modulus and strength of the discontinuous fiber reinforced composites are lower compared to their continuous counterparts.

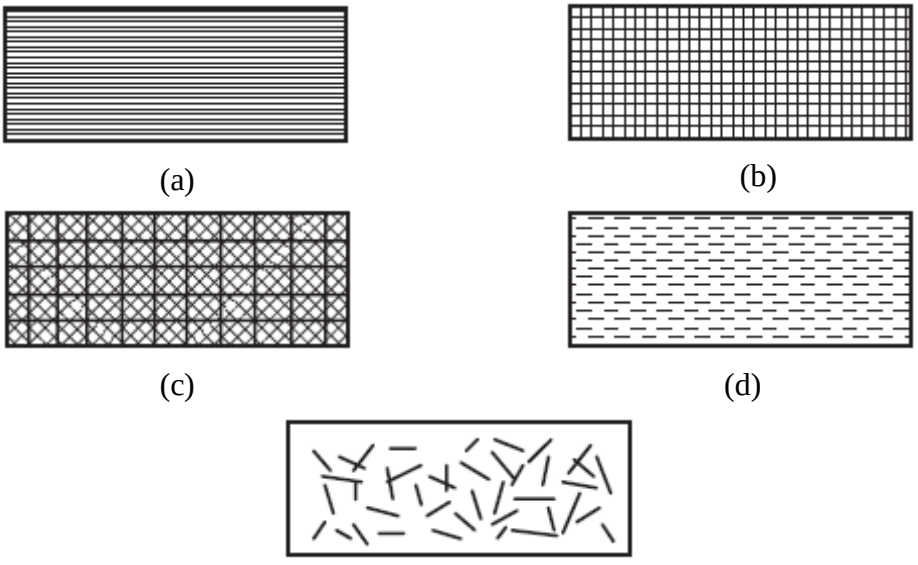

Fig. 1.1 Classification of different types of fibers [9]
(a) Unidirectional continuous fiber, (b) Bidirectional continuous fiber,
(c) Multidirectional continuous fiber, (d) Unidirectional discontinuous fiber,
(e) Random discontinuous fiber

Different types of fibers have been categorized in Figure 1.1. Unidirectional fibers are arranged in one direction only and provide orthotropic features. Strength in longitudinal axis is highest whereas it is low in transverse and other directions for unidirectional fibers. Bidirectional fiber (woven fiber) composites have fibers arranged in two directions and, provide equal strength in both, longitudinal and transverse direction, *i.e.*, closer to isotropic features compared to unidirectional fibers. Multidirectional fiber composites have more than two directions of fiber placements in the lamina and provide the nearly isotropic features. Random discontinuous fiber is the best choice to have the good isotropic features compared over all types of fiber categories as the fibers are oriented randomly in all the directions.

1.1.2 Matrix

The primary functions of the matrix in a FRP are to keep the fibers in place, provide a barrier against an adverse environment, transfer stresses between the fibers, and to protect the fiber surface from mechanical degradation.

1.1.2.1 Different matrix materials

Broadly, matrix materials may be classified into the following three basic categories.

(i) Metallic: The modulus and the yield strength of most of the metals are higher than the polymers. Besides this, the mechanical properties of the metals can be increased by various mechanical and thermal treatments [9]. However, the metals have a number of disadvantages too. Most of the metals possess high density, less corrosion resistance, and high melting temperature which leads to high processing temperatures. Aluminum alloys, stainless steel, and titanium are few of the typical examples of metal-matrix materials.

(ii) Ceramic: Ceramics are highly stable in high-temperature applications and possess high hardness, high modulus, and high resistance to corrosion. Though the ceramics are highly capable of bearing thermal shocks, their high brittleness, and less resistance to crack propagation results in less fracture toughness. Based upon the structural application, the ceramics can be classified into two categories, *i.e.*, oxides, and non-oxides. Alumina (Al_2O_3) and mullite (Al_2O_3-SiO_2) are the two most common types of oxide ceramics. The traditional non-oxide ceramics are aluminum nitride, silicon carbide, boron carbide, and silicon nitride [9].

(iii) Polymer matrix: The word *polymer* is the combination of two Greek words *'poly'* and *'mer'*. *'Poly'* means *'many'*, and *'mer'* means *'parts'* or the basic *'entity'* of polymer. When these *'parts'* are linked in repetition, they form a large molecule which is called polymer. Depending upon the types of *'mer'*, the polymer can be classified in number of categories, *i.e.*, based on the nature of polymer, polymer structure, its thermal behavior, polymerization, and its preparative techniques [32]. Thermoset and thermoplastic, based on the nature of polymer, are the two main kinds of polymers used in the fiber-reinforced composite materials.

Thermoplastic polymers: These polymers can be reshaped using heat and pressure due to their weak intermolecular bonds. Typical thermoplastic polymers are nylons, thermoplastic polyesters, polycarbonates, polyacetals, polyamide-imide, polysulfone, polyether ether ketone, polyetherimide, and polyphenylene sulfide.

Thermoset polymers: Due to crosslinking, these polymers cannot be reshaped once they are solidified. Few examples of thermoset polymers are epoxy, polyester, vinyl ester, phenolics, and cyanate ester.

Compared to the metallic and the ceramic matrix composites, the polymer-matrix composite materials offer following advantages:

- Light in weight due to low density of the polymers.
- Better application in corrosive environment.
- Low processing temperatures which facilitate a low manufacturing cost.
- Reinforcing high modulus fibers, *i.e.*, glass and carbon fiber into polymer-matrix offers high strength to weight ratio.

1.2 Manufacturing Techniques

Hand-layup is the oldest manufacturing technique which is used to manufacture polymer matrix composites. In this technique, fibers from the roll (continuous fibers) are cut and incorporated into a thin layer of matrix to form a lamina of thickness in the range of 0.1–1 mm. Placing few laminas in one stack results in a laminate, which is cured at room temperature using accelerator/catalyst. Although it is a reliable technique, its rate of production is very low, and it requires more labor. On the other hand, curing at elevated

temperature and pressure for specific time is essential to transform uncured or partially cured FRP into a solid composite laminate. High cure temperatures are required to initiate the chemical reaction. Generally, the resins are highly viscous, and to enable them to flow in the mold requires adequate pressure. High pressure also helps to consolidate individual un-bonded plies into a bonded laminate. The magnitude of curing temperature, pressure, and duration significantly affects the quality and the performance of the produced composite material. The curing cycle depends on a number of factors, *i.e.*, cure temperature, resin chemistry, catalyst reactivity, and the presence of inhibitors accelerators [9].

A number of processes involve these factors (temperature, pressure, and time) in different ways. A brief discussion of typical composite manufacturing techniques is given below.

1.2.1 **Compression molding**

Compression molding technique is popular to manufacture parts with the complex shape at a high production rate. Non-uniform thickness, bosses, flanges, ribs, shoulders, and holes can be easily made using compression molding technique, which in turn may reduce the secondary operation such as welding, drilling, and forming. Therefore, compression molding technique is a primary method to manufacture many structural components in automotive industries which may include, bumpers, rod wheels, and leaf springs [9]. A schematic diagram of the compression molding technique is shown in Figure 1.2.

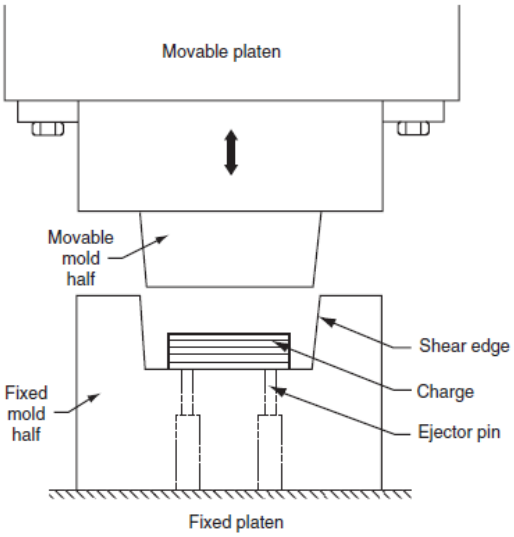

Fig. 1.2 Compression-molding process [9]

The process begins with placement of pre-cut sheet molding compounds (SMCs) known as charge, onto the bottom half of the preheated cavity. After that, the top half of the mold is lowered down with a controlled rate until a preset pressure is built upon the charge. With increasing pressure, SMCs starts to flow in the mold and fills the cavity. The molding pressure depends upon the length of flow, fiber content, and the part complexity. Usually, the temperature of mold is set in a range of 130°C–160°C. The mold is opened up after achieving an adequate degree of cure. The final product is removed from the mold with the help of ejector pins.

1.2.2 Bag molding

Bag molding process is used in the industry where high production rate is not the prime requirement. The material for this particular application comes in the form of prepregs, *i.e.*, the combination of fiber and partially cured resin. These prepregs are stacked in the mold one above the other as per required thickness. Bleeder cloth is placed on the top of the stack to absorb the excessive resin during the molding cycle. The complete stack is placed inside a thin heat-resistant vacuum bag. Complete assembly is put in autoclave machine under heat, vacuum, and external pressure. During the heating of prepreg in autoclave, the viscosity of the resin first decreases and then increases rapidly due to curing reaction and produces the solid cured composite laminate.

1.2.3 Pultrusion process

Pultrusion is a continuous molding process used to produce straight, long members of uniform cross-section. Solid rods, flat sheets, hollow tubes, and beams are the most common examples of the products produced by the pultrusion molding process.

1.2.4 Filament winding

Filament winding is a process in which a yarn of resin is cured after wrapping it around a rotating mandrel. Axisymmetric hollow composites such as pressure vessels, and pipelines are the main applications of the filament winding.

1.2.5 Resin transfer molding

The thermoset resin is injected into a closed mold in the resin transfer molding process. Depending upon the type of resin being used, the resin is cured either at room temperature or at higher temperature.

There are other manufacturing processes which are typically used for manufacturing parts specifically from thermoplastic materials. Few of those techniques are matched die forming, hydroforming, thermoforming, and diaphragm forming.

1.3 Applications of Composite Materials

The potential use of fiber reinforced composites (FRCs) exists in number of engineering fields. The primary structural application areas include aircraft, automotive, space, infrastructure, sporting goods, and marine. FRP composites are also used in furniture (e.g., chair springs), medical industry (e.g., implants, bone plates for fracture fixation), and in number of industrial products, such as power transmission shafts, oxygen tanks, and step ladders.

1.3.1 Aircraft and military

The main reason for using FRPs in aircraft applications is weight saving, which can lead to an increase in payload, significant fuel saving, and higher speeds [33]. Higher corrosion and fatigue resistance are also very important factors of FRPs to reduce maintenance and repair costs [10]. Besides this, aerodynamic shapes can be easily achieved using FRPs in comparison to the metal alloys.

1.3.2 Space

The primary reason behind the use of FRC in space vehicles is the weight saving [34]. Carbon fiber-reinforced epoxy tubes are used in truss structures of interplanetary satellites, and low earth orbit satellites to support solar array panels, optical benches, antenna reflectors, and other modules [35].

1.3.3 Infrastructure

FRPs have a great potential for replacing reinforced concrete and steel in buildings, bridges, and other civil structures [36]. The primary reason for selecting these composites is their corrosion resistance, light-weight, and high strength to weight ratio [9]. Besides new bridge construction, FRC are also used for upgrading, and strengthening deteriorating and damaged bridges [37].

1.3.4 Automotive

FRCs dominates other traditional metals in motorsports where high speed of the vehicle is the primary goal [38]. Machinery components prepared from composites such as drive

shafts give advantages of fast response and good vibration damping [39]. E-glass fiber-reinforced SMCs composites are used for exterior body components, such as the hood or door panels [40]. While manufacturing these components, discontinuous glass fibers are randomly dispersed in polyester or a vinyl ester resin. Due to low cost, E-glass fiber is preferred over carbon fiber. Compression molding process is used for making SMC parts. To obtain a 'Class A' surface finish, the in-mold coating is used for the exterior molded surface with a flexible resin. There are number of automotive underbody components made of FRPs such as bumper beams, radiator supports, roof frames, door frames, and timing chain covers, etc. [9].

1.3.5 Marines

FRPs have been used in sailboats, fishing boats, dinghies, lifeboats, and yachts due to their high strength and light weight [41].

1.3.6 Sports

The main advantages of using FRPs in sports goods are weight reduction, design flexibility, and vibration damping. The composites can be used to make tennis rackets, bicycle frames, baseball bats, golf club shafts, sailboats and kayaks, snow and water skis, surfboards, snowboards, arrows, fishing rods, archery bows, hockey sticks, javelins, helmets and exercise equipments [9].

1.4 Joining of Composite Materials

The applications of composites in real work situations need these composites to be joined with each other or with other metallic/non-metallic/alloy components. On the other hand, it is also not always easy to manufacture and transport a big structure of a composite material. Therefore, it is convenient to manufacture various smaller parts and then join them together as per requirement [13]. The joining seems to be simple, but it is much more than that because stress concentration due to drilled holes is a critical issue which can cause a structural failure [42]. Depending upon the application area and complexity of the structure, broadly the joints can be classified into following two main categories:

(i) Adhesive Joints (permanent)
(ii) Mechanical Joints (semi-permanent or temporary)

Applications involving frequent quality checks and maintenance require disassembly of various components. Adhesive joints, being permanent, may damage the primary components made of composites while opening the joints for maintenance. However, the mechanical joints facilitate easy assembly and disassembly when required and thus preferred over adhesive joints.

1.4.1 Adhesive joints

These joints are prepared using adhesive (epoxy, cyanoacrylates, phenolic, anaerobic, silicones, or methyl acrylate) as filler material, and two substrates (adherents). Adhesives are selected on the basis of service environment, type of composites, and cost of application. Adhesive failure and cohesive failure are the two primary type of failures in adhesive joint. The failure between the adhesive and adherent occurring at the interface is called adhesive failure. When the bond between the substrate material and the adhesive has high strength and the inherent strength of the adhesive or substrate is low, then cohesive failure occurs [43]. The factors, *i.e.*, type of adhesive, mechanical properties of adhesive, wettability of adhesive, and adherent bonding between adherent and adhesive, affect the failure of adhesively bonded joints.

1.4.2 Mechanical joints

Mechanical joints are temporary joints which can be used to assemble/disassemble the parent components. The repair and maintenance without destroying the parent components is the main reason of favoring mechanical joints over adhesive joints. The mechanical joints include fastener, rivet, screw and pin joints. Holes are drilled on the respective positions depending upon the number of fasteners to be used in a particular composite joint. The drilling of holes into the composite specimens becomes the prime cause of stress concentration. Other causes of structural failure of mechanical joints are loading direction, fasteners failure, fiber pull out, delamination, and location of the hole in composite plates [44].

1.5 Design of Mechanical Joints

The mechanical joints may fail either due to the failure of the composite plate or the fastener. If the fasteners are stronger than the composite plate, the focus goes on the behavior of composite plate and types of failure in the composite plate. The failure behavior of the composite plate is investigated in the pin joint as well as bolted joint.

1.5.1 **Pin joints**

In a pin joint, a pin is inserted into the drilled hole through the composite plate. The pin joints are studied to investigate the failure behavior of the composite plates as they facilitate easy assembly and disassembly with no clamping force on the composite plates [45]. Stress concentration and local damage are set up in pin joints which further lead to a decrease in joint strength [46, 47]. The exerted load causes failure in the composite plate as the pin is stronger than the composite plate, and is not affected by the applied load. Hence, the joint's strength entirely depends on the strength of the composite plates.

1.5.2 **Bolted joint**

It is a semi-permanent mechanical joint which involves threaded fasteners, washers, and bolt torque to assemble the primary components. In addition to the in-plane forces apparent in the pin joints, out-of-plane compressive forces are present in the bolted joints, which at the initial stage try to reduce the displacement, delamination, and through-thickness expansion. A bolted joint can be classified on the basis of the external force acting on the joint. If the line of action of the externally applied load is parallel to the bolt axes, the joint is called a tensile joint. If the line of action of the externally applied load is perpendicular to the bolt axes, the joint is called a shear joint. The shear joint have large applications in the assembly of different structural parts. Whereas, the tensile joint is used in the applications which require to prevent leakage in two clamped members.

The components of a shear bolted joint include the fastener and parts to be joined together. The force exerted by the bolt is the primary feature of a bolted joint. This initial clamping force ensures that the clamped parts remain in contact throughout the life of the joint and improve the performance of joints. Washers used in the joint minimize the embedment of bolt head and nut into the clamped parts, aid in tightening, reduce stress concentration around the hole, and distribute the initial axial preload over a larger area of the clamped parts.

1.5.3 **Failure modes**

For the design of mechanical joints, the failure analysis around the hole is highly critical and demands a careful investigation. Figure 1.3 shows three basic modes of failure in single pin/bolted joint, *i.e.*, net-tension, shear-out, and bearing mode [48]. The net-tension

and shear-out failure modes are catastrophic, which occurs without any warning whereas the bearing mode of failure demonstrates the maximum load carrying capacity [49, 50].

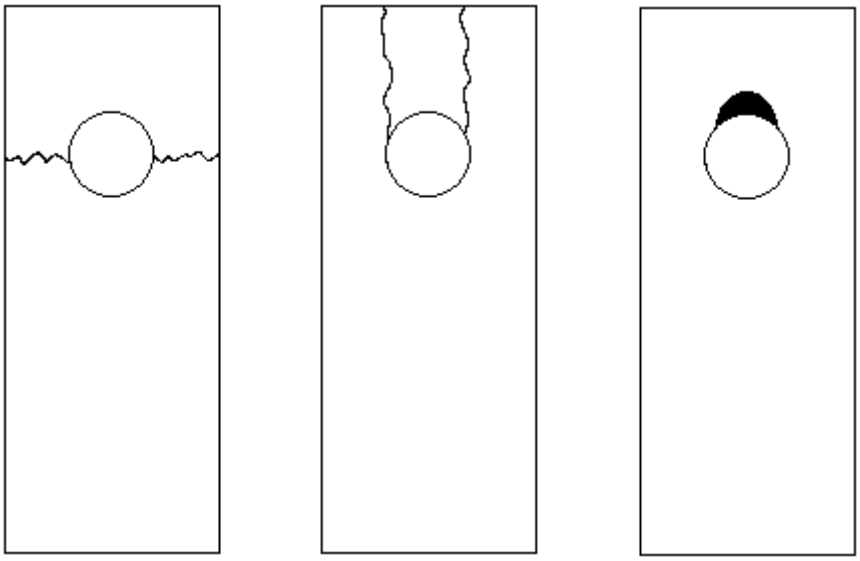

(a) (b) (c)

Fig. 1.3 Basic failure modes (a) net-tension, (b) shear-out, and (c) bearing [48]

(i) Net-tension failure: In the net-tension mode of failure, the split occurs across the width of the specimen, *i.e.*, perpendicular to the loading direction. It generally occurs, when the width-to-hole diameter ratio is minimal [51]. The strength, P_t, in net-tension of the plate is estimated using equation (1.1) [52].

$$P_t = (W - D) \times t \times \sigma_t \tag{1.1}$$

where, σ_t is the tensile stress, W is the width of the specimen, D is the hole diameter, and t is the thickness of the plate.

(ii) Shear-out failure: In the shear-out failure, the material ahead of the hole towards free edge, moves out along the longitudinal edges of the specimen. The shear strength, P_s, of the plate is defined by the equation (1.2) [49].

$$P_s = 2 \times E \times t \times \tau_s \tag{1.2}$$

where, τ_s is the shear stress, E is the edge distance, *i.e.*, the distance from the edge to the center of the hole and t is the thickness of the plate.

(iii) Bearing failure: This type of failure mode occurs when the plate is unable to bear with the crushing force exerted by the fasteners or the pin, and the hole widens towards free edge in the direction of the applied force. Bearing strength, P_c, of the plate is given by equation (1.3) [46].

$$P_c = D \times t \times \sigma_c \tag{1.3}$$

where, σ_c is the bearing or crushing stress, D is the hole diameter and t is the thickness of the plate.

1.6 Strength Parameters

To control the failure of the composite joints, the primary focus of the designer is always on the joint strength. The following parameters affects the strength of the joints [53, 54].

(i) Material: It includes the type of fiber material and its arrangement (weaving method), type of matrix material, and stacking sequence of the composite laminate.

(ii) Geometry: It includes the geometry, *i.e.*, length, width, and thickness of the composite plate, the location, and the size of the hole in the composite plate.

(iii) Fastener*:* It includes the type, size, and torque of fastener. It also includes the size of the hole and its clearance.

(iv) Design: It includes the application of the joints depending upon the loading type, loading direction, type of joint, *i.e.*, single lap and double lap, the geometry of joint, *i.e.*, pitch, width, edge distance, and hole pattern, and the environmental conditions.

1.7 Aging Effects on Polymer Matrix Composites

Polymer matrix composites (PMCs), and FRPs used in marine and aerospace structures are generally exposed to high level of humidity and temperature. Consequently, the durability and performance of the structures made of PMCs, and FRPs have become a primary concern for composite designers. The hygrothermal aging due to the combined effect of temperature and moisture causes the degradation of mechanical properties in the PMCs [55]. Due to the strong correlation between the moisture uptake and rate of degradation, it is crucial to understand the diffusion process in PMCs to predict their long-term durability [56-58]. The polymer swelling due to moisture absorption leads to weakening of the fiber-matrix interface and diminish the long-term durability of the FRPs [59-61]. Colossal research is being carried out globally to develop PMCs with higher

moisture barrier properties. Due to the increased diffusion path based on its tortuosity, nanoclay is emerged to be an excellent filler to resist the moisture uptake in the polymers [62]. Organomodified nanoclay (OMMT) has shown a significant enhancement in the mechanical, thermal and moisture barrier properties of the polymers [63-66].

1.8 Improvements in Performance of FRPs

The performance of the FRPs can be improved by different methods. It can be through optimizing the manufacturing processes for maximum performance of the FRPs [67]. On the other hand, it can also be in terms of some add-on materials or processes into the FRPs. Following are the two popular techniques being used these days.

1.8.1 Nanofillers

By creating a structure of nanometer-scale, the fundamental properties of materials, such as melting temperature, charge capacity, magnetic properties, and their color, can be changed without any modification in the chemical composition of the material [68]. Nanoscale structures have very high surface-to-volume and aspect ratio making them an ideal choice for use in polymer-matrix composite materials and gives them a new name, *i.e.*, polymer nanocomposites. In nanocomposites, particles filled has at least one of its dimensions in the nanometer range (1 nanometer = 10^{-9} m). Nanoparticles dispersed in the polymer-matrix increase the interfacial area between the matrix and the reinforced fiber, which in turn improves the bond strength as well as the individual properties of the polymer matrix. Therefore, the performance of FRCs can be improved with the addition of nanofillers resulting in an increased modulus and strength of the fiber reinforced plastic composites [22, 25, 28, 29]. These composites show superior mechanical, thermal, electrical, and optical properties [26-30].

Few common nanoparticles used in PMCs and FRPs are montmorillonite organoclays (MMT), carbon nanotubes (single-wall (SWNTs), multi-wall (MWNTs), and small diameter (SDNTs)), carbon nanofibers (CNFs), nanotitanium oxide (TiO_2), nanoaluminum oxide (Al_2O_3), and nanosilica (N-silica).

1.8.2 Fiber surface treatments

For efficient stress transfer from matrix to fiber and vice versa, strong bonds at the fiber-matrix interface are essential. Fiber surface treatments have emerged to improve the fiber

wettability with the matrix and enhance the fiber-matrix interfacial bond strength [21]. Organofunctional silicon compounds, known as silanes, are the most prevalent type of coupling agents used with the glass fiber.

1.9 Motivation and Objectives of the Present Work

These days FRPs are receiving colossal interest by many researchers over the conventional metals and alloys due to its high strength to weight ratio. A new evolution in FRPs is nanocomposites, which involves the use of nanofillers to provide better mechanical and moisture barrier properties compared to ordinary FRPs. It is seen that various parameters, *i.e.*, the geometry of joint, stacking sequence, type of fasteners, bolt hole clearance, and bolt torque have been studied to investigate the strength of mechanical joints. Some work is reported on the performance improvement of the mechanical joint using nanofiller at room temperature. In real life, large number of the applications work in hygrothermal environmental conditions which affects the FRP nanocomposites.

Various researchers have investigated the effects of hygrothermal conditions on the mechanical properties of the FRP nanocomposites. No research is conducted on hygrothermal effects on mechanical joints made of nanocomposites. The rate of moisture penetration, the influence of moisture and temperature, can be substantially reduced by incorporating nano-sized hydrophobic additives into polymers. Nanoclay has been widely used to improve the mechanical properties of epoxy nanocomposites. In addition to nanofillers, metal inserts can also be used to enhance the performance of the mechanical joints. A very less work has been reported on the use of metal inserts to improve the joint performance.

The overall objective of the present work is to increase the load-bearing capacity of the mechanical joints at room temperature as well as in severe weather conditions, which involves temperature, moisture, and UV radiation. The specific objectives of the present work are:

- Fabrication and improvements in mechanical joints prepared from fiber reinforced composite laminates with addition of nanofillers (e.g., nanoclay etc.).

- To study the effects of metal inserts on the strength of mechanical joints prepared from fiber reinforced composite laminates.
- Hygrothermal aging on the mechanical properties of the prepared joints.
- Numerical analysis for the prediction of the strength of mechanical joints under hygrothermal effects.

1.10 Thesis Overview

This thesis has been divided into seven chapters. Two different types of mechanical joints, *i.e.*, pin joint and bolted joint have been studied. Initially, to investigate the optimal geometric parameters, pin joints were studied along with the effect of nanoclay and metal inserts at room temperature. After optimizing the geometry of the composite plate and the nanoclay content, bolted joints were studied to investigate the combined effect of bolt torque and nanoclay at room temperature. Finally, the performance of the bolted joints incorporating nanoclay has been investigated in severe weather conditions.

Chapter one (Introduction) gives the basics about the composite materials, its constituents, manufacturing methods, and applications. It signifies the importance of joints and the different modes of their failure. It also gives the different parameters that affect the performance of the joints in the composite materials. The performance issues related to composite joints exposed to severe environmental conditions have been discussed.

Chapter two (Literature Review) discuss the available literature on the performance of the mechanical joints in different conditions. It discusses the importance of nano-fillers in the enhancement of the mechanical properties of composite materials. The available literature also gives an insight of the nano-fillers in the composite materials used in severe weather conditions.

Chapter three (Materials and Methods) shows the outline of experimental works conducted in the present work. This chapter is divided into three parts: the materials, methods, and testing used for the characterization and performance evaluation of mechanical joints.

Chapter four (Performance Analysis of Single Hole Pin Joint) discusses the contribution of metal insert and nanoclay into the performance of single hole pin joint. The geometric parameters, *i.e.*, edge distance-to-hole diameter (E/D) ratio and width-to-hole diameter (W/D) ratio were varied from 2 to 5 and 3 to 6, respectively.

Chapter five (Performance Analysis of Single Hole Bolted Joint) shows the performance analysis of single lap single bolt joint at room temperature. The effect of nanoclay and bolt torque on the single lap bolt joint has been investigated in this chapter. The geometric parameters, *i.e.*, E/D and W/D ratios were varied from 2 to 5 and 3 to 6, respectively. The effect of bolt torque varying over a range of 0–5 Nm was investigated on the performance of the bolt joint.

Chapter six (Aging of Bolted Joints) discusses the effect of hygrothermal and accelerated aging on the performance of double lap single bolt joint. Design of experiments were conducted to analyze the effect of individual factors such as temperature, exposure duration, bolt torque, and material type. The contribution of nanoclay has also been investigated in the performance of the bolted joint. Numerical analysis of the double lap bolted joint has been performed and results were compared with the experimental ones.

Finally, chapter seven (Conclusions and Future Work) summarizes the basic conclusions of the present work and also gives some directions for the future research.

Chapter 2
Literature Review

Comprehensive literature on the performance of PMCs, FRPs, and their mechanical joints has been studied and presented in this chapter. Fiber reinforced polymer composites have found a large number of applications in the industry. Different components are assembled together using a joint to make a structure. In mechanical joints, holes are drilled in the composite plates to accommodate fasteners. The drilled holes become the prime reason of stress concentration in the joints and make them weakest part of the construction. The strength of the joints in fiber reinforced polymer composites depends on the various parameters, *i.e.*, type and number of the fasteners, material, and geometric parameters used in the joints. Various investigations by different researchers in the field of PMCs, FRPs, and their mechanical joints have been discussed in this chapter. Broadly literature review is classified into two categories:

(i) Effect of different parameters on the strength of mechanical joints.

(ii) Hygrothermal effects on PMCs and FRPs.

2.1 Effect of Different Parameters on the Strength of Mechanical Joints

The strength of the mechanical joint depends upon different parameters, *i.e.*, material (fiber material and its density, matrix material, and filler material used), type of fabric (unidirectional, bidirectional, knitted, etc.), ply orientation, types of fasteners, bolt torque, and the most important; the geometry of the joint. Several investigations are reported on different parameters to improve the mechanical performance of the joints.

Chang *et al.* [69] presented a two-step method to predict the failure strength and failure mode of mechanically fastened fiber reinforced composite laminates. At first, the stress distribution in the laminate was estimated by using a finite element method. After that, the failure load and failure mode were predicted using a proposed failure hypothesis along with the Yamada's failure criterion which is given by equation (2.1).

$$\left(\frac{\sigma_x}{X}\right)^2 + \left(\frac{\sigma_{xy}}{S_c}\right)^2 = e^2 \begin{cases} e < 1 \; no \; failure \\ e \geq 1 \; failure \end{cases} \tag{2.1}$$

where, σ_x and σ_{xy} are the longitudinal and shear stresses in a ply, respectively. X is the longitudinal tensile strength of the ply and S_c is the shear strength of the laminate. The effect of geometry and ply orientation on the failure strength and failure modes were investigated. With decrease in the hole diameter, the load carrying capacity of the joint reduced with a precondition of W/D > 3. Increasing edge distance resulted in higher failure loads for $[0°/\pm45°/90°]_s$ and $[0°/90°]_s$ layups provided the E/D < 4. For E/D ≥ 4, improvement in the failure load was not much significant. The effect of geometric parameters on the bearing strength of single pinned joint was investigated by Okutan *et al.* [49] in woven glass-epoxy laminated composites. Failure propagation and failure type were seen for the single-hole pin-loaded specimen. The load carrying capacity of the single pinned joint increased with increase in the geometric parameters, *i.e.*, E/D and W/D ratios. The critical geometric ratios were determined as E/D = 2 and W/D = 3. In another study on single pinned joint, the numerical and experimental studies were carried out by Icten and Karakuzu [70] and Icten *et al.* [46] in woven Kevlar epoxy composite plates. The failure load and failure modes were estimated for different geometries of the pinned joint. For the finite element analysis, a 2D finite element code was developed using Maximum Stress, Hoffman, and Hashin failure criteria. To evaluate the effect of joint geometry, parametric studies were carried out on the E/D and W/D ratios. Considering the E/D ratio, the weakest design was observed with E/D = 1 representing shear-out failure mode. With a focus on the W/D ratio, the net-tension failure mode was observed for W/D = 2. Increasing E/D and W/D ratio beyond the critical values demonstrated increased bearing strength. The bearing strength of the single pinned joint is also influenced by the stacking sequence of the laminates. Okutan and Karakuzu [71] studied the response of pin joints in E-glass epoxy laminated composites for two different ply orientations, *i.e.*, $[0°/\pm45°]_s$ and $[90°/\pm45°]_s$. In addition, a static progressive failure analysis was performed using finite element methods. The bearing strength was influenced by the stacking sequence of the laminate. The laminates with $[0°/\pm45°]_s$ stacking sequence represented higher bearing strength than the laminates with $[90°/\pm45°]_s$ stacking sequence. A range of laminate configuration and specimen geometry was considered by Baba [72] for the performance analysis of the single pinned joint in glass-epoxy composite laminates. The laminates of $[90°/\pm45°]_s$ and $[/\pm45°]_s$ ply orientation failed more suddenly as compared to other lay-ups. Effect on net-tension

failure was due to W/D ratio whereas E/D ratio influenced the shear-out failure. Tercan *et al.* [73] investigated the bearing strength of a weft-knitted 1×1 rib glass-fiber composite plate pinned-joint in three directions, *i.e.*, 0°, 45° and 90°. Geometric parameters, *i.e.*, E/D, and W/D were systematically varied during experiments. It was shown that the bearing values obtained from the longitudinal directions are stronger than the cross and 45° directions. In each direction, maximum bearing strength was achieved for E/D and W/D ratios of ≥ 4. An orthogonal fabric was transformed into a non-orthogonal fabric of small weaving angles by Cesim [74] to examine the bearing strength of pinned joints in woven fabric composites. The E/D, and W/D ratios were taken as 1 to 3, and 3 to 4, respectively. The contribution of small weaving angles was more in the laminates of multi-directional stacking sequence. However, the layups with identical orientations demonstrated lower load carrying capacity compared to the layups in different directions. Asi [50] used woven fabrics with different linear densities of 200, 270, and 300 g/m^2 as reinforcements in epoxy resin. Single-hole pin loaded specimens of each material were tested in tension with varying values of E/D and W/D ratios. Bearing strength of glass-epoxy composite pinned joints was associated with the geometric parameters, linear densities of woven fabric, void content, and fiber volume fraction. At first, the bearing strength of the pinned joint increased with increase in the linear density of the fabric. Whereas, a further increase in the linear density of the fabric reduced the bearing strength due to higher void content and crimp levels of the specimen. An analytical method was developed by Aluko [75] to predict the bearing strength of the pinned joint in composite using the Yamada-Sun failure criterion along with the characteristic curve model. The characteristic dimensions that define the characteristic curve were obtained by stress analysis associated with no-bearing. With increasing W/D ratio, the strength of the joint increased. The analytical results showed a good agreement with the experimental results in the literature. Pisano *et al.* [48] carried out upper and lower bounds to the failure load multiplier of statically loaded joints, fastening orthotropic laminates in-plane stress conditions via a limit analysis numerical procedure at lamina level. Such a layer-by-layer approach as shown in Figure 2.1, took into account the actual stacking sequence of the laminate. The failure loads predicted through layer-by-layer formulation had less percentage error with the experimental results available in the literature. The failure

modes and damage progress was also described in a better way considering the ply orientations.

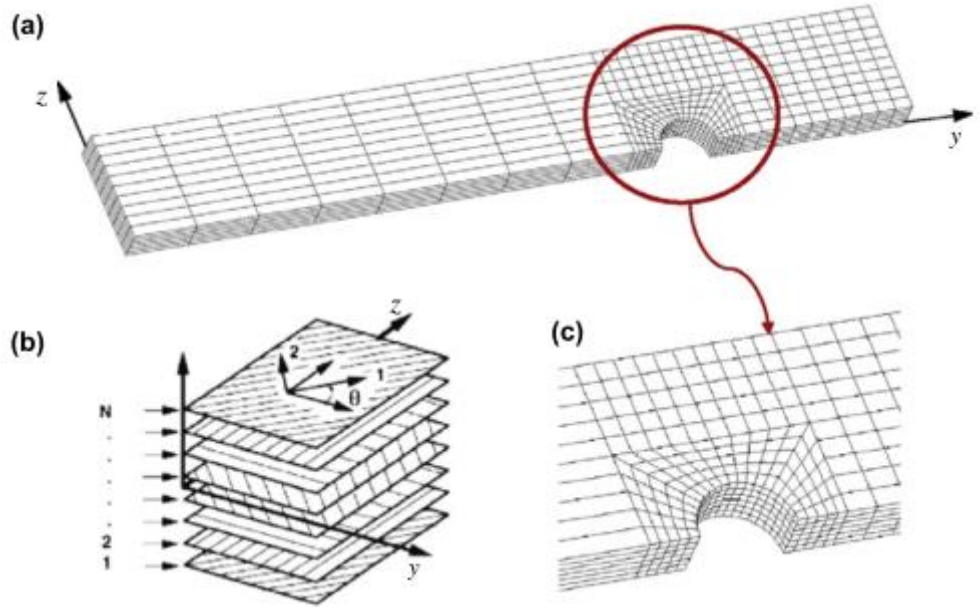

Fig. 2.1 Finite element model of the pin-loaded plate: (a) FE mesh adopted with multilayered shell elements (16 nodes per element, 16 + 16 GPs per layer) ranging between 250 and 330; (b) material axes (1,2) specifiable for each layer within the element; (c) finer mesh around the fastener hole [48].

Another refined finite element model was presented by Irisarri *et al.* [42] to predict the bearing strength of mechanically fastened joints in CFRP laminates. The model took into account the delamination onset and propagation using cohesive elements. The ply behavior was described through a viscoelastic model combined with a progressive damage approach. The failure of the ply was modeled using a mesoscopic failure criterion based on the Hashin's assumptions given by equation (2.2).

$$\begin{cases} FF: f_1 = \left(\frac{\langle \epsilon_{11} \rangle_+^2}{X_{\epsilon_t}^2}\right) + \left(\frac{\langle \epsilon_{11} \rangle_-^2}{X_{\epsilon_c}^2}\right) \\ FF: f_2 = \left(\frac{\langle \epsilon_{22} \rangle_+^2}{Y_{\epsilon_t}^2}\right) + \left(\frac{\langle \epsilon_{22} \rangle_-^2}{Y_{\epsilon_c}^2}\right) + \left(\frac{\epsilon_6^2}{S_{\epsilon_c}^2}\right) \end{cases} \tag{2.2}$$

where, X_{ϵ_t} and X_{ϵ_c} are the longitudinal strains to failure respectively in tension and in compression, Y_{ϵ_t} and Y_{ϵ_c} are the transverse strains to failure respectively in tension and in compression and S_{ϵ_c} is the shear strain to failure. Besides the effect of material, stacking sequence, and geometric parameters, the proposed model also captured the friction and

pin-hole clearance. The effect of clamping forces on damage onset and bearing strength of the bolted joint was also captured upto some extent. Ilic *et al.* [76] developed a computational procedure to analyze initial failure load for pin-loaded holes at layered composite structures using finite element methods. The influence of stacking sequences of layered composites containing pin-loaded holes was also investigated. Tsai-Wu failure theory along with the characteristic curve was used to perform the numerical analysis of the joint. A close agreement was observed between numerical and experimental results. A different method to access the damage development process in single pinned joints in glass-epoxy composite laminates was presented by Ondurucu *et al.* [51]. SEM was performed on the specimens tested under bearing loads. The effect of joint geometry and stacking sequence was considered. The failure load and failure modes were influenced by geometric parameters and the stacking sequence of the laminate. The failure in the shear-out specimens appeared in the form of cracks within the matrix in the direction of applied loads. Whereas, the bearing specimens showed brittle fracture on the fibers. Another experimental and numerical work on the single pinned joint was reported by Turan *et al.* [77] to determine failure loads and failure modes in unidirectional carbon/epoxy composite laminates. Parametric studies were carried out to determine the effect of fiber orientation and joint geometry. Hashin failure criteria was used in ANSYS software to predict the failure loads and failure modes through numerical analysis. It was concluded that when the E/D and W/D ratios are equal to 5, the failure load reach its highest value. Also, maximum and minimum failure loads were shown for 0° and 15° fiber orientations respectively, with reference to the loading direction. Hashin and maximum stress criteria were used by Zhang *et al.* [78] to predict the life of 3D braided composite under fatigue and tension loading. Li *et al.* [47] performed a probabilistic analysis on the bearing strength of a composite pin joint using a Subset Simulation technique. A two-dimensional finite element analysis was utilized for the deterministic progressive damage analysis. It was concluded that the failure criteria and the degradation rules have a significant effect on the deterministic as well as probabilistic analysis of the bearing strength of the joint.

To investigate the performance of two holes in the pinned joints Karakuzu *et al.* [45, 79, 80] studied the failure load, failure mode, and bearing strengths of single and double hole

pinned joints in a woven glass-vinylester composite plate subjected to traction forces by two serial/parallel rigid pins. The behavior of composite plates with respect to the edge distance-to-hole diameter (E/D), the distance from the upper or the lower edge of the specimen to the centre of hole-to-hole diameter (K/D), and the distance between two holes-to-hole diameter (M/D) ratios were observed experimentally and numerically. Hashin failure criteria given by equations (2.3–2.6), was used to obtain failure load and failure mode.

Fiber failure in case of tensile stresses in the longitudinal direction (fiber direction) is given by equation (2.3).

$$f_f = \left(\frac{\sigma_1}{X_t}\right)^2 + \left(\frac{\tau_{12}}{S}\right)^2, \sigma_1 \geq 0 \tag{2.3}$$

Fiber failure in compression is predicted by using equation (2.4)

$$f_f = -\frac{\sigma_1}{X_c}, \sigma_1 < 0 \tag{2.4}$$

Matrix failure in case of tensile transverse stresses is given by equation (2.5)

$$f_m = \left(\frac{\sigma_2}{Y_t}\right)^2 + \left(\frac{\tau_{12}}{S}\right)^2, \sigma_2 \geq 0 \tag{2.5}$$

Matrix failure in case of compressive transverse stresses is given by equation (2.6)

$$f_m = \left(\frac{\sigma_2}{2S}\right)^2 + \left(\frac{\tau_{12}}{S}\right)^2 + \left[\left(\frac{Y_c}{2S}\right)^2 - 1\right]\frac{\sigma_2}{Y_c}, \sigma_2 < 0 \tag{2.6}$$

where, f_f and f_m are the failure index for the fiber and the matrix. σ_1 and σ_2 are stresses setup in longitudinal and transverse directions, respectively, X_t and Y_t are the tensile stress limits, and X_c and Y_c are compressive stress limits in longitudinal and transverse directions, respectively, and S is the in plane shear stress. In the case of serial pinned joints, W/D > 3 was recommended to obtain the bearing failure mode. Shear-out mode did not occur on the inner hole. Whereas, outer hole failure mode was dependent on the E/D ratio. Shear-out failure mode was observed on the outer hole while E/D = 1. In the case of parallel pinned joints, the E/D ratio had more impact on the bearing strength compared to the M/D, and K/D ratio. Similar study was carried out by Aktas *et al.* [81] to investigate the failure load and failure mode of glass fiber reinforced composite plates

with single and double parallel pinned joints experimentally and numerically. E/D and W/D ratios were varied over the range of 2 to 5. The numerical study was performed using ANSYS software and Yamada-Sun failure criterion given by equation (2.7), was used for failure analyses.

$$\left(\frac{\sigma_1}{X}\right)^2 + \left(\frac{\tau_{12}}{S}\right)^2 = e^2 \quad e \geq 1\ failure;\ e \leq 1\ no\ failure \tag{2.7}$$

In case of single pinned joint, keeping W/D constant, specimens with E/D = 2 demonstrated minimum failure loads. On the other hand, keeping E/D constant, minimum loads were obtained with W/D = 2. In the case of double pinned joints, the maximum bearing load was achieved at E/D ≥ 4, and W/D ≥ 4. Another study was carried out by Aktas [82] to investigate the failure load and failure mode of woven glass-epoxy composite plates with one and two serial pinned joints. Two variables, *i.e.*, the width of the specimen to the diameter of the holes ratio, and the distance from the free edge of the plate to the diameter of the first hole ratio, were investigated experimentally and numerically. Yamada Sun failure criteria along with the characteristic curve were used to predict the failure load and failure modes of the pinned joint. Maximum failure loads were observed at E/D = 4, and W/D = 4.

Three and four pin joints were studied experimentally and numerically by Nanda *et al*. [83] using uni-directional glass-epoxy composite laminates. In addition to side width-to-diameter (S/D), and edge-to-diameter (E/D) ratios, the variation in the pitch-to-diameter ratio (P/D) was also found significant, which eventually influenced damage propagation between holes. A 2D finite element model was developed using ANSYS software. To predict failure load and to differentiate failure modes, the Tsai–Wu failure criteria given by equations (2.8–2.10), along with material property degradation, was used in the analysis.

$$F_i\sigma_i + f_{ij}\sigma_i\sigma_j \geq 1 \tag{2.8}$$

$$F_1\sigma_{11} + F_2\sigma_{22} + F_{11}\sigma_{11}^2 + F_{22}\sigma_{22}^2 + F_{66}\sigma_{12}^2 + 2F_{12}\sigma_{11}\sigma_{22} \geq 1 \tag{2.9}$$

with $$F_1 = \left(\frac{1}{X_T} - \frac{1}{X_C}\right); \quad F_2 = \left(\frac{1}{Y_T} - \frac{1}{Y_C}\right); \quad F_{11} = \left(\frac{1}{X_T X_C}\right);$$

$$F_{22} = \left(\frac{1}{Y_T Y_C}\right); \qquad F_{66} = \left(\frac{1}{S^2}\right); \qquad F_{12} = \frac{1}{2\sqrt{X_T X_C Y_T Y_C}}; \tag{2.10}$$

where, σ_{ij} are the layer-stresses in the ij direction; X_T, and Y_T are the tensile strengths, X_C, and Y_C are the compressive strengths in longitudinal and transverse directions, respectively and S is the shear strength of the ply. A 3D finite element analysis on multi-pin joint was performed by Nanda *et al*. [84]. The von-Mises failure criteria was used to predict the failure in the glass epoxy composite joints using equivalent material properties. The FEA with equivalent material properties model along with von-Mises stress criteria gave results which were close to the experimental ones. Karakazu *et al.* [85] investigated the failure load, failure mode, and bearing strength in a woven glass-vinylester plate with three pins joint. Three geometric parameters, *i.e.*, edge distance-to-hole diameter ratio (E/D = 1 to 5), the ratio of longitudinal distance between two holes-to-hole diameter (F/D = 2, 4, 6), and transverse distance between hole-to-hole diameter ratio (G/D = 3 to 5) were considered to investigate their effect on failure load and failure mode of the pinned joint. The two holes near the free edge showed the similar type of failure modes. Shear-out failure mode was observed near the two parallel holes at E/D = 1, whereas other specimen showed bearing failure mode. Pisano *et al.* [86, 87] presented numerical results to validate a design methodology implementing two finite element based limit analysis numerical procedures, *i.e.*, the Elastic Compensation Method, and the Linear Matching Method. The methodology was used to determine the upper and lower bounds to the peak load multiplier of multi-pin joints in composite laminates. The numerical results were compared with the large number of experimental findings available in the literature and were in good agreement. An analytical model was developed by Olmedo *et al.* [88] to predict the progressive bearing failure of pin-loaded composite laminates. The model combined a spring-mass model to reproduce the stiffness of the composite pinned-joint and two-dimensional stress analysis to predict the bearing failure mode. The model was used to analyze pin joined laminates with any stacking sequence. The model provided an accurate method to predict bearing failure of the pinned joint in the composite laminates. The initial stiffness and first peak load were predicted with an error of less than 5% and less than 7%, respectively.

Bolt torque in the bolted joints exert a lateral compressive force onto the composite plate and thus distribute the stresses within the contact region at the initial stage of loading. To investigate the effect of bolt torque and the bolt hole clearance on the bolt joint

performance, Sen *et al.* [89] studied the bearing strength and failure mode of bolted joints in glass-epoxy composite plates. To observe the failure mechanism under various torque, three levels of torque were considered, *i.e.*, 0, 3 and 6 Nm. Diameters of the bolt and the circular hole were fixed as 5 and 6 mm, respectively to study effects of the clearance. E/D and W/D ratios were varied from 1 to 5, and 2 to 5, respectively. Laminated plates were stacked as three different groups $[0°/0°/45°/-45°]_s$, $[0°/0°/45°/45°]_s$, and $[0°/0°/30°/30°]_s$, symmetrically. Bearing strength was increased with the increase in torque, E/D and W/D ratios. Cohesive Zone Elements (CZEs) were used by Atas and Soutis [90] to develop a strength prediction method for bolted joints in CFRP composite laminates. The influence of the non-linear shear stress-shear strain behavior on the strength and subcritical damage development of the CFRP laminates was demonstrated using the center notched cross-ply specimens. The non-linear behavior was concluded to be necessary for accurate subcritical damage predictions. The strength of the joints was predicted within 10% and 21% accuracy for the quasi-isotropic and the cross-ply laminates, respectively. Zhang *et al.* [91] presented a progressive damage analysis (PDA) based characteristic length method (CLM) with only unidirectional layer properties required to predict the failure of multi-bolt joints in composite plates. It was concluded that the material degradation rules might lead to a significant influence on the failure load. Instead of complete property degradation, Camanho's property degradation rules predicted failure loads with a good agreement with the experiments.

Another important aspect in the mechanical joints is the clearance at the pin/bolt hole interface. Murthy *et al*. [92] carried out the numerical analysis on clearance fit in which the pin is of smaller diameter as compared to the hole. If there is no clearance at the interface, then the contact status does not change with load levels, and it becomes a case of a linear problem. However, in the case of pin/fasteners of smaller diameter than the hole, the problem becomes non-linear due to changing partial contact/separation regions. It was concluded that the conventional assumption of cosine distribution for the contact pressure between the pin and the plate in the analysis leads to underestimation of bearing failure load and overestimation of shear and tensile failure loads. McCarthy *et al.* [93] developed a finite element model as shown in Fig. 2.2, to study the effects of the bolt–hole clearance on the mechanical behavior of single-bolt, single-lap bolted composite

(graphite/epoxy) joints. Issues in modeling the contact between the joining parts, which affect the efficiency and the accuracy of the model were presented. The results predicted through the model were compared with the experimental data.

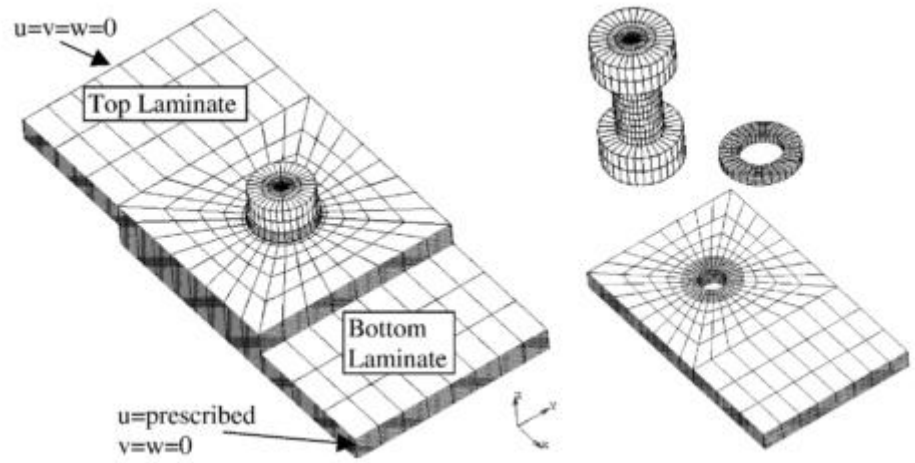

Fig. 2.2 Finite element model with boundary conditions [93]

Zhai *et al*. [94] performed experiments to investigate the effect of bolt-hole clearance and bolt torque on single-bolt, countersunk composite joints. Bolt-hole clearance intensified the surface strain concentration and the out-of-plane deformation of the joints. Though the bolt torque alleviated the surface strain concentration, a little effect was observed on the out-of-plane deformation. In another numerical study, Esmaeili and Chakherlou [95] investigated the effects of torque tightening on the stress distribution in double lap simple bolted and hybrid (bonded-bolted) joints. To determine the bolt clamping force resulting from the bolt tightening at different applied torques for both kinds of joints, a special experimental method was designed using a steel hollow cylinder that was placed between the plate and the nut. Results revealed that the amounts of resultant stresses were reduced by increasing the bolt torque due to compressive stresses. Furthermore, in the hybrid joints, the stress concentration around the hole reduced significantly. It was also concluded that hybrid joints have better static strength than simple joints for all levels of the bolt torque.

Different types of fasteners can also influence the performance of the mechanical joints. Qin *et al.* [54] carried out the experimental and numerical studies to demonstrate the effect of different fasteners on mechanical behaviors of composite bolted joints.

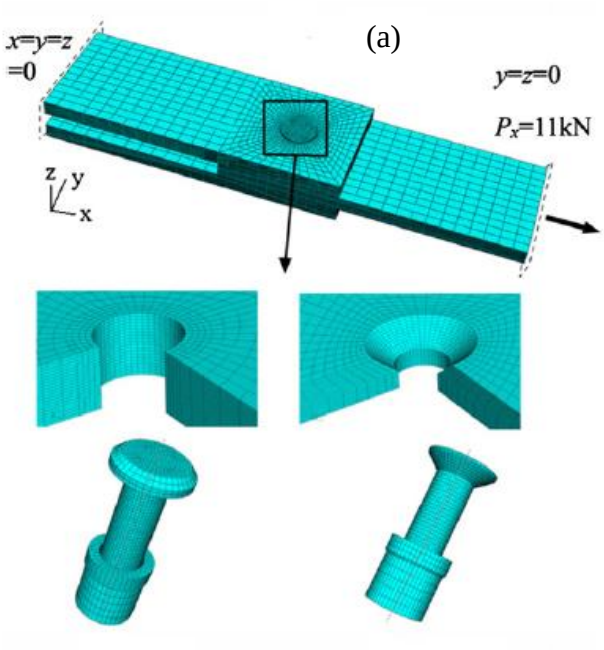

Fig. 2.3 FE mesh, loading and boundary condition of bolted joints (a) global mesh and boundary condition (b) local mesh of protruding head joint and (c) local mesh of countersink joint [54]

As shown in Fig. 2.3, composite joints assembled using protruding head or countersink fasteners were used to study the mechanical behavior which was justified using finite element analysis. The countersink fasteners caused lower initial failure loads compared to the protruding head fasteners. The final failure displacement was larger by 1 mm in case of countersink joints than the protruding head joints. The nonlinearity onset load were higher in case of protruding head joints compared to the countersunk head joints. Joints with the protruding heads demonstrated 4.5% higher rupture strength than the countersink head joints.

Tremendous improvements have been reported by nanofillers in the performance of fiber reinforced plastics. Nanoparticles dispersed into the matrix increased the specific surface area of the composite material and improved the interfacial bond strength. The effect of nanofillers has also been investigated on the performance of mechanical joints. Asi [96] carried out an experimental study to investigate the bearing strength of pin joints in GFRP filled with different proportions of Al_2O_3 particles. Single hole pin-loaded specimens with 7.5, 10 and 15 wt.% of the filler in the matrix were tested in tension. The composite specimens with 10 wt.% of Al_2O_3 particle content demonstrated highest bearing strength.

Further increase in the Al_2O_3 particle content resulted in a decrease of the bearing strength. In another study, the effects of unfilled, TiO_2 and ZnS filled GFRP were investigated on the strength of bolted fasteners and hybrid fasteners under tensile loading by Arun *et al.* [97]. Bolt configurations were chosen as 2, 3 and 4 to analyze the effect of number of bolts on the joint strength. It was found that addition of filler material has increased the static tensile strength of bolted fasteners and hybrid fasteners along with the change in the failure mode of joint. Singh *et al.* [98] investigated the bearing strength and failure modes of pin joints with the addition of nanoclay as a filler material. The effect of different geometric parameters, *i.e.*, E/D and W/D, and the ply orientations were also studied for single hole pinned joints prepared from glass-epoxy nanocomposite laminates. The layups with [0°/90°/0°] stacking sequence demonstrated 10–12% higher bearing strength than the layups with [0°/45°/0°] orientation. The failure modes were dependent on the geometry of the joint. Singh *et al*. [99] used a finite element approach to evaluate elastoplastic material properties of the particle reinforced composites.

Holes are to be drilled into the composite plates to fix fasteners into the mechanical joints. Delamination occurs around the hole during drilling of the GFRP laminates [100], and the drilled holes into the composite plate lead to stress concentration into the joint. During testing of the joints under structural loads, damage first starts in the vicinity of the hole. One idea was to increase the stiffness of the elements local/near to the hole to improve the load-bearing capacity of the mechanical joint. To address such idea, Nilsson [101] incorporated a bonded metallic insert in the hole to increase the failure load in the graphene-epoxy bolted joints. Incorporating metal insert into the hole facilitated to reduce the stress concentrations around the hole and thus achieve higher failure loads. The strength of the adhesive and the stiffness of the metal insert influenced the failure load of the joint. Metal inserts of two different materials, *i.e.*, aluminum and epoxy were used by Herrera-Franco and Cloud [102] in the hole of a single pinned joint. Stress-strain distribution in the single pin lap joints was analyzed using hard and soft metal inserts. In case of soft metal inserts, bearing stress was reduced by 50% at a distance of two radii of the hole. The shear strain was also reduced by 50% in the bearing region at approximately two radii from the hole. Using hard metal insert, *i.e.*, of aluminum, bearing stress was reduced by 75% and 90% in the bearing region and at the edge of the hole in the ligament

regions, respectively. Camanho and Matthews [103] developed a 3D finite element model of bolted joint. The effect of insert material and its thickness was also studied to improve the performance of the joint. The bonded metallic inserts redistributed the radial stresses around the hole and reduced the stress concentration in the bearing plane. Considering the thickness and hardness of the insert material in terms of joint performance, the thin insert of aluminum were recommended over steel. Using thick metal insert changed the failure mode to net-tension and were not recommended. A novel type of bonded metallic insert with tapered ends, which resulted in a delay in the onset of damage in the composite, was proposed by Camanho *et al*. [104]. The experimental and numerical analysis was performed to improve the strength and the efficiency of single-shear bolted joints. Incorporating bonded metallic inserts, increased the load corresponding to the damage onset, ultimate failure loads, and efficiency of the joint. Mara *et al*. [105] used metallic inserts in the hole to tackle reduced stiffness and joint efficiency due to hole clearance and loss of bolt tension due to creep deformation. Effect of metallic inserts on the bolt tension relaxation, the stiffness and the load bearing behavior of joints was analyzed experimentally and numerically. Bolt tension relaxation was minimized, and the load transfer by friction was found to be feasible and the joint efficiency was increased in terms of stiffness and strength.

2.2 Aging Environment Effects on PMCs and FRPs

Components prepared from FRPs for applications such as aircraft, marines, automotive, infrastructure are exposed to hygrothermal conditions such as rain, temperature, and humidity. Therefore, it is necessary to study the effects of hygrothermal conditions on the performance of composite materials and its joints.

The polymer swells upon exposure to moisture, and the combined effect of moisture and temperature has shown a significant degradation in epoxy and reduced the performance of the composite materials. On the other hand, nanoparticles, for example, organo montmorillonite nanoclay has shown tremendous improvement in the resistance to degradation of epoxy due to moisture absorption at higher temperatures. Chow *et al.* [63] studied the water absorption, and hygrothermal aging of organomontmorillonite (OMMT) reinforced polyamide 6/polypropylene, with and without maleated PP (MAH-g-PP). Samples were immersed in hot water at three different temperatures (30, 60 and

90°C) and weight gains were recorded periodically. The percentage gain at any time (M_t) as a result of moisture absorption was determined by equation (2.11)

$$M_t(\%) = \frac{W_w - W_d}{W_d} \times 100 \tag{2.11}$$

where, W_d and W_w denotes the weight of dry material and the weight of material after hygrothermal exposure. Equation (2.12) was used to express weight gain in two different parameters, *i.e.*, Diffusion Coefficient (D) and Equilibrium moisture content (M_m).

$$\frac{M_t}{M_m} = 1 - \frac{8}{\pi^2} \exp\left[-\left(\frac{Dt}{h^2}\right)\pi^2\right] \tag{2.12}$$

where, h is the thickness of the specimen and t is the time. Equilibrium moisture content (M_m) and the Diffusion Coefficient (D) were found to be dependent on the OMMT loading, MAH-g-PP concentration, and immersion temperatures. After exposure to hygrothermal ageing, both the tensile modulus and strength of the PA6/PP nanocomposites diminished. Addition of MAH-g-PP compatibilizer increased retentionability in modulus and strength (in the wet and redried states), of nanocomposites when subjected to hygrothermal ageing. Equilibrium moisture content and diffusion constant remarkably reduced in comparison to neat PA6/PP. Aircraft grade epoxy–clay nanocomposites based on tetraglycidyl-4, 40 diaminodiphenylmethane (TGDDM) cured with diaminodiphenyl sulphone (DDS) were synthesized by Liu *et al*. [106]. High-pressure mixing method was used to disperse nanoclay into acetone only and epoxy/acetone solution. X-ray diffraction (XRD) demonstrated an increase in basal spacing of the nanoclay. From transmission electron microscopy (TEM) images, agglomerates of nanoclay were found broken into several clay platelets. Fracture toughness and strain energy release rate of the epoxy system was significantly enhanced with the addition of nanoclay. It was concluded that the significant reduction in the diffusivity and the maximum water uptake of the epoxy resin was due to addition of the nanoclay. The effect of the nature of glass fiber surface in the water absorption of glass fibers/epoxy composites was studied by Olmos *et al.* [107]. Three different silane coatings were used to change the surface of glass fiber. To study the water absorption process in composites, gravimetry and FTNIR were used. Considerable delay in water accessibility was shown at the interface which depends on the nature of the glass fiber

surface. Liu *et al*. [108] presented models for the water absorption behavior of epoxy–clay nanocomposites. Diffusion models for epoxy including the Fick's law, diffusion with time-varying diffusivity, Langmuir model of diffusion, and diffusion models for composites were reviewed. Models were developed for diffusivities of intercalated and exfoliated nanocomposites. Diffusion models developed for different types of nanocomposites were confirmed through experiments by Liu *et al*. [109]. Specimens of neat epoxy and epoxy/nanocomposites were immersed in distilled water at constant temperatures of 23°C, 50°C and 80°C for 5000 hours and examined for water absorption behavior. The equilibrium moisture content of the nanocomposites was measured, and diffusivities were determined by fitting Fick's Law, Langmuir model of diffusion (LMD) and diffusion with time varying diffusivity (DTVD) to the experimental data, employing a least-square approach. The effects of materials, dispersion processes and morphology on water uptake behavior of nanocomposites were investigated. The epoxy clay interface influenced the water uptake behavior of the epoxy. The diffusivity and maximum water uptake increased with untreated clay loading. However using organoclay, the maximum water uptake and diffusivity decreased with clay loading. The reduction ratio was dependent on the quality of the dispersion of the nanoclay. High pressure mixing (HPM) method showed better dispersion and thus better tortuosity effect. The water uptake and diffusivity were reduced by 20% using HPM to disperse organoclay. In another study on the epoxy/MMT nanocomposites, Glaskova and Aniskevich [110] examined moisture absorption behavior using four filler wt.%,, *i.e.*, 0, 2, 4 and 6. For the highest filler content, diffusivity reduced to about half of the diffusivity as for neat epoxy resin. Clay nanoparticles acted as an efficient barrier against moisture transport. Sorption process was described by Fick's model with good agreement for all contents of clay as well as for all environmental conditions. The nanoclay reduced the adverse effect of moisture on the properties of nanocomposites. The impact of tap water and sea water exposure on the mechanical and physical properties of GFRP composite laminates was studied by Aldajah *et al*. [58]. The symmetric laminates lost a total of 60% of the flexural stiffness and 55% when exposed for 2000 hours to sea water and tap water, respectively whereas, anti-symmetric specimens lost 28% and 29.4% when exposed to the similar conditions. It was concluded through the SEM micrographs that the major loss of the stiffness is due to the adhesion loss between the fiber and the epoxy. In another study of seawater exposure,

Lee *et al.* [111] dispersed multi-walled carbon nanotube (MWCNT) in epoxy to investigate its effect on the tensile and fracture behaviors of epoxy nanocomposites. Unmodified, oxidized, and silanized MWCNTs of 0.1 wt.% were used to fabricate the nanocomposite. Irrespective of moisture absorption, silane-modified specimens showed higher elastic modulus, tensile strength, and transmittance than unmodified or acid-modified specimens. Tensile strength and elastic modulus decreased for moist nanocomposites compared with dry nanocomposites. Fracture toughness of oxidized and silanized MWCNT/epoxy nanocomposites was not significantly different, whereas unmodified specimens showed lower fracture toughness, irrespective of moisture absorption. It was predicted that moisture absorption and especially NaCl molecules in seawater had caused rapid degradation in MWCNT/epoxy nanocomposites resulting in weak interfacial bonding due to epoxy swelling. Adding some work into the numerical analysis of the nanocomposites under hygrothermal conditions, Lo *et al*. [112] developed a four-node quadrilateral plate element based on the global-local higher-order theory (GLHOT) to study the response of thick multilayered composite plates due to a variation in temperature and moisture concentrations. Numerical results revealed that the relationship between the hygrothermal response of laminated plates and the rise of temperature and/or moisture concentrations was no longer linear. Balakrishnan *et al.* [113] investigated water absorption and hygrothermal degradation, and soil burial analysis on polylactic acid montmorillonite nanocomposite (PLA/MMT) and linear low density polyethylene (LLDPE) toughened PLA/MMT nanocomposites. It was shown that the maximum moisture absorption (M_m) and diffusivity (D) of PLA and PLA/LLDPE increased with the addition of MMT (2 phr). Beyond this, a decrease in diffusivity of both composites was observed using 4 phr MMT due to agglomeration. Increasing the temperature from ambient to 60°C, maximum moisture absorption, and diffusivity increased. Continuous exposure to water at high temperature (60°C) resulted in hygrothermal degradation of both nanocomposites. Soil burial test revealed a decrease in impact strength. An optimization procedure for stiffened panels under hygrothermal and mechanical loads was developed by Marin *et al*. [114]. The procedure composed of two steps. Firstly, the response of the panel was obtained by a neural network system using the results of finite element analyses and, secondly, a multi-objective optimization problem was solved using a genetic algorithm. The neural network implemented in the

first step used a sub-problem approach which allowed to consider different ranges of temperature. The ANN reduced the computational cost by 92.8% with a suitable accuracy. Comparing the reference and the optimal panels, the mass reduced about 0.54%, and the tension between the stringers and the skin, and the hygrothermal strains decreased until 7.55% and 6.48%, respectively in specific load cases. Starkova *et al.* [115] investigated the thermo-mechanical properties of an epoxy resin filled with multi-wall carbon nanotubes (MWCNT), and thermally reduced graphene oxide (TRGO). Samples were exposed to hot distilled water. Addition of low contents of MWCNTs and TRGO reduced the water sorption capacity of the epoxy and improved its resistance to hydrothermal aging. A considerable drop of about 90°C in the glass transition temperature (Tg) of the neat epoxy was observed, whereas this shift in Tg was merely 8°C in the case of nanocomposites. Use of TRGO demonstrated better improvements in thermo-mechanical properties over MWCNTs for both hydrothermally exposed and unexposed conditions. In another study presented by Jen and Huang [116], the hygrothermal effect on the static and fatigue strengths of multiwalled carbon nanotubes (CNTs)/epoxy composites was investigated. Humidity itself showed less influence on the static and fatigue strengths of nanocomposites, compared with combined effects of temperature and humidity. At 40°C/85% RH condition, interfacial adhesion between carbon nanotube surface and epoxy were found to be significantly weakened. Usage of 0.5wt.% CNT content increased static and fatigue strength compared with neat epoxy. Hamim and Singh [117] investigated the degradation of fracture toughness, flexural strength, and flexural modulus, due to the combined effect of moisture and elevated temperature on EPON 862, Somasif MAE, and Nanomer I.28E clay-epoxy nanocomposites. Interface weakening, hydrolysis, and chain scission, responsible for the observed effect, was reported. Although incorporation of nanoclay in the epoxy matrix could not fully stop the degradation, it was observed that the studied properties, in general, were less severely degraded for epoxy-clay nanocomposites compared to neat epoxy specimens.

The effect of environmental conditions has been studied not only in polymer matrix composites but also in fiber-reinforced plastic composites. Singh *et al.* [30] prepared fiber reinforced nanocomposites using epoxy resin, unidirectional E-glass fiber and natural

montmorillonite Closite 30B nanoclay with 3 different levels (1 wt.%, 3 wt.%, 5 wt.%) using hand layup method. The fiber content in three composites was taken as 30 wt.% of the total weight of the composite. Epoxy resin; diglycidyl ether of bisphenol A (DGEBA) and hardener (polyamine) mixed in 10:4 weight ratios was used. Tensile, flexural and hardness tests were carried out to assess the performance of the material. Optimum values for all tests were predicted for 3 wt.% nanoclay composite and compared to 1 wt.% and 5 wt.% nanoclay composites. Samples were immersed in water and NaOH at 45°C for 30 days to check durability. Mechanical properties degradation was more severe in NaOH as compared to pure water. A progressive failure analysis model involving hygrothermal effects to predict the failure of composite structures in hygrothermal environments was presented by Zhang *et al*. [15]. The temperature-induced modification of stiffness and strength parameters were involved in the stress analysis model, failure criterion and in material property degradation. The proposed model was verified by testing specimens made of carbon/bismaleimide composites with two typical lay-ups. Firdosh *et al.* [14] predicted the long-term durability of 0 to 5 wt.% nanoclay/vinylester/glass fiber nanocomposites exposed to the accelerated hygrothermal environment. Experiments at 30°C, 50°C and 60°C with 95% relative humidity were conducted for 75 days. Tensile strength retention was estimated for one year of aging, as a function of the duration of exposure, using the Arrhenius rate model. Observed values of tensile strength retention for vinylester/glass at 30°C, 50°C and 60°C were 59%, 48%, and 43%, respectively. The corresponding strength retentions predicted for 4 wt.% nanoclay/vinylester/glass were 81.1%, 77.9% and 76.4%. An analytical model was also developed to assess long-term performance over a period of ten years.

The effect of different environmental conditions has been studied extensively in the performance of PMCs and FRPs, whereas a little work is reported on the performance of the joints under different environmental conditions. Park and Kim [118] studied the high-velocity transverse impact of composite joints by hailstones. The damage area versus impact kinetic energy was found to increase dramatically for impacts beyond the failure threshold. Delamination of the composite originated at the bond overlap termination facing away from the impact side. Numerical simulation of the impact was conducted, and the results showed that the plies where delaminations were observed to occur

demonstrated the highest peel and shear stresses. A novel finite element based framework was developed by Zhang and Rowland [119] to study the effect of extreme temperatures on damage progression in carbon-fiber reinforced composite pinned joints. A progressive damage method incorporating Hashin damage criteria was implemented in the model. The model was verified with a double-shear pin joint tensile test conducted at room temperature. Soykok *et al*. [20] determined the effects of the thermal condition and tightening torque on the failure load and failure behavior of glass-epoxy composite lap joints. The load-carrying capacity of the joint decreased gradually by increasing the temperature level. Tightening torque contributed to the joint strength and was effective not only at room temperature but also at elevated temperatures. In another experimental study, Soykok *et al*. [13] investigated the influence of hot water immersion on mechanically fastened joints prepared from glass fiber/epoxy. Prior to the joint assembly and testing, the specimens were exposed to hot water at different levels of temperatures, *i.e.*, 50, 70, and 90°C for the duration of 1 and 2 hours. Tensile tests revealed that the failure behavior of joints in aged specimens was strictly related to the temperature applied and exposure time in hot water. Both, raising water temperature, and extending immersion time showed adverse effects on the mechanical properties of the joint. Kapidzic *et al*. [120] investigated the bearing failure process in quasi-isotropic carbon-epoxy laminate and the influence of biaxial bolt load on the bearing strength. A comparative study was carried out for unidirectional and bidirectional bolt loads at elevated temperature. A numerical model was also developed to compare with experimental results. Microscopic study of the bearing plane was performed to support the numerical computations. It was shown that delamination did not affect maximum bearing load, but is still important to understand and accurately model the bearing failure process. Biaxial loads did not show any extra effect on maximum bearing load. It was found that the bolt hole clearance and pretension are the important parameters which affect the bearing type of failure.

The ultraviolet (UV) radiations of the short wavelengths, *i.e.*, of nanometer range, present in the Sun spectrum, have also shown a significant effect on the degradation of polymer materials. The exposure to a combination of ultraviolet radiation along with moisture and temperature causes severe degradation and microstructural changes in the PMCs and

FRPs. Kumar *et al.* [16] studied the degradation of carbon fiber reinforced epoxy laminates exposed to a combination of UV and condensation. The degradation mechanism was identified by examining the micrographs of the composite surface, and monitoring weight loss and/or gain. To reveal the degradation chemistry, FTIR was performed. The degradation of mechanical performance of the material was determined through a uniaxial tensile test on various specimen configurations subjected to accelerated aging conditions. A cyclical exposure of 1000 hours, matrix erosion was observed leading to a reduction in the mechanical properties of the composite material and thus reduced the transverse tensile strength of the material by 29%. There was a decrease in transverse modulus also but not as severe as the reduction in the tensile strength. Epoxy-organoclay nanocomposite degradation under UV condensation cycle was studied by Woo *et al.* [18, 121]. Microcracks were observed in neat and nanocomposites after 300 hours of UV exposure. The color of the neat epoxy and nanocomposite specimen was darkened upon the UV exposure. Upon UV exposure, a gradual drop in the luminance value for all the specimens was observed, and after 700 hours, it reached a plateau. Mouzakis *et al.* [122] constructed an environmental chamber to test the combined effect of temperature, humidity and UV radiation on polymers and composites. Dynamic mechanical analysis (DMA) reported a reduction in the strength, and a gain in the stiffness of the aged materials. Residual mechanical properties were investigated, and a positive contribution of organoclay was observed in the barrier characteristics to the UV condensation exposure. Boubakri *et al.* [123] studied the characteristics of thermoplastic polyurethane (TPU) exposed to artificial weathering conditions in a UV chamber. The morphology, mechanical and thermal properties were investigated by scanning electron microscope (SEM) images, universal testing machine (UTM) and differential scanning calorimetry (DSC), respectively. The TPU material was colorless initially, turned yellow after 6 hours and brown after an exposure of 72 hours. Further exposure to UV did not change the color of the specimen. The formation of micro-cracks was observed through SEM micrographs. In another study on the organomontmorillonite (OMMT) reinforced nanocomposites, Chang and Chow [19] studied the effect of UV radiation on glass fiber/epoxy nanocomposites. Different loading of organomontmorillonite (OMMT) content, *i.e.*, 0, 1, 2, 3, and 4 wt.% were considered for the experiments. Good retention-ability was observed in flexural modulus and

strength of epoxy hybrid nanocomposites exposed to accelerated weathering conditions. However, fracture toughness was significantly reduced after exposure to UV radiation. Acoustic emission technique along with mechanical testing was used by de Souza Rios *et al.* [124], to characterize the damage areas of composite plates of three different thicknesses exposed to UV radiation. Accelerated aging influenced the mechanical, thermal and morphological behavior of the composite material. Thinner composite demonstrated a reduction in modulus of elasticity and tensile strength. The Izod impact test demonstrated a reduction in the impact strength of 3 and 6 mm thick specimens. Nicholas *et al.* [125] investigated the microstructure and impact behavior of TPU exposed to the accelerated aging environment. Colorimetry was performed to evaluate the color change of specimen due to UV exposure. Color change and chemical structure degradation increased with aging duration. More than 700 hours were taken for 70% of the total color change. In another study of carbon-epoxy composites, Barbosa *et al.* [126] studied the effect of accelerated environmental conditions in an aging chamber with controlled humidity, temperature, and UV radiation. Fourier-Transform Infrared (FTIR) Spectroscopy, SEM, Dynamic Mechanical Analysis (DMA), mass variation, and inter-laminar shear strength and compressive strength tests were performed to investigate changes within the material. The changes in the material were observed by fiber exposure, mass loss, chemical alteration, and increased crack density.

2.3 Conclusion from the Literature Review

The work done by different researchers on mechanical joints can be concluded as follows:

(i) Geometric parameters, E/D, and W/D have a significant effect on the strength of the mechanical joint. Increasing E/D and W/D ratios increase the strength of the mechanical joint.

(ii) Incorporation of filler materials into matrix improves the performance of polymer composites.

(iii) The combined effect of water and temperature results in a weight loss and strength reduction in FRPs.

(iv) Nanoclay loading of 3 to 4 wt% gives better tensile strength retention after hygrothermal aging, compared to the material without nanoclay. Water absorption rate and maximum moisture content reduced upon using nanofiller content.

(v) Silane coating on the glass fiber surface improves the interfacial bond strength between epoxy and glass fiber.

(vi) Incorporation of metal insert reduces stress concentration around the hole and improves joint efficiency.

While several researchers worked on the performance of mechanical joints under normal environmental conditions, others investigated the effect of different environmental conditions on the structure-property degradation of the PMCs and FRPs. Very few of the researches focused on the performance of the mechanical joints exposed to different environmental conditions. On the other hand, incorporating nanofillers into the FRPs have shown improvements in mechanical performance not only at room temperature but also in different environmental conditions. Hence, the present work deals with the performance analysis of mechanical joints under varied environmental conditions. To improve the joint resistance to degradation due to moisture and temperature attack, nanofiller, *i.e.*, nanoclay, has been used to make high performance GFRP nanocomposites.

Chapter 3
Materials, Methods, and Testing

Different materials, methods along with the testing procedures used to make the fiber-reinforced composite laminates are discussed in the present chapter.

3.1 Materials

Epoxy, hardener, accelerator, glass fabric, and metal inserts were used as different materials for preparation of pin joint specimens.

3.1.1 Resin

The DGEBA (diglycidyl ether of bisphenol-A) based epoxy (L-12), hardener (K-12), and accelerator (K-13), supplied by Atul Ltd., Gujarat, India, were used in the present work. The properties of epoxy, hardener, and accelerator are shown in Tables 3.1 to 3.3.

Table 3.1 Physical properties of the epoxy resin

Description	Density (g/cm^3)	Viscosity (mPa.s)
Epoxy (L-12)	1.1–1.2	9000–12000
Hardener (K-12)	1.15–1.25	150–230
Accelerator (K-13)	0.88–0.92	<10

Table 3.2 Processing properties of the epoxy resin

Property	Resin: Hardener : Accelerator mix ratio (by wt.)	Initial mix viscosity	Pot life of mix (< 5 Kg)	Gel time
Condition	-	@ 40°C	@ 80°C	@ 80°C
Unit	w/w	cPs	Minutes	Minutes
Value	100 : 100 : 0.1–2	450	60	150

Table 3.3 Mechanical properties of the epoxy resin (L-12 + K-12 + K-13)

Property	Value
Specific gravity	1.80–1.85
Tensile strength (MPa)	70–90
Tensile modulus of elasticity (GPa)	15–16
Compressive strength (MPa)	190–210
Flexural strength (MPa)	100–120
Impact strength (kJ/m^2)	4–7

3.1.2 Glass fiber

E-glass fiber 'Advantex' of two different types of constructions, *i.e.*, unidirectional of 1200 gsm, and 2D plain woven of 360 gsm, were used as reinforcement in the present work. The glass fiber was supplied by Owens Corning India Pvt. Ltd, Mumbai, India. The physical and mechanical properties of the glass fiber are shown in Table 3.4.

Table 3.4 Physical and mechanical properties of the glass fiber

Property	Test method	Value
Density	ASTM D1505	2.62 g/cc
Thermal linear expansion 0–300°C	ASTM D696	6 ppm/C
Softening point	ASTM C338	916°C
Tensile strength at 23°C	ASTM D2101	3100–3800 MPa
Elastic modulus	Sonic method	80–81 GPa
Elongation at the breaking load	ASTM D2101	4.6%

3.1.3 Nanoclay

Natural montmorillonite modified Cloisite 30B was used as nanofiller to enhance the mechanical properties of the epoxy. The nanoclay was supplied by Nanoshell, Wilmington, Delaware, USA. Typical properties of the nanoclay are shown in Table 3.5.

Table 3.5 Typical properties of the nanoclay

Organic modifier	Modifier concentration	Typical dry particle size	Purity	Moisture	Weight loss on ignition
MT2EtOH	90 meq/100g clay	< 80 nm	99%	< 2%	30%

3.1.4 Fastener

High tensile fasteners manufactured by commercial available brand ''Unbrako'' with a metric size of 4 mm in diameter have been used in the present work. Lock nut has been used to avoid undesired loosening of the nut-bolt assembly. The mechanical properties of the fasteners used in joints are shown in Table 3.6.

Table 3.6 Mechanical properties of the fastener

Description	Material	Ultimate tensile strength (MPa)	Tensile load (kN)
4 mm dia socket head cap screw	Alloy steel	1300	11.4

3.1.5 Metal insert

The metal inserts prepared from mild steel were used to redistribute the stresses and reduce the stress concentration around the hole. The physical and chemical properties of the metal insert material are shown in Table 3.7 and 3.8, respectively.

Table 3.7 Physical properties of the mild steel material

Property	Value
Density	7.87 g/cc
Tensile yield strength	370 MPa
Tensile modulus	205 GPa

Table 3.8 Chemical composition of the mild steel material

Property	Value (%)
Iron (Fe)	98.8–99.3
Phosphorous (P)	≤ 0.039
Sulfur (S)	≤ 0.049
Carbon (C)	0.15–0.19
Manganese (Mn)	0.61–0.89

3.2 Methods

The following sections give the description of the processes in the preparation and characterization of the materials used in the present work.

3.2.1 Manufacturing methods

The manufacturing of glass fiber reinforced composite laminates involves several processes. Initially, several glass fabric sheets were cut to the adequate size as per the mold. Then the epoxy resin was prepared. High viscous stirring followed by sonication is used to disperse the nanoclay into the epoxy. After the preparation of epoxy resin, the hand layup technique was used to prepare the laminates. Different processes used to make composite laminates are discussed in the following section.

3.2.1.1 Mixing

The mixtures of hardener and nanoclay were prepared using a high viscous stirrer at 8000 rpm for 15 minutes and brought to a state where the constituents were equally distributed throughout the mixture. The viscosity of the hardener is lower than the epoxy resin, which eventually helped to mix nanoclay into the resin.

The high viscous stirrers are used for laminar mixing of liquids with high viscosities in which turbulent mixing flow cannot be obtained easily without a significant amount of heat generation.

3.2.1.2 Sonication

After mixing in high viscous stirrer, the mixture was sonicated for 70 minutes in Oscar probe sonicator, Oscar Ultrasonics Pvt. Ltd., Maharashtra, India. The ultrasonic waves were passed through the mixture so that the constituent particles get agitated. Sonication was done with the current of 0.6 Amp, and pulse on-off time as 10 and 2 seconds, respectively. Small quantities of the mixture were used in repeated cycles to increase the efficiency of the probe sonicator. After completion of the sonication process, the epoxy resin was mixed using high viscous stirrer for 10 minutes at 8000 rpm.

3.2.1.3 Hand layup

Hand layup is an old and simple technique used to stack up a number of fabric layers adhered to epoxy. To start with, a Teflon sheet was placed over the shelf. With the help of a brush, the epoxy was applied onto the Teflon sheet. Placing the first layer of the glass fiber on the Teflon sheet, resin was applied on it and then second layer was placed over the first layer. Repeating these steps several times, two different stackups of 3 and 9 layers were prepared using two different fabrics, *i.e.*, unidirectional glass fiber, and 2D plain woven glass fiber. The hand roller was used to remove any entrapped air particles between the layers and to facilitate the laminate to stick together.

3.2.1.4 Compression molding

It is a closed-mold composite manufacturing process that uses heat and pressure to mold a material. In the compression molding process, a laminate was placed between the heating metal plates. The temperature, pressure, and hold time were set to the optimized levels. The combination of heat and pressure produces a laminate with low void content and high fiber volume fraction. The compression molding used in the present work has the capacity of 500 kN.

3.2.2 Aging methods

The temperature and moisture plays a vital role in the degradation of the fiber reinforced polymer composites. On the other hand, ultraviolet radiations of short wavelength can

also affect the durability of the FRCs. Following are the different methods used in the present work for the aging of the fiber reinforced composite specimens.

3.2.2.1 Hydrothermal aging

The specimens were submerged in distilled water in a digital water bath to analyze the effect of temperature and moisture. The bath used in the present work is LSB-24 supplied by Spectra Lab Instruments Pvt. Ltd., Mumbai, Maharashtra, India. The specimens were exposed to different temperatures and durations to estimate the effects of temperature and exposure time on the performance of the composite laminate and its joints.

3.2.2.2 Accelerated aging

The accelerated weathering test was performed to study the effect of accelerated aging conditions on the specimens made with neat epoxy and epoxy with nanoclay content. The accelerated weathering test was performed using a QUV accelerated weathering tester Model QUV/spray with solar eye irradiance control (Q-Lab Corporation, USA) with ASTM D1544 standard as its reference. The specimens were illuminated with UVB lamp emitting ultraviolet (UV) with short wavelengths of 295 nm with an irradiance of 1.0 w/m^2. UV-B radiation carries the shortest wavelength of sunlight found on earth's surface. Therefore, UVB lamps are widely used in quality control, research and development for fast and cost-effective results. The specimens were exposed to a total of 500 hours of cyclical ultraviolet (UV) exposure, 8 hours of ultraviolet (UV) radiation at 60°C followed by 4 hours of condensation at 50°C. The environment in the chamber was maintained at 100% relative humidity at elevated temperatures.

3.2.3 Characterization methods

The following are the different methods used for the characterization of the material used in the present work.

3.2.3.1 X-ray diffraction (XRD)

The powder X-ray diffraction (XRD) patterns of samples were obtained on a PANalytical X'Pert PRO diffractometer using Cu–Kα radiation. It was taken in low angle 2θ range of 0–10° and wide-angle 2θ range of 10–80° with current and tube voltage of 40 mA and 45 kV, respectively.

3.2.3.2 Scanning electron microscopy (SEM)

The surface morphology of the samples was analyzed by scanning electron microscope (JEOL JSM–6510 LV) at an accelerating voltage of 20 kV. Before the analysis, sample was coated with gold of 50 μm thickness with the help of automatic sputter coater (Polaron) to prevent sample charging problems.

3.2.3.3 Field emission scanning electron microscopy (FESEM)

Field emission scanning electron microscopy using FESEM SU8010 HITACHI at an accelerating voltage of 15 kV was performed to determine the presence and distribution of nanoclay into the epoxy.

3.2.3.4 Fourier transform infrared (FTIR) spectroscopy

To determine possible chemical changes into the composite material subjected to different aging conditions, Fourier transform infrared (FTIR) spectroscopy of specimens was performed using PerkinElmer make, Spectrum 2 model, FT-IR spectrometer. FTIR was performed for both the aged and unaged material to compare the results. The range of spectra was 400–4000 cm^{-1} with a resolution of 2 cm^{-1}. Specimens were conditioned in a desiccator before analysis.

3.2.3.5 Mechanical properties using universal testing machine (UTM)

The different mechanical properties, *i.e.*, tensile modulus, tensile strength, compressive strength, and shear strength of the prepared composite laminate were tested on 10 Ton capacity Dak System Inc. India make universal testing machine. The mechanical failure of the joints were tested on the in-house Zwick-Roell Universal Testing Machine–Model Z010, Zwick-Roell, Germany.

3.2.4 ASTM standards

The following are the different ASTM standards used for testing in the present work.

3.2.4.1 ASTM D3039

The tensile testing of the composite laminates was performed according to the ASTM D3039 standard. The specimens as shown in Fig. 3.1 were tested under tensile load on a universal testing machine at cross-head speed of 2 mm/min.

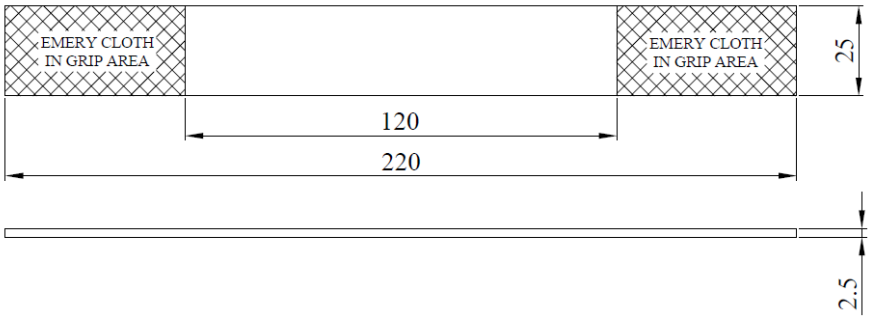

Fig. 3.1 Tensile test specimen as per ASTM D3039 (dimensions in mm)

3.2.4.2 ASTM D695

To determine the compressive strength of the laminates, ASTM D695 was used. The specimens as shown in Fig. 3.2 were tested under compressive load on a universal testing machine at cross-head speed of 1.3 mm/min.

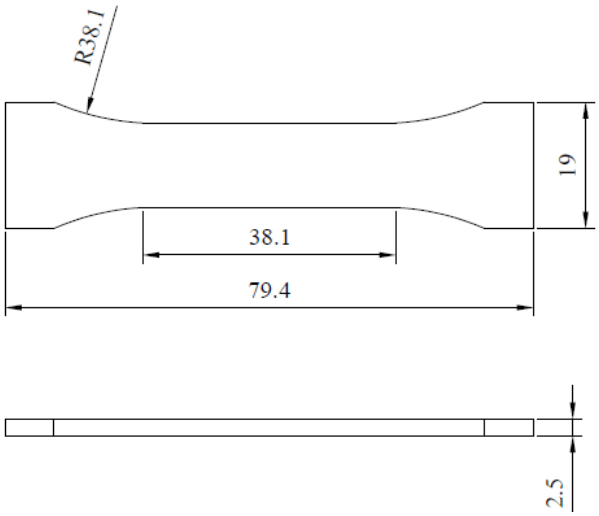

Fig. 3.2 Compressive test specimen as per ASTM D695 (dimensions in mm)

3.2.4.3 ASTM D5379

The shear testing of the composite laminates was performed according to the ASTM D5379. The specimens as shown in Fig. 3.3 were tested under shear load on a universal testing machine at cross-head speed of 2 mm/min.

3.2.4.4 ASTM D5961

To determine the effect of different parameters such as material variation, bolt torque, and aging conditions, the geometry of the bolted joint was fixed according to ASTM D5961. The geometry used in the present work is shown in Fig. 3.4.

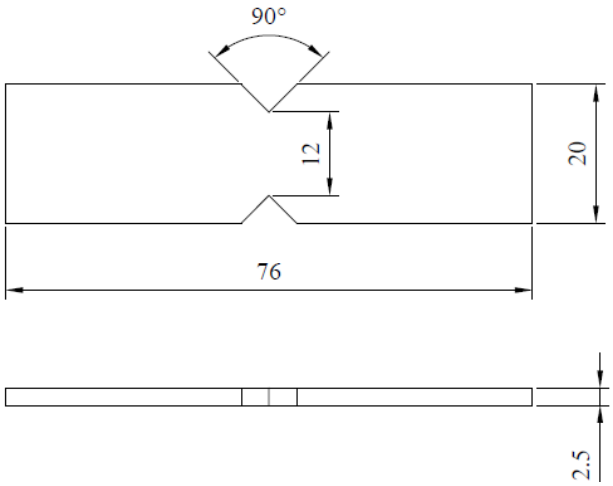

Fig. 3.3 Shear test specimen as per ASTM D5379 (dimensions in mm)

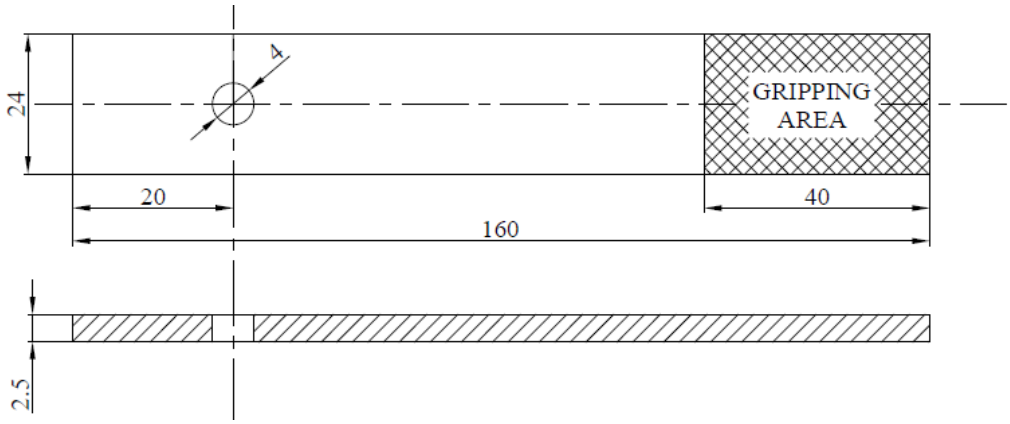

Fig. 3.4 Bolt joint test specimen as per ASTM D5961 (dimensions in mm)

3.2.4.5 ASTM D1544

The accelerated aging of the specimens was performed according to ASTM D1544 in an accelerated weathering tester. The specimens were exposed to a total of 500 hours of cyclical ultraviolet (UV) exposure, 8 hours of ultraviolet (UV) radiation at 60°C followed by 4 hours of condensation at 50°C. The environment in the chamber was maintained at 100% relative humidity at elevated temperatures

3.3 Composite Laminate Preparation and Testing

The process starts with the cutting of the glass fabric from the roll to the size adequate for compression molding. After cutting a sufficient number of laminas, epoxy resin was prepared as per ratio provided by the supplier which is shown in Table 3.2. To analyze

the effect of nanoclay on the performance of glass epoxy composite, two different types of materials have been prepared. One is fiber reinforced in neat epoxy and other is fiber reinforced in epoxy modified with nanoclay.

The laminate of desired thickness was prepared using the hand-layup technique. Once the composite laminate was ready, it was cured at room temperature for 36–48 hours. The laminate was then cured in compression molding machine. The curing parameters used in compression molding machine were optimized for maximizing the mechanical properties of the laminates prepared from the selected material.

3.3.1 Optimization of curing parameters

The temperature and pressure affect the laminate thickness and void content, which in turn have significant effects on the mechanical properties of the composite laminates [127]. Moreover, catalyst mixed in epoxy resin starts their reaction at room temperature. As per the current procedure, laminates were kept at room temperature for 36 to 48 hours before putting into the compression mold. The pre-phase time, *i.e.*, time to build up curing temperature in compression mold is generally more than 30 minutes. The laminates are kept in the mold during this temperature ramp-up time. Therefore, it was important to optimize process parameters, *i.e.*, pressure, temperature and hold time for curing composite laminates in compression molding machine. The design of experiments is used in the present work to reduce the number and cost of experimentation. For the design of experiment, number of techniques are available with, Taguchi method is the most commonly used to reduce the number of experimental trials.

3.3.1.1 Taguchi method

Taguchi developed a family of fractional factorial experimental matrices, called Orthogonal Arrays (OAs) which can be used under various situations to optimize the process parameters and improve the results [128-132]. To calculate the deviation between desired and experimental value of performance characteristic, a loss function is defined, which is further transformed into signal-to-noise (S/N) ratio. S/N ratio is further classified as shown in equations (3.1)–(3.3).

$$\text{Nominal is the best: } \frac{S}{N} = 10\ \log\left(\frac{\bar{y}}{S_{\bar{y}}^2}\right) \tag{3.1}$$

Larger is the better: $\frac{S}{N} = -10\ \log\left(\frac{1}{n}\sum_{i=1}^{n}\frac{1}{y_i^2}\right)$ (3.2)

Smaller is the better: $\frac{S}{N} = -10\ \log\left(\frac{1}{n}\sum_{i=1}^{n} y_i^2\right)$ (3.3)

Where, $\bar{y}$ is the average of observed data, n is the number of observations, S_y^2 the variance of y with y is the observed data.

In the present study, the objective is to maximize the strength of the material. Therefore, equation (3.2), 'Larger is the better' is used to calculate the S/N ratios.

In the present study, three factors, *i.e.*, pressure, temperature and holding time with four levels each have been selected for analysis. The degree of freedom of the problem is 9. A fractional factorial design using standard L_{16} orthogonal array having 15 degree of freedom, which is larger than the degree of freedom of the current problem, has been adopted here. Different levels of control factors are shown in Table 3.9.

Table 3.9 Factors and levels considered in compression molding process

Factor	**Levels**			
	0	**1**	**2**	**3**
A–Pressure (kN)	100	120	140	160
B–Temperature (°C)	90	120	150	180
C–Hold time (min)	10	20	30	40

Table 3.10 Tensile and compressive strength of the laminates cured at different levels of pressure, temperature, and duration

Experimental run	**Factor**			**Tensile strength (MPa)**	**Compressive strength (MPa)**
	A	***B***	***C***		
1	0	0	0	349	199
2	0	1	1	368	212
3	0	2	2	377	234
4	0	3	3	378	227
5	1	0	1	368	190
6	1	1	0	377	216
7	1	2	3	390	249
8	1	3	2	390	246
9	2	0	2	377	234
10	2	1	3	390	249
11	2	2	0	390	243
12	2	3	1	395	256
13	3	0	3	377	230
14	3	1	2	390	244
15	3	2	1	395	250
16	3	3	0	390	238

The tensile and compressive strengths for the different experimental runs are shown in Table 3.10. These tests were conducted on German make Zwick-Roell Universal Testing Machine.

To determine the best values of temperature, pressure and hold duration that simultaneously maximizes the tensile and compressive strength, the values of both tensile and compressive strength are normalized in the range of 0 to 1 to get a comparable sequence. μ_t and μ_c are the membership functions [129] associated with tensile and compressive strength, respectively and are defined by equations (3.4) and (3.5).

$$\mu_t = 1 - \frac{T}{T_{max}} \tag{3.4}$$

$$\mu_c = 1 - \frac{C}{C_{max}} \tag{3.5}$$

Where, T and C are the normalized values of tensile and compressive strength, respectively which are calculated using equation (3.6) corresponding to each experimental trial. Based on experimental results, T_{max} and C_{max} are the maximum normalized values of tensile and compressive strength. For the simultaneous maximization of tensile and compressive strength, the area *A* (FGHIJF) shown in Fig. 3.5 should be as maximum as possible. The area *A* can be calculated using equation (3.7).

$$X_n = \frac{X_i - min}{max - min} \tag{3.6}$$

$$A = \frac{1}{2}[T\ (1 - \mu_t) + C\ (1 - \mu_c)] \tag{3.7}$$

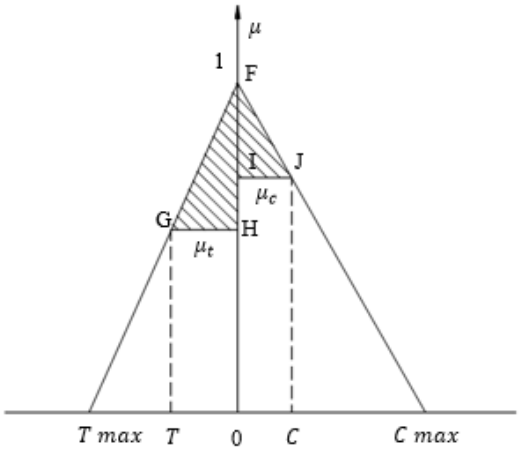

Fig. 3.5 Membership functions for tensile and compressive strength of the composite laminates

Table 3.11 Experimental run, normalized values, area and signal-to-noise ratio

Experiment No.	Normalized value		Area	Signal-to-noise ratio
	Tensile strength	Compressive strength		
1	0	0.13	0.01	-40.63
2	0.41	0.33	0.14	-17.02
3	0.60	0.66	0.40	-7.79
4	0.63	0.56	0.35	-8.97
5	0.41	0	0.08	-21.38
6	0.60	0.39	0.26	-11.60
7	0.89	0.89	0.79	-1.97
8	0.89	0.84	0.75	-2.41
9	0.60	0.66	0.40	-7.79
10	0.89	0.89	0.79	-1.97
11	0.89	0.80	0.71	-2.85
12	1	1	1	0.00
13	0.60	0.60	0.36	-8.66
14	0.89	0.81	0.73	-2.71
15	1	0.90	0.91	-0.78
16	0.89	0.72	0.66	-3.58

Normalized values (0 to 1) of the tensile and compressive strength of the composite laminates prepared in different experimental runs are listed in Table 3.11. Taking area (*A*) as a single response, S/N ratios have been calculated. The reaction rate of epoxy increases and curing time decreases with increase in cure temperature [133, 134]. Analysis of means has been performed using the calculated S/N ratio, and is shown in Table 3.12. The table also shows the rank of the process parameters affecting the multi-performance response based on the Delta (Δ) statistics.

Table 3.12 Response for signal-to-noise ratios

Process parameters	Level 1	Level 2	Level 3	Level 4	Δ(Max-min)	Rank
A (Pressure)	-18.60	-9.34	-3.15	-3.93	15.45	2
B (Temperature)	-19.61	-8.32	-3.35	-3.74	16.26	1
C (Duration)	-14.67	-9.79	-5.18	-5.39	9.49	3

From the S/N ratio graph shown in Fig. 3.6, it is clearly visible that the curing temperature has a significant effect on the mechanical strength of the composite material. As the mold set temperature increases, the degree of cure of the epoxy increases resulting in higher mechanical properties.

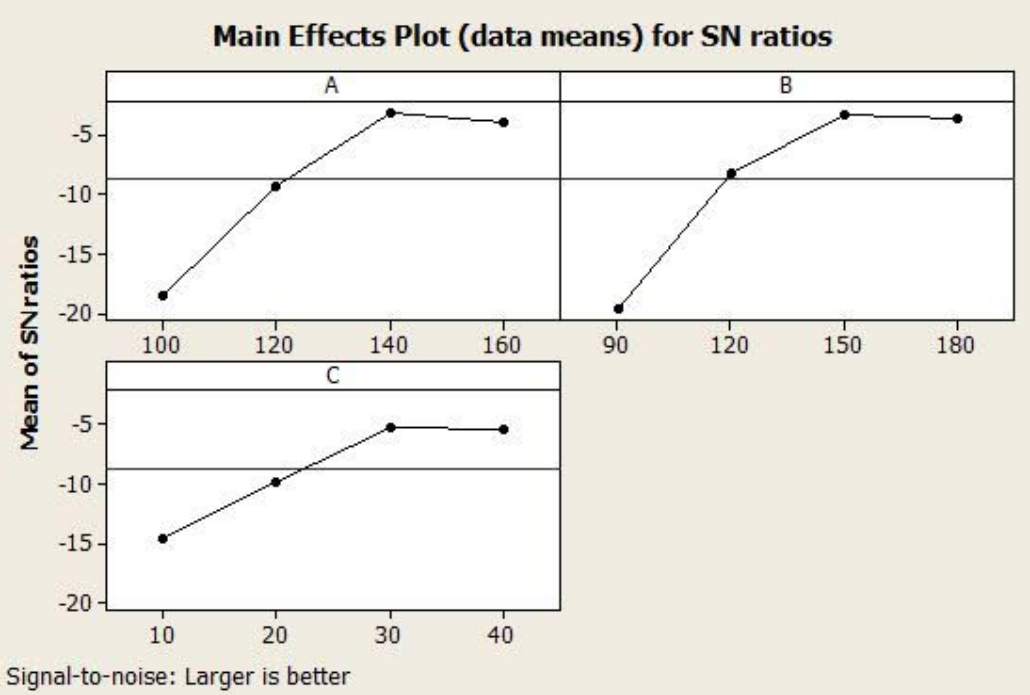

Fig. 3.6 S/N ratio plots of the combined response of the tensile and the compressive strength of the laminates cured at different levels of pressure, temperature, and duration

As shown in S/N ratio plots, the effect of curing time is significantly reduced beyond 30 minutes. As seen in the S/N ratio plots, increasing pressure from 100 to 140 kN increases the strength of the composite material. The cure pressure has also shown significant improvements in the mechanical properties of the composite materials as it reduces the void content [127]. Hence the optimum strength can be achieved using the pressure of 140 kN, temperature of 150°C and holding time of 30 minutes.

The relative significance of the process parameters is established using analysis of variance (ANOVA), as shown in Table 3.13. The p-value below 0.5 (at 95% confidence interval) for all parameters shows that all the process parameters are significant. The results obtained are verified by performing confirmation test at optimized process parameters. The confirmation test for tensile and compressive strengths gave the values as 410 MPa and 270 MPa, respectively, which are greater in comparison to all responses shown in Table 3.10.

So, the optimum parameters, *i.e.*, pressure of 140 kN, temperature of 150°C and holding time of 30 minutes, were further used for the preparation of laminates in the present work.

Table 3.13 Analysis of variance for SN ratios

Source	DF	Seq SS	Adj SS	Adj MS	F	P
A (Pressure)	3	607.85	607.85	202.62	14.14	0.004
B (Temperature)	3	689.86	689.86	229.95	16.04	0.003
C (Duration)	3	240.59	240.59	80.20	5.60	0.036
Residual Error	6	85.99	85.99	14.33		
Total	15	1624.29				

3.3.2 Estimation of appropriate wt.% of nanoclay

To determine the appropriate wt.% of nanoclay required to be mixed in the epoxy, the nanoclay concentration was varied from 1 to 5 wt.%. After varying the nanoclay concentration, the crystallographic studies were carried out on the epoxy nanocomposites using X-ray diffraction (XRD) test. XRD detects the periodically stacked clay platelets and was carried out in a Panalytical X-ray diffractometer with Cu K_α radiation (λ=1.54Å). The scanning 2θ range was from 0.5° to 10° at 1° /min. Bragg's Law [135] was used to determine the d-spacing. The XRD results shown in Table 3.14 indicates an increase in d-spacing between the platelets of nanoclay. The interlayer spacing of the epoxy modified with nanoclay ranges between 43.2–44.1 Å, which is almost double than the pure nanoclay (Cloisite 30B) powder, *i.e.*, 21.9 Å. An increase in d-spacing values indicates that polymer was able to enter the interlayer spacing between platelets which swell the clay and an intercalated structure was obtained for the resulting nanocomposite.

Table 3.14 d-spacing of nanoclay and nanocomposites of different wt.% of nanoclay

Set No.	Clay loading	Angle (2θ)	d-spacing (Å)
1	Cloisite 30B	4.0305	21.904
2	1 wt.%	2.0019	44.094
3	2 wt.%	2.0487	43.083
4	3 wt.%	1.9987	44.160
5	4 wt.%	2.0405	43.260
6	5 wt.%	2.0246	43.601

Tensile strength for each nanocomposite after varying the nanoclay content from 0 to 5 wt.% is shown in Fig. 3.7. It is observed that the tensile strength of the nanocomposite material increases with increasing the amount of nanoclay content up to 3 wt.%. The increase in tensile strength up to 3 wt.% of nanoclay was due to increase in the specific surface area of the nanocomposite material. However, increasing nanoclay concentration beyond 3 wt.% resulted in the formation of agglomerates which eventually decreased the

specific surface area and resulted in the reduced tensile strength of the nanocomposite [136].

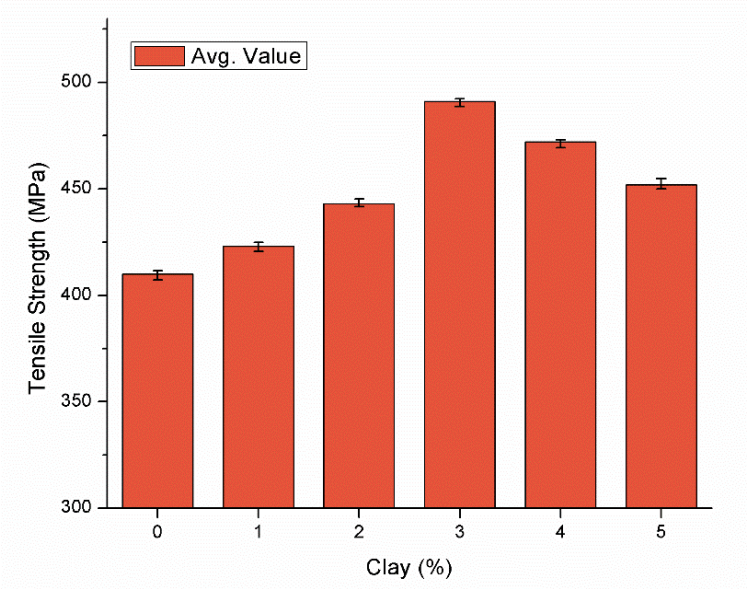

Fig. 3.7 Effect of nanoclay wt.% on the tensile strength of the composite laminate

FESEM micrograph of epoxy with 3 wt.% of nanoclay content is shown in Fig. 3.8. The figure shows the uniform distribution of nanoclay in epoxy.

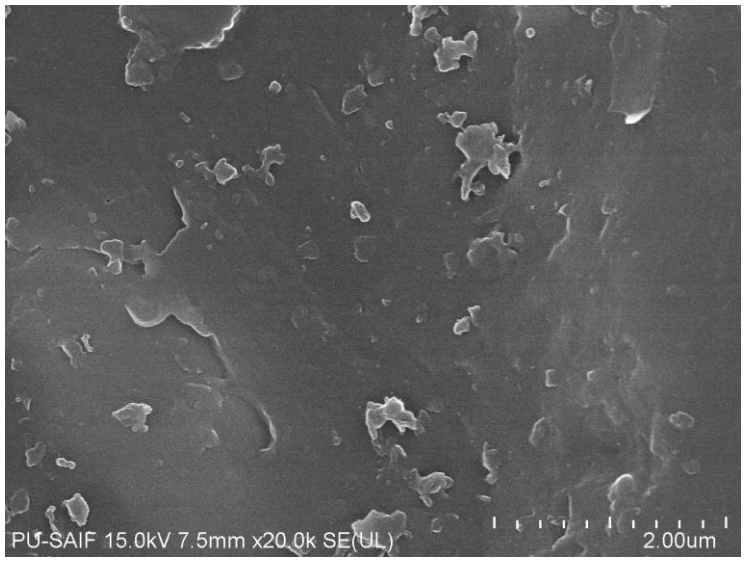

Fig. 3.8 FESEM micrograph of epoxy modified with 3 wt.% of nanoclay

3.3.3 Mechanical properties of the laminate

The laminates were prepared at the optimized values of the curing parameters, *i.e.*, pressure, temperature, and duration. Tensile, shear and compression testing has been done as per ASTM D3039, D5379, and D695 respectively. The mechanical properties of the composite laminates prepared from bi-directional, and unidirectional glass fabric are shown in Table 3.15, and Table 3.16, respectively.

Table 3.15 Mechanical properties of composite laminate prepared from bidirectional glass fiber with and without the addition of nanoclay content

Property	**Symbol (Units)**	**Without nanoclay**	**With nanoclay (wt.%)**				
			1	**2**	**3**	**4**	**5**
Longitudinal modulus in tension	E_1 (GPa)	21.68	23.24	25.12	27.04	29.11	31.25
Transverse modulus in tension	E_2 (GPa)	21.68	23.24	25.12	27.04	29.11	31.25
Longitudinal strength in tension	X_t (MPa)	410	423	443	491	472	452
Transverse strength in tension	Y_t (MPa)	410	423	443	491	472	452
Longitudinal strength in compression	X_c (MPa)	270	279	295	327	323	315
Transverse strength in compression	Y_c (MPa)	270	279	295	327	323	315
Shear strength	S (MPa)	104	106.9	110.2	114.4	114.1	113.7
Poisson ratio	ν_{12}	0.148	0.146	0.143	0.139	0.135	0.132

Table 3.16 Mechanical properties of laminates prepared with unidirectional glass fiber and neat epoxy [98]

Mechanical Property	Symbol (Units)	Value
Longitudinal modulus	E_1 (GPa)	12.8
Transverse modulus	E_2 (GPa)	7.8
Laminate shear strength	s (MPa)	155.68
Longitudinal strength in tension	X_t (MPa)	390.76
Transverse strength in tension	Y_t (MPa)	255.98
Poisson ratio	v_{12}	0.32
Longitudinal strength in compression	X_c (MPa)	324.11
Transverse strength in compression	Y_c (MPa)	224.45

3.4 Closure

The present chapter gave the description of the materials, basic processes, and methods used for the preparation and characterization of laminates. The curing parameters used in the preparation of laminates were optimized using Taguchi method. The laminates were prepared with the addition of 1 to 5 wt.% of nanoclay content. It was seen that the tensile strength of the glass fiber reinforced epoxy composites increased up to 3 wt.% of nanoclay content.

The next chapter deals with the failure analysis of single hole pin joints prepared with the addition of 3 wt.% of nanoclay content.

Chapter 4
Performance Analysis of Single Hole Pin Joint

This chapter deals with improvements in failure loads of pin joints through metal inserts and nanofillers. Metal inserts reduced the stress concentration around the hole and redistributed stresses at the pin/hole interface, which eventually increased the ultimate failure load of the joint. Studies have been performed using two different materials. A pilot study was done using metal insert on already available and characterized material, *i.e.*, unidirectional glass fiber reinforced polymer composite. The geometric parameters, *i.e.*, edge distance-to-hole diameter (E/D) ratio and width-to-hole diameter (W/D) ratio were varied from 2 to 5 and 3 to 6, respectively. Progressive damage analysis along with Hashin failure criteria was performed to predict failure loads and failure modes in pin joints, numerically. Progressive damage analysis gave a good correlation with experimental findings.

Due to a significant contribution of metal insert into the failure load of the pin joint, the study has been extended using nanofillers along with the metal inserts in the 2D plain woven glass fiber reinforced plastic composite. To investigate the effect of nanoclay content, 1 to 5 wt.% of nanoclay was mixed in epoxy. The increase in tensile strength up to 3 wt.% of nanoclay was observed which was due to increase in the specific surface area of the nanocomposite material. Dispersed nanoclay filler particles act as mechanical interlocking between fiber and epoxy matrix which creates a high friction coefficient. The optimal nanoclay content of 3 wt.% was finally used to prepare nanocomposite laminates.

4.1 Pin Joint Configurations

In the present work, a plate (length L, width W, thickness t) with a single pin-hole, shown in Fig. 4.1, was used. The diameter, D, of the hole was fixed to 4 mm. A gradual increasing and uniform load was applied on the plate through a rigid pin inserted into the hole. The pin located at the center of the hole resists the applied load. Because of symmetry of the geometry and other boundary conditions about the center line of the specimen, no bending forces are present during tensile testing of the specimen.

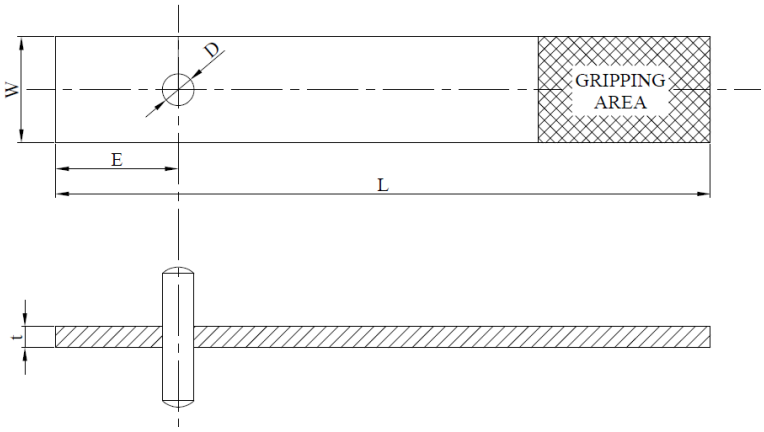

Fig. 4.1 Geometry of the specimen without metal insert

Table 4.1 Various values of E/D and W/D ratios

E/D	E(mm)	W/D	W(mm)	t (mm)	D (mm)
2	8	3	12	3	4
3	12	3	12	3	4
4	16	3	12	3	4
5	20	3	12	3	4
2	8	4	16	3	4
3	12	4	16	3	4
4	16	4	16	3	4
5	20	4	16	3	4
2	8	5	20	3	4
3	12	5	20	3	4
4	16	5	20	3	4
5	20	5	20	3	4
2	8	6	24	3	4
3	12	6	24	3	4
4	16	6	24	3	4
5	20	6	24	3	4

E/D and W/D ratios in the specimen were varied over the range of 2 to 5 and 3 to 6, respectively. Table 4.1 shows the different E/D and W/D ratios for which the samples were prepared. Thereafter, the metallic inserts as shown in Fig. 4.2, were press fit into the holes of each of the specimens.

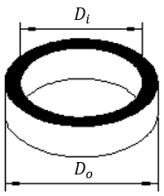

Fig. 4.2 Geometry of the metal insert

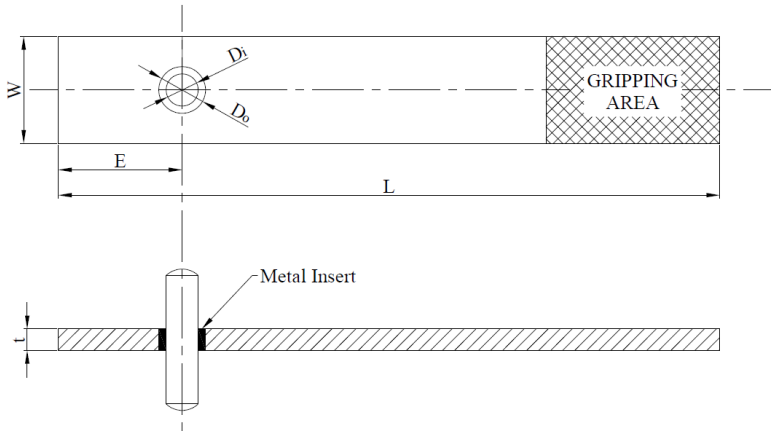

Fig. 4.3 Geometry of the specimen with metal insert

For the comparison of strength of specimens with and without the metal inserts, the inner diameter (D_i) of the metal inserts was taken as 4 mm which was same as the diameter (D) of the holes in the specimens without the metal inserts. The outer diameter (D_o) of the metal insert was 6 mm. The actual images of specimens fitted with metal insert are shown in Fig. 4.3 and 4.4.

(a)

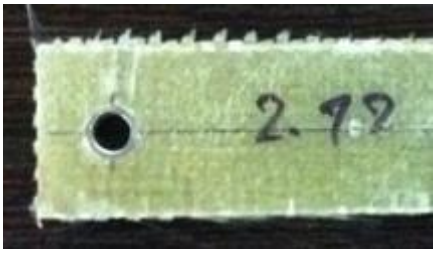

(b)

Fig. 4.4 Metal inserts in composite specimens made of
(a) unidirectional fiber (b) bidirectional fiber

4.2 Joint Testing

To analyze the effect of metal inserts and nanoclay, the prepared pin joint configurations were tested under tensile load on Zwick-Roell Universal Testing Machine with a capacity

of 10 kN. The test setup to analyze the failure load capacity of the joints is shown in Fig. 4.5. It is assumed that the specimen is symmetric to its sides and the hole is drilled exactly at the centerline of the specimen. The test setup is also considered to be symmetric and balanced with respect to the applied load and no out-of-plane forces are present while the testing of the joints. Metal inserts were press-fitted into drilled holes in specimens and a rigid pin was inserted into the metal insert. The load was applied to the rigid pin through a metal fixture held in one of the grippers of the universal testing machine. The other side of the laminate was held in the second gripper of the universal testing machine. The load-displacement curves were obtained through an electromechanical and displacement controlled universal testing machine. The machine applied a steadily increasing displacement with an electric motor and gear arrangement with no backlash. The crosshead travel was set to 2 mm/min in the present study. The force was measured by the load cell, and the displacement was derived from the crosshead travel. Because of geometric symmetry and other boundary conditions about the center line of the specimen, it was assumed that no bending forces are present during tensile testing of the specimen.

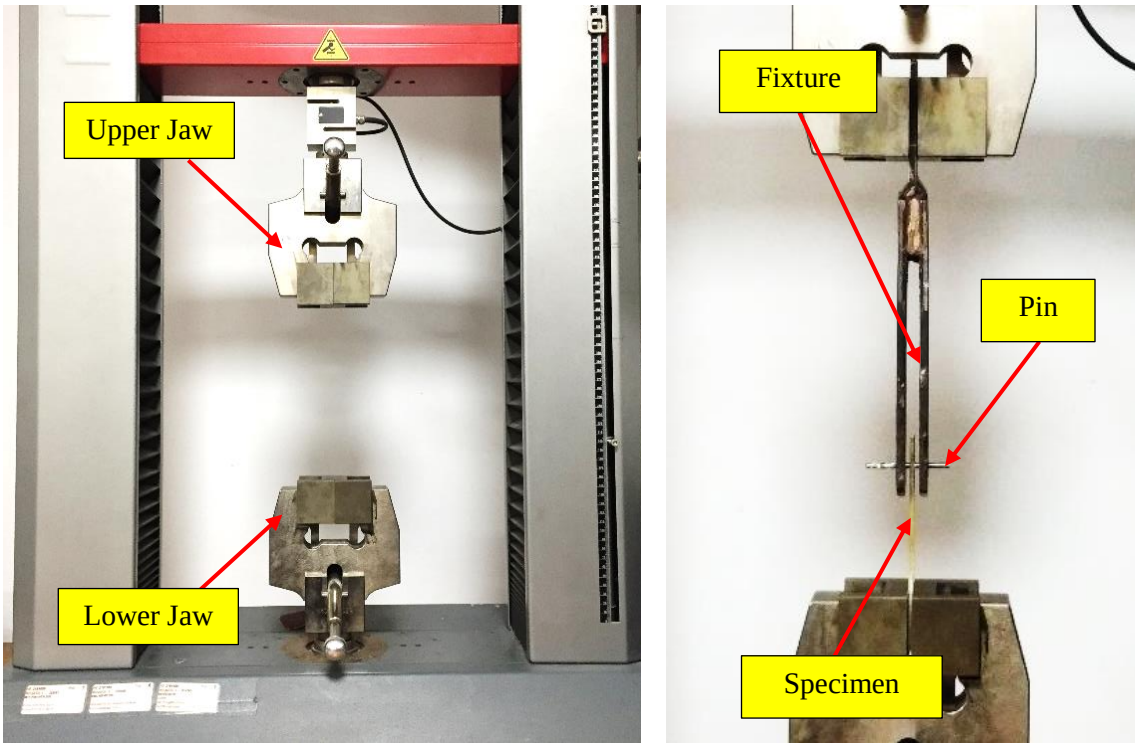

(a) (b)

Fig. 4.5 Test setup to analyze the load bearing response of pinned joints
(a) Universal Testing Machine and (b) Specimen held in UTM jaws

4.3 Numerical Analysis

The failure, in general, is assumed as complete de-functioning of the structure. In case of composite laminates, there are a number of local damages before it loses its entire strength. The ultimate failure of the laminate takes place due to the gradual accumulation of damage in the constituent phases of the composite laminates, *i.e.*, fiber and matrix.

Therefore, to consider the damage initiation and damage evolution, Progressive Damage Analysis (PDA) along with Hashin failure criteria was used for the numerical analysis of the composite joint. A gradual increasing load has been applied to the specimen modeled with and without metal inserts. Load ramps up from zero and goes on increasing till the onset of the damage in the first element. After that, material properties degrade as defined in the damage evolution law. At this moment, the specimen may be capable of bearing a specific increment in the load. If the specimen is not able to bear the load increment, then damage further occurs in other elements. This iterative procedure leads to the damage progress in the composite material. The damage progresses with respect to geometry of the specimen, and the maximum value of the failure index, failure modes and ultimate failure loads were predicted for composite joints.

The entire process has been performed in ANSYS software using finite element analysis. The geometry, shown in Fig. 4.1 and 4.3, were modeled in ANSYS modeler and then imported to ACP Pre-Module, where layer by layer composite definition was given to the model. The number of layers, *i.e.*, three for unidirectional fiber, and nine for bidirectional fiber, were stacked and simulated.

Hashin failure criteria [137] using equations (4.1) to (4.4) was used to perform the progressive failure analysis of the composite.

Fiber failure used for tensile and compressive loadings in the longitudinal direction (fiber direction) is given in equations (4.1) and (4.2), respectively.

$$f_f = \left(\frac{\sigma_1}{X_t}\right)^2 + \left(\frac{\tau_{12}}{S}\right)^2, \sigma_1 \geq 0 \tag{4.1}$$

$$f_f = -\frac{\sigma_1}{X_c}, \sigma_1 < 0 \tag{4.2}$$

Matrix failure for tensile and compressive loadings in the transverse direction is given by equations (4.3) and (4.4), respectively.

$$f_m = \left(\frac{\sigma_2}{Y_t}\right)^2 + \left(\frac{\tau_{12}}{S}\right)^2, \sigma_2 \geq 0 \tag{4.3}$$

$$f_m = \left(\frac{\sigma_2}{2S}\right)^2 + \left(\frac{\tau_{12}}{S}\right)^2 + \left[\left(\frac{Y_c}{2S}\right)^2 - 1\right]\frac{\sigma_2}{Y_c}, \sigma_2 < 0 \tag{4.4}$$

Where, f_f and f_m are failure index for the fiber and the matrix. σ_1 and σ_2 are stresses setup in longitudinal and transverse directions, X_t and X_c are tensile and compressive stress limits in the longitudinal direction, Y_t and Y_c are tensile and compressive stress limits in the transverse direction, S is shear stress in the plane. Due to the woven structure in the bidirectional fiber reinforced composite, $X_t = Y_t$ and $X_c = Y_c$ in Hashin's equations.

4.4 Results and Discussion

The following section gives the experimental and numerical results of the pin joints prepared from unidirectional and bidirectional fiber reinforced composites.

4.4.1 Unidirectional fiber reinforced composite

4.4.1.1 Experimental results

Figure 4.6 shows the graphical plots for the force and the displacement variations for the specimens with and without the metal inserts.

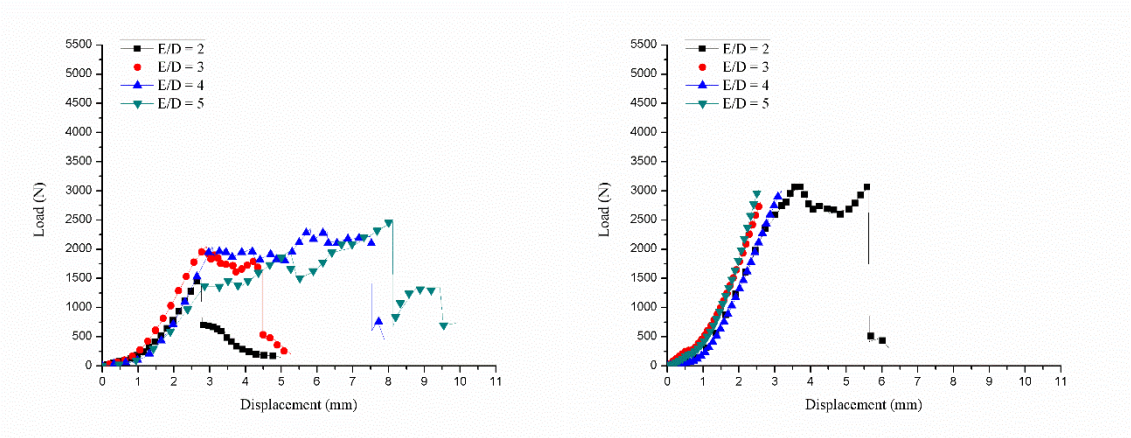

(a) (b)

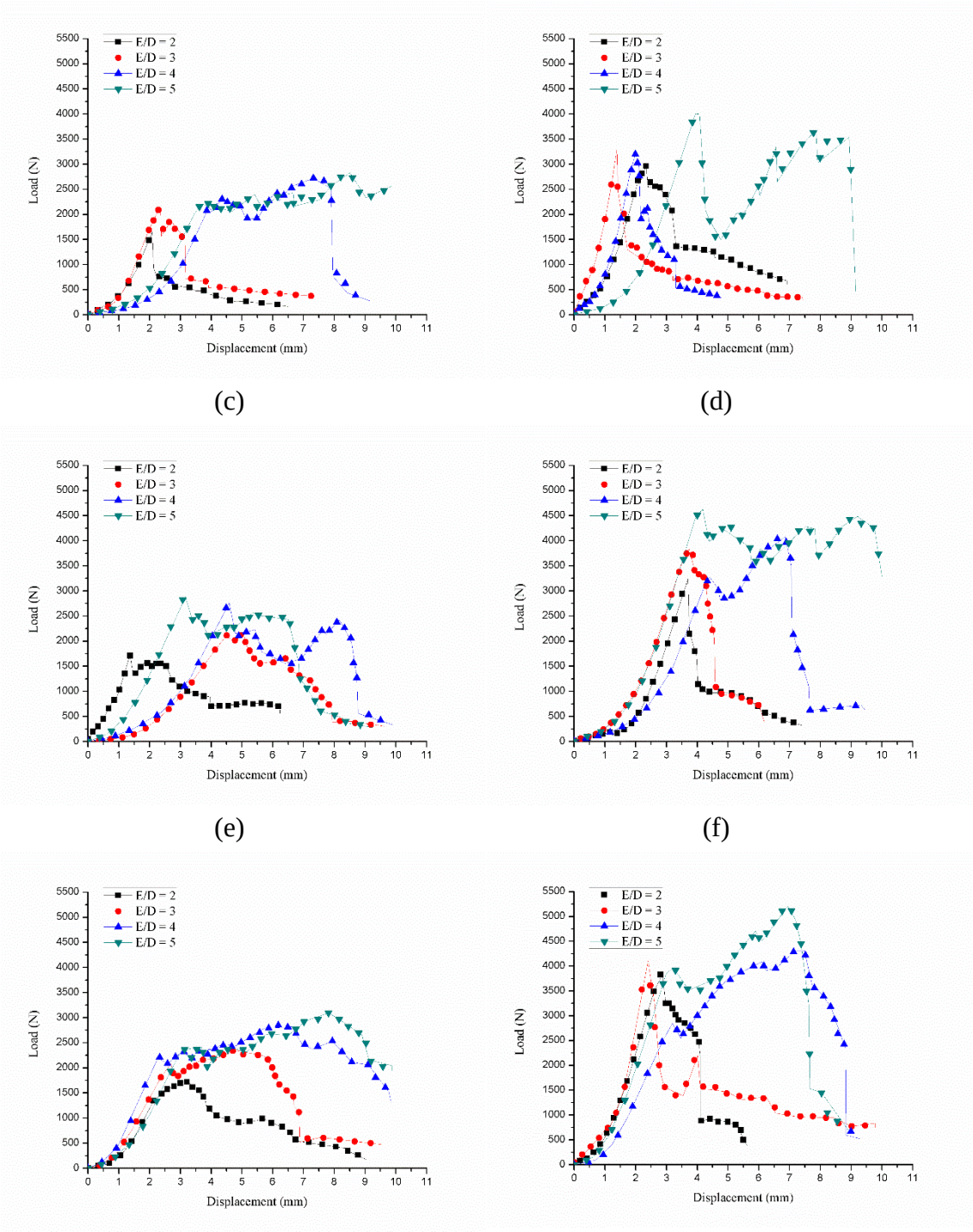

Fig. 4.6 Load vs displacement graphs from the UTM tensile test for specimens with and without the metal inserts: (a) W/D = 3 (without insert), (b) W/D = 3 (with insert), (c) W/D = 4 (without insert), (d) W/D = 4 (with insert), (e) W/D = 5 (without insert), (f) W/D = 5 (with insert), (g) W/D = 6 (without insert), (h) W/D = 6 (with insert)

These plots are used to predict the type of failure mode in the specimens. There are three basic failure modes in pin joints, *i.e.*, net-tension, shear-out and bearing [98]. Joint failure with the shear-out and net-tension mode is immediate. But the failure with the bearing mode is not sudden and have less serious consequences than the shear-out and net-tension types of failure modes. The designer avoids the net-tension and shear-out failure mode as compared to bearing failure modes [98]. It can be seen from Fig. 4.6 that, at the lower values of W/D ratio, the specimens with metal inserts fail with net-tension mode as the distance of the metal insert to the side edge of the specimen is very small. The net-tension mode can be predicted from the instant drop in the graph. The failure mode of the specimens change from net-tension to the bearing failure mode with the increase in W/D and E/D ratios. The bearing failure mode can be predicted from the multiple peaks in the graphs. It is also clear from Fig. 4.6 that the failure loads for specimen incorporating metal inserts are higher as compared to the specimens without metal inserts.

The ultimate failure loads for different joint configurations with and without metal inserts are shown in Table 4.2. It is clearly observed from the table that the metal inserts have increased the failure load for each joint configuration.

Table 4.2 Ultimate failure loads for various levels of E/D and W/D ratios

E/D	W/D	Failure loads (N)	
		No inserts	Metal inserts
2	3	1501	2890
3	3	2051	3000
4	3	2356	3100
5	3	2475	3010
2	4	1650	2960
3	4	2130	3300
4	4	2767	3346
5	4	2830	4010
2	5	1730	3243
3	5	2135	3850
4	5	2800	4100
5	5	2880	4640
2	6	1732	3850
3	6	2350	4105
4	6	2860	4351
5	6	3096	5205

Fig. 4.7 shows the effect of E/D and W/D ratios on the ultimate failure loads for the specimens with and without the metal inserts. It shows that the failure load for specimen with metal inserts having minimum configuration of E/D and W/D ratios as 2 and 3 respectively is 92% larger as compared to the specimen without the metal inserts. Similarly, for the highest joint configuration of E/D and W/D ratios of 5 and 6 respectively, the failure load increases by 68% for the specimen with metal insert in comparison to the specimen without the metal insert.

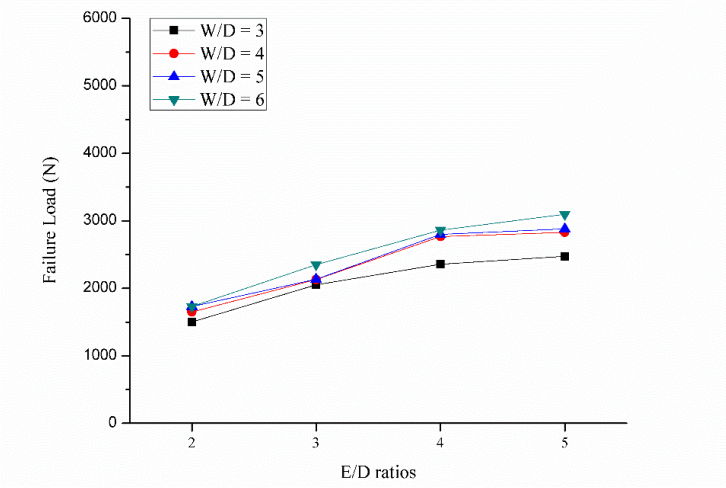

(a)

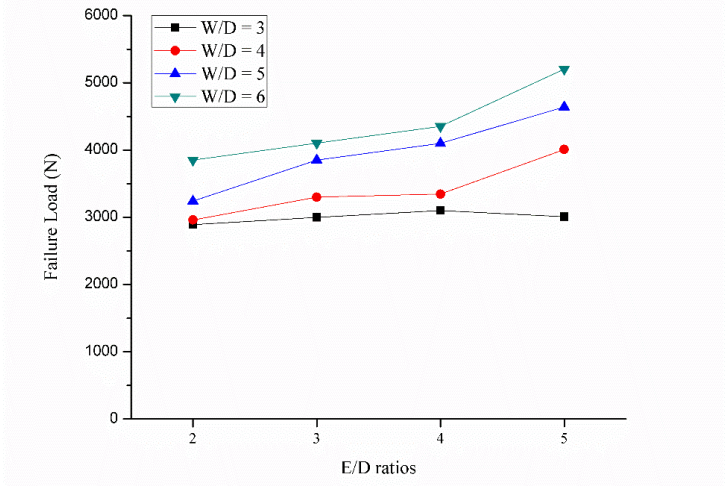

(b)

Fig. 4.7 Ultimate failure load for the specimen.
(a) without metal inserts (b) with metal inserts

Table 4.3 summarizes the failure modes for different pin joint configurations, where S, NT, and B signifies the shear-out, net-tension and bearing type of failure modes. Introducing the metal inserts in the composite joint changes the failure modes of the joints [101].

Table 4.3 Failure modes for various levels of E/D and W/D ratios

S. No.	E/D	W/D	Failure modes	
			No inserts	Metal inserts
1	2	3	S	NT
2	3	3	S	NT
3	4	3	B	NT
4	5	3	B	NT
5	2	4	S	S
6	3	4	S	S
7	4	4	B	S
8	5	4	B	B
9	2	5	S	S
10	3	5	S	S
11	4	5	B	B+S
12	5	5	B	B
13	2	6	S	S
14	3	6	B+S	S
15	4	6	B	B
16	5	6	B	B

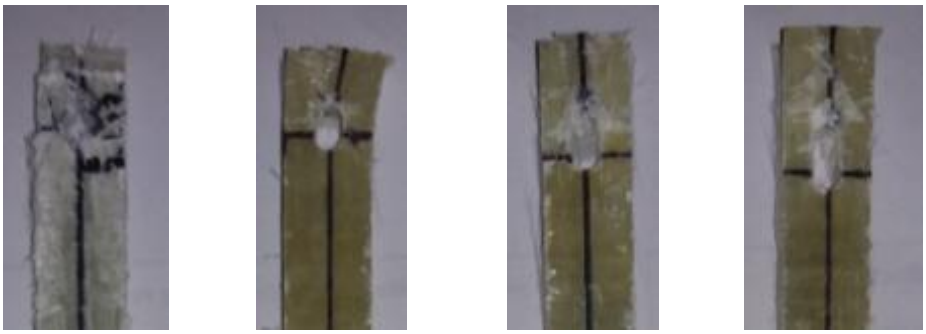

Specimens without metal inserts

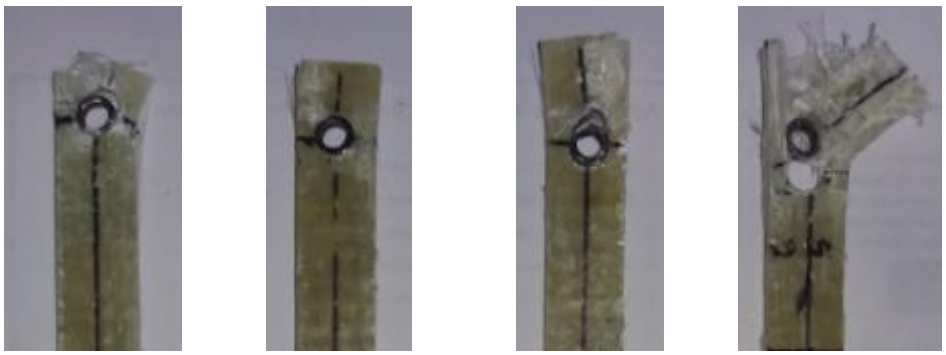

Specimens with metal inserts

(a)

Specimens without metal inserts

Specimens with metal inserts

(b)

Fig. 4.8 Failure modes of specimens with and without inserts, geometric parameters (a) E/D=2, W/D=3; E/D=3, W/D=3; E/D=4, W/D=3; E/D=5, W/D=3 and (b) E/D=2, W/D=6; E/D=3, W/D=6; E/D=4, W/D=6; E/D = 5, W/D=6

Table 4.3 shows that for the lower values of W/D ratios, different failure mode, *i.e.*, net-tension is observed for the specimens with the metal inserts as compared to the specimens without the metal inserts. It is due to the reason that the side edge to hole distance reduces for the lower value of W/D ratio. Although the failure load value is very high for lower value of W/D ratios but the lower value of W/D are to be avoided due to net-tension type of failure which is a catastrophic type of failure. The actual images for some of the specimens are shown in Fig. 4.8.

4.4.1.2 Numerical results

Progressive damage analysis along with Hashin failure criteria were used for the numerical analysis of the joint. The geometry shown in Fig. 4.1 was modelled. Mesh using a mapped face meshing technique with brick elements was generated as shown in Fig. 4.9.

Fig. 4.10 shows a 6000 N tensile force divided in 6 steps; starting from 0 and reaching up to 6000 N (max.), that was applied onto the hole edge in longitudinal direction.

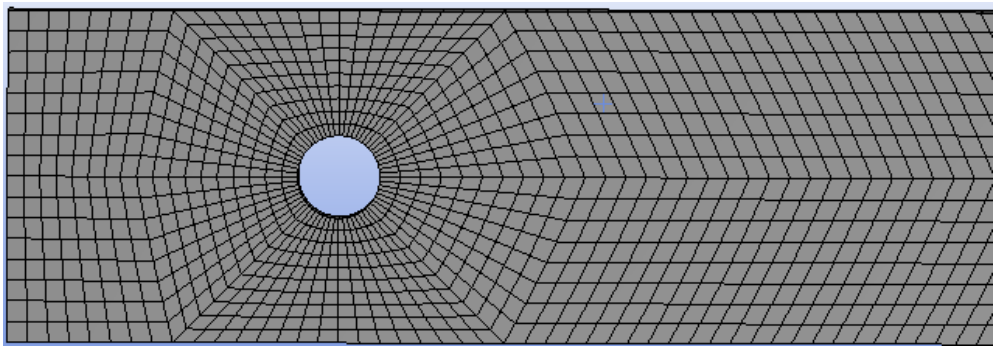

Fig. 4.9 Generated mesh for a particular specimen

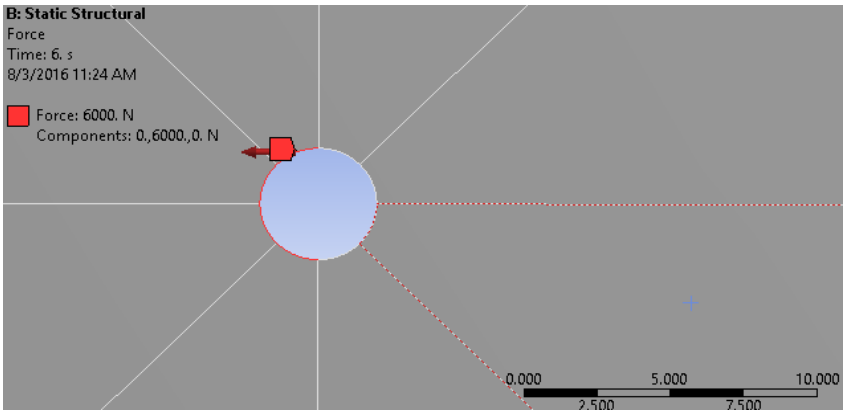

Fig. 4.10 Tensile load applied on the hole boundary

During the progressive failure analysis, the load begins with the 0 value and increases gradually with small increments. Initially, failure started in the middle layer which was known to be the first failure and was mainly because of matrix compression. The reason behind early failure of the middle layer was the fiber orientations of 90^{o} w.r.t. applied load. After middle ply failure, corresponding load initially taken by the middle layer was further distributed to outer layers, *i.e.*, layer 1 and 3. Further increase of load causes last failure (outer layer failure) and the load corresponding to the last failure was significantly large compared to the first ply failure load. Fibers while being at 0^{o} w.r.t. loading direction in 1st and 3rd layer were mainly responsible for carrying tensile loads in the outer layers. Fig. 4.11 shows the damage propagation for weakest joint configuration, *i.e.*, E/D = 2 and W/D = 3, in the two outer layers, *i.e.*, layers at 0^{o} orientations with respect to the applied tensile load. As seen in the figure, failure initially begins towards side edge but further propagates towards free edge and reach the free edge causing shear out failure.

Figure 4.11(a) and (b) shows that the damage initiates towards side edge around the hole surface and propagates further in the same direction. Figure 4.11(c) shows that the damage starts propagating towards free edge of the specimen and further approach free edge, confirming shear out failure mode of the specimen. The shear-out failure mode was due to the lesser margin between the free edge and the hole. Specimens with large E/D and W/D ratios, *i.e.*, E/D ≥ 4 and W/D ≥ 3, fail in bearing mode.

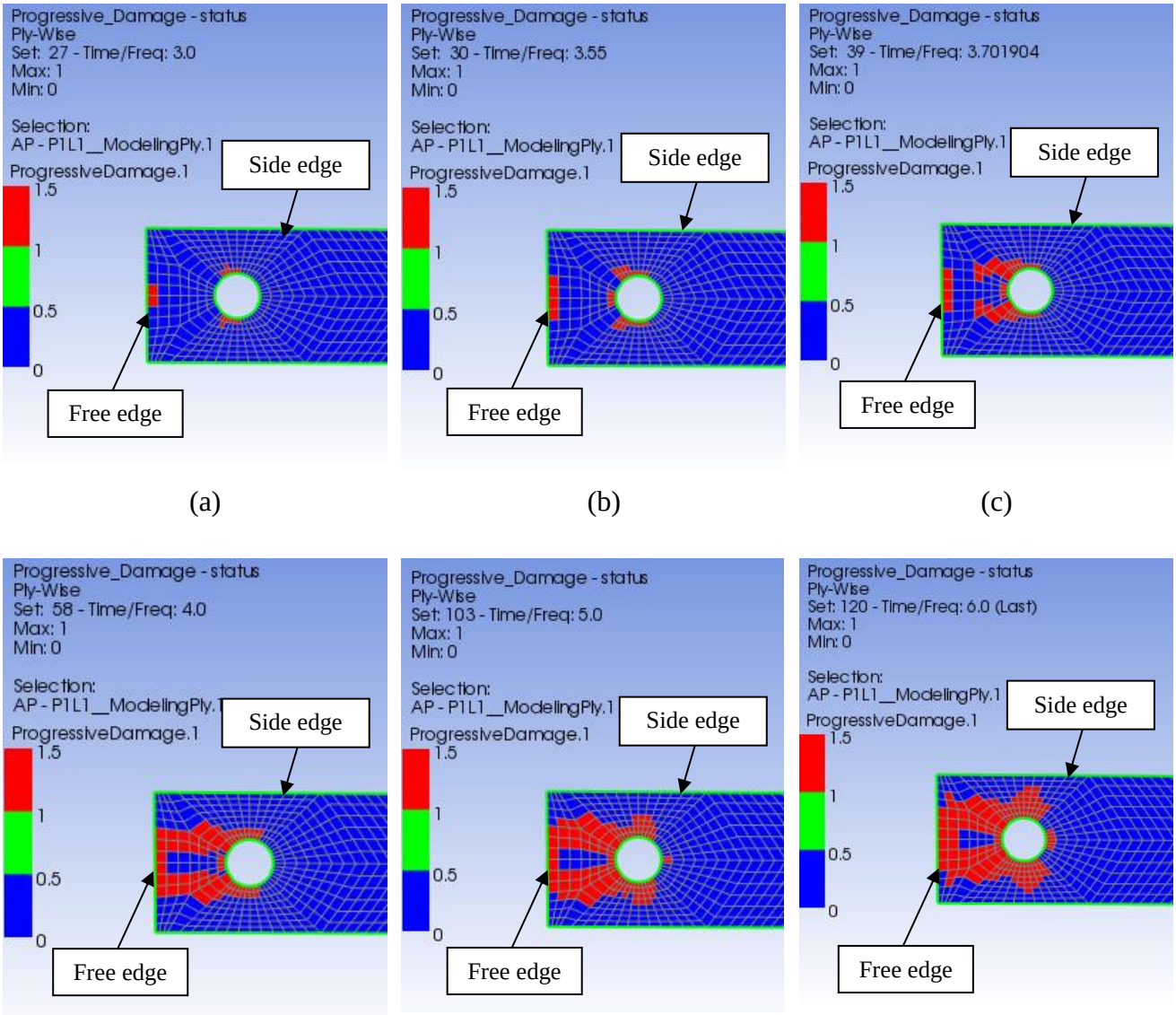

Fig. 4.11 Progressive damage status under tensile load at different stages for E/D = 2 and W/D = 3 in the outer layer

Figure 4.12 shows the progressive damage contour plots for the specimen having E/D = 5 and W/D = 6 for middle layer, *i.e.*, layers at 90^{o} orientations with respect to the applied

tensile load. It is observed from the figure that the failure begins around the hole surface towards side edge and then propagates towards free edge. Representing the pure bearing failure, damage does not reach up to the free edge of the specimen.

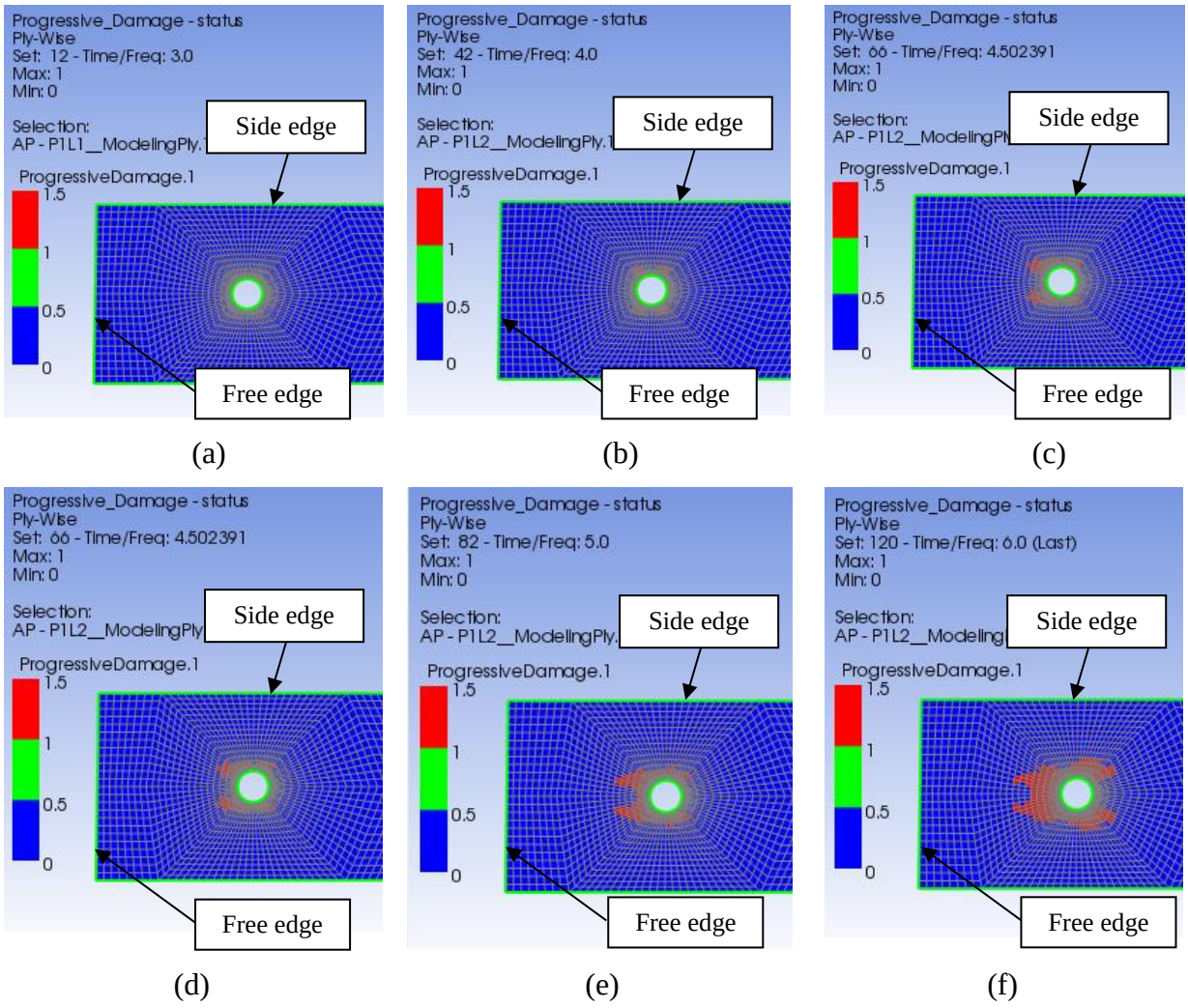

Fig. 4.12 Progressive damage status under tensile load at different stages for E/D = 5 and W/D = 6 in the middle layer

Fig. 4.13 shows numerical failure loads for composite specimens with and without the metal inserts. The effect of E/D and W/D ratios on the failure load is clearly visible in the plots. The failure load increases with increase in E/D and W/D ratios. Use of metal inserts has clearly shown the increase in first (middle ply) and last (outer ply) failure loads.

In general, last failure loads are significantly larger than the first failure load. This confirms the mechanics behind the composite layer by layer structure, which tells that

failure in middle layer which is at 90^o to the applied load, occurs because of matrix failure and is basically due to the compressive force applied by the pin on the matrix, whereas failure in outer layers, aligned with the applied loads, are due to the tensile fiber failure and have large failure load values in comparison to the middle ply failure.

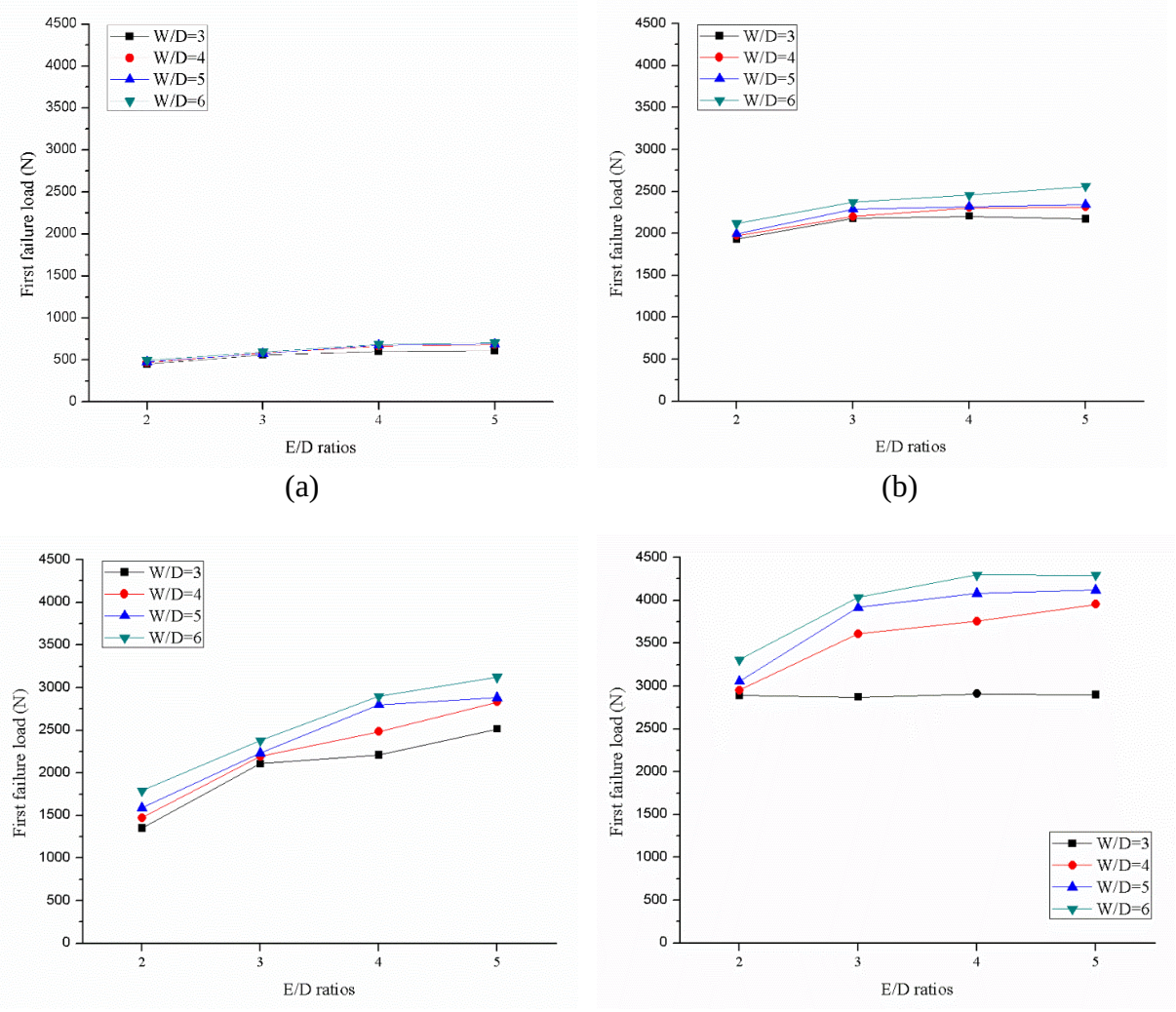

Fig. 4.13 Failure loads for different specimen from numerical analysis
(a) First failure load without insert, (b) First failure load with insert,
(c) Last failure load without insert, (d) Last failure load with insert

Figure 4.14 shows the comparison of the numerical with the experimental results. The results show the good agreement between each other for the different geometric parameters.

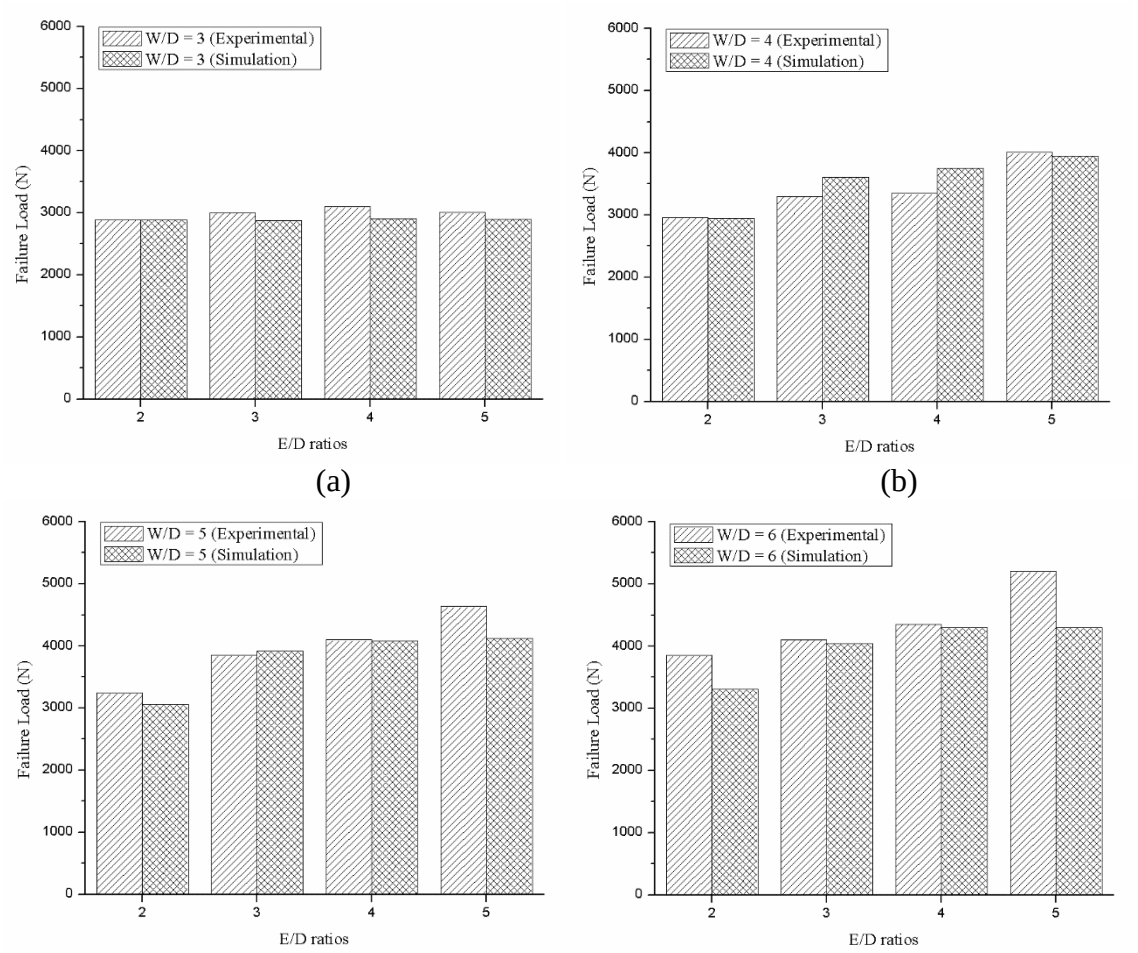

Fig. 4.14 Comparison of experimental and numerical results
(a) W/D = 3, (b) W/D = 4, (c) W/D = 5, (d) W/D = 6

4.4.2 Bidirectional fiber reinforced composite

The mechanical properties of the fiber reinforced composites highly depends upon the direction of fiber reinforced. In case of unidirectional fiber reinforced composites, the maximum tensile strength of the composite laminate corresponds to the direction of the fiber. However, to obtain better mechanical strengths in both of the directions, *i.e.*, longitudinal and the transverse direction, different ply orientations are adopted. To serve the purpose of balanced properties in both the directions, an alternative stacking sequence of 0/90° fiber orientations can be used. On the other hand, bidirectional (2D) plain woven fabrics are woven in such a way that they exhibit almost similar properties in both of the directions when used in the composite laminates. The minor difference between the linear density of the warp and the fill can be easily taken care of using alternate stacking sequence of 0/90° ply orientations. Also, the woven fiber reinforced composite possess

better impact resistance compared to the unidirectional fiber reinforced composites. The structural integrity of the woven fabric is also better compared to the unidirectional fabrics. Unidirectional fabrics are more prone to fiber misalignment compared to the woven fabrics.

The bearing strength of the composite pin joint increases with increase in woven linear density of the glass fabric, but up to an extent. Further increase in the woven linear density promotes void contents and higher crimp levels, which certainly affects the performance of the fiber reinforced composite joints [50]. In another study, a slight increase in mechanical properties was reported due to increase in number of layers up to certain extent [138]. Therefore, considering all the consequences, a 2D plain woven fabric of 360 gsm was preferred over the unidirectional fabric of 1200 gsm.

4.4.2.1 Experimental results

Failure loads of different joint configurations, *i.e.*, with and without metal inserts, prepared with bidirectional fiber without nanoclay content are shown in Fig. 4.15.

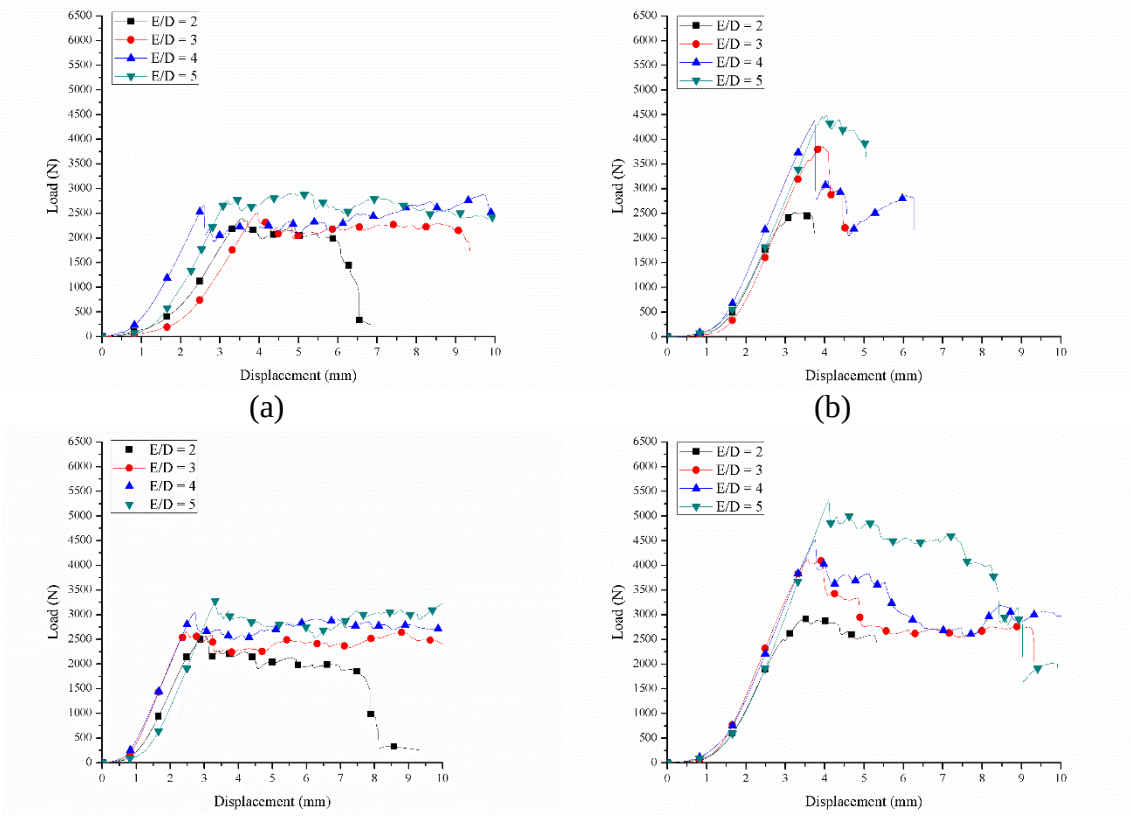

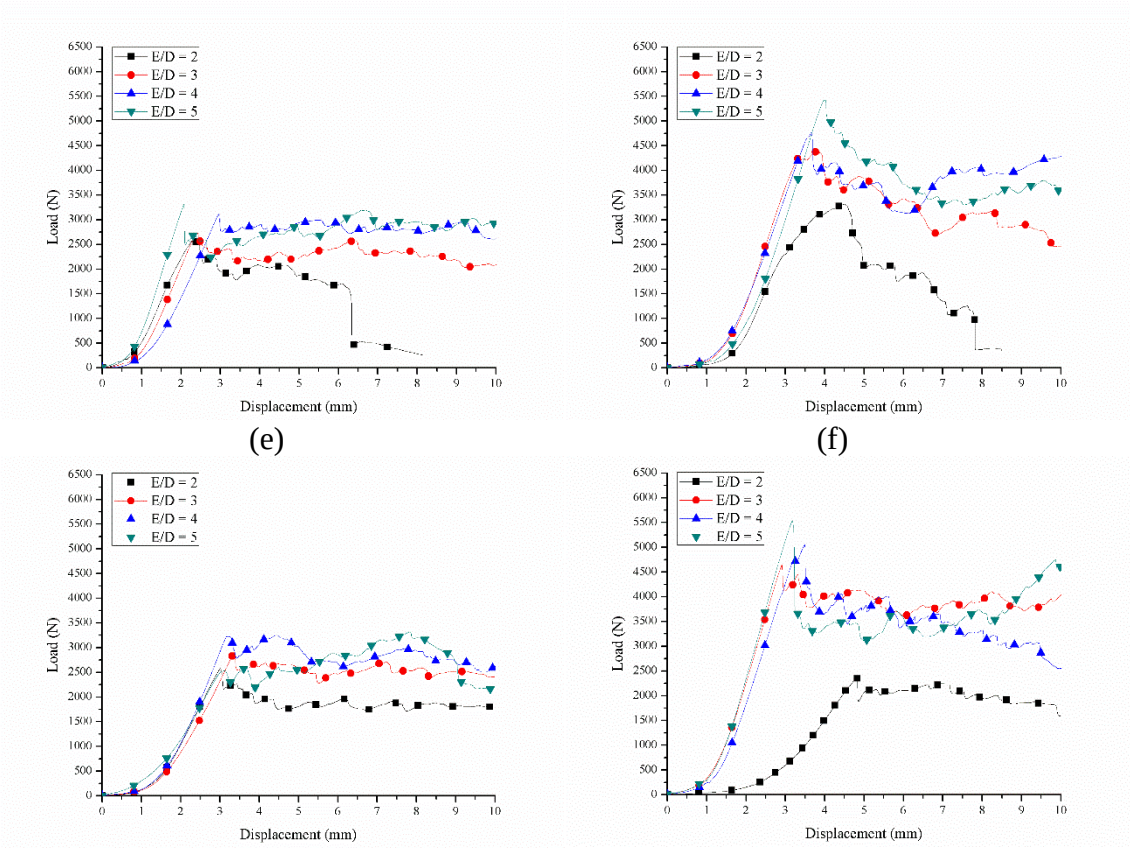

Fig. 4.15 Load vs displacement plots for different specimens, with and without metal insert prepared without nanoclay, tested under tensile load for (a) W/D = 3 (without insert), (b) W/D = 3 (with insert), (c) W/D = 4 (without insert), (d) W/D = 4 (with insert), (e) W/D = 5 (without insert), (f) W/D = 5 (with insert), (g) W/D = 6 (without insert), and (h) W/D = 6 (with insert)

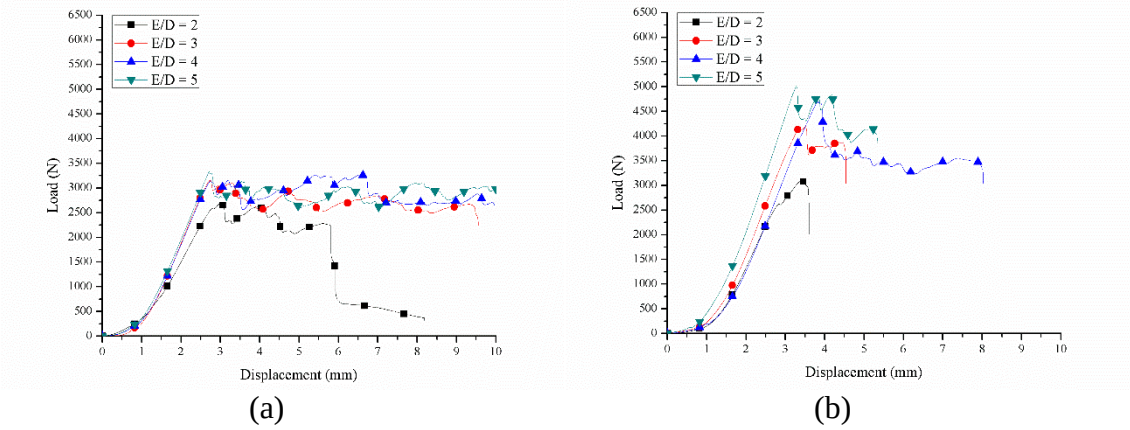

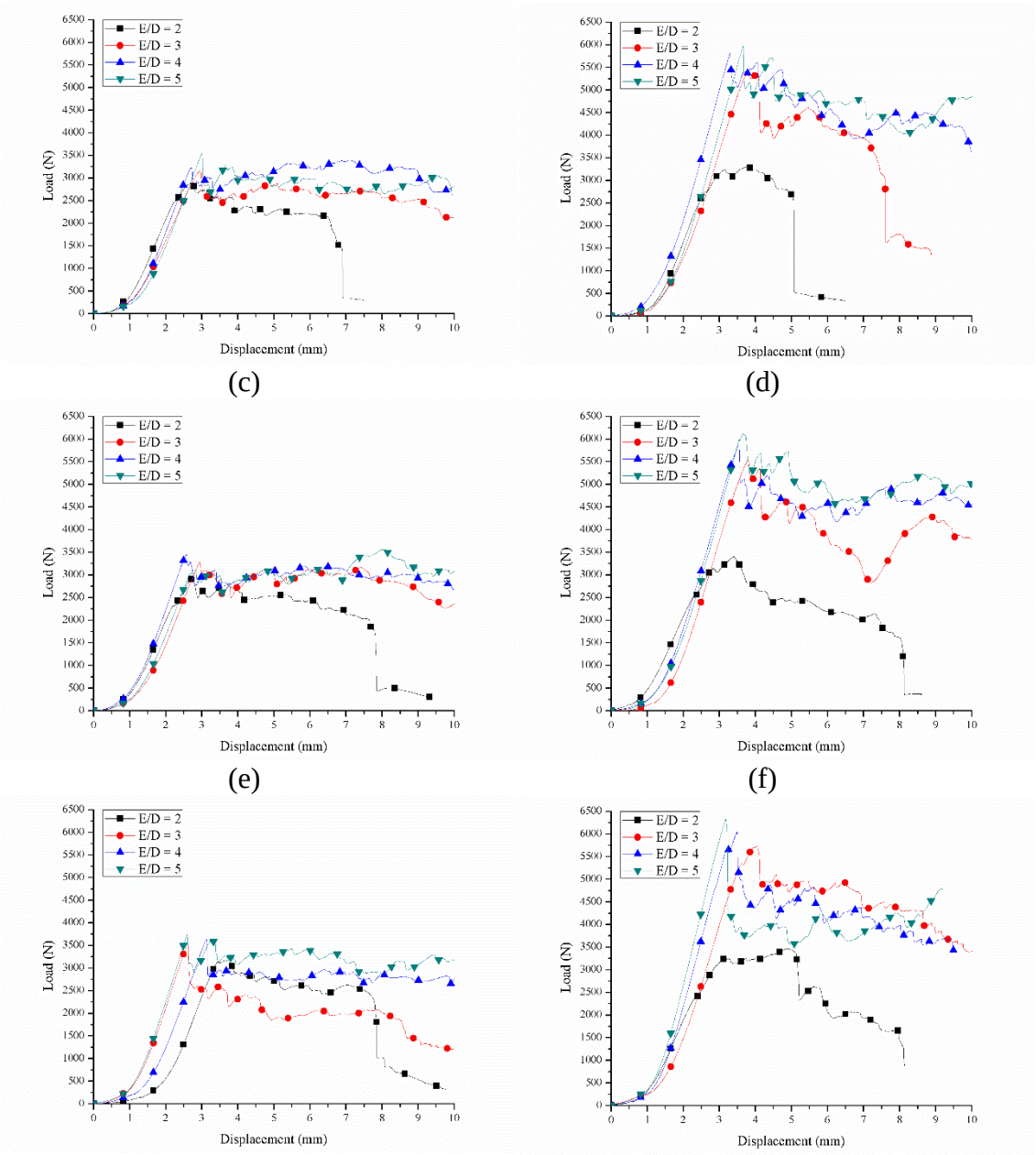

Fig. 4.16 Load vs displacement plots for different specimens, with and without metal insert prepared with 3 wt.% of nanoclay, tested under tensile load for (a) W/D = 3 (without insert), (b) W/D = 3 (with insert), (c) W/D = 4 (without insert), (d) W/D = 4 (with insert), (e) W/D = 5 (without insert), (f) W/D = 5 (with insert), (g) W/D = 6 (without insert), and (h) W/D = 6 (with insert)

The contribution of nanoclay to the failure load of different joint configurations, *i.e.*, with and without metal inserts, is shown in Fig. 4.16. The numerical values of ultimate failure loads from Figs. 4.15 and 4.16 are summarized in Table 4.4. It is observed (from Fig. 4.15, Fig. 4.16 and Table 4.4) that incorporating metal inserts has significantly improved

the maximum failure load. Metal inserts redistributed the stress around the hole and reduced the stress concentration which eventually increased the failure load of the joint. Increasing E/D and W/D ratio have shown a positive effect on the failure load of the joint. Comparing Fig. 4.15 and 4.16, a marginal improvement is observed in the failure load of all joint configurations prepared with nanoclay.

Table 4.4 Ultimate failure load for different joint configurations tested under tensile load

Sr. No	W/D	E/D	Ultimate failure load (N)			
			Neat		Nanoclay	
			Without insert	With insert	Without insert	With insert
1	3	2	2394	2520	2702	3102
2	3	3	2510	3860	3151	4193
3	3	4	2875	4380	3266	4697
4	3	5	2916	4480	3355	5015
5	4	2	2565	2930	2886	3311
6	4	3	2652	4115	3163	5400
7	4	4	3043	4520	3392	5817
8	4	5	3278	5320	3542	5976
9	5	2	2574	3318	2944	3400
10	5	3	2728	4385	3278	5530
11	5	4	3112	4760	3450	5875
12	5	5	3314	5419	3565	6120
13	6	2	2583	3450	3174	3460
14	6	3	2902	4650	3530	5731
15	6	4	3253	5049	3634	6048
16	6	5	3319	5540	3761	6321

There is net-tension, shear-out or bearing type of failure mode in joints [98]. Joint failure with the shear-out and net-tension mode is immediate. However, the failure with the bearing mode is not sudden and have less severe consequences than the shear-out and net-tension types of failure modes. Keeping the material, fiber reinforced angle and lay-up as fixed, failure modes depends upon geometric parameters of joints. The designer avoids the net-tension and shear-out mode of failure by selecting the proper value of E/D and W/D ratios. The shear-out, net-tension or bearing failure mode can be quickly judged from load-displacement curves of specimens. The sudden drop in the load-displacement curves represents the net-tension failure mode. If the curve drops with the zig-zag formation, then it is a shear-out failure mode. However, if the curve moves forward with the zig-zag formation without a significant drop, then it is a bearing failure mode.

Analyzing load-displacement curves and actual images of all failed specimens, failure modes of each joint configuration has been summarized in Table 4.5, where NT, S, and B signify the net-tension, shear-out and bearing type of failure modes.

Table 4.5 Failure modes for different joint configurations tested under tensile load

Sr. No	W/D	E/D	Neat		Clay	
			Without bush	With bush	Without bush	With bush
1	3	2	S	NT	B+NT	NT
2	3	3	B	NT	B	B+NT
3	3	4	B	NT	B	B+NT
4	3	5	B	NT	B	B+NT
5	4	2	B+S	S	B+S	S
6	4	3	B	B+S	B	B+NT
7	4	4	B	B	B	B
8	4	5	B	B	B	B
9	5	2	B+S	S	B+S	S
10	5	3	B	B+S	B	B
11	5	4	B	B	B	B
12	5	5	B	B	B	B
13	6	2	B+S	S	B+S	B+S
14	6	3	B	B	B	B
15	6	4	B	B	B	B
16	6	5	B	B	B	B

It can be seen from Figs. 4.15 and 4.16 that nearly all joints without metal inserts have shown the shear-out or bearing failure mode. However, joints with metal inserts have shown net-tension failure mode for lower values of W/D ratios. It can be seen from Figs. 4.15(b) and 4.16(b) that for W/D = 2 and E/D = 2 to 5, all specimens have net-tension type of failure mode. It is due to the reason that the distance between the side edge and the hole edge is very less for W/D=2.

It can be seen from Table 4.5 that for lower values of edge distance, *i.e.*, E/D = 2, joints failed in shear-out mode or a combination of bearing and shear-out failure mode. The shear-out mode occurs because of less distance between the edge and the hole boundary, whereas, net-tension occurs due to less margin available to the side edge of the composite specimen. For joints without metal inserts, a pure bearing mode of failure is observed for $E/D \geq 3$ and $W/D \geq 4$. However, joints with metal inserts showed pure bearing failure modes for $E/D \geq 4$ and $W/D \geq 4$. The different failure modes were determined from the load-displacement graphs.

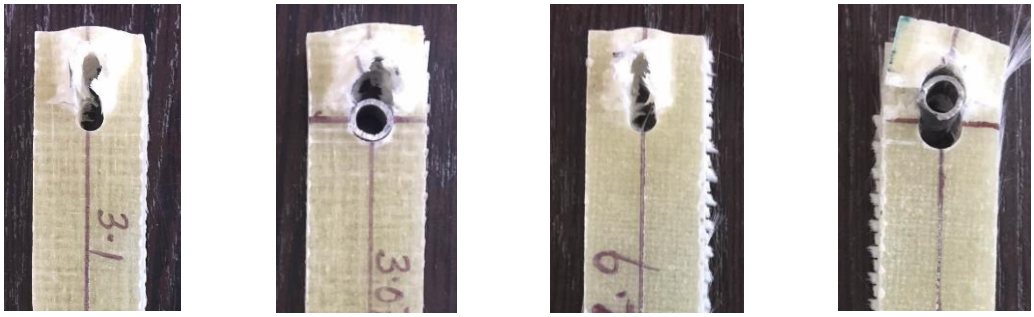

(a) (b) (c) (d)

Fig. 4.17 Actual images of the selected failed specimen for E/D = 3 and W/D = 3
(a) neat without metal insert, (b) neat with metal insert
(c) clay without metal insert, (d) clay with metal insert

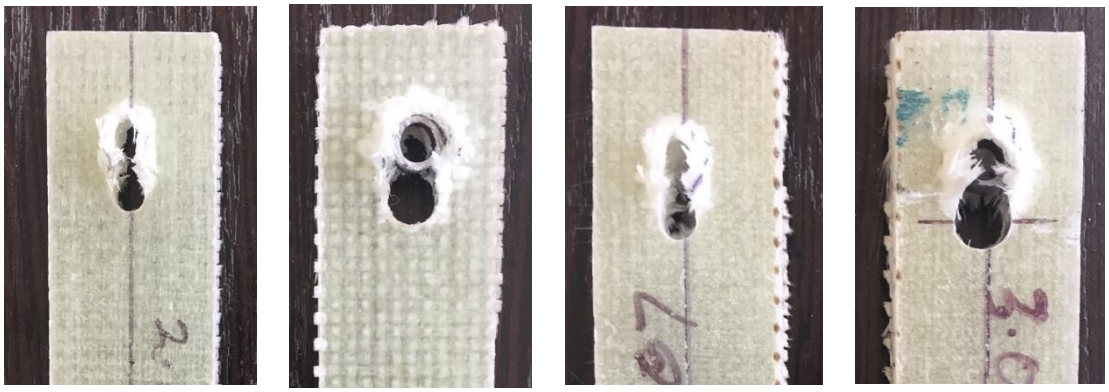

(a) (b) (c) (d)

Fig. 4.18 Actual images of the selected failed specimen for E/D = 5 and W/D = 5
(a) neat without metal insert, (b) neat with metal insert
(c) clay without metal insert (d) clay with metal insert

Actual images of tested specimens for two different geometric configurations are shown in Figs. 4.17 and 4.18.

The maximum failure loads for different joint configurations, *i.e.*, with and without metal insert and with and without nanoclay are shown in Figs. 4.19 and 4.20. The effect of E/D, W/D and metal inserts on the ultimate failure load of joints prepared from neat epoxy and epoxy modified with nanoclay is clearly visible from figures. Analyzing the trend of plots in Figs. 4.19 and 4.20, it is observed that incorporating metal inserts has increased the maximum failure load of joints. Besides metal inserts, nanoclay content also has shown its positive effect on the failure load of joints. The addition of nanoclay acts as a mechanical interlock between the glass fiber and the epoxy which increases the friction coefficient. It also increases interfacial properties of the material which have a positive effect on its failure load.

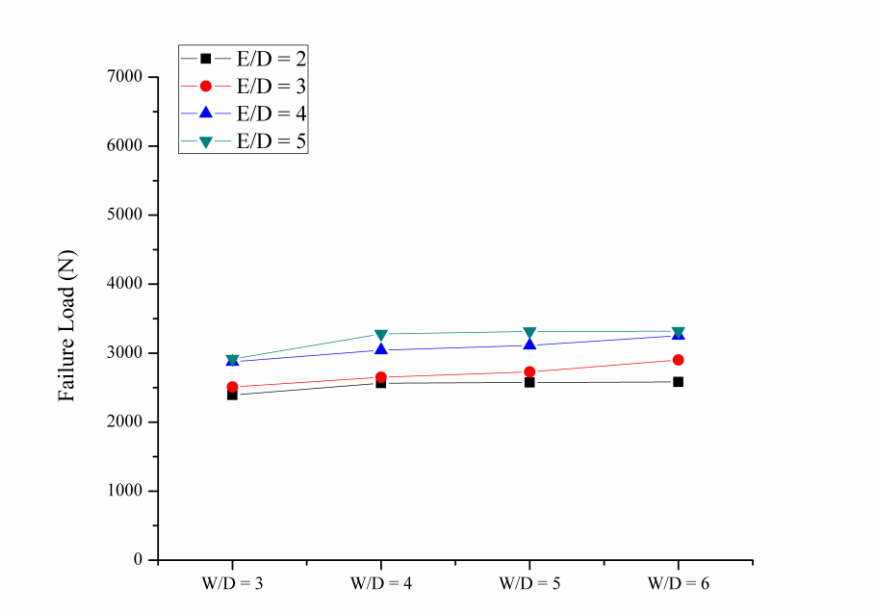

(a)

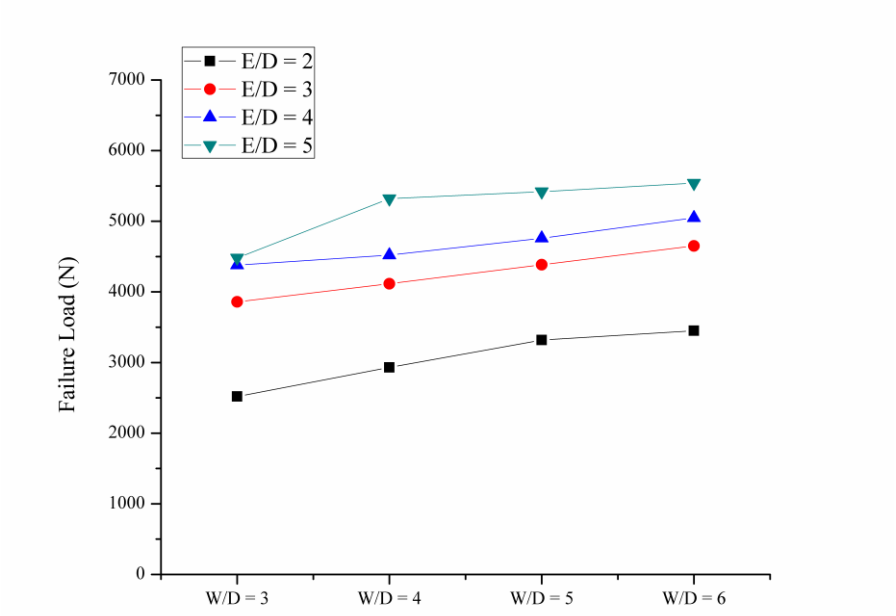

(b)

Fig. 4.19 Ultimate failure loads for joints prepared from glass fiber, neat epoxy and (a) without metal insert (b) with metal insert

Though a little improvement of failure load is seen in lower values of E/D ratio, *i.e.*, E/D = 2, increasing the value of E/D ratio beyond 2 shows significant contribution of metal inserts in the improvement of the failure load of the joint. A maximum of 71% and 67% improvement in the failure load has been shown by metal inserts for joints prepared with and without the nanoclay, respectively.

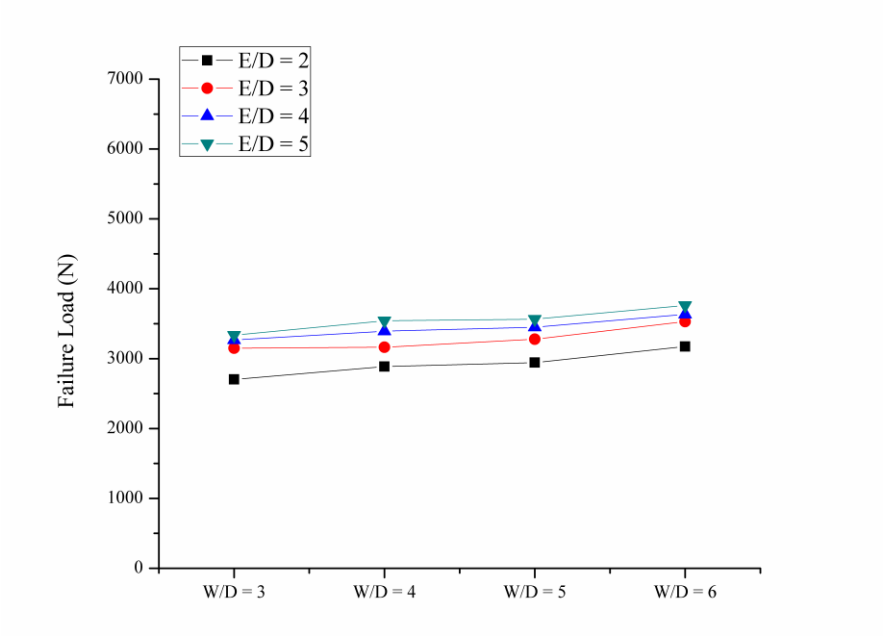

(a)

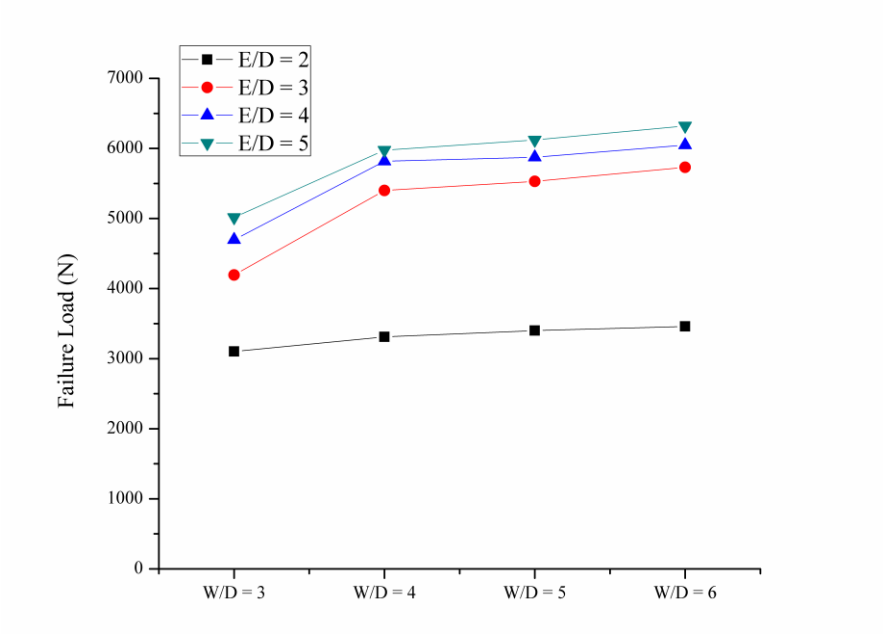

(b)

Fig. 4.20 Ultimate failure loads for joints prepared from glass fiber, epoxy modified with nanoclay and (a) without metal insert (b) with metal insert

4.4.2.2 Numerical results

The model was made as per Fig. 4.1. Mesh was generated using edge sizing and mapped face meshing technique, as shown in Fig. 4.21.

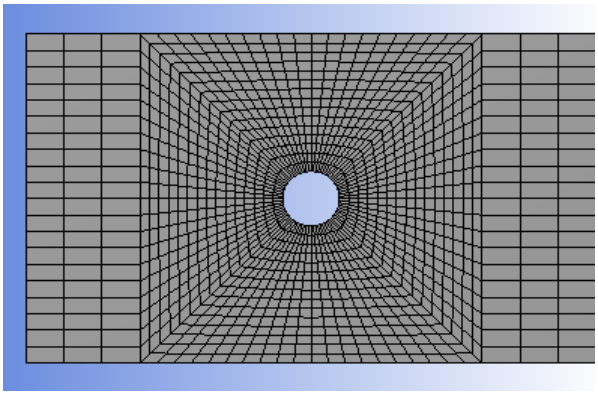

Fig. 4.21 Refined mesh around the pin-hole of a particular specimen

A ramped bearing force was applied onto the hole edge in the longitudinal direction, as shown in Fig. 4.22.

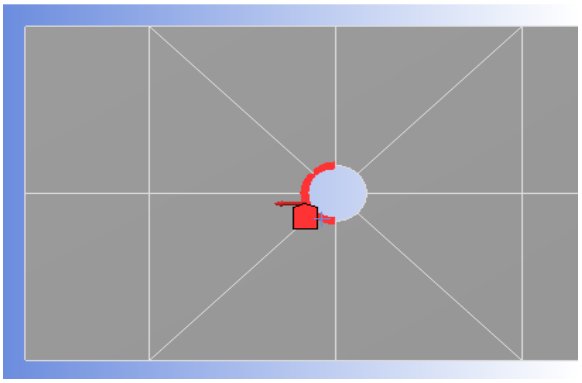

Fig. 4.22 Bearing load applied on the hole boundary of a particular specimen

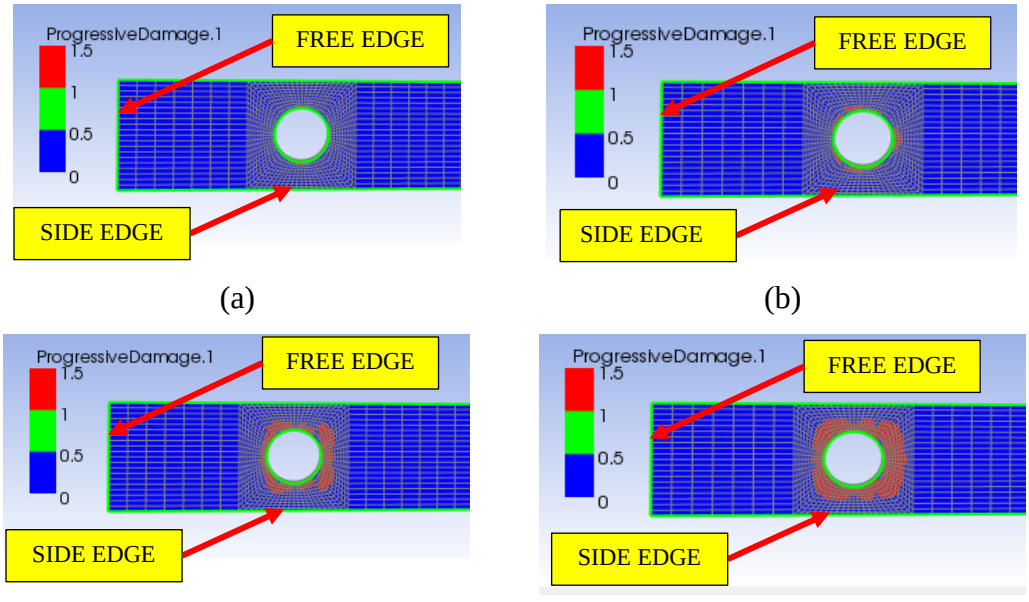

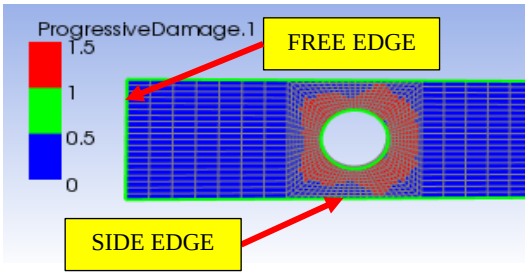

(e)

Fig. 4.23 Net-Tension failure mode status for E/D = 5 and W/D = 3 with metal insert at (a) 20%, (b) 40%, (c) 60%, (d) 80%, (e) 100% of applied load

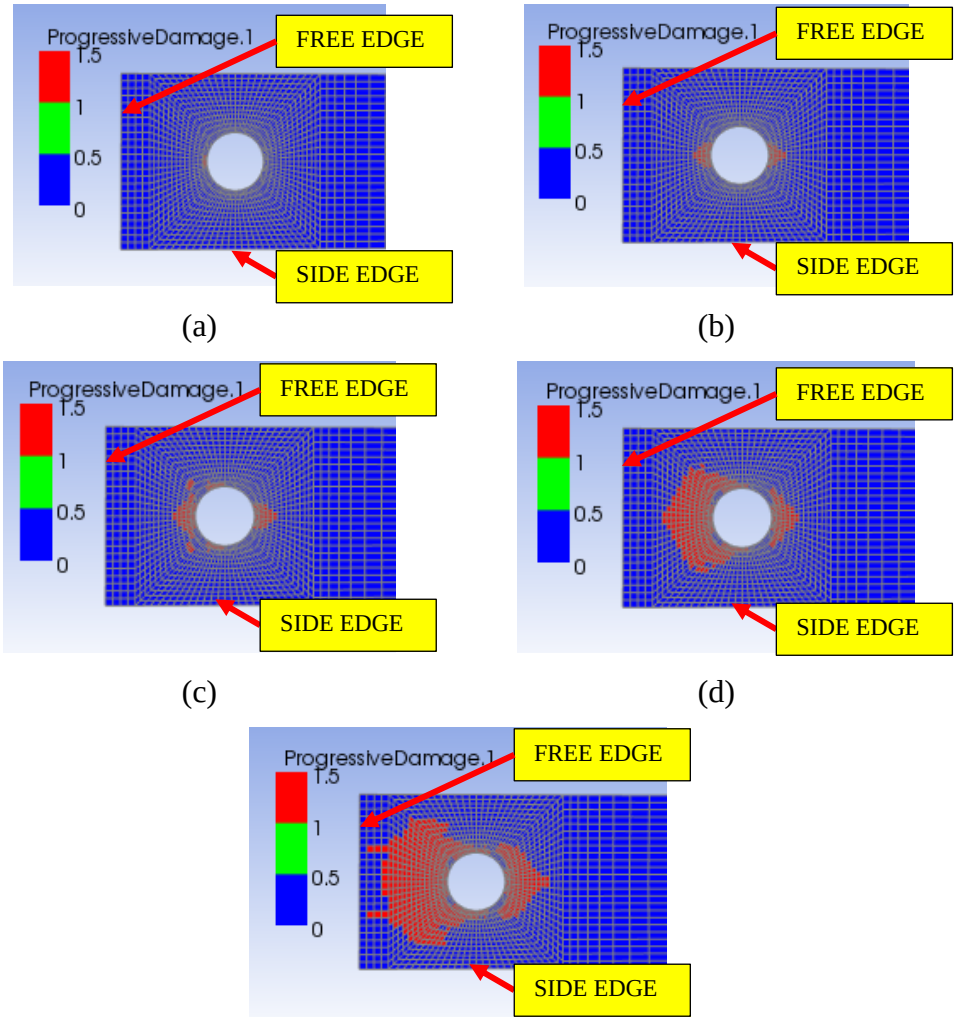

(a) (b)

(c) (d)

(e)

Fig. 4.24 Shear-out failure mode status for E/D = 2 and W/D = 3 without metal insert at (a) 20%, (b) 40%, (c) 60%, (d) 80%, (e) 100% of applied load

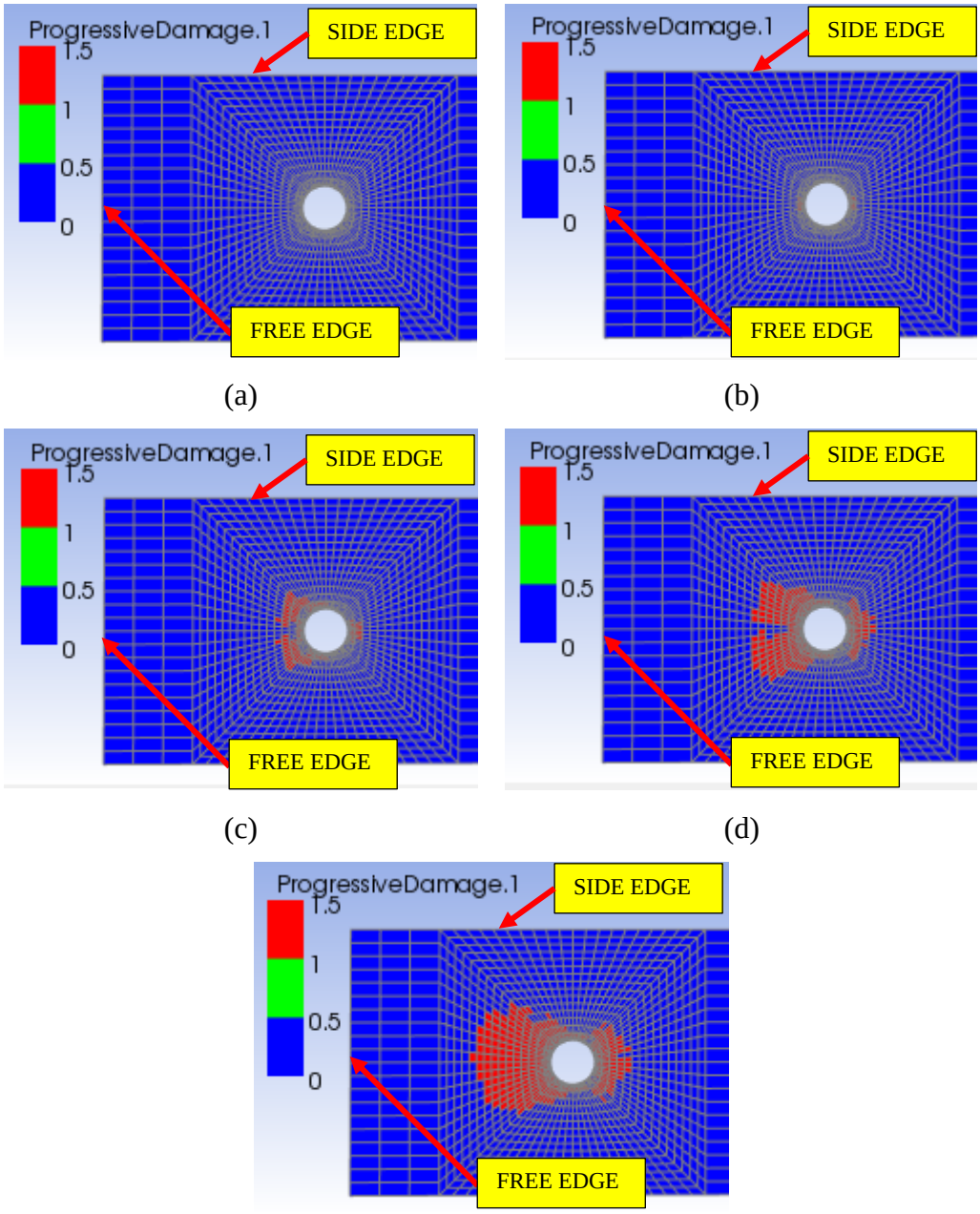

Fig. 4.25 Bearing failure mode status for E/D = 5 and W/D = 6 without metal insert at (a) 20%, (b) 40%, (c) 60%, (d) 80%, (e) 100% of applied load

Figure 4.23 shows the failure mode of pin joints with metal inserts and Figs. 4.24 and 4.25 show different failure modes of pin joints without metal inserts for one of the different geometric configurations. These figures concentrate on the hole with the free edge and the side edge for demonstrating different types of failure modes without showing the full length of joints. The cumulative damage in all layers of the composite specimen is shown in these figures. As given by Hashin failure criteria, some of the

elements failed due to matrix compression. However, some failed due to fiber tension. The higher mesh density, makes it difficult to mention the type of failure in each of the individual element. Figure 4.23 shows the net-tension failure mode of the pin joint with metal insert under a tensile load of 4800 N with geometric parameters of E/D=5 and W/D=3. It can be seen from the figure that the damage begins around the hole initially and then propagates towards the side edges as the applied load ramps up to the full value, confirming the net-tension failure mode of the joint. The shear-out failure mode of the pin joint without the metal insert under a tensile load of 3000 N with geometric parameters of E/D=2 and W/D=3 is shown in Fig. 4.24. The figure shows that the damage propagates to the free edge instead of the side edge of the joint as the distance between the free edge and the hole is smaller than the distance between the side edge and the hole. The damage propagation towards the free edge confirms the shear-out failure mode in the joint. The increase in E/D and W/D ratios leads to the bearing failure mode. The bearing failure mode of the joint under a tensile load of 4000 N is shown in Fig. 4.25 with geometric parameters of E/D=5 and W/D=6. Damage progress can be seen as the load increases from 20% to full 100% of the applied load. A pure bearing failure is observed from the figure.

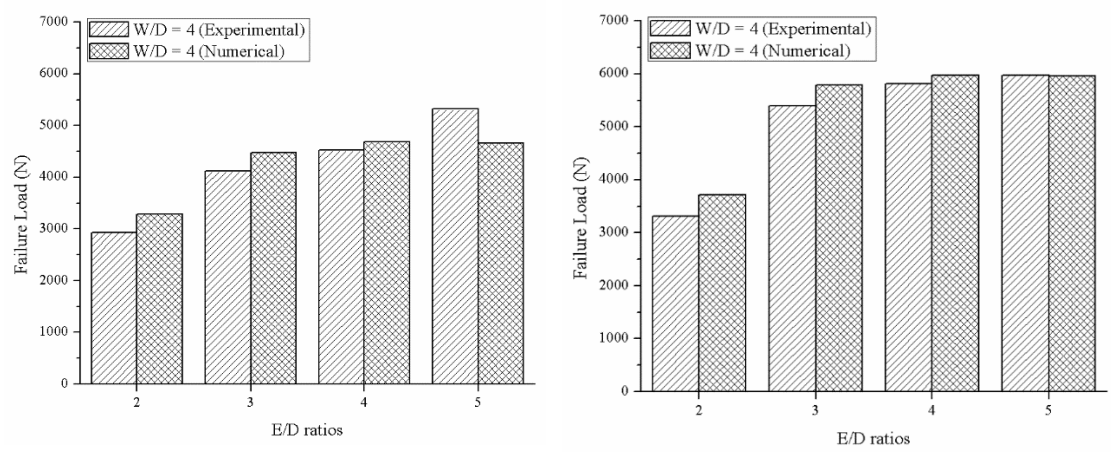

(a) (b)

Fig. 4.26 Experimental and numerical failure loads compared for a selected joint configuration with metal insert (a) without nanoclay and (b) with nanoclay

The comparison of experimental and numerical results for selected joint configurations are shown in Fig. 4.26. It is seen from the figure that failure loads predicted through the

numerical analysis are within the 10% acceptable differences with the experimental results which give a good correlation between the results.

4.5 Closure

The present chapter deals with the improvement of pin joint performance using metal inserts and nanoclay. The study has been carried out on two different materials, *i.e.*, unidirectional fiber reinforced composite and the bidirectional fiber reinforced composite. Initially the effect of metal insert has been investigated in unidirectional fiber reinforced composite. A positive contribution of metal insert in the failure load of the pin joint in unidirectional fiber reinforced composite plates lead to further study on bidirectional fiber reinforced composite material. In the later study, along with the metal inserts, the effect of nanoclay is also investigated on the pin joint performance. Using nanoclay showed a maximum of 26% and 31% improvement in the failure load of joints prepared with and without metal inserts, respectively.

The work presented in this chapter focused on the failure analysis of the pin joint. The physics of the pin joint is relatively simple than the bolted joint as there are no out-of-plane compressive forces present in the pin joint. To extend the scope of mechanical joint, next chapter deals with the failure analysis of the single lap single bolt joint.

Chapter 5
Performance Analysis of Single Hole Bolted Joint

This chapter deals with the effect of nanoclay bolt torque on the performance of single lap single bolt joints. Bolted joints were prepared from woven glass fiber reinforced laminates incorporating nanoclay content with 3 wt.% which was optimized for maximum tensile strength. Different geometric parameters, *i.e.*, edge distance-to-hole diameter (E/D) ratio and width-to-hole diameter (W/D) ratio were varied over the range of 2 to 5. To analyze the effect of bolt torque, different levels of torque, *i.e.*, 0, 3 and 5 Nm were considered for the failure analysis of the joint. Progressive Damage Analysis along with the Characteristic Curve method and Hashin Failure Criteria was performed to predict the failure load and failure modes in the bolted joints, numerically.

5.1 Single Lap Joint

Single lap joint was prepared from the laminates which were characterized at optimum values of pressure, temperature and curing time for maximum strength as discussed in Chapter 3. To fabricate the single lap joint, composite laminates were cut to the desired size using diamond cutter followed by drilling a hole of 4 mm diameter. While drilling, a flat plywood was firmly held below the specimen to avoid delamination at the outer layer when drill passed through the other side of the specimen.

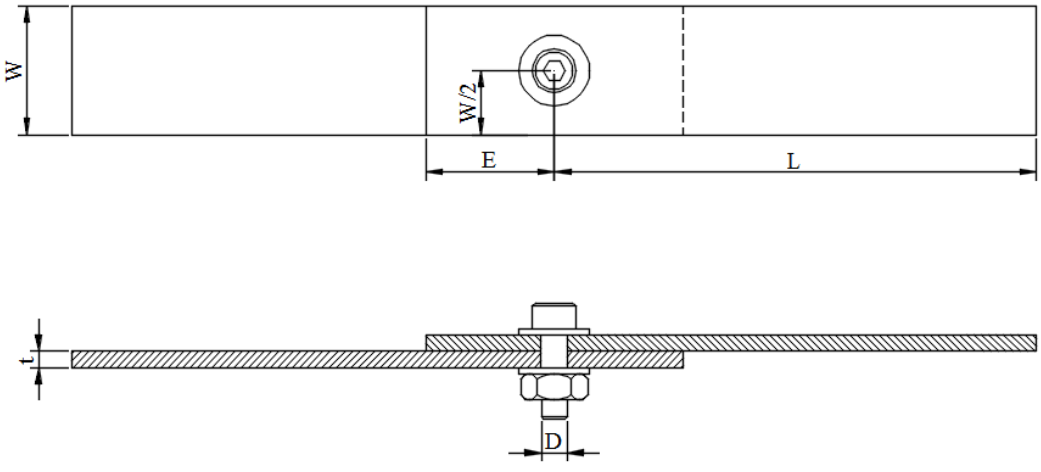

Fig. 5.1 Geometry of single lap joint

Delamination was inspected visually and the specimens showing delamination were discarded. It was assumed that the delamination at micro-level in the hole surface will not affect the relativity of the results in the present study. Thereafter, the two strips of the cut specimen were assembled using nut, bolt, and washer to form a lap joint. The geometry of the lap joint is shown in Fig. 5.1.

To analyze the joint for different geometric parameters, the values of E/D and W/D ratios were varied from 2 to 5. The different design configurations of bolted joint by varying different geometric parameters are shown in Table 5.1.

Table 5.1 Geometry of the specimens tested under tensile load

Ratios		**Diameter of hole (mm)**	**E (mm)**	**W (mm)**	**Thickness (mm)**	**Length from hole to edge (mm)**
W/D = 2	E/D = 2	4	8	8	2.5	80
	E/D = 3	4	12	8	2.5	80
	E/D = 4	4	16	8	2.5	80
	E/D = 5	4	20	8	2.5	80
W/D = 3	E/D = 2	4	8	12	2.5	80
	E/D = 3	4	12	12	2.5	80
	E/D = 4	4	16	12	2.5	80
	E/D = 5	4	20	12	2.5	80
W/D = 4	E/D = 2	4	8	16	2.5	80
	E/D = 3	4	12	16	2.5	80
	E/D = 4	4	16	16	2.5	80
	E/D = 5	4	20	16	2.5	80
W/D = 5	E/D = 2	4	8	20	2.5	80
	E/D = 3	4	12	20	2.5	80
	E/D = 4	4	16	20	2.5	80
	E/D = 5	4	20	20	2.5	80

5.2 Experimental Results

Tensile tests were performed on the single lap joint on German make Zwick-Roell Z010 Model Universal Testing Machine at a crosshead speed of 2 mm/min. The test setup is shown in Fig. 5.2. Minimum five specimens were tested for each configuration.

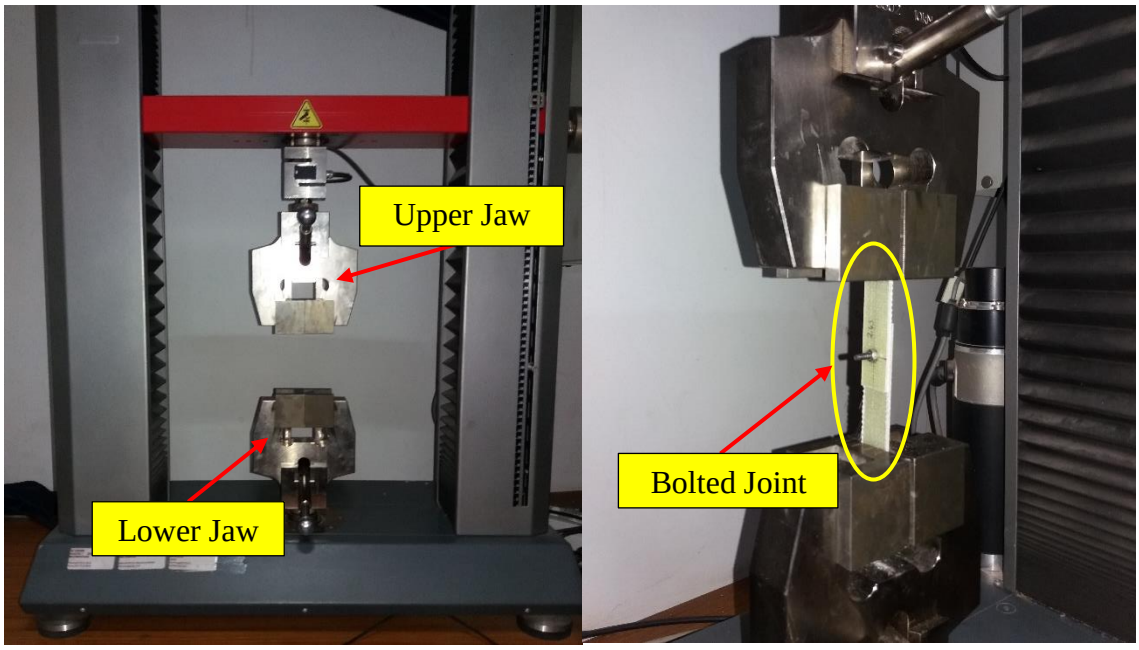

Fig. 5.2 Tensile testing of the single lap joint on universal testing machine (UTM)

The failure behaviors of single lap joints prepared from the laminates made without and with nanoclay content are shown in Fig. 5.3 and 5.4, respectively. It is observed that the load-displacement curves were linear up to the initial failure, *i.e.*, the first peak point of the curve. To predict the ultimate failure of the joint, the load was further increased. With the increase in the load, there was more increase in the strain rate as compared to the stress rate which was due to the fact that the material already had an initial failure. Moreover, with the increase in load there came the effect of eccentric loading and then the secondary bending which may also contributed into the non-linear nature of the curve. As shown in Fig 5.3 (a) and 5.4 (a), increasing E/D ratio for the joints with W/D = 2, not much improvement in failure load is observed. There is sudden drop in the load-displacement curve which represents the net-tension type of failure mode. This is because of the less margin between the hole and the side edge of the specimens. The failure load increases with increase in both E/D and W/D ratios. For W/D = 4 and 5, as shown in Figs. 5.3 (c), 5.3 (d), 5.4 (c), and 5.4 (d), increasing E/D ratio has shown a significant improvement in the failure load. Comparing joint configurations with identical E/D ratios, it is clear from the Figs. 5.3 and 5.4 that, increasing W/D ratio has increased the maximum displacement to the ultimate failure of the joint. For W/D = 4 and 5, maximum displacement to the ultimate failure is quite large. The load-displacement curve moves

forward in a zig-zag pattern with the multiple peak points which represents the bearing failure mode.

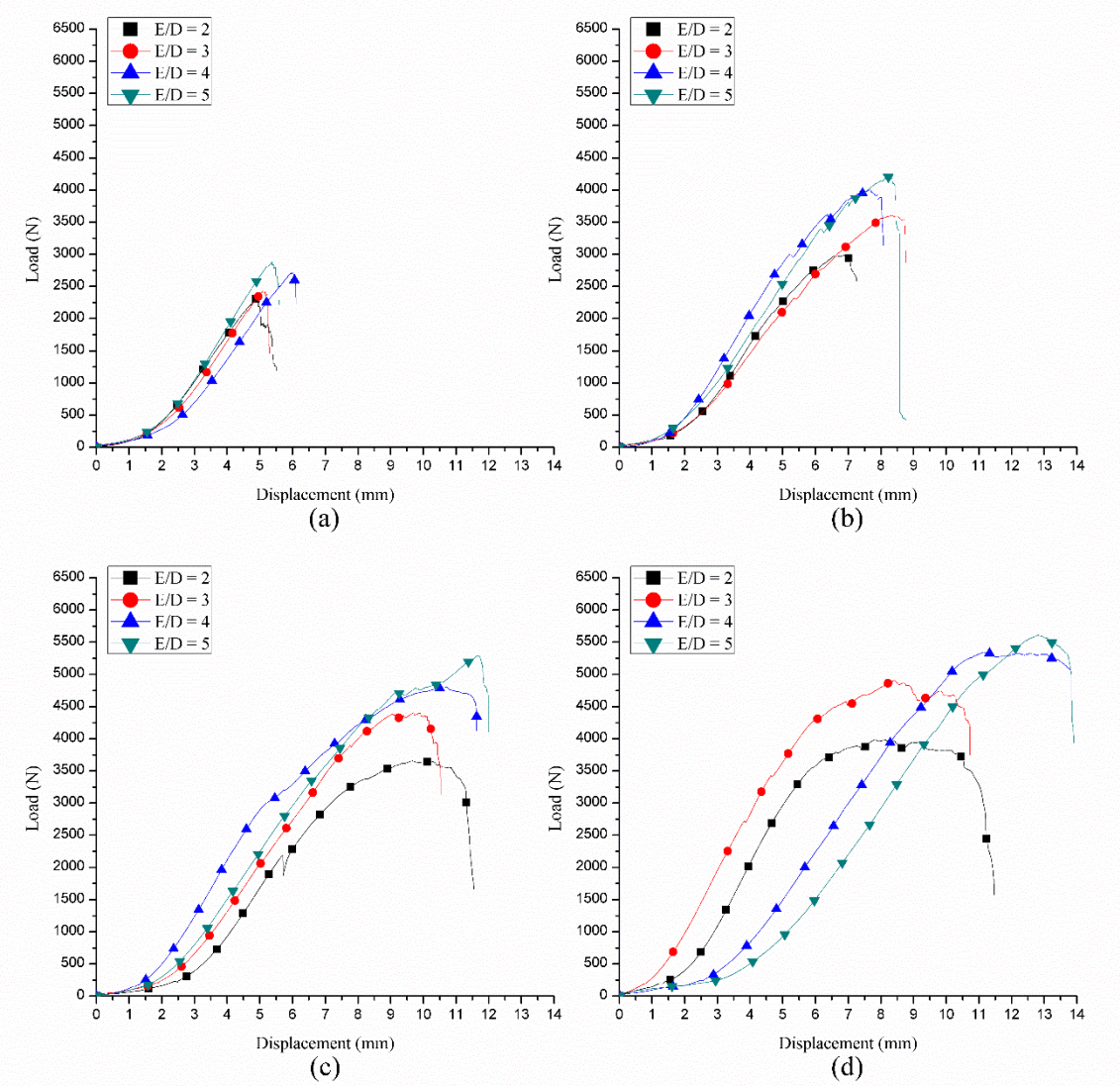

Fig. 5.3 Load vs displacement plots for the joints without nanoclay with 0 Nm torque at (a) W/D = 2, (b) W/D = 3, (c) W/D = 4, (d) W/D = 5

Incorporating 3 wt.% of nanoclay compared to the joints prepared with neat epoxy has increased the failure load in almost all joint configurations. There is a significant improvement of about 15–20% with the addition of nanoclay for configurations W/D > 3 and E/D > 3. This is due to the promoted interfacial bonding between fiber and epoxy [19, 115]. Mechanical properties of the epoxy are also improved as an individual using nanofillers.

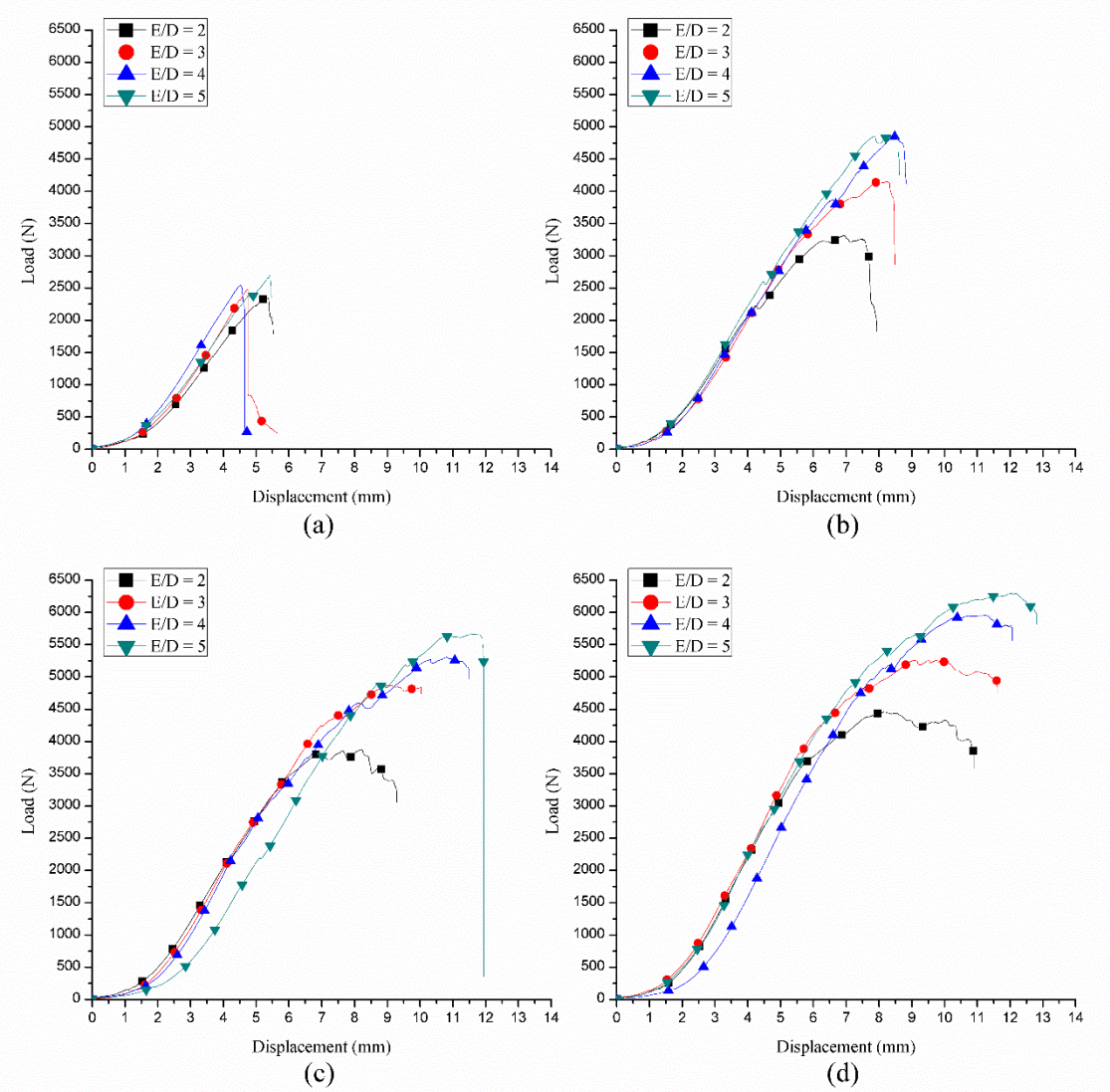

Fig. 5.4 Load vs displacement plots for the joints with nanoclay with 0 Nm torque at (a) W/D = 2, (b) W/D = 3, (c) W/D = 4, (d) W/D = 5

Table 5.2 Failure modes observed for different joint configurations

Set No.	Ratios		Failure mode	
	W/D	E/D	Neat	Clay
1	2	2	NT	NT
2	2	3	NT	NT
3	2	4	NT	NT
4	2	5	NT	NT
5	3	2	NT	NT
6	3	3	NT	NT
7	3	4	NT	NT
8	3	5	NT	NT
9	4	2	NT	NT
10	4	3	NT	B+NT

11	4	4	B+NT	B
12	4	5	B+NT	B
13	5	2	B	B
14	5	3	B	B
15	5	4	B	B
16	5	5	B	B

The failure modes for different joint configurations with and without nanoclay are shown in Table 5.2. A pure bearing failure mode is observed in all W/D = 5 joint configurations for joints prepared from laminates without nanoclay. However, in case of joints prepared from laminates with nanoclay, pure bearing is seen in W/D ≥ 4 and E/D ≥ 4 joint configurations.

W/D = 3, E/D = 3 W/D = 4, E/D = 3 W/D = 5, E/D = 3

(a)

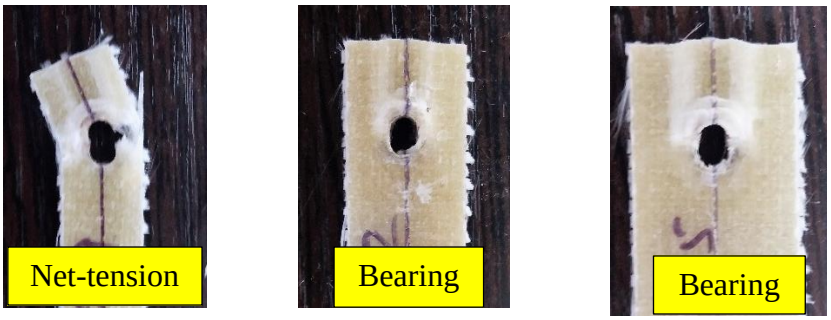

W/D = 3, E/D = 3 W/D = 4, E/D = 3 W/D = 5, E/D = 3

(b)

Fig. 5.5 Actual images of the specimens depicting the failure modes of the joints made of composite using (a) neat epoxy, and (b) epoxy modified with nanoclay

Figure 5.5 shows actual images of some of the specimens depicting the failure modes. Comparing specimen prepared with and without the nanoclay for W/D = 4, E/D = 3 joint configuration as shown in Fig. 5.5 (a) and (b), it is clearly seen that nanoclay has improved the failure mode from bearing followed by net tension to the pure bearing. It is

also seen that the maximum displacement before catastrophic failure is increased by increase in the edge and width of the specimen. Increasing the edge and width dimensions facilitates more time before the complete loss of the joint strength and its functionality. Hence keeping W/D ≥ 4 and E/D ≥ 4 will lead to a bearing mode of failure and reduce the chance of sudden uninformed failures.

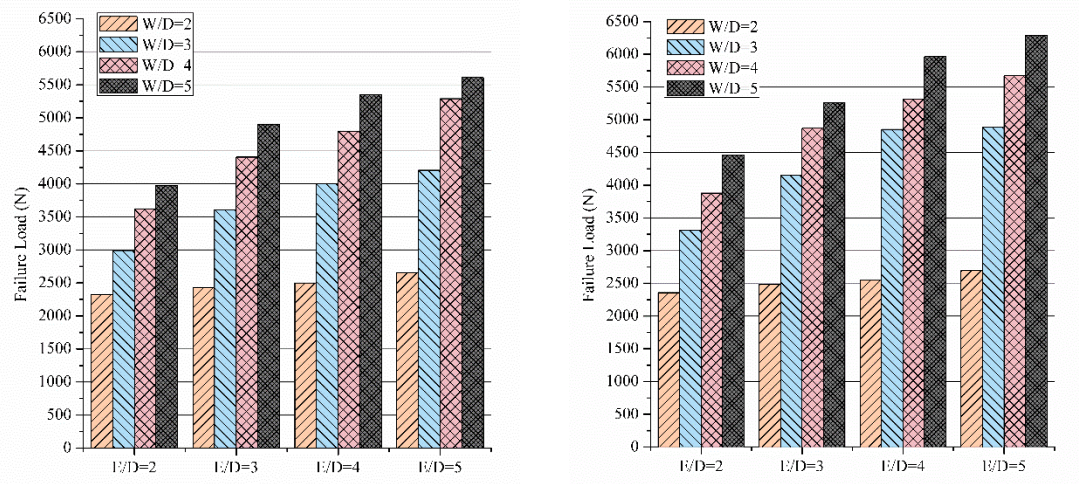

Fig. 5.6 Maximum failure loads for the joints with different E/D and W/D ratios made of composite using (a) neat epoxy, and (b) epoxy modified with nanoclay

A comparison of maximum failure loads for all joint configurations prepared from laminates with neat epoxy and with 3 wt.% of nanoclay is shown in Fig. 5.6. It is clearly seen from the figure that incorporating the nanoclay into the epoxy has improved the maximum failure load by about 18%.

5.2.1 Effect of torque in the bolted joint

In case of mechanically fastened joints, bolt tightening torque is an important factor which is necessary for locking of the joint in place and significantly affects the performance of the joint. To analyze the effect of torque on the joint performance, the geometry configuration was fixed to E/D and W/D ratios to be 4 as the joint with E/D and W/D ≥ 4 had the bearing failure mode. The torque on the said configuration was varied from 0 to 5 Nm. A calibrated torque wrench was used to tighten the bolts, and it was assumed that the applied particular torque level was similar in all joint configurations. Lock nut was used to avoid the bolt loosening while joint testing. Hand tightening was assumed to be of 0 Nm torque. The effect of increasing the torque on the

strength of the joint is shown in Fig. 5.7. Failure load increases with increasing bolt torque. It is clear from the Fig. 5.7 that increasing torque reduces the maximum displacement before the ultimate failure. The specimens with higher torque values have less displacement to failure compared to the specimens with lower torque settings. Comparing neat and nanoclay joint configurations, increased joint stiffness is observed for the joints prepared from laminates with nanoclay content.

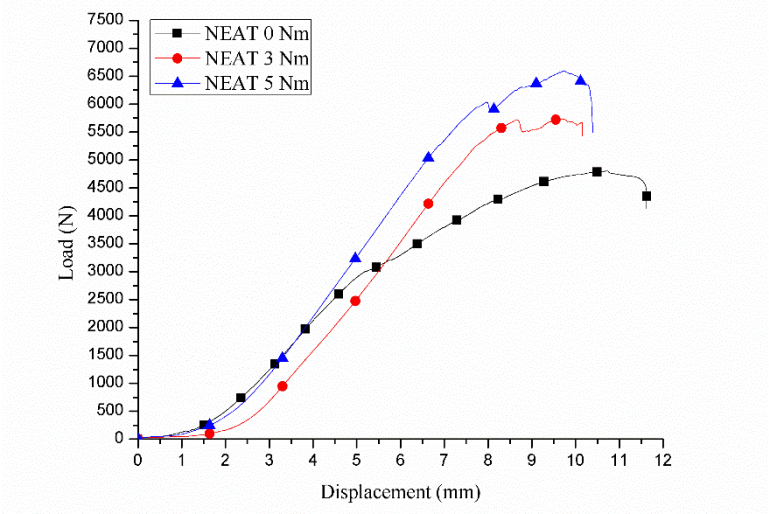

(a)

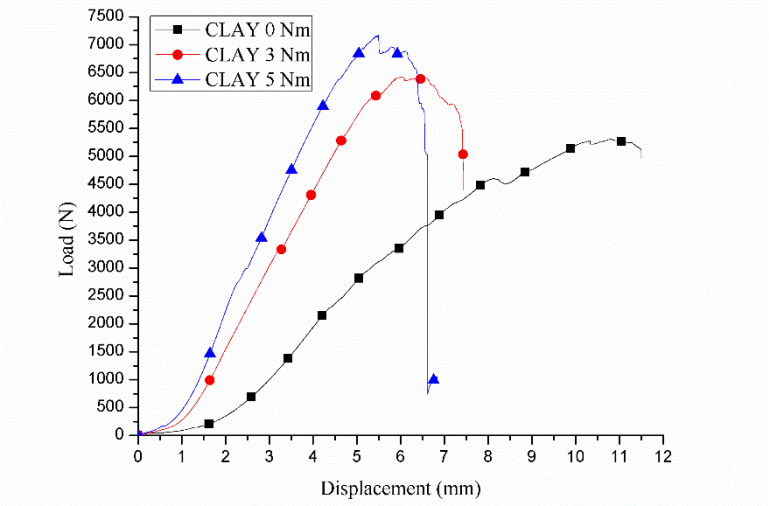

(b)

Fig. 5.7 Effect of torque on the failure load of the joint with E/D = 4 and W/D = 4 with neat epoxy, and (b) epoxy modified with nanoclay

Comparison of maximum failure load for the composite joints prepared from neat and nanoclay considering torque variation has been presented in Fig. 5.8. It is observed that

increasing bolt torque significantly improves the failure load and hence the joint performance. For joints prepared from laminates without nanoclay, failure load increased by 19% and 37% with increasing torque from 0 Nm to 3 Nm and 5 Nm, respectively. Comparing neat and nanoclay joint configurations, almost same amount of improvement is imparted to joints performance with increasing torque to the equal levels.

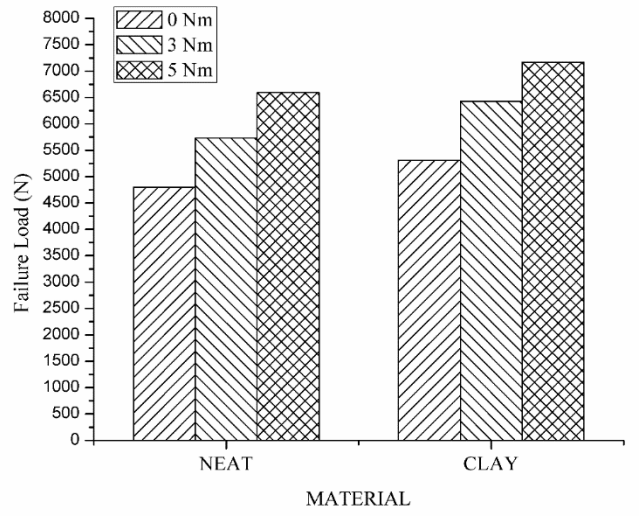

Fig. 5.8 Maximum failure loads for the joints with E/D = 4 and W/D = 4 at different torque settings

5.2.2 Regression analysis

Regression analysis [24] has been performed after fixing the geometry configuration, *i.e.*, E/D and W/D ratios to be 4 as the joint with E/D and W/D ≥ 4 had the bearing failure mode.

Table 5.3 Analysis of variance

Source	DF	Adj SS	Adj MS	F-value	P-value	Percentage contribution
Regression	2	3867125	1933563	376.92	0.000	-
M	1	525104	525104	102.36	0.002	13.52
T	1	3342021	3342021	651.49	0.000	86.08
Error	3	15390	5130			0.39
Total	5	3882515				

Regression analysis is performed to determine the influence of nanoclay and bolt torque on the failure load of the composite joint. Regression investigates and models the relationship between a response, *i.e.*, the failure load (F_L), and the predictors, *i.e.*, the material type (M) and the torque (T) in the present study. In particular, regression

analysis is often used to determine how the response variable changes with change in a particular predictor variable. The analysis of variance given in Table 5.3, shows the amount of variation in the response data explained by the predictors and the amount of variation left unexplained. As shown in Table 5.3 (p-value < α at 95% confidence interval), there is a valuable impact of the bolt torque as well as the material variation on the failure load of the joint. The p-value for regression is 0.000, indicating that at least one of the regression coefficients is significantly different than zero. From the p-value and percentage contribution of the predictors, *i.e.*, material and torque shown in Table 5.3, it is clearly visible that the response, *i.e.*, failure load is largely influenced by the torque (p = 0.000) as compared to the material variation (p = 0.002). The predictive failure load values were determined using the equation (5.1) which was given by regression.

$$F_L = 4739.8 + 197.2\,M + 363.2\,T \tag{5.1}$$

where, F_L is the failure load (in N), M is the material variation (wt.% of nanoclay), and T is the torque (in Nm).

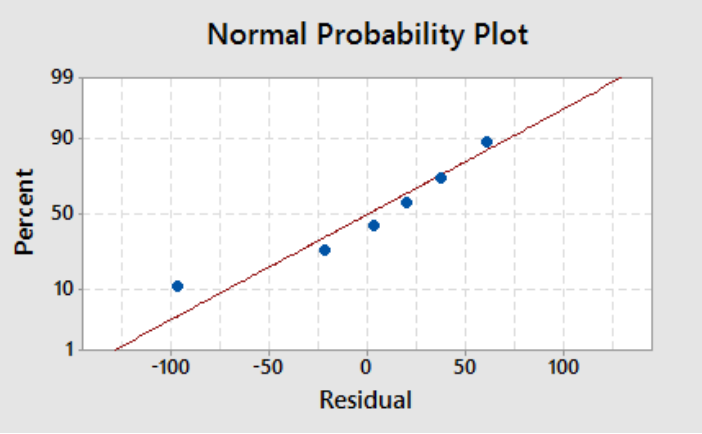

Fig. 5.9 Residual plots for the failure load

The residual plot for the failure load is shown in Fig. 5.9. The percentage error in the experimental and the predicted value through the regression equation is less than 2.4%.

5.3 Numerical Analysis

Finite Element Analysis of the single lap bolted joint was performed using ANSYS structural analysis module. Material properties of the composite specimen were taken as

given in Table 3.14. For the failure analysis of the joint progressive damage analysis along with the characteristic curve method has been performed.

5.3.1 Characteristic curve method

Stresses around the bolt hole in the composite plate are high due to stress concentration and evaluation of failure near the bolt hole may give premature results, which actually does not happen in real life situations. Therefore, to overcome the problem of stress concentration, characteristic curve method has been used to predict the failure of the single lap composite joint [69, 91]. The curve is drawn as shown in Fig. 5.10 as per the equation (5.2) by using the characteristic lengths.

$$r_c = \frac{D}{2} + R_{ot} + (R_{oc} - R_{ot})cos\theta \tag{5.2}$$

Where, r_c is the radius of characteristic curve, D is diameter of the hole, R_{ot} is characteristic length in tension, R_{oc} is characteristic length in compression. Angle, θ can be measured either clockwise or anticlockwise from the axis of applied load due to the symmetry of the curve.

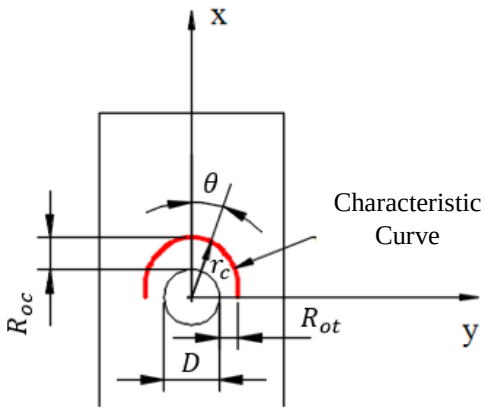

Fig. 5.10 Description of the characteristic curve [69]

In the present work, the characteristic lengths in tension and compression are obtained numerically. The Finite Element Analysis has been performed on the open hole laminates to determine the characteristic lengths in tension and compression [91].

The laminate was modeled with a particular E/D and W/D ratio. The laminate was subjected to the symmetrical tensile load (F). The mean tensile strength was calculated using equation (5.3).

$$\text{Mean Tensile Strength } = \frac{F}{(W-D)t} \tag{5.3}$$

Where, W is the width of the plate, D is the diameter of the hole and t is the thickness of the laminate. The distance from the hole edge to the point where the equivalent stress is equal to the mean tensile strength is called the characteristic length in tension.

A compressive force (F) was applied to the hole. The bearing strength of the specimen was calculated using equation (5.4).

$$\text{Mean Bearing Strength } = \frac{F}{Dt} \tag{5.4}$$

Where, D is the diameter of the hole and t is the thickness of the laminate. Then the point ahead of the hole was located such that the equivalent stress was equal to the mean bearing strength. The distance from the edge of the hole to this point where the equivalent stress becomes equal to the mean bearing stress is called the characteristic length in compression.

For the damage initiation, Hashin failure criteria using equations (4.1) to (4.4) was used to perform the progressive failure analysis of the composites.

Maximum failure index(FI_{max}), the maximum value among f_f and f_m in tension and compression, is used for determining the failure modes and the failure loads. Based on the location of maximum failure index on the characteristic curve, failure modes have been identified. Equation (5.9) gives the failure modes on the basis of angle (θ_f) measured on the characteristic curve.

$$\begin{aligned} &0° \leq \theta_f \leq 15° \quad : \text{Bearing} \\ &30° \leq \theta_f \leq 60° : \text{Shear-out} \\ &75° \leq \theta_f \leq 90° : \text{Net-tension} \end{aligned} \tag{5.9}$$

Failure load of the single lap composite joint is determined using equation (5.10)

$$Failure\ Load = \frac{F}{FI_{max}} \tag{5.10}$$

Where, F and FI_{max} are the values of applied force and maximum value of failure index respectively.

5.3.2 Loads and boundary conditions

The applied loads, boundary conditions, and contact regions for the finite element analysis are shown in Fig. 5.11.

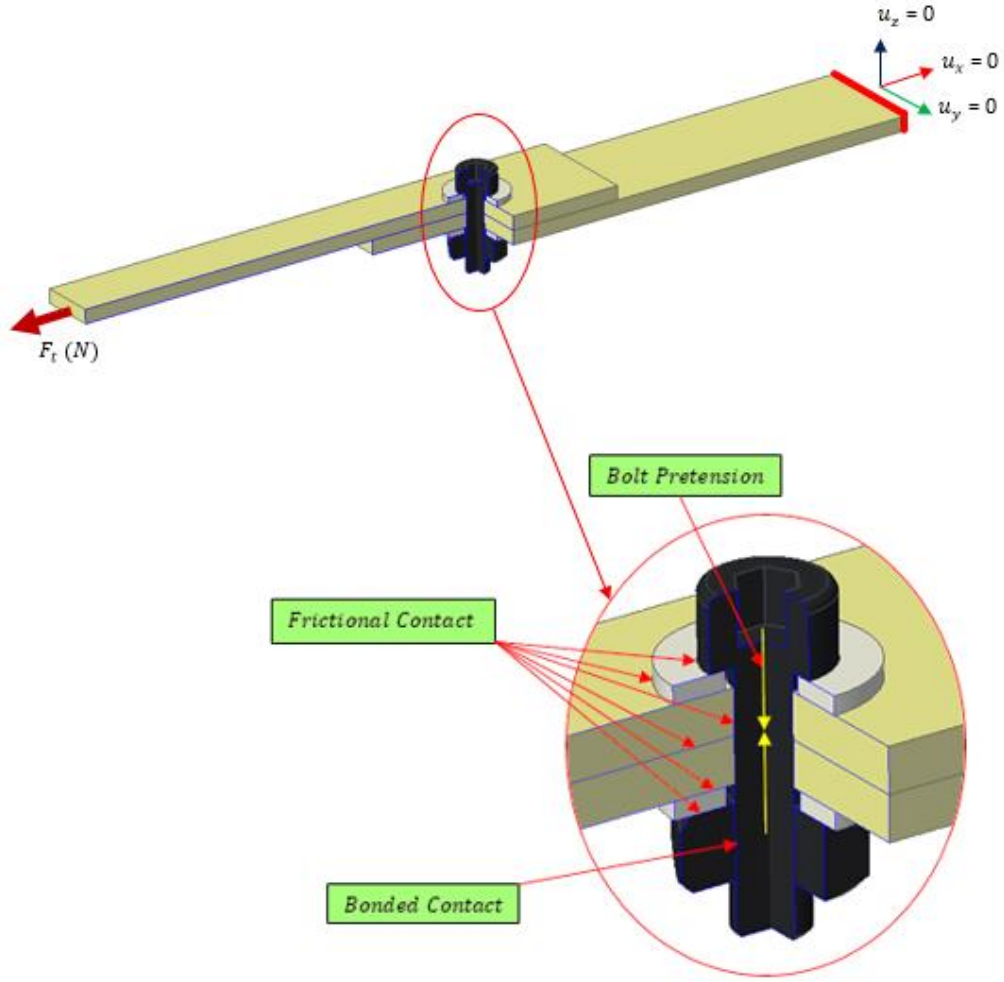

Fig. 5.11 Loads, boundary conditions and contacts set up in the numerical analysis of the joint

One side of the lap joint is fixed in all the directions while on the other side of the joint an arbitrary tensile load, F_t of 4000 N is applied. Frictional contact behavior have been considered in all contact regions except the contact between nut and bolt which represents the locked condition and is taken as bonded. Complete mesh of single lap joint is shown in Fig. 5.12. Multizone mesh method has been used with all Quad elements. Mesh density was determined by performing the convergence study. A refined mesh used along the characteristic curve is shown in Fig. 5.13. Analysis has been done in two steps. In the first step, bolt pre-tension is applied and in the second step, bolt pre-tension is locked and tensile load is applied.

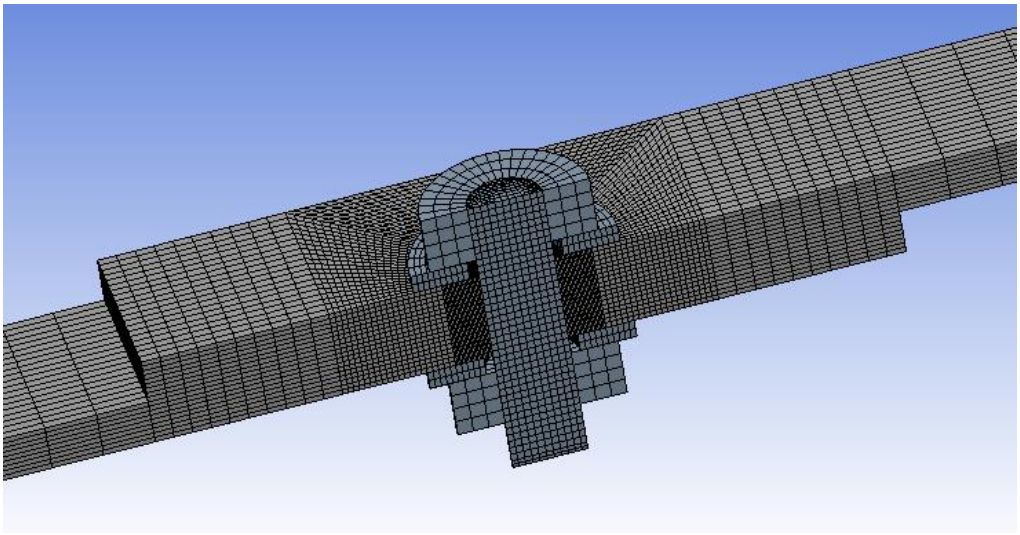

Fig. 5.12 Complete mesh of the single lap joint

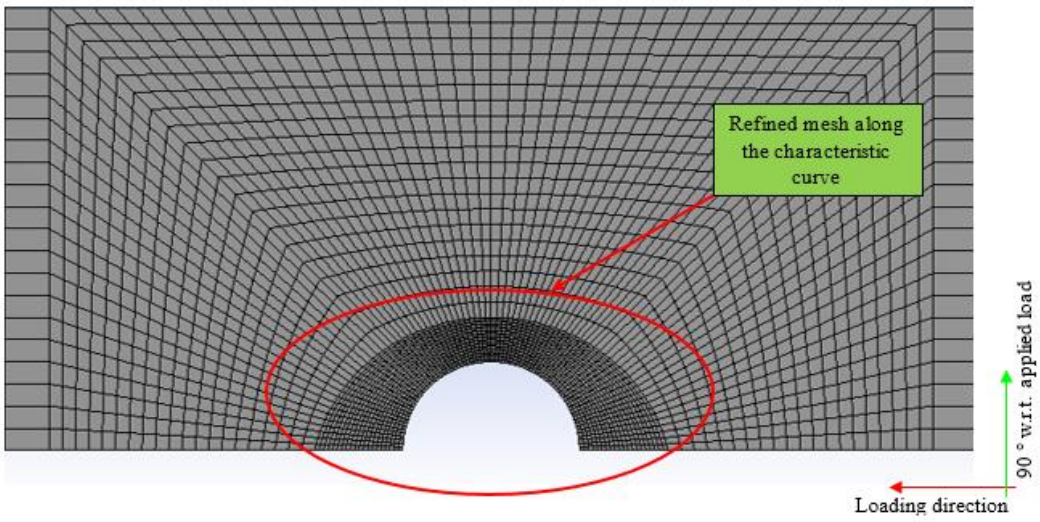

Fig. 5.13 Refined mesh around the hole in the composite joint

The average experimental and the numerically predicted failure loads of the single lap composite joint are shown in Table 5.4. It can be seen from the Table that the failure load increases with increase in E/D and W/D ratios and there is a close agreement between experimental and numerical results.

Table 5.4 Failure loads obtained from numerical analysis of the joint for different levels of geometric parameters

Set No.	Geometry level		Failure load (N)			
			Experimental		Numerical	
	W/D	E/D	Neat	Clay	Neat	Clay
1	2	2	2327	2357	2510	2602
2	2	3	2427	2480	2532	2624
3	2	4	2500	2545	2537	2630
4	2	5	2654	2694	2539	2658
5	3	2	2990	3315	3140	3411
6	3	3	3609	4147	3771	4350
7	3	4	4000	4852	4168	5036
8	3	5	4205	4884	4415	4884
9	4	2	3618	3878	3785	4076
10	4	3	4405	4868	4598	5116
11	4	4	4800	5309	5045	5590
12	4	5	5290	5668	5512	5945
13	5	2	3981	4457	4152	4644
14	5	3	4905	5263	5056	5542
15	5	4	5345	5963	5639	6279
16	5	5	5610	6294	5817	6546

The damage status for the lowest and highest joint configurations is shown in Fig. 5.14. It can be seen from the figure that for the low width specimen, *i.e.*, W/D = 2 the damage begins near the hole and progress towards the side edge leading to the net-tension failure mode. Therefore, it is again confirmed through the numerical analysis that the specimens with a low value of W/D fails in a sudden manner and is catastrophic in nature which should be avoided. It is due to the less material margin available to the sides of the hole. Whereas, for the high width specimen, *i.e.*, W/D = 5, the damage begins around the hole and progress towards the free edge but could not reach the free end and represents the bearing failure mode. Damage to the inner and outer layers is different due to the eccentricity of the applied load. Layers near the washer are under compression, whereas layers near the neutral axis, *i.e.*, mating contact of the two composite plates are under tension due to out of plane displacement. Therefore, maximum damage in any of the layer through the thickness of the composite plate has been considered for the failure analysis.

The numerically predicted maximum failure load for the single lap joint with E/D = 4 and W/D = 4 is shown in Fig. 5.15. It is clearly visible that the failure load increases with increase in the bolt pre-tension.

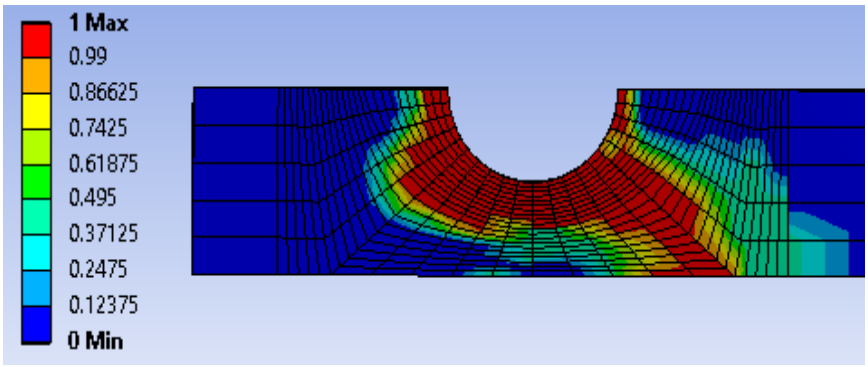

(a)

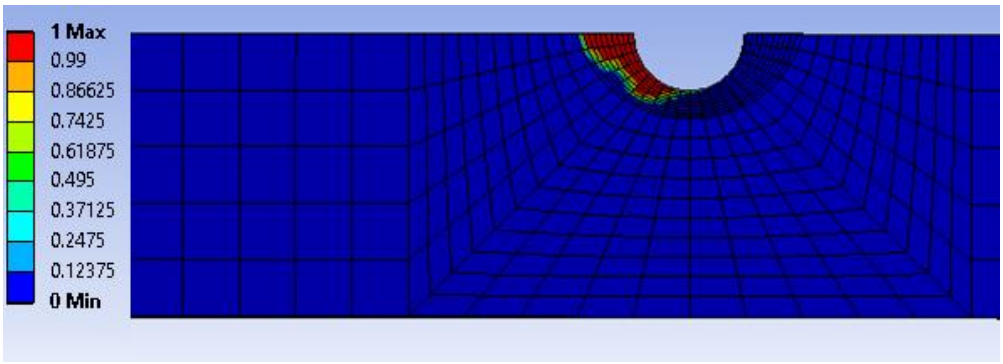

(b)

Fig. 5.14 Damage status of the composite joint for (a) W/D = 2 and E/D = 2, (b) W/D = 5 and E/D = 5

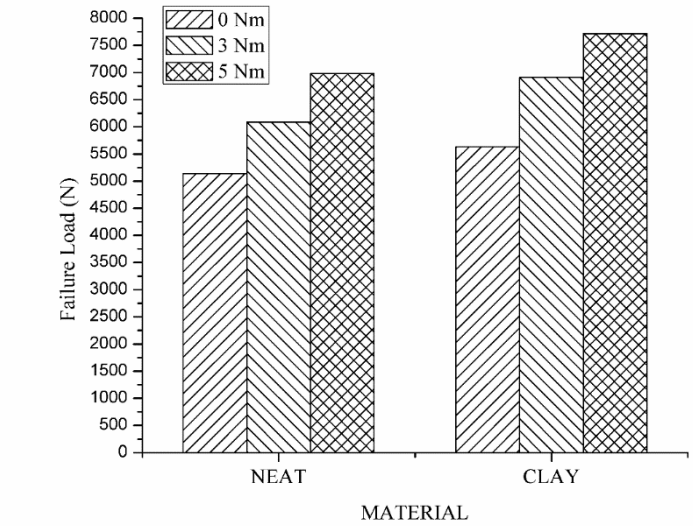

Fig. 5.15 Maximum failure loads for the joints with E/D = 4 and W/D = 4 at different torque settings

5.4 Closure

In this chapter, the effect of nanoclay and bolt torque on the failure of single bolt lap joints prepared from glass fiber reinforced nanocomposite laminates have been investigated. Bolted joints were prepared using neat and 3 wt.% of nanoclay content. Incorporating 3 wt.% of nanoclay has shown improvement in failure load of the bolted joints. The effect of joint geometry was determined by varying E/D and W/D ratios from 2 to 5. Failure load of the bolted joint increases by increasing E/D and W/D ratios. The failure mode of the joints were highly dependent on the geometry of the joint. Bolt torque varied over a range of 0 to 5 Nm demonstrated significant effect on the behavior of single lap bolted joint. Increasing bolt torque has shown an increase in the failure load and stiffness of the bolted joint. Numerical analysis has been performed for all design configurations using characteristic curve method and Hashin Failure Criteria. A good agreement is observed between numerical and experimental results.

This chapter focused on the failure analysis of single lap single bolt joint at room temperature. Extending the work further, next chapter deals with the failure analysis of the double lap single bolt joint. The joint is studied for its performance analysis at room temperature as well as accelerated aging conditions.

Chapter 6
Aging of Bolted Joints

The present chapter deals with the aging of the bolted joints prepared from glass fiber reinforced plastics. Two different types of aging environments, *i.e.*, hygrothermal aging, and accelerated aging, are performed in the present study. Bolted joints were prepared from woven glass fiber reinforced composite laminates with the addition of 3 wt.% of nanoclay content. Nanoclay acts as a mechanical interlock between the fiber and the epoxy and thus improves the interfacial bonding. A good dispersion of nanoclay improves moisture barrier properties which in turn reduces the degradation of the composite material during hygrothermal conditions [110]. To design the bolted joint, ASTM D5961 was used and the geometric parameters, *i.e.*, edge distance-to-hole diameter (E/D) ratio and width-to-hole diameter (W/D) ratio were fixed to 5 and 6, respectively. The effect of different levels of torque, *i.e.*, 0, 2 and 4 Nm were considered for the failure analysis of the joint.

For hygrothermal aging, three different temperatures, *i.e.*, 25, 50, and 75°C along with three different duration of exposure, *i.e.*, 1, 2 and 3 weeks were considered. A full factorial design of experiment was conducted on important control factors, *i.e.*, water temperature, exposure time, bolt torque, and material variation. It was found that the hygrothermal conditions degraded the material with temperature as the most contributing factor.

For accelerated aging, a maximum of 500 hours cyclical ultraviolet exposure was given to the specimens as per ASTM D1544. A full factorial design of experiment was conducted on important control factors, *i.e.*, aging time, bolt torque, and material variation. It was found that the strength of the joints prepared with and without the nanoclay content decreased with the increase in the duration of aging. However, the joints with the nanoclay content had higher failure loads.

6.1 Joint Configurations

ASTM D5961, standard for testing the bearing response of the composite joints, was used to design and test the specimens prepared from neat epoxy and epoxy modified with 3 wt.% of nanoclay content. Geometric parameters, *i.e.*, E/D and W/D ratios were taken

as 5 and 6, respectively as per the ASTM D5961 standard. To insert a bolt, the diameter (D) of the hole was fixed as 4 mm. The effect of bolt torque on the joint performance was also taken into consideration in the present work.

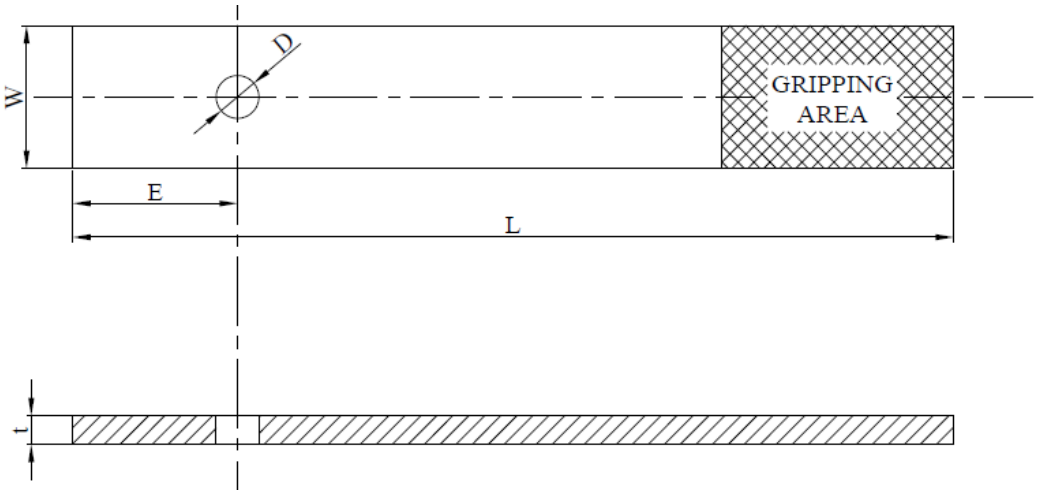

(a)

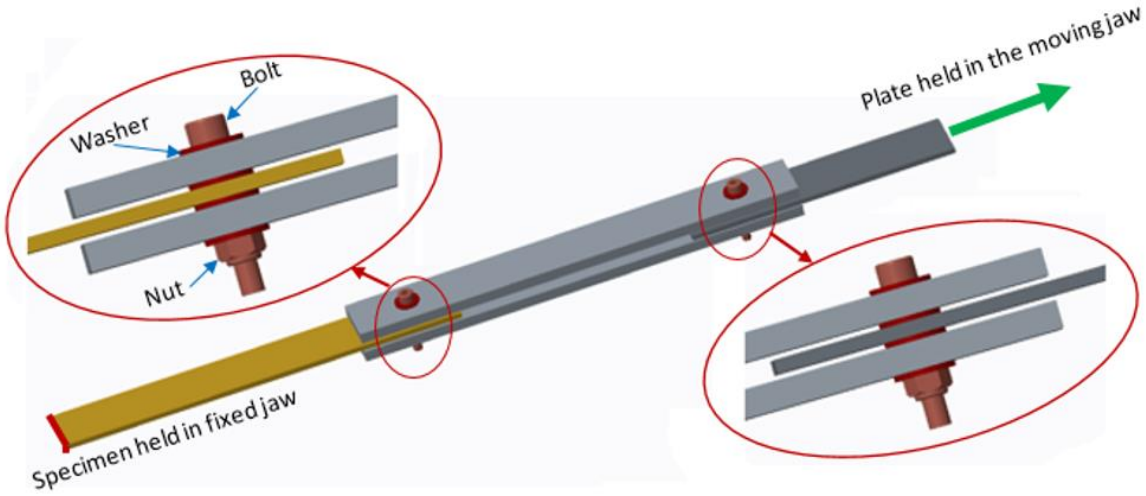

(b)

Fig. 6.1 (a) Specimen and (b) fixture schematic design

The joints were tested under tensile loads on the Zwick-Roell Universal Testing Machine with a capacity of 10 kN at a crosshead speed of 2 mm/min. The composite specimen as shown in Fig. 6.1, was held in the lower jaw of the UTM and a gradual increasing load was applied to the plate. The applied load is resisted by a bolt seated at the center of the hole. The symmetry in design and boundary conditions along the center line of the bolted joint prevented the effect of bending moment during the tensile testing of the specimens.

6.2 Aging

Various outdoor applications have to deal with moisture and temperature. Besides this, in areas where the intensity of the Sun is very high, the effect of UV radiations on the composite material becomes crucial factor to study. Therefore, two separate studies, *i.e.*, hygrothermal aging (combined effect of temperature and moisture), and accelerated aging (cyclical exposure to ultraviolet radiations and moisture) have been performed.

6.2.1 Hygrothermal aging

All the specimens for characterization and for testing of bolt joints, were immersed in distilled water in a digital water bath with LSB-24 model supplied by Spectra Lab Instruments Pvt. Ltd., Mumbai, Maharashtra, India. To estimate the effect of different factors, aging was performed with different factors and their levels as shown in Table 6.1.

Table 6.1 Different factors and their levels for the design of experiment

Factor	**Levels**		
	1	**2**	**3**
A–temperature (°C)	25	50	75
B–time (Weeks)	1	2	3
C–torque (N-m)	0	2	4
D–material	Neat	Nanoclay	-

6.2.2 Accelerated aging

The accelerated weathering test was performed using a QUV accelerated weathering tester Model QUV/spray with solar eye irradiance control (Q-Lab Corporation, USA) with ASTM D1544 standard as its reference. The specimens were illuminated with UVB lamp emitting ultraviolet (UV) with short wavelengths of 295 nm with an irradiance of 1.0 w/m^2. UV-B radiation carries the shortest wavelength of sunlight found on earth's surface. Therefore, UVB lamps are widely used in quality control, research and development for fast and cost-effective results. The specimens were exposed to a total of 500 hours of cyclical UV exposure, 8 hours of UV radiation at 60°C followed by 4 hours of condensation at 50°C. The environment in the chamber was maintained at 100% relative humidity level at elevated temperatures. The results were compared for 0, 250, and 500 hours of exposure of specimens to the given conditions.

6.3 Joint Testing

The specimens were clamped in the fixture and tightened to the desired torque level using a calibrated torque wrench. Three different levels of torque, *i.e.*, 0, 2, and 4 Nm were used to tighten the bolted joints before testing. The prepared joints were tested under tensile loads on the Zwick-Roell Universal Testing Machine with a capacity of 10 kN at a crosshead speed of 2 mm/min.

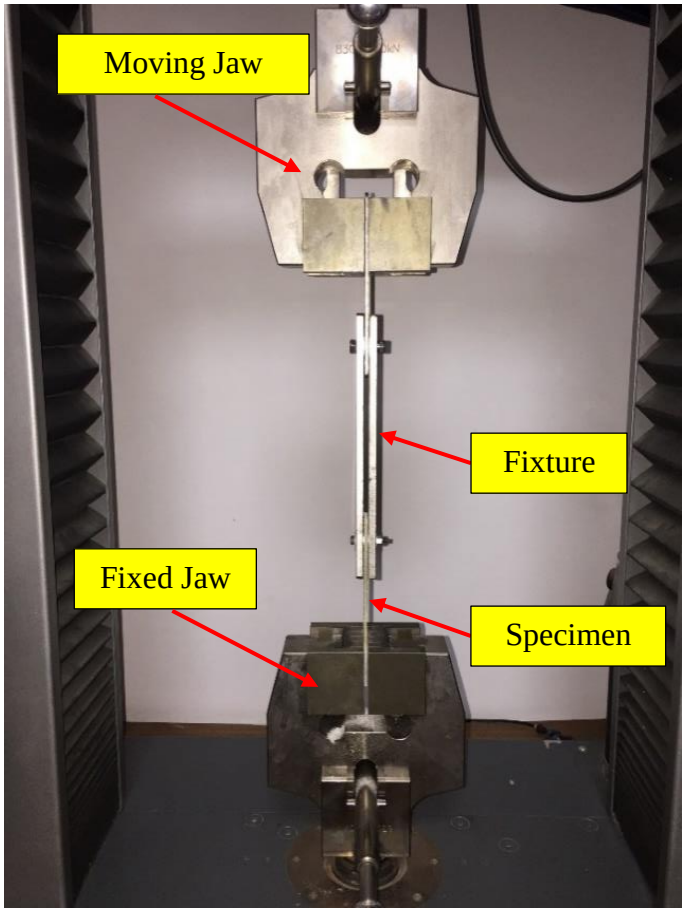

Fig. 6.2 Experimental setup for joint testing

The experimental setup is shown in Fig. 6.2. A gradual increasing and uniformly distributed load was applied on the plate, and a stationary bolt located at the center of the hole resisted the applied load. Symmetrical geometry and boundary conditions avoided the bending forces during tensile testing of the specimens.

6.4 Results and Discussion

The following section discusses the results of the hygrothermal and accelerated aging on the failure loads of the bolted joints.

6.4.1 **Hygrothermal aging**

6.4.1.1 Effect on mechanical properties of the composite

The composite specimen aged for different temperatures and durations have been tested under tensile loads on the universal testing machine.

The trends of the strength reduction can be seen in Fig. 6.3. As shown in the figure, the tensile strength of the composite specimen reduces with increasing water temperature and duration. The moisture absorption is quite different in epoxy and the glass fiber. Consequently, the hygrothermal stresses set up in the fiber and the matrix are different. Due to the water-polymer interaction, swelling occurs in the epoxy which further leads to de-bonding at the fiber-matrix interface. Due to these weak interfacial bonds, the mechanical performance of the composite is diminished. Before testing on the universal testing machine, the specimens were redried after hygrothermal aging. The combined action of water and temperature might have formed new micro-cavities. Upon redrying these micro-cavities act as stress concentrators, which may lead to the initiation of cracks in the matrix and a further decrease in the mechanical performance of the composite [65]. Given a strong correlation between the moisture uptake and the structure-property degradation, the rate of strength retention is significantly affected by the water temperature in the fiber reinforced polymer composites. Since all materials at higher temperatures have more diffusion coefficients than at lower temperature, with an increase in the water temperature, the rate of moisture uptake increases and consequently the strength retention decreases significantly. Comparing Figs. 6.3 (a) and (c), it is observed that the specimen submerged in water at 25°C have a significantly high rate of strength retention than the ones submerged at 75°C. As the time progresses, the percent strength retention in the nanocomposite specimen is more in comparison to the composite made with neat epoxy. Comparing the slopes of the trend between neat and the nanocomposites, variation can be seen in the rate of degradation. Nanocomposite specimen have slightly lower rate of degradation compared to the neat composite. This is due to the tortuosity of nanoclay, which eventually hampers the moisture absorption into the composite due to the zig-zag pattern. The nanoclay improves the interfacial properties of the composite material.

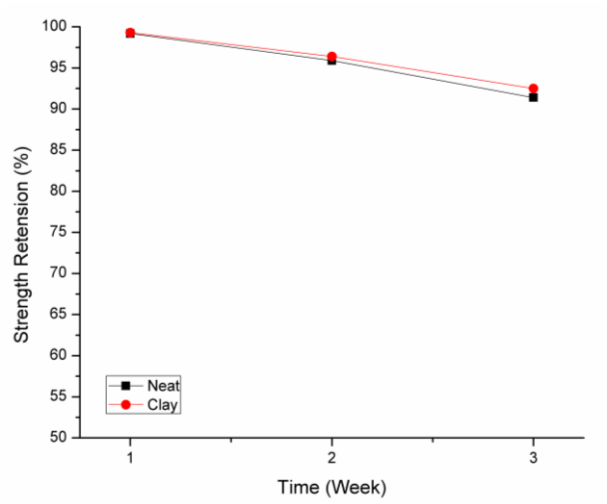

(a)

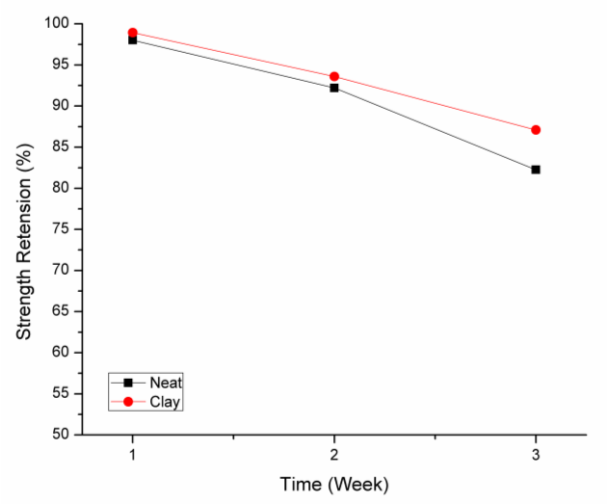

(b)

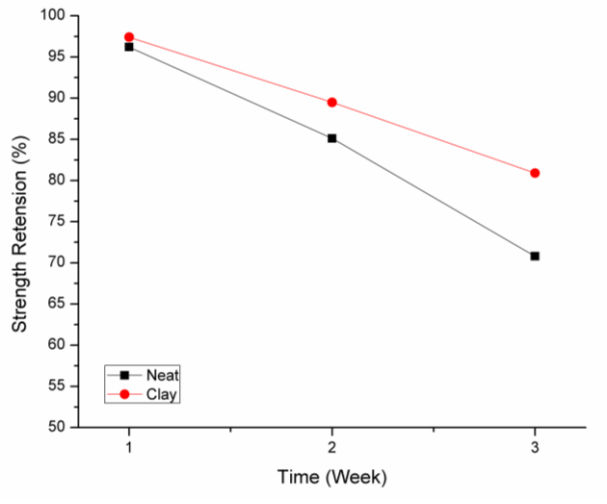

(c)

Fig. 6.3 Tensile strength retention of composite laminates aged under different temperatures (a) 25°C, (b) 50°C, and (c) 75°C

The nanoclay platelets increase the specific surface area and act as a mechanical interlock between the fiber and the epoxy. After 3 weeks, neat specimens aged to different temperatures (25°C, 50°C, and 75°C) have shown a percent strength retention of 91.2%, 82.2%, and 70.7, respectively. However, for the similar conditions, specimens made of nanocomposite showed a percent strength retention of 92.5%, 87.2%, and 80.9%, respectively. The percent tensile strength retention after hygrothermal aging for individual trials has been summarized in Table 6.2.

Table 6.2 Aging effect on different mechanical properties of the composite laminate

Sr. No.	Temperature (°C)	Time (week)	Tensile strength		Tensile strength retention	
			MPa		%	
			Neat	Nanoclay	Neat	Nanoclay
1	Unaged		410	491	100.0	100.0
2	25	1	407	488	99.3	99.4
3	25	2	393	473	95.9	96.3
4	25	3	375	454	91.5	92.5
5	50	1	402	485	98.0	98.8
6	50	2	378	460	92.2	93.7
7	50	3	337	428	82.2	87.2
8	75	1	394	478	96.1	97.4
9	75	2	349	439	85.1	89.4
10	75	3	290	397	70.7	80.9

6.4.1.2 Effect on joint performance

The full factorial design of experiment was used for the performance analysis of the joints. The load versus displacement plots of individual joint configurations exposed to the hygrothermal aging environment are shown in Figs. 6.4 and 6.5 for neat composite and composite with nanoclay content, respectively. For all of the load displacement curves, the load begins to increase with a linear slope. However, after reaching near to its maximum load carrying capacity, the curve moves forward in the horizontal direction with a zig-zag pattern which represents the bearing failure mode. Carefully observing the effect of torque in all the plots, it was found that joint stiffness increases with an increase in the bolt torque. The peak load is higher, and the corresponding displacement is less for joints tightened to higher torque as compared to the joints with the lower torque values.

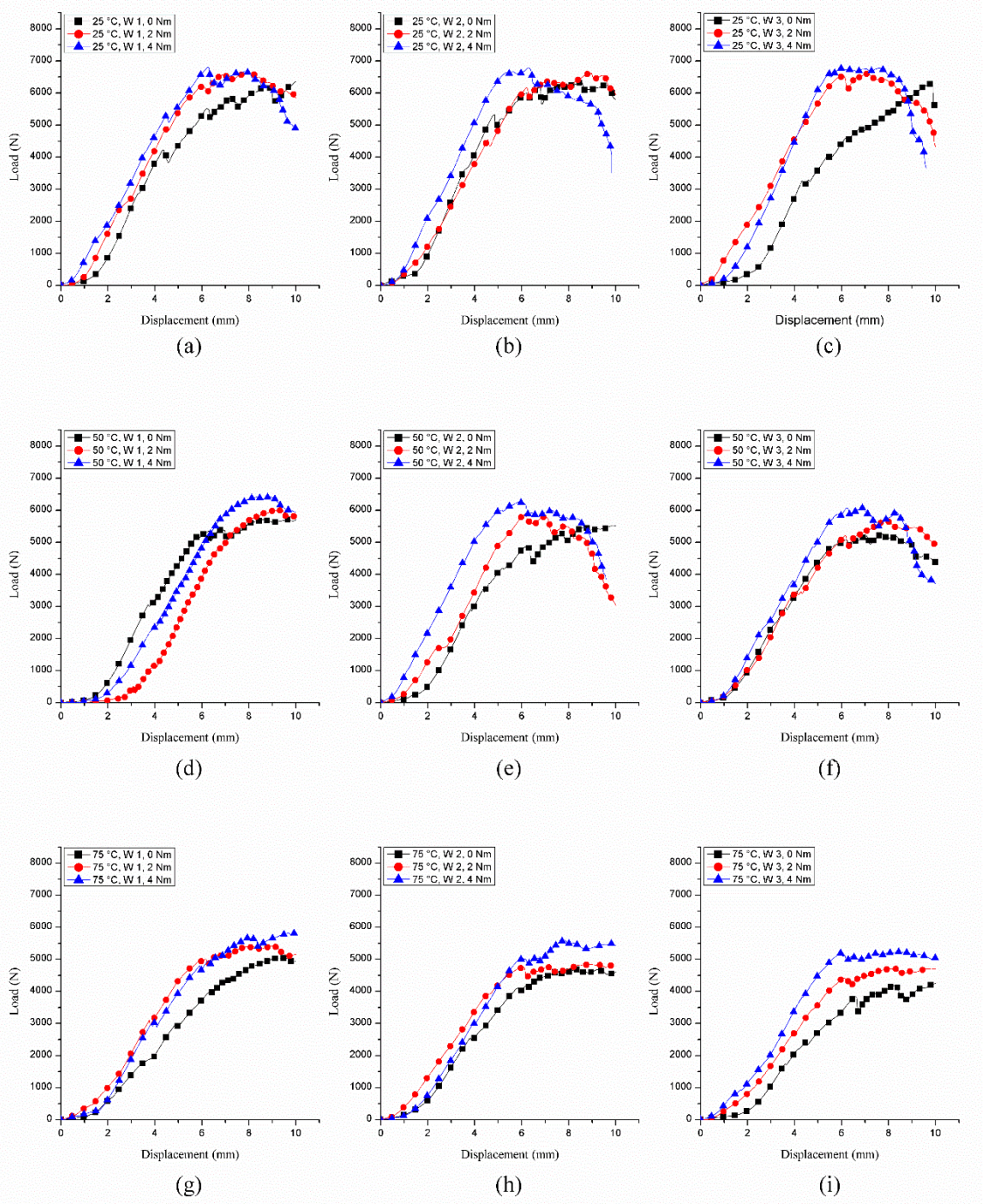

Fig. 6.4 Load vs. displacement graphs for neat composite joints aged at different temperatures (25ºC, 50ºC, 75ºC) and different durations (weeks *i.e.*, W1, W2, W3)

The higher the torque, the higher are the lateral compressive forces on the specimen, which eventually increase the joint stiffness and reduce the joint displacement in the initial phase and hence increase the ultimate failure load of the joint.

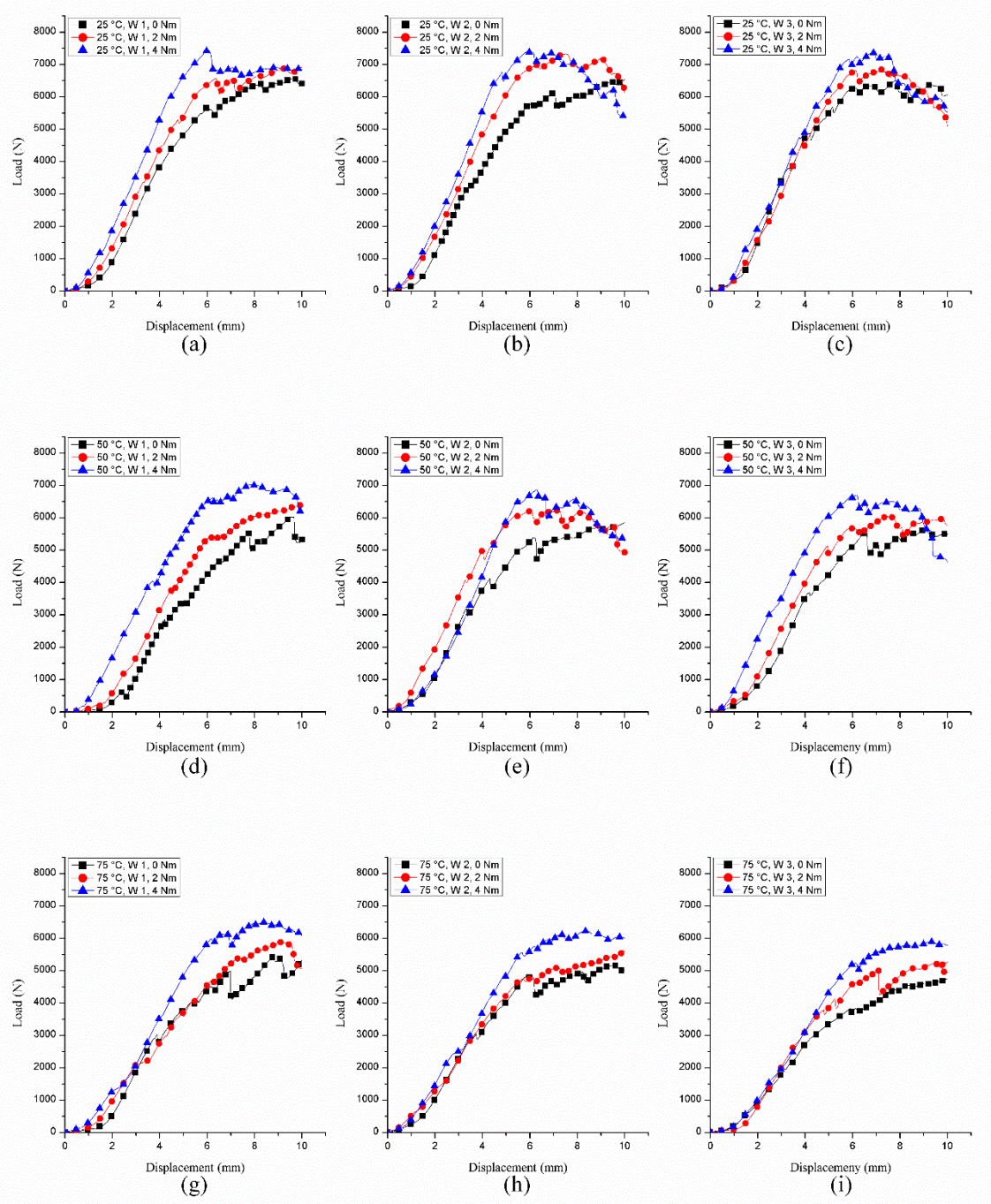

Fig. 6.5 Load vs. displacement graphs for nanocomposite joints aged at different temperatures (25^{o}C, 50^{o}C, 75^{o}C) and different durations (weeks *i.e.*, W1, W2, W3)

It is seen from the figures that the ultimate failure loads decreases with an increase in the water temperature and the duration of exposure to the hygrothermal aging environment. It is due to the fact that the material degrades with the exposure to the environmental conditions. The water-polymer interaction causes epoxy swelling and results in weak fiber-matrix interfacial bonds [139]. As can be seen from the slopes of the figures that

there is a difference between the joint stiffness as the torque value increases from 0 to 2 Nm and from 2 Nm to 4 Nm. All the bolted joint configurations have demonstrated the bearing failure mode for neat as well as nanocomposite joints. The values of the ultimate failure loads for the full factorial design are shown in Table 6.3.

Table 6.3 Ultimate failure loads for the joints aged at different levels of temperature and time and tested using different torque levels

Sr. No.	Factor			Material			
				Neat		with Nanoclay	
	Temperature (°C)	Time (Weeks)	Torque (Nm)	Failure load (N)	% reduction	Failure load (N)	% reduction
1	Unaged		0	6460	-	6590	-
2	Unaged		2	6640	-	6930	-
3	Unaged		4	6840	-	7450	-
4	25	1	0	6358	1.6	6578	0.2
5	25	2	0	6327	2.1	6527	1.0
6	25	3	0	6310	2.3	6502	1.3
7	25	1	2	6623	0.3	6923	0.1
8	25	2	2	6611	0.4	6880	0.7
9	25	3	2	6602	0.6	6851	1.1
10	25	1	4	6805	0.5	7435	0.2
11	25	2	4	6785	0.8	7385	0.9
12	25	3	4	6774	1.0	7364	1.2
13	50	1	0	5712	11.6	6026	8.6
14	50	2	0	5510	14.7	5849	11.2
15	50	3	0	5255	18.7	5637	14.5
16	50	1	2	6009	9.5	6399	7.7
17	50	2	2	5865	11.7	6230	10.1
18	50	3	2	5649	14.9	6052	12.7
19	50	1	4	6416	6.2	7030	5.6
20	50	2	4	6269	8.3	6866	7.8
21	50	3	4	6075	11.2	6703	10.0
22	75	1	0	5042	22.0	5470	17.0
23	75	2	0	4680	27.6	5164	21.6
24	75	3	0	4253	34.2	4753	27.9
25	75	1	2	5416	18.4	5887	15.1
26	75	2	2	5112	23.0	5595	19.3
27	75	3	2	4705	29.1	5222	24.6
28	75	1	4	5849	14.5	6493	12.8
29	75	2	4	5589	18.3	6225	16.4
30	75	3	4	5235	23.5	5895	20.9

The ultimate failure loads for the unaged joints prepared with neat epoxy and epoxy with nanoclay content are shown in Figs. 6.6.

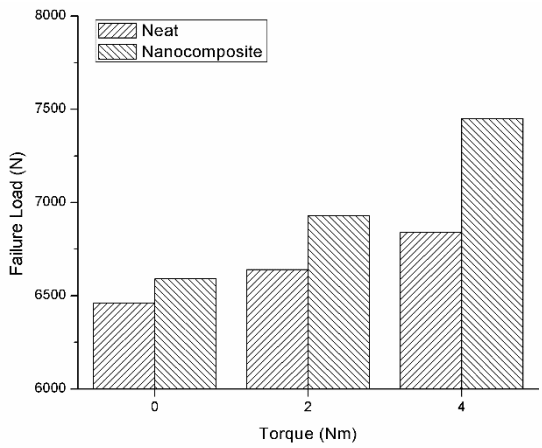

Fig. 6.6 Ultimate failure load of unaged joints

It can be seen from Fig. 6.6 that the failure load increases with the increase in torque. It is due to the fact that the torque applied to the joint strengthens it by distributing the force on the joints through the washer. It can also be seen that the failure load is higher in specimens prepared with the addition of nanoclay content as compared to specimens with neat epoxy. It is due to the fact that the addition of nanoclay content increases the failure load of the material by acting as mechanical interlock which in turn helps to increase the failure load along with the torque.

Figure 6.7 shows the ultimate failure loads for the aged joints prepared with neat epoxy and epoxy with nanoclay content. It is seen from the figure that the ultimate failure load of the bolt joint decreases with duration of exposure. Temperature has shown a significant effect on the failure loads of the joints. Comparing the failure load of the corresponding joint configurations, with the increase in the temperature, the failure load of the joints decrease significantly. As shown in Figs. 6.7 (a) and (d), at 25°C, there is no significant degradation even after 3 weeks. Figures 6.7 (b) and (e) show that the joints aged at 50°C have higher rate of degradation. The highest rate of degradation is observed in the specimens with the exposure to 75°C. Comparing the neat and the nanocomposite joints as shown in Figs. 6.7 (a), (b), (c) and (d), (e), (f), respectively, nanoclay has demonstrated a significant contribution to the improvement in the failure load of the joint. For all the temperature levels, failure loads for the bolted joints are always higher in the joints prepared with the addition of nanoclay as compared to the neat composite. Comparing the nanoclay over neat joint configurations, even after the aging of 3 weeks, the effect of torque is relatively large in joints prepared from nanocomposite material.

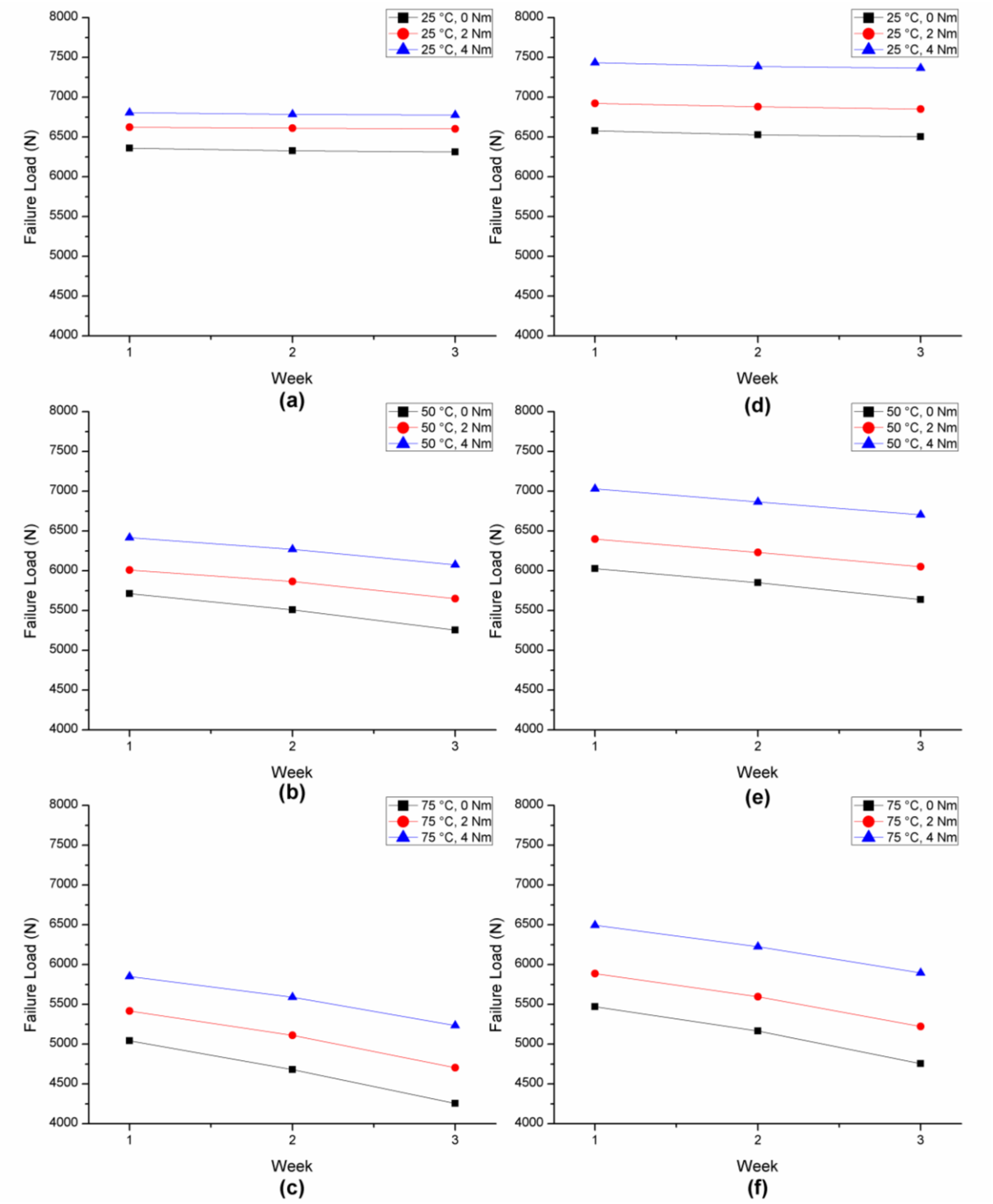

Fig. 6.7 Ultimate failure loads for aged joints made of neat epoxy aged at (a) 25ºC, (b) 50ºC, (c) 75ºC, and epoxy with nanoclay aged at (d) 25ºC, (e) 50ºC, (f) 75ºC

The ultimate failure load of the joints made of nanocomposite material is increased significantly with an increase in the applied torque. This has happened due to the ability

of the nanoclay to maintain the structural integrity of the nanocomposite material under hygrothermal aging conditions. The nanoclay resists the effect of moisture and helps to reduce the fiber-matrix de-bonding of the material.

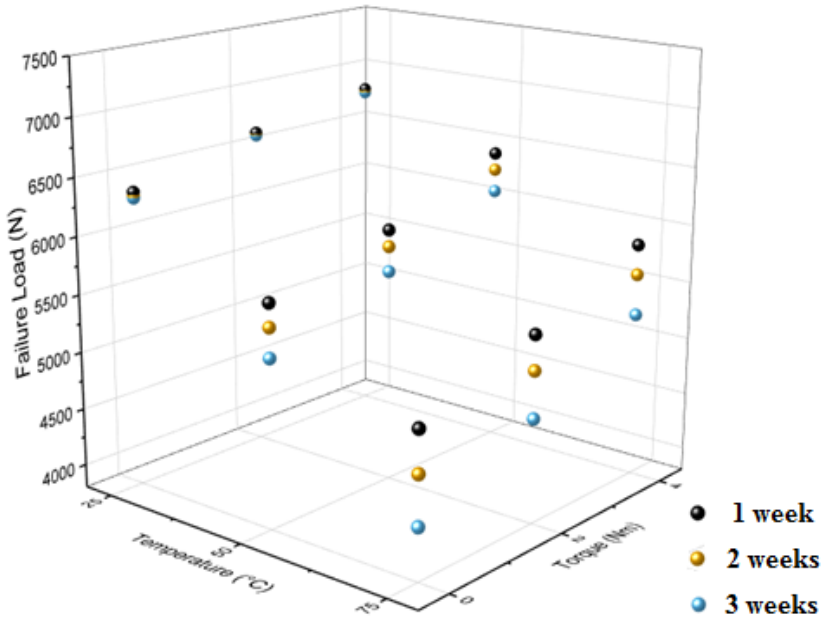

(a)

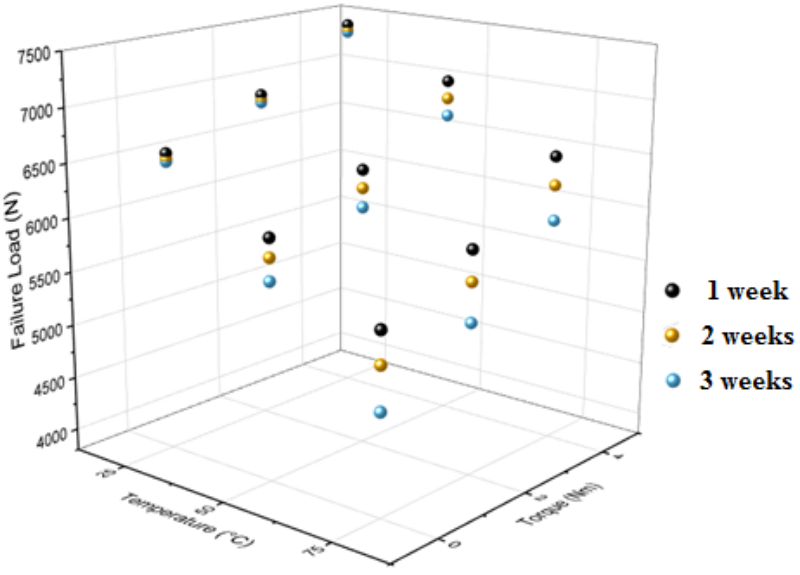

(b)

Fig. 6.8 Ultimate failure loads for aged joints made of (a) neat, and (b) nanocomposite specimens

As shown in Table 6.3, percent decrease in failure loads of the neat composite bolted joints is maximum of 2.3%, 18.7%, and 34.2% at 25°C, 50°C, and 75°C, respectively.

Whereas, for the similar conditions in joints with nanocomposite material, it is 1.3%, 14.5%, and 27.9%.

The overall comparison of the ultimate failure loads between neat and nanocomposite bolted joints is shown in Fig. 6.8, which details about the variation of the failure load with respect to temperature, and the torque. It can be seen from the figure that the ultimate failure loads of all joint configurations are higher for joints prepared from nanocomposite as compared to the neat epoxy. No significant reduction in the failure load is observed in joints aged at 25°C. However, increasing the temperature to 50°C and then 75°C has demonstrated a significant reduction in failure loads of joints for both neat as well as nanocomposite materials. Comparing gaps between spheres representing different levels of duration, the effect of duration is found to be minimum in specimens aged at 25°C, whereas it is maximum in specimens aged at 75°C. The moisture uptake is directly related to the water temperature. At lower temperature, *i.e.*, 25°C, the moisture absorption is very slow. By increasing water temperature, the moisture absorption rate increases and consequently the water-polymer interaction is promoted resulting in degradation of the mechanical properties of the composite materials and reduction in joint performance, thereof.

The actual images of unaged and aged specimens to 75°C for 3 weeks, failed in the tensile test, are shown in Fig. 6.9. All the specimens show the bearing failure mode. As the torque increases, the incident pressure exerted by washer onto the composite specimen increases, which eventually helps to distribute the stresses over a comparatively wider area. Therefore, joints with high torque settings possess high joint stiffness and larger failure loads. From the Fig. 6.9, it is seen that as the torque applied to the joint increases, the visible area under damage increases. In hand tightened condition, *i.e.*, 0 Nm torque, area under damage is narrow in width, and the stresses transferred to the specimen are localized compared to the specimens with high torque settings. Besides this, for the said torque level, the delamination near the hole surface also confirms the low incident pressure exerted by washer on the composite specimen.

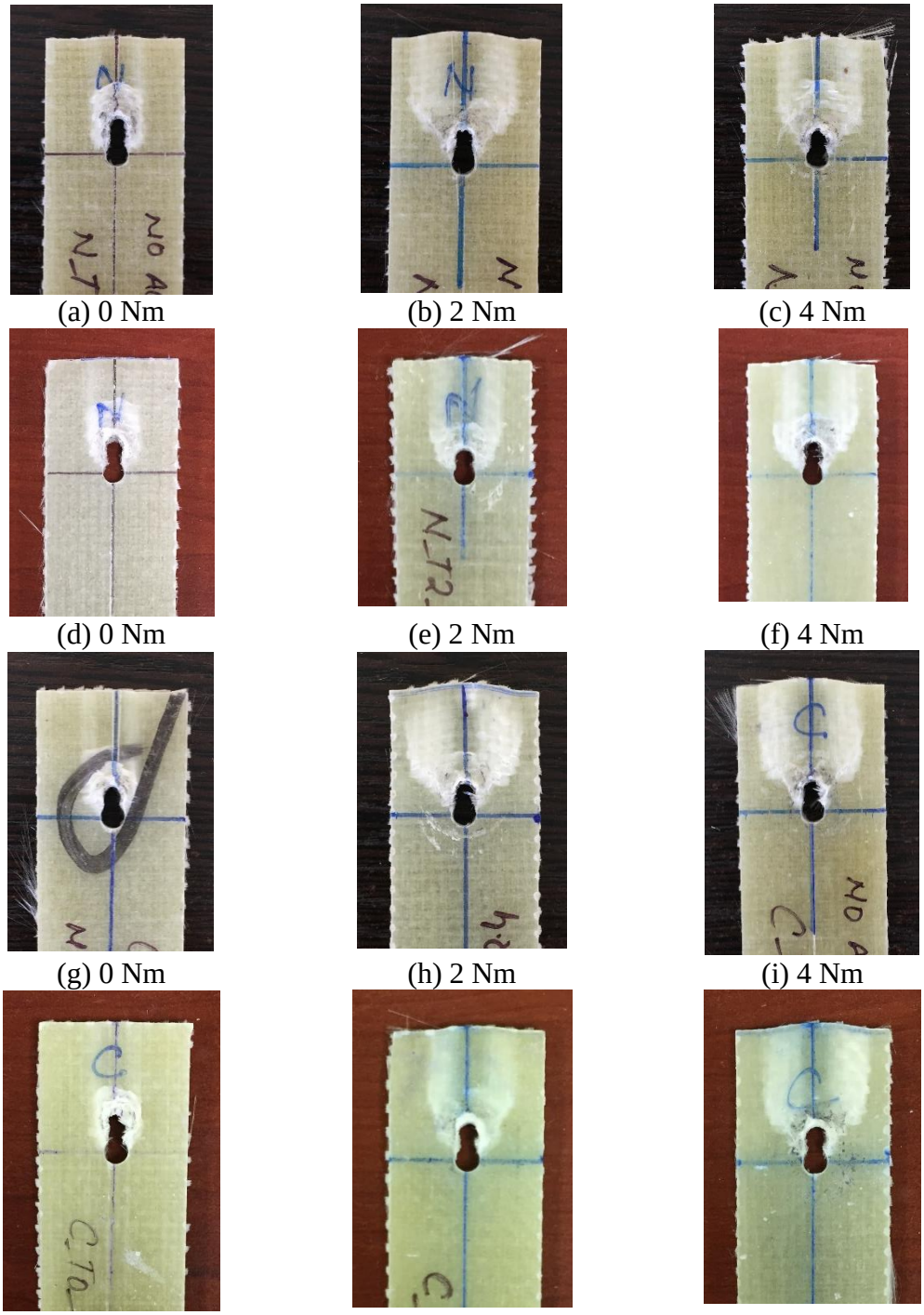

(a) 0 Nm (b) 2 Nm (c) 4 Nm

(d) 0 Nm (e) 2 Nm (f) 4 Nm

(g) 0 Nm (h) 2 Nm (i) 4 Nm

(j) 0 Nm (k) 2 Nm (l) 4 Nm

Fig. 6.9 Actual images of the selected failed joint specimens
(a) Neat unaged with 0 Nm, (b) Neat unaged with 2 Nm, (c) Neat unaged with 4 Nm, (d) Neat aged at 75°C for 3 weeks with 0 Nm, (e) Neat aged at 75°C for 3 weeks with 2 Nm, (f) Neat aged at 75°C for 3 weeks with 4 Nm, (g) Nanocomposite unaged with 0 Nm, (h) Nanocomposite unaged with 2 Nm, (i) Nanocomposite unaged with 4 Nm, (j) Nanocomposite aged at 75°C for 3 weeks with 0 Nm, (k) Nanocomposite aged at 75°C for 3 weeks with 2 Nm, (l) Nanocomposite aged at 75°C for 3 weeks with 4 Nm

6.4.1.3 Scanning electron microscopy (SEM)

The hygrothermal exposure induces significant microstructural changes in the glass fiber reinforced laminates.

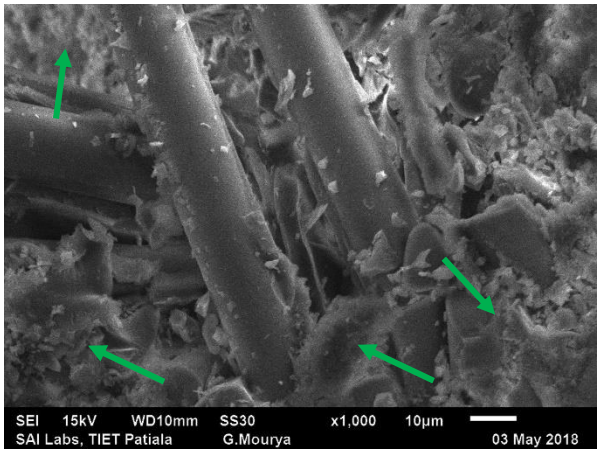

(a)

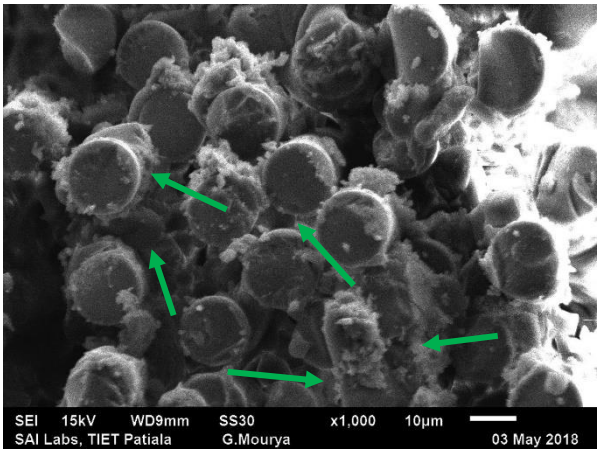

(b)

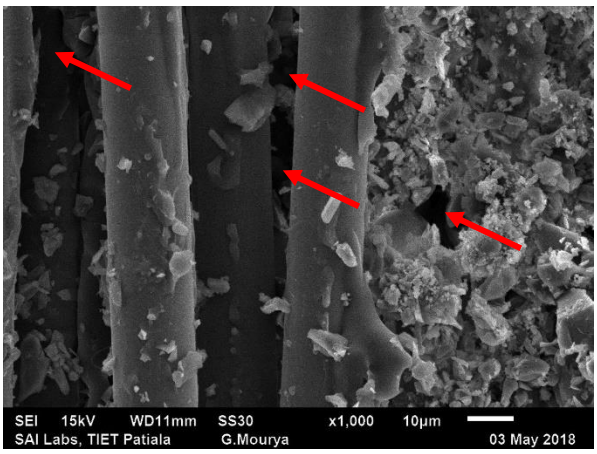

(c)

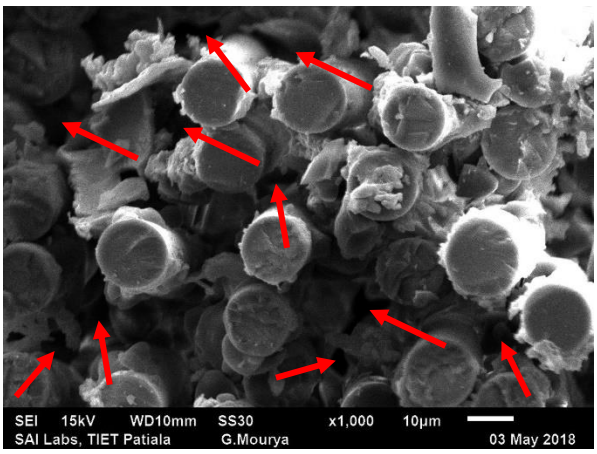

(d)

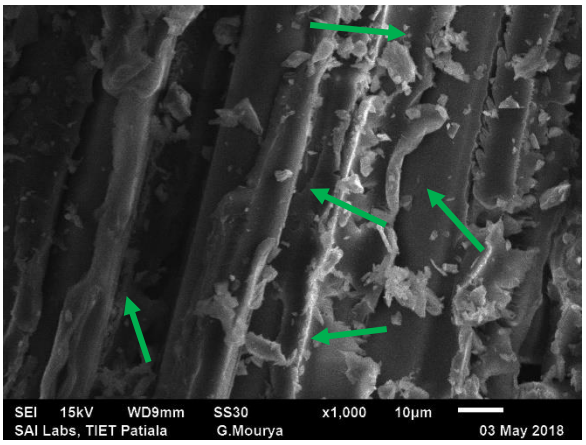

(e)

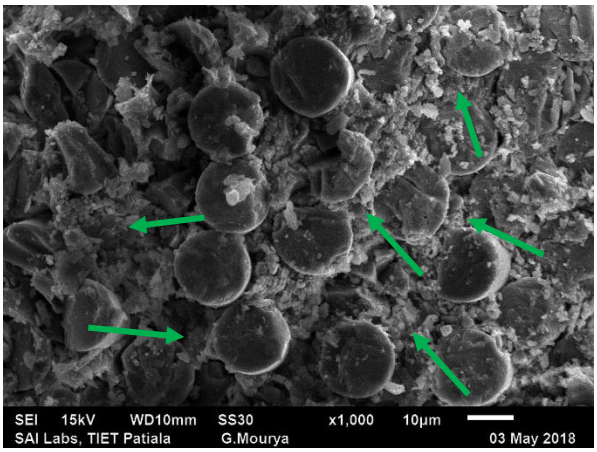

(f)

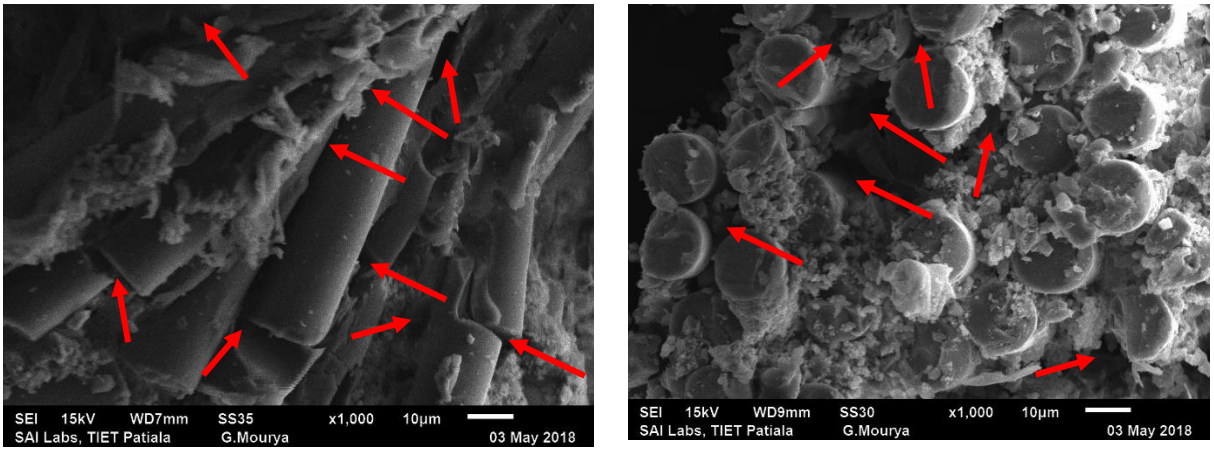

(g) (h)

Fig. 6.10 SEM images of fractured specimens made of neat composite (a), (b) unaged, (c), (d) aged at 75°C for 3 weeks and nanocomposite (e), (f) unaged, (g), (h) aged at 75°C for 3 weeks

To investigate the microstructural changes in the composite material subjected to aging, SEM images, shown in Fig. 6.10, were taken for the unaged and aged specimens. Figs. 6.10 (a), (b) and (e), (f) show that the fibers are intact with the matrix for unaged specimens made of neat and nanocomposite material, respectively. A good adhesion of epoxy on the fiber surface is observed, and fibers are closely placed even after fracture of the specimen. The neat specimen aged at 75°C for 3 weeks, as shown in Fig. 6.10 (c) and (d), have an epoxy loss and fiber-matrix de-bonding in some portions. For the corresponding condition in the specimen with nanoclay content as shown in Fig. 6.10 (g) and (h), there is lesser loss and degradation of the epoxy. Nanoclay acts as a barrier to moisture and consequently helps to resist the degradation of the nanocomposite under combined attack of moisture and temperature [14]. Moreover, nanoclay also enhances the fiber matrix interfacial properties which further helps to counter-attack the effect of environmental conditions [19].

6.4.1.4 Statistical analysis

Regression analysis has been performed to determine the influence of different parameters, *i.e.*, water temperature, exposure time, bolt torque, and material variation on the failure load of the composite joint. Regression investigates and models the relationship between a response (failure load (F_L)), and the predictors (temperature (A), time (B), torque (C) and material (D)) in the present study. In particular, regression

analysis is often used to determine the change in the response variable with respect to parameters. The analysis of variance given in Table 6.4 shows the amount of variation in the response data explained by the predictors and the amount of variation which is left unexplained.

As shown in Table 6.4 (p-value < α at 95% confidence interval), there is a valuable impact of the temperature, time, torque and the material on the failure load of the joint. The p-value for regression is 0.000, indicating that at least one of the regression coefficients is significantly different than zero. From the p-value and percentage contribution of the predictors, *i.e.*, the temperature (*A*), time (*B*), torque (*C*) and material (*D*) shown in ANOVA table, it is clearly visible that the response, *i.e.*, failure load (F_L), is largely influenced by all predictors, *i.e.*, *A*, *B*, *C*, and *D*. However, comparing the percentage contribution of each predictor, temperature is having the highest contribution of 60.2%.

Table 6.4 Analysis of variance

Source	DF	Adj SS	Adj MS	F-value	P-value	% Cont.
Regression	4	27825220	6956305	297.87	0.000	96.0
A	1	17437584	17437584	746.68	0.000	60.2
B	1	1222499	1222499	52.35	0.000	4.2
C	1	6451600	6451600	276.26	0.000	22.3
D	1	2713537	2713537	116.19		9.4
Error	49	1144327	23354			4.0
Total	53	28969547				

The predictive failure load values were determined using the regression equations (6.1) and (6.2) for neat and nanocomposite, respectively.

$$F_L = 7182.9 - 27.86\,A - 184.4\,B + 211.9\,C \quad (6.1)$$

$$F_L = 7631.3 - 27.84\,A - 184.3\,B + 211.7\,C \quad (6.2)$$

where, F_L is the failure load (N), A is the temperature (°C), B is the time (weeks), and C is the torque (Nm). The residual plot for the failure load is shown in Fig. 6.11. The percentage error in the experimental and predicted value through the regression equation is less than 2.3%.

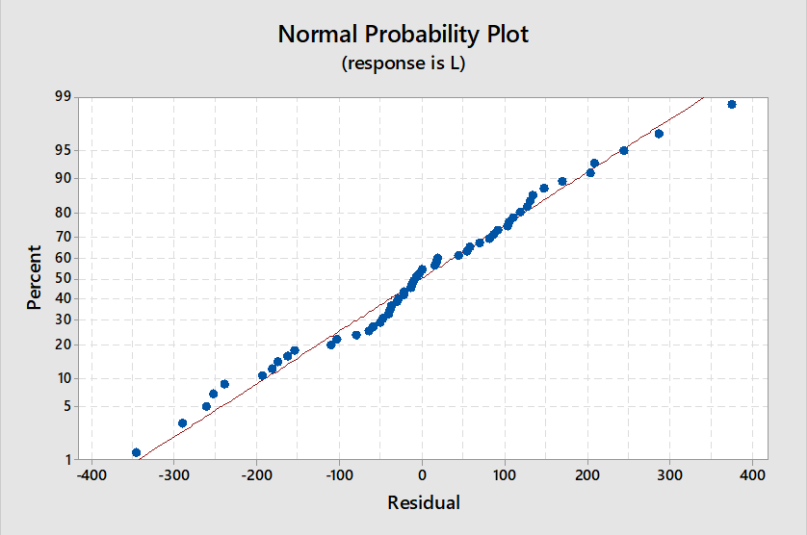

Fig. 6.11 Residual plots for the failure load ($\boldsymbol{F_L}$)

6.4.2 **Accelerated aging**

The second portion of the study was related to the accelerated aging of the composite laminates and the bolted joints. The accelerated aging was done with cyclical exposure to UV radiation and condensation to investigate the structure-property degradation in the composite material and its joints.

6.4.2.1 Fourier-transform infrared (FTIR) spectroscopy

Accelerated weathering test induces various chemical changes in epoxy networks through UV radiation, heat, and moisture [19]. To determine possible chemical changes into the composite material subjected to different aging conditions, FTIR spectroscopy of specimens was performed using PerkinElmer make, Spectrum 2 model, FT-IR spectrometer to compare the aged and unaged material. The range of spectra was 400 to 4000 cm^{-1} with a resolution of 2 cm^{-1}. Specimens were conditioned in a desiccator before analysis. Six specimens, one from each configuration, *i.e.*, neat epoxy with 0, 250 and 500 hours of exposure and epoxy with 3 wt.% of nanoclay content with 0, 250, 500 hours of exposure were tested in the FTIR.

The FTIR spectra of unaged and aged specimens are shown in Fig. 6.12. Peaks at 2920, and 2850 cm^{-1} relates to C-H stretching of the monomer units [126], and the peak at 2644 cm^{-1} is most likely related to hydroxyl groups. The peak at 1730 cm^{-1} represents the C=O stretching of esters. C-O-C symmetric and asymmetric stretch of ethers is shown by peaks at 1030 cm^{-1}. The peak at 828 cm^{-1} represents the possible C-H bending of aromatic

compounds. Due to accelerated aging, chemical changes are suggested by the results. Possible changes can be seen due to the peaks at 1120, 1170, 1606 and 3457 cm^{-1}. Besides this, the major difference between the spectra corresponding to the aged and unaged specimen is the intensity of bands. The peak at 1120 cm^{-1} represents the C-O-C stretch of ethers. C-F stretching of alkyl halides is shown by peaks at 1170 cm^{-1}. The peak at 1606 cm^{-1} represents the N-H bending of amides. The broad peak at 3457 cm^{-1} shows the O-H stretching of the carboxylic acids.

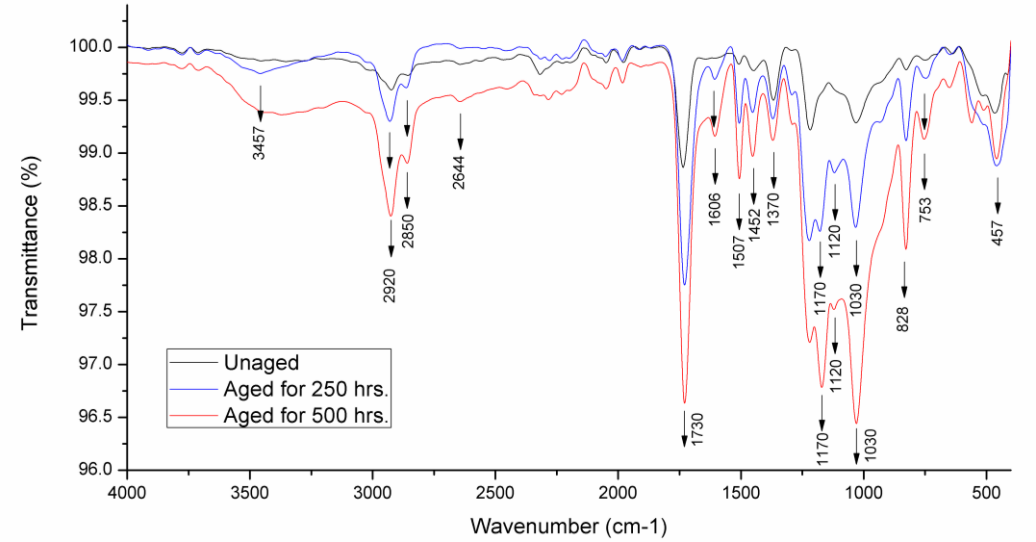

Fig. 6.12 FTIR spectra for unaged and aged composite specimens

6.4.2.2 Effect on mechanical properties of the composite

For characterization of the composite material, the tensile, compression and shear tests were performed using ASTM D3039, ASTM D695, and ASTM D5379, respectively. The tests were performed on specimens with neat epoxy and epoxy with 3 wt.% of nanoclay content on both the unaged and aged conditions.

Table 6.5 Aging effect on different mechanical properties of the composite laminate

Aging time (Hours)	**Tensile Strength (MPa)**		**Compressive strength (MPa)**		**Shear Strength (MPa)**	
	Neat	**Nanoclay**	**Neat**	**Nanoclay**	**Neat**	**Nanoclay**
Unaged	410	491	270	327	104	114.4
250	342.8	441.8	243	297.5	93.2	107.3
500	292.3	390.4	209.7	278.9	84.2	102.8

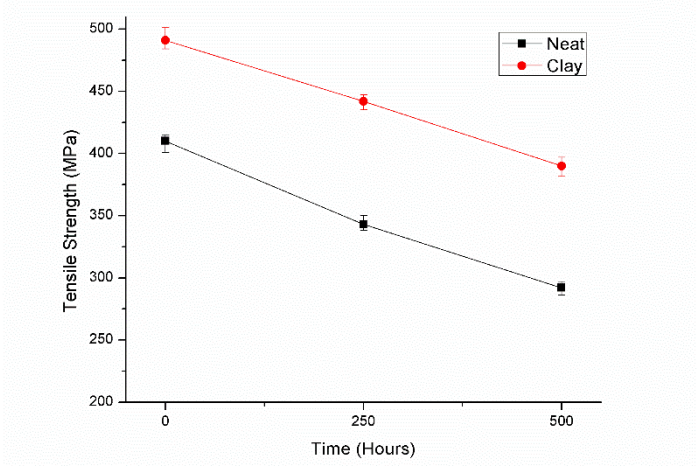

(a)

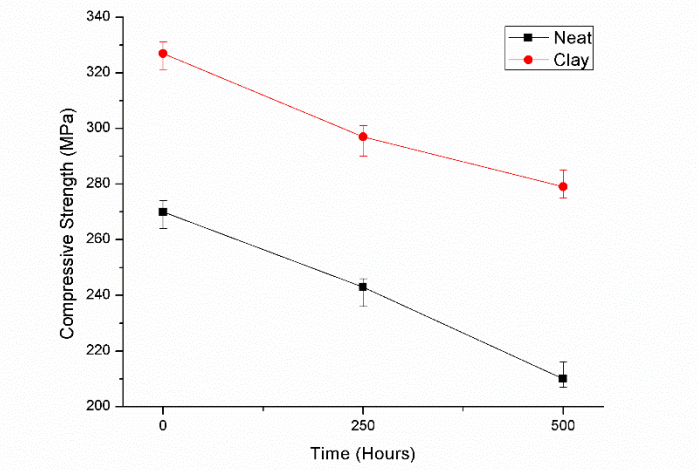

(b)

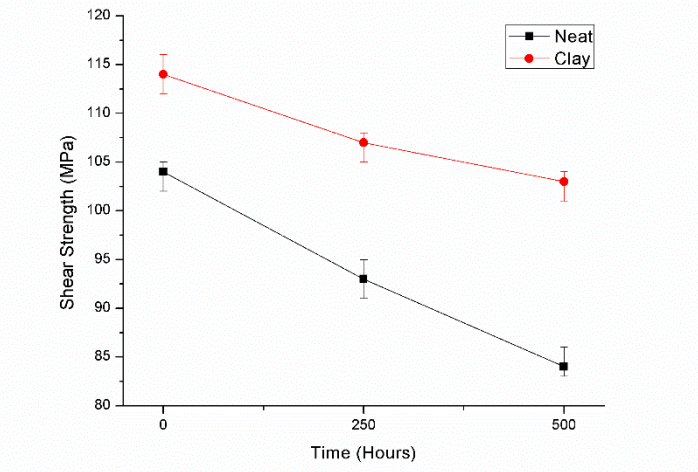

(c)

Fig. 6.13 Mechanical properties of the unaged and aged composites (a) Tensile strength, (b) Compressive strength, (c) Shear strength

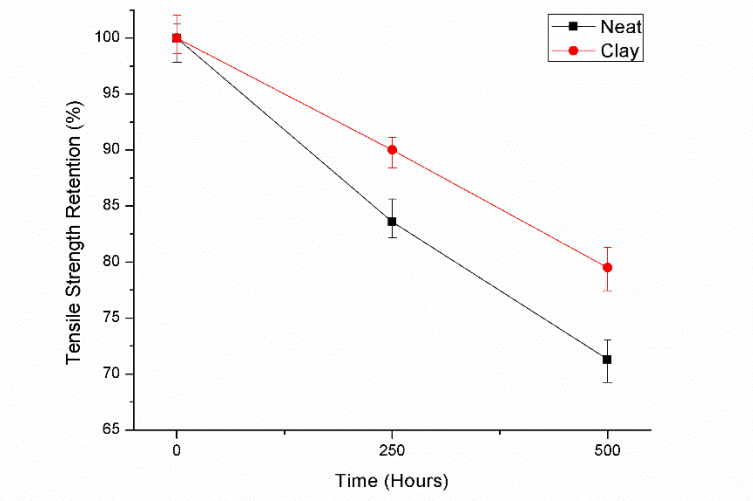

(a)

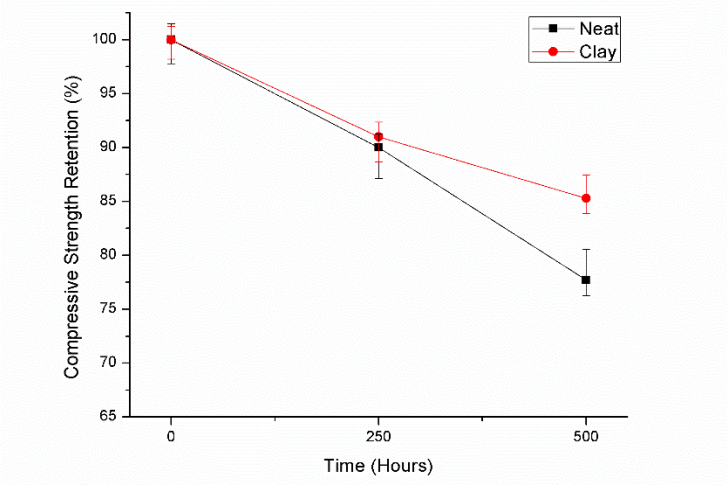

(b)

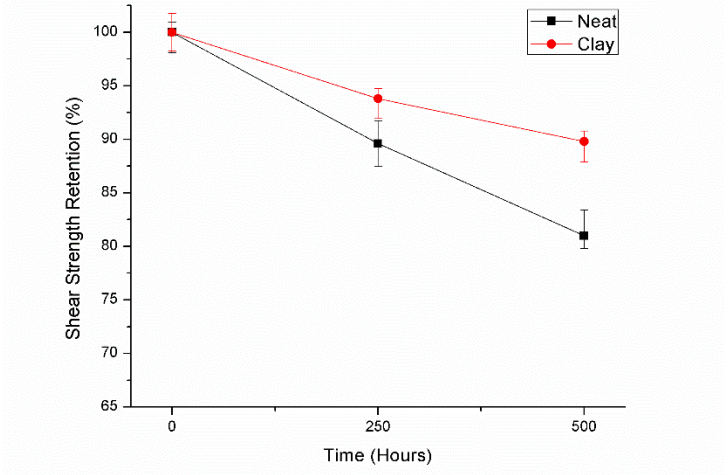

(c)

Fig. 6.14 Strength retention in the unaged and aged composites
(a) Tensile strength, (b) Compressive strength, (c) Shear strength

The tensile, compressive, and shear strengths of the unaged and aged composite material are shown in Fig. 6.13 (a), (b), and (c), respectively. A significant reduction in all the mechanical properties is observed due to the aging of the material. As the duration of aging increases, the mechanical properties decrease. It is observed that the degradation is not uniform between the first span of 0–250 hours and the second span of 250–500 hours. It is due to the reason that higher moisture absorption and UV attack takes place in the initial stage of accelerated aging. According to Fick's law of diffusion [140], the moisture absorption in the initial stage is more and has a linear slope.

Moreover, the UV rays in the initial stage attack epoxy on the outer surface of the composite specimen. As the time progresses, the glass fabric layer below the top layer of the epoxy restricts the UV attack on the inner layers. The mechanical properties of the unaged and aged composite specimens are also listed in Table 6.5.

The percent strength retention in the composite specimens at different time intervals is shown in Fig. 6.14. As the time progresses, the percent strength retention in the nanocomposite specimen is more in comparison to the composite made with neat epoxy. It is due to the tortuosity of nanoclay which eventually hampers the moisture absorption into the composite due to the zig-zag pattern.The nanoclay improves the interfacial properties of the composite material. The nanoclay platelets increase the specific surface area and act as a mechanical interlock between the fiber and the epoxy [141]. A strength retention of 79.5%, 85.3%, and 89.8% is observed in tensile, compressive, and shear strengths, respectively, after the aging of 500 hours in laminate with nanoclay content whereas it is 71.3%, 77.7%, and 81% strength retention in laminate with neat epoxy.

6.4.2.3 Effect on joint performance

To determine the effect of accelerated aging on the performance of the bolted joints, the joints were prepared from neat epoxy laminates and laminates with 3 wt.% of nanoclay contents. The prepared joints were subjected to accelerated aging for 250 and 500 hours.

Table 6.6 shows the different controlling factors and their levels for investigating the performance of the bolted joint under accelerated aging. The full factorial design of experiments was used for the performance analysis of the joints. To determine the effect of each possible combination of the controlling factors, response surface methodology

(RSM) has been implemented. Table 6.7 shows the design for the experiment on the bolted joints.

Table 6.6 Factors and levels considered for the performance analysis of the joint

Factor	**Levels**		
	1	**2**	**3**
A–Aging Time (Hours)	0	250	500
B–Torque (Nm)	0	2	4
C–Material	Neat	Nanoclay	-

Table 6.7 Design of experiment

Run order	**Std. order**	**Factor**		
		Material	**Time (Hours)**	**Torque (Nm)**
1	14	Nanoclay	0	0
2	24	Nanoclay	250	2
3	25	Nanoclay	250	2
4	13	Neat	250	2
5	2	Neat	500	0
6	20	Nanoclay	250	0
7	1	Neat	0	0
8	11	Neat	250	2
9	12	Neat	250	2
10	9	Neat	250	2
11	10	Neat	250	2
12	15	Nanoclay	500	0
13	6	Neat	500	2
14	4	Neat	500	4
15	3	Neat	0	4
16	19	Nanoclay	500	2
17	21	Nanoclay	250	4
18	8	Neat	250	4
19	22	Nanoclay	250	2
20	18	Nanoclay	0	2
21	23	Nanoclay	250	2
22	5	Neat	0	2
23	17	Nanoclay	500	4
24	7	Neat	250	0
25	16	Nanoclay	0	4
26	26	Nanoclay	250	2

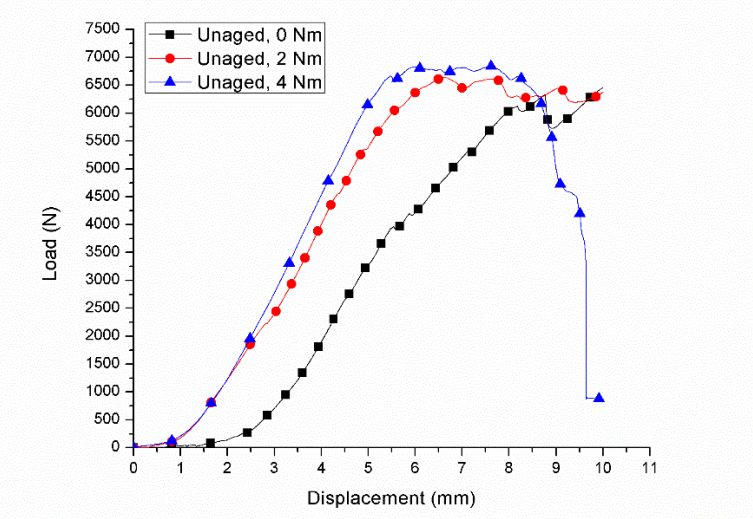

(a)

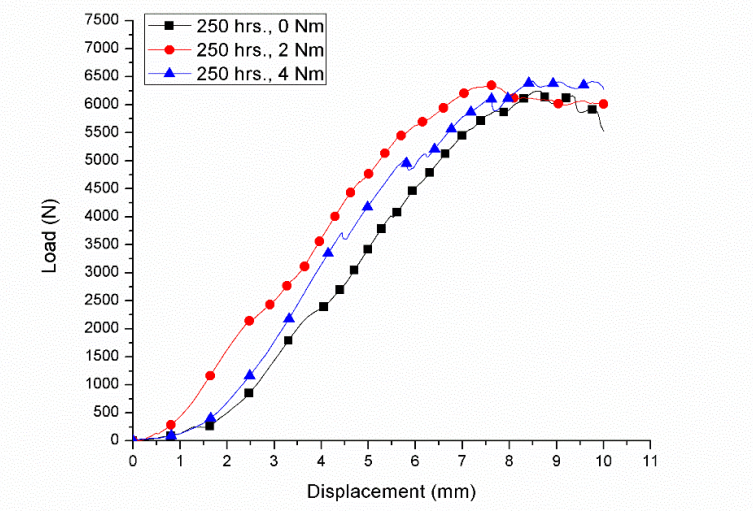

(b)

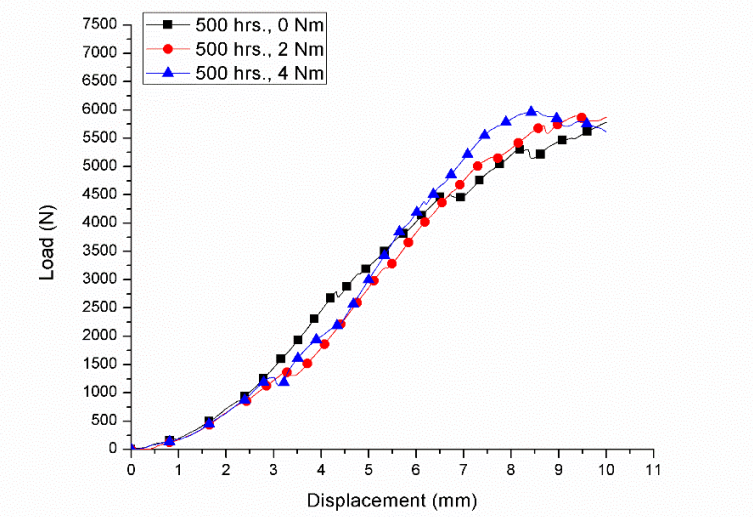

(c)

Fig. 6.15 Load vs. displacement plots for unaged and aged joints made with neat epoxy

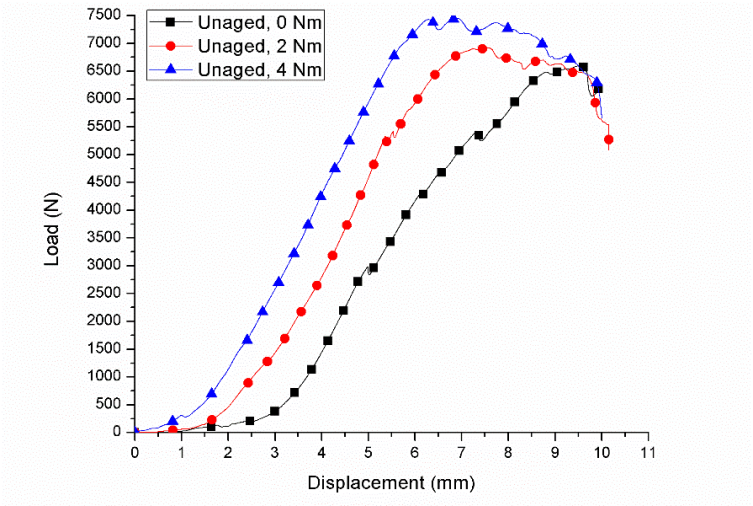

(a)

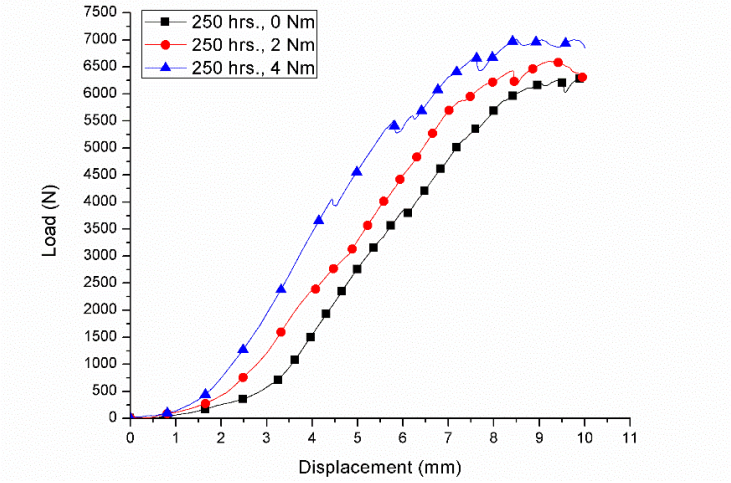

(b)

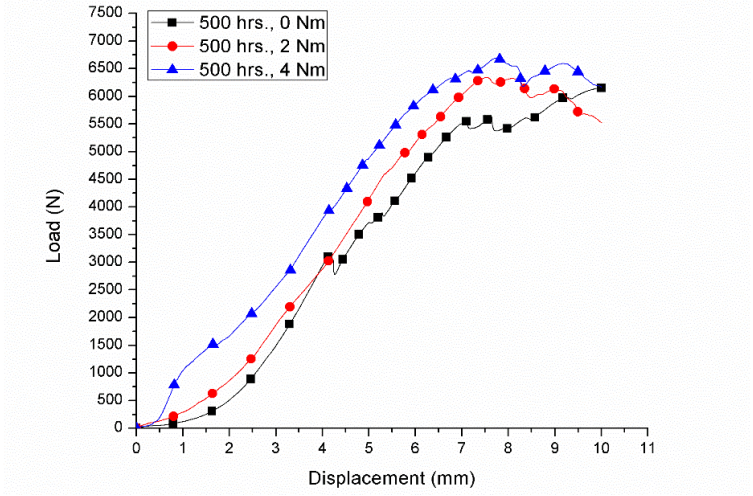

(c)

Fig. 6.16 Load vs. displacement plots for unaged and aged joints made with epoxy modified with nanoclay

The load versus displacement plots for bolted joints made of neat epoxy and epoxy with nanoclay content are shown in Figs. 6.15 and 6.16, respectively. It is observed from the figures that the ultimate failure loads decrease with increase in the duration of exposure to the accelerated aging environment. It is because the material degrades with the exposure to the environmental conditions. It is observed from Fig. 6.15 (a) that the failure load increases with the increase in torque value from 0 to 4 Nm. The effect of bolt torque is more in unaged joints compared to the aged joints as can be seen from Fig. 6.15 (b) and (c). As the duration of aging increases, the contribution of the bolt torque is reduced. Comparing the slope of all the curves among the Figs. 6.15 and 6.16, a loss in the stiffness of the joints is also observed with the duration of exposure. However, comparing Fig. 6.15 (c) and Fig. 6.16 (c), the stiffness retention looks better in case of nanocomposite compared to the neat composite materials. Comparing Figs. 6.15 and 6.16, the overall ultimate failure loads are higher for the joints made of nanocomposite than the neat composite. The nanoclay added in the epoxy resists the moisture and have lesser fiber-matrix de-bonding as compared to the neat specimens. For all tensile tests, the load increases and reaches the maximum value. Thereafter, the curve moves forward with the zig-zag pattern confirming the bearing failure mode as per the ASTM D5961 standard.

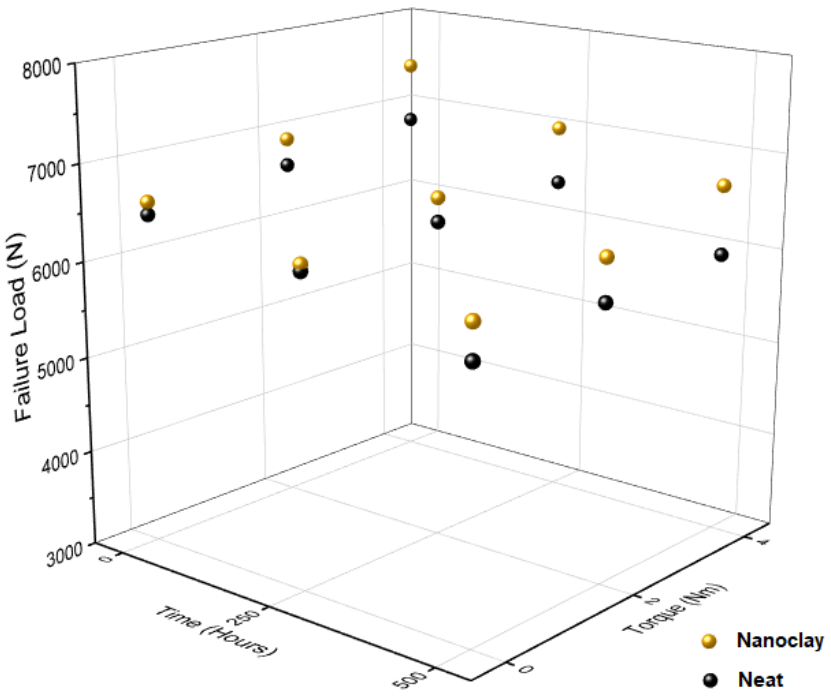

Fig. 6.17 Ultimate failure loads for joints made of neat and nanocomposite laminates

Figure 6.17 shows the comparison of failure loads for unaged and aged joints prepared using neat, and nanocomposite, respectively for different torque conditions. In case of neat composite, the joints with 0 Nm torque showed 3.4% and 10.5% decrease in failure loads after 250 and 500 hours of exposure, respectively. The joints tightened with 2 Nm torque showed a reduction of 4.3% and 11.2% in failure load for the corresponding aging conditions. A drop of 6.1% and 12.7% in failure load is observed in joints with 4 Nm torque for said aging conditions. For the nanocomposite material, the joints with 0 Nm torque showed 4.2% and 6.6% decrease in failure loads after 250 and 500 hours of exposure, respectively. The joints tightened with 2 Nm torque showed a reduction of 4.6% and 8.3% in failure load for the corresponding aging conditions. A drop of 5.9% and 10.2% is observed in joints with 4 Nm torque for said aging conditions.

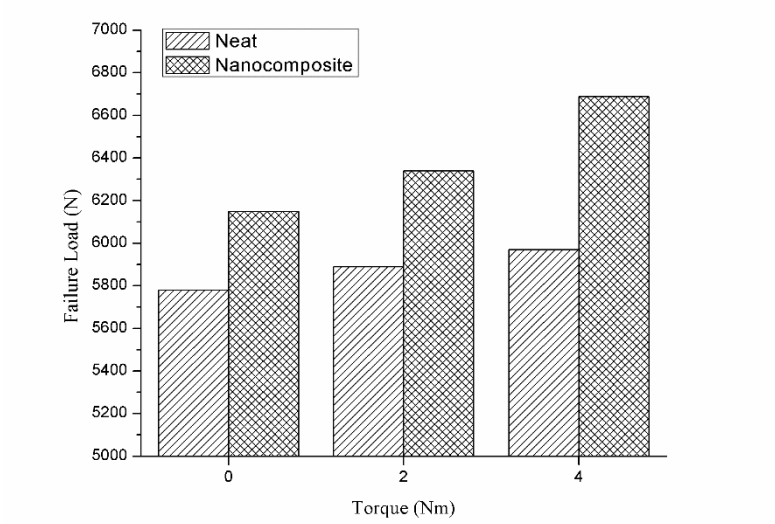

Fig. 6.18 Comparison of ultimate failure loads for joint configurations aged for 500 hours

Figure 6.18 shows the comparison of failure load for specimens prepared using neat epoxy and epoxy with nanoclay content for 500 hours of aging. The joints with nanoclay content have demonstrated higher ultimate failure loads compared to the joints made of neat epoxy. Comparing the nanoclay over neat joint configurations, even after the aging of 500 hours, the effect of torque is relatively large in joints prepared from nanocomposite material. The ultimate failure load of the joints made of nanocomposite material is increased significantly with an increase in the applied torque, which happened due to the ability of the nanoclay to maintain the structural integrity of the nanocomposite material

under accelerated aging conditions. The nanoclay resists the moisture and helps to reduce the fiber-matrix de-bonding of the material.

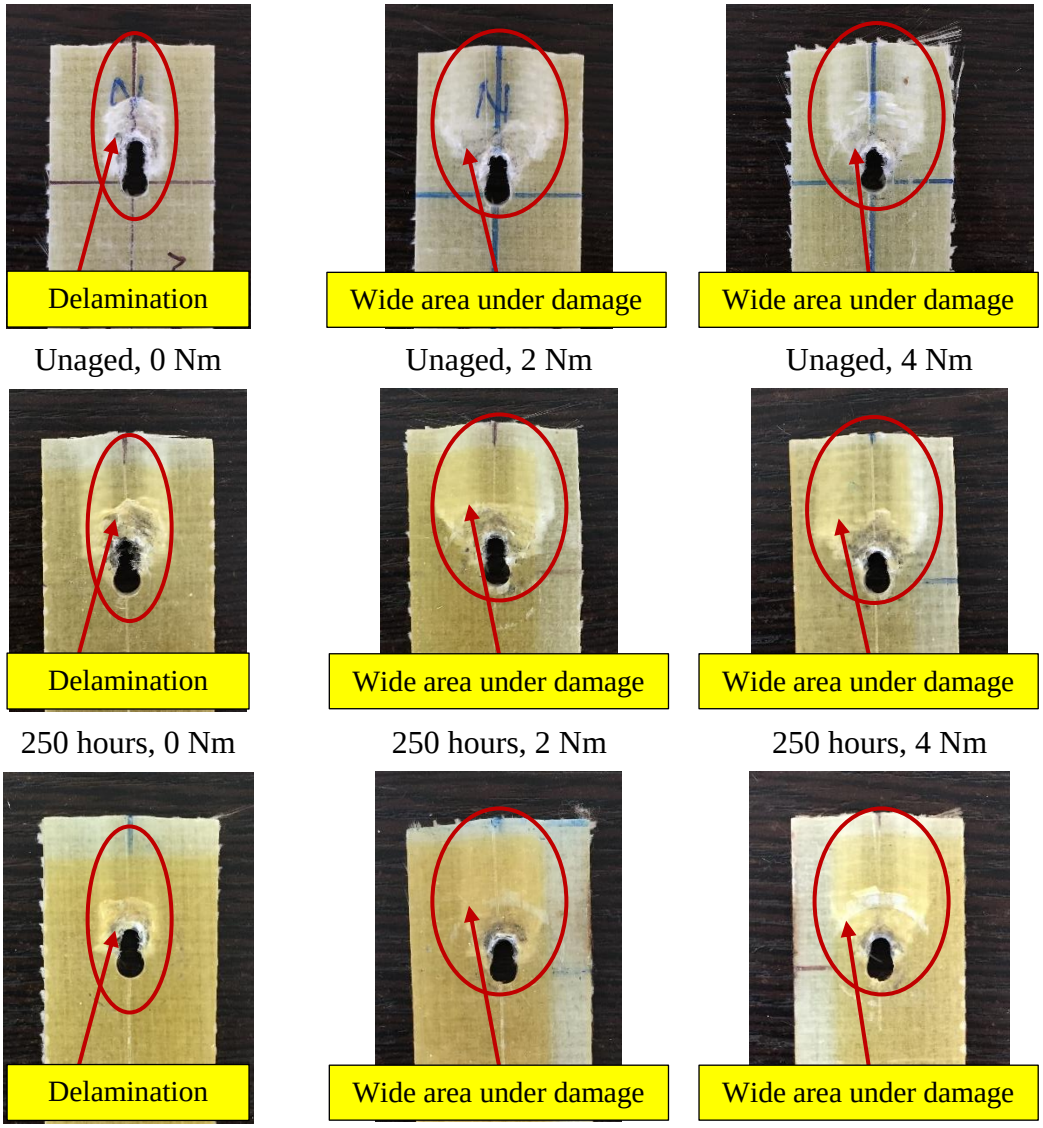

Fig. 6.19 Actual images of the tested specimen prepared from neat epoxy

The actual images of the tested aged specimens prepared from laminate with neat epoxy are shown in Fig. 6.19. From the visual inspection, the colors of the unaged and aged specimens look different. The specimens aged for 250 to 500 hours had a change in color appearance from creamish to a golden brown. All the specimen shows the bearing failure mode. As the torque increases, the incident pressure exerted by washer onto the composite specimen increases, which eventually helps to distribute the stresses over a comparatively wider area. Therefore, joints with high torque settings possess high joint

stiffness and larger failure loads. From the Fig. 6.19, it is seen that as the torque applied to the joint increases, the visible area under damage increases. In hand tightened condition, *i.e.*, 0 Nm torque, area under damage is narrow, and the stresses transferred to the specimen are localized compared to the specimens with high torque settings. Besides this, for the said torque level, the delamination near the hole surface also confirms the less incident pressure exerted by washer on the composite specimen.

6.4.2.4 Scanning electron microscopy

The UV exposure along with moisture and temperature induces significant microstructural changes in the glass fiber reinforced laminates. To investigate the microstructural changes in the composite material subjected to aging, SEM was performed on the unaged and aged specimens as shown in Fig. 6.20. Figure 6.20 (a) and (d) shows that the fibers are intact with the matrix for unaged specimens made of neat and nanocomposite laminates, respectively. Good adhesion of epoxy on the fiber surface is observed, and fibers are firmly placed even after fracture of the specimen. The neat specimen aged to 250 hours as shown in Fig. 6.20 (b) have an epoxy loss and fiber-matrix de-bonding in some portions. Due to increased H^+ and OH^- ions, the water molecules aggravate the photo-oxidative reaction of neat and nanocomposite materials [16]. The water molecules can also be located on free volume sites between polymer molecules, which in turn improves the mobility of free radicals within the surface layer and consequently accelerate the photo-degradation [142]. For the corresponding condition in the specimen with nanoclay content as shown in Fig. 6.20 (e), there is lower loss and degradation of the epoxy. As the aging time increases to 500 hours, the loss of epoxy in neat specimen increases significantly, and the loosening of the fiber-matrix bond can be seen from the Fig. 6.20 (c). Comparing Figs. 6.20 (a) and (c), a clear effect of aging time on the degradation of the structural properties can be seen in the specimen with neat epoxy. UV exposure generated polymer radicals by molecular chain scission on the polymer surface. The fragments might have linked to the neighboring molecule improving the degree of cross-linking. The increased embrittlement due to cross-linked molecules might be the reason behind the generation of microcracks. Further widening of the microcracks exposes material below the surface to an aging attack and accelerates the degradation process [18].

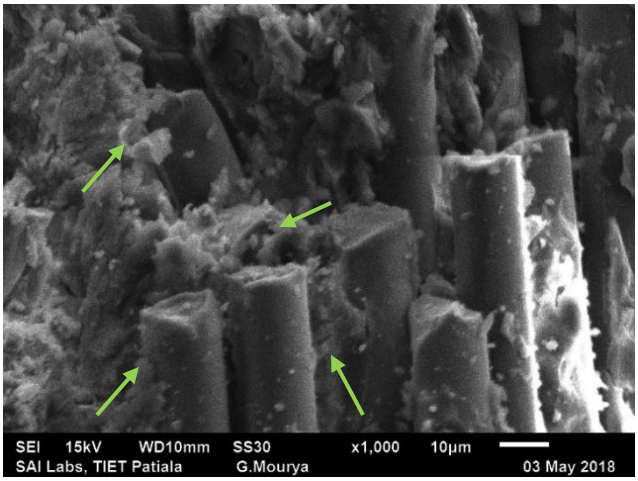

(a)

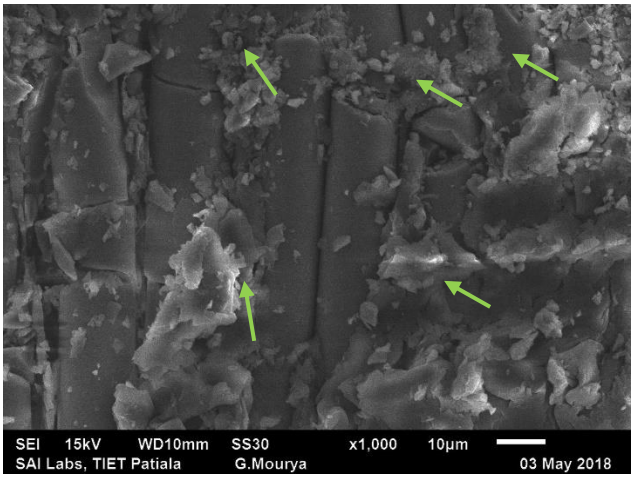

(d)

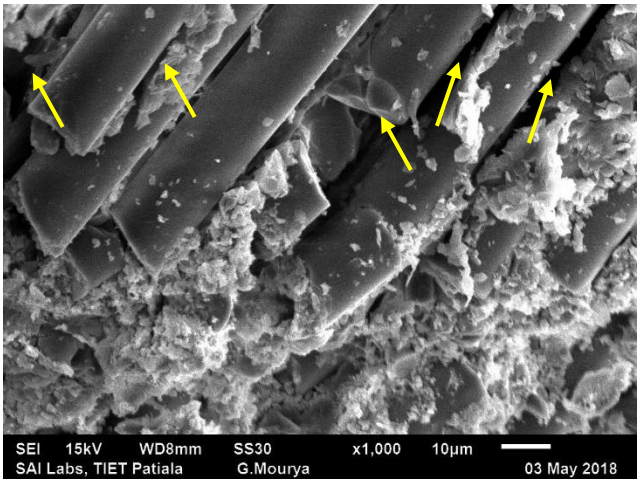

(b)

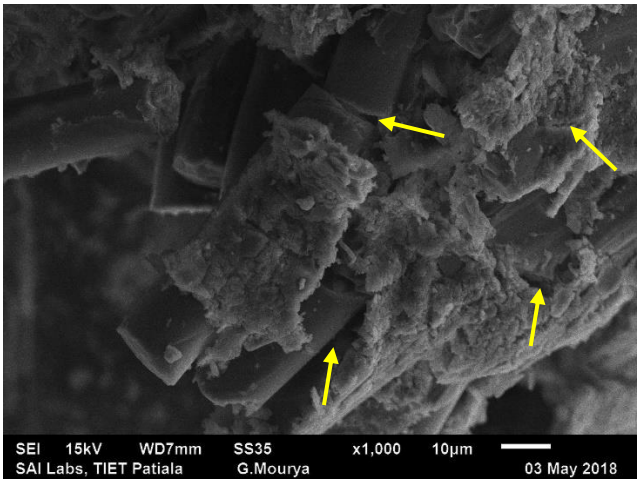

(e)

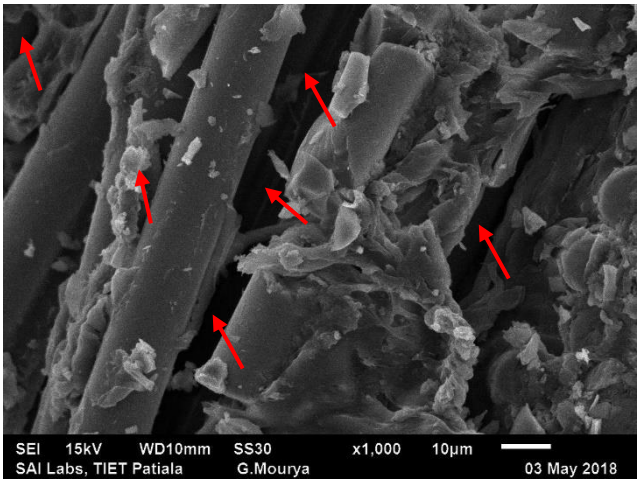

(c)

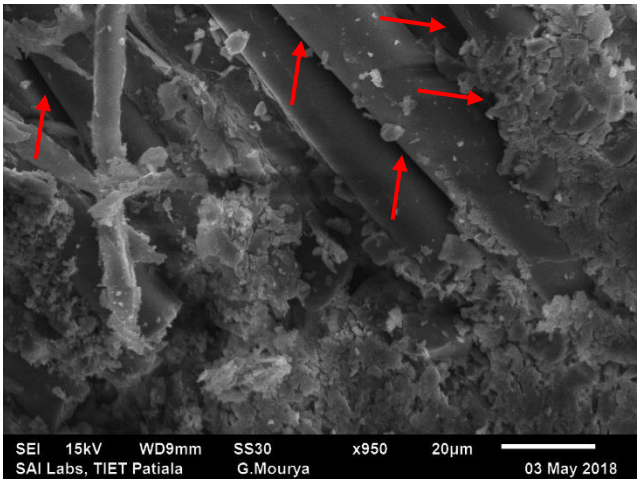

(f)

Fig. 6.20 SEM micrographs of
neat composite (a) unaged, (b) aged for 250 hours, (c) aged for 500 hours and
nanocomposite (d) unaged, (e) aged for 250 hours, (f) aged for 500 hours

The initial presence of microcracks in the material subjected to accelerated aging facilitates further propagation of cracks while structural testing of the material under various loading conditions. The corresponding condition of 500 hours in specimen made of nanocomposite materials is shown in Fig. 6.20 (f). It can be seen that there was an epoxy loss and fiber-matrix de-bonding with the lesser overall severity of degradation as compared to the neat composite specimens. Nanoclay acts as a barrier to moisture, and as a result, helps to resist the degradation of the nanocomposite under accelerated aging conditions.

6.4.2.5 Statistical analysis

A total of 26 experiments have been performed to analyze the bolted joint performance through response surface methodology (RSM).

Table 6.8 Failure loads for different joint configurations

Run order	Std. order	Factor			Failure load (N)
		Material	Time (Hours)	Torque (Nm)	
1	14	Nanoclay	0	0	6590
2	24	Nanoclay	250	2	6600
3	25	Nanoclay	250	2	6500
4	13	Neat	250	2	6350
5	2	Neat	500	0	5780
6	20	Nanoclay	250	0	6310
7	1	Neat	0	0	6460
8	11	Neat	250	2	6390
9	12	Neat	250	2	6370
10	9	Neat	250	2	6410
11	10	Neat	250	2	6395
12	15	Nanoclay	500	0	6150
13	6	Neat	500	2	5890
14	4	Neat	500	4	5970
15	3	Neat	0	4	6840
16	19	Nanoclay	500	2	6340
17	21	Nanoclay	250	4	7010
18	8	Neat	250	4	6420
19	22	Nanoclay	250	2	6770
20	18	Nanoclay	0	2	6920
21	23	Nanoclay	250	2	6645
22	5	Neat	0	2	6640
23	17	Nanoclay	500	4	6690
24	7	Neat	250	0	6240
25	16	Nanoclay	0	4	7450
26	26	Nanoclay	250	2	6550

RSM is a technique to build empirical models to optimize the output response which is dependent upon the different control factors. RSM explores the relationship between several explanatory variables and one or more response variables [143]. In the present work, the failure load for the corresponding bolt joint configurations is taken as the response variable with the values given in Table 6.8.

Table 6.9 shows the analysis of variance (ANOVA) which was performed on the experimental results. ANOVA is a statistical technique used to check if means of two or more groups are significantly different from each other [144]. The p-value less than 0.050 indicates the significance of different factors. As can be seen from Table 6.9, factors '*A*', '*B*', '*C*', '*A*×*B*' and '*B*×*C*' are the significant terms for failure load. Therefore, they are considered as significant variables for each response of failure load. To analyze the overall significance of the model, the R^2 value is calculated. With respect to the current model, the R^2 value is 0.9471, which means that the model can explain 94.71% variation in the response for failure load. The percentage contributions of factors *A* (time), *B* (torque), and *C* (material) are 44.42%, 21.67%, and 23.52%, respectively. The duration of aging is the most significant factor that affects the failure load.

Table 6.9 Analysis of variance

Source	**DF**	**Adj SS**	**Adj MS**	**F-value**	**p-value**	**Contribution (%)**
Model	8	3010316	376290	56.91	0.000	96.40
Linear	3	2798571	932857	141.10	0.000	89.61
A	1	1387200	1387200	209.82	0.000	44.42
B	1	676875	676875	102.38	0.000	21.67
C	1	734496	734496	111.09	0.000	23.52
Square	2	4824	2412	0.36	0.700	0.15
A×*A*	1	4309	4309	0.65	0.431	0.13
B×*B*	1	2115	2115	0.32	0.579	0.06
2-Way Interaction	3	206921	68974	10.43	0.000	6.62
A×*B*	1	32513	32513	4.92	0.040	1.04
A×*C*	1	22533	22533	3.41	0.082	0.72
B×*C*	1	151875	151875	22.97	0.000	4.86
Error	17	112395	6611			3.59
Lack-of-fit	9	67635	7515	1.34	0.344	2.16
Pure Error	8	44760	5595			1.43
Total	25	3122712				100

The regression models are used to predict the effect of control factors on the response, *i.e.*, failure load (F_L). The failure loads can be predicted for neat and nanocomposite materials using equation (6.3), and (6.4), respectively.

$$F_L = 6509.7 - (1.055 \times A) + (74.8 \times B) - (0.000447 \times A \times A) + (4.89 \times B \times B) - (0.1275 \times A \times B) \quad (6.3)$$

$$F_L = 6534.2 - (0.708 \times A) + (187.3 \times B) - (0.000447 \times A \times A) + (4.89 \times B \times B) - (0.1275 \times A \times B) \quad (6.4)$$

To check the validity of the equations (6.3) and (6.4), and to analyze the difference between the predicted and the experimental results, a confirmation test has been performed. Table 6.10 shows the predicted and actual results for selected joint configurations.

Table 6.10 Confirmation test for selected joint configurations

Factor *A* (time)	Factor *B* (torque)	Factor *C* (material)	Predicted load (N)	Experimental load (N)	% error
250	3	Neat	6390	6270	1.8
0	5	Neat	7006	6869	1.9
250	3	Nanocomposite	6839	6980	2
0	5	Nanocomposite	7593	7471	1.6

The control factor *B* (torque) has been increased a little beyond the DOE limit and is set to 5 Nm for two trials out of four for the confirmation test. The percentage error between the predicted and the experimental results is ≤ 2%. However, the accuracy of the model is subjected to certain limits of the control parameters. The effect of individual control factor on the failure load can be seen from the contour plots given in Fig. 6.21. It is observed from the slope of the contour plots that the load-bearing capacity of the material reduces with the increase in the aging duration. The cyclical exposure to UV and moisture have degraded the structural properties of the composite materials, which eventually reduced the joint performance. It is in the form of epoxy swelling, fiber-matrix de-bonding and cracks in the epoxy resulted from thermal shocks due to cyclical exposure to different temperatures, UV, and moisture. In comparison to the neat, the ultimate failure loads of the nanocomposite joints aged to different durations, *i.e.*, 0, 250, and 500 hours, are higher. The matrix, dispersed phase, and the interface are three primary elements which influence the properties of the composite material. Addition of nanoclay

in the form of dispersed phase into the epoxy acts as a mechanical interlock between the matrix and the fiber which in turn improves the interfacial bond strength of the glass fiber reinforced plastics and its joints. The X-ray diffraction tests performed on the epoxy modified with nanoclay has demonstrated an intercalated structure. Hence, the polymer chains are intercalated between the silicate layers, resulting in a well-ordered multilayer morphology built up with alternating inorganic and polymeric layers. This alternating layer morphology increases the contact surface between the epoxy and the silicate layer, resulting in a better epoxy-clay adhesion effect [19].

The moisture absorption by the epoxy and the fiber is entirely different, and consequently, volumetric expansion is different for epoxy and the fiber which setup localized stress and strain in the composite material. Compared to the ambient conditions, thermal and swelling stresses are higher in the severe conditions, which results in de-bonding of the epoxy and the glass fiber. However, this structure-property degradation due to accelerated aging is less aggressive in the case of nanocomposites. The addition of nanoclay hampers the moisture absorption into the composite and maintains the interfacial properties of the material. The tortuosity of nanoclay particles reduces the moisture absorption rate into the nanocomposite and thus improves the retention in the load-bearing capacity of the joints. As per SEM micrographs shown in Fig. 6.20, the composite specimen incorporating nanoclay demonstrated a good adhesion between the fiber and the epoxy even after accelerated aging. Comparing Figs. 6.20 (c) and (f), it is observed that after accelerated aging of 500 hours, nanoclay has maintained the fiber matrix bonding in a better way compared to the neat composite. The microstructural integration of fiber and epoxy also depends upon aging time. As seen in Fig. 6.20, with an increase in time, the fiber-matrix bond loosen and epoxy loss increases. Comparing unaged specimens (Fig. 6.20 (a)) and specimen aged to 500 hours (Fig. 6.20 (c)), a significant difference is observed in the fiber-matrix integration. Higher de-bonding of fiber-matrix and epoxy loss is observed for the said neat composite specimens after aging of 500 hours as compared to the nanocomposite specimens shown in Fig 6.20 (b) and (f). Nanoclay itself improves the individual properties of the matrix by bridging the micro-cracks and limiting their propagation to delay major cracks and ultimate fracture. The excellent

barrier characteristics of the nanoclay can also delay the penetration of oxygen and free radicals into the polymer, which is essential for the process of photo-degradation [18].

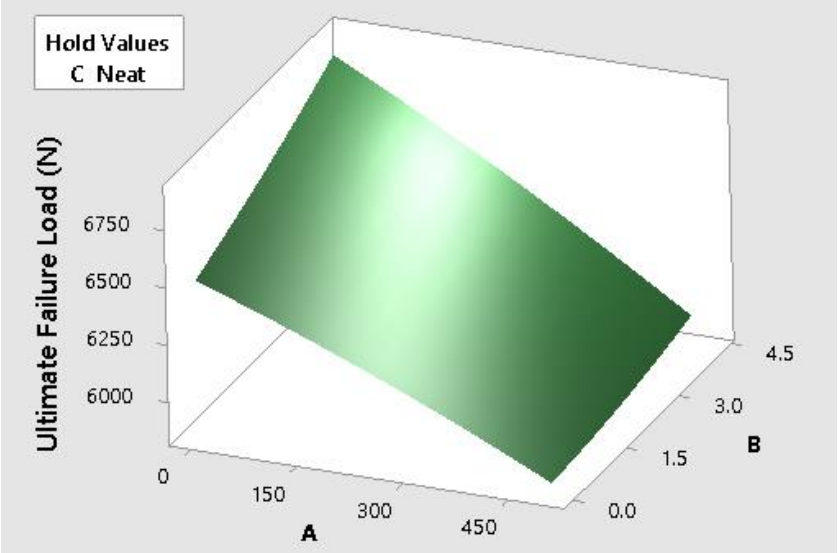

(a)

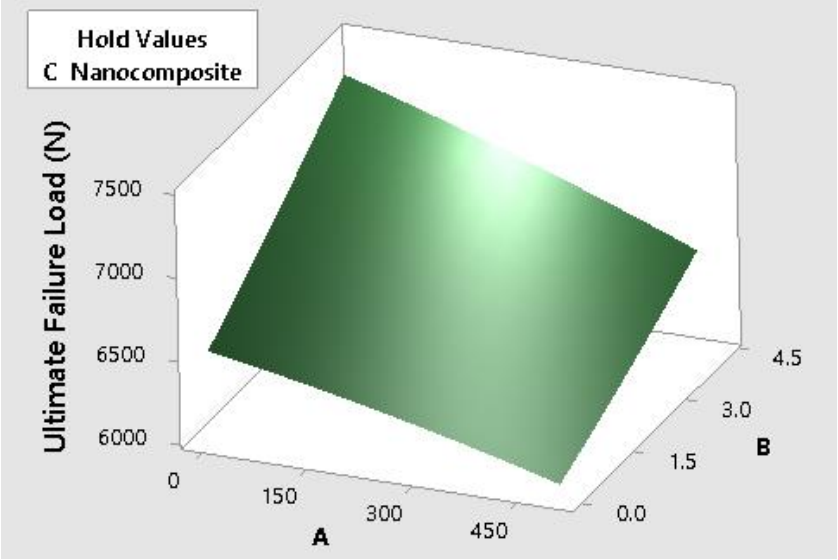

(b)

Fig. 6.21 Surface plots for failure load of joints made of (a) neat epoxy, and (b) epoxy modified with nanoclay

With the increase in the torque, the failure loads of the joints increase for both the materials. Using nanoclay in the glass fiber reinforced plastics has also shown a contribution towards the bolt torque efficiency. Comparing the surface plots shown in Figs. 6.21 (a) and (b), it is observed that the accelerated aging duration has less effect on the torque efficiency in the joints made of nanocomposite compared to neat composite.

Compared to the nanocomposite, the fiber matrix bonds have loosened, and the epoxy has more severe degradation in the neat composite material due to which the applied torque could not maintain the joint stiffness and could not enhance the ultimate failure load of the joint. The contribution of the torque can be seen by comparing the slope of the surface plots for 500 hours, where torque effect is significantly large in nanocomposite joints compared to the joints made of neat composite material.

6.5 Numerical Analysis of the Bolted Joint

Finite element analysis of the bolted joint was performed using ANSYS structural analysis module. In-situ material properties were considered for numerical analysis. Progressive damage analysis along with Hashin failure criteria has been performed for the numerical analysis of the joint. To avoid the premature results due to stress concentration present in the vicinity of the hole, characteristic curve has been used. The curve is drawn as shown in Fig. 5.10 as per the equation (5.2) by using the characteristic lengths. The characteristic lengths in tension and compression are obtained numerically. The finite element analysis has been performed on the open hole laminates to determine the characteristic lengths in tension and compression [91].

The laminate was modeled with E/D and W/D ratios to be 5 and 6, respectively. The laminate was subjected to the symmetrical tensile load (F). The mean tensile strength was calculated using equation (5.3). The point from the edge of the hole in the transverse direction was located such that the equivalent stress is equal to the mean tensile strength. The distance from the hole edge to the point where the equivalent stress is equal to the mean tensile strength is called the characteristic length in tension.

A compressive force (F) was applied to the hole. The bearing strength of the specimen was calculated using equation (5.4). The point ahead of the hole was located such that the equivalent stress was equal to the mean bearing strength. The distance from the edge of the hole to this point where the equivalent stress becomes equal to the mean bearing stress is called the characteristic length in compression.

For the damage initiation, Hashin failure criteria using equations (4.1) to (4.4) was used to perform the progressive failure analysis of the composites. Maximum failure index (FI_{max}), the maximum value among f_f and f_m in tension and compression, is used for

determining the failure modes and the failure loads. Based on the location of the maximum failure index on the characteristic curve, failure modes have been identified using equation (5.9). Failure load of the double lap composite joint is determined using equation (5.10).

6.5.1 **Loads and boundary conditions**

The applied loads, boundary conditions, and contact regions for the finite element analysis are shown in Fig. 6.22.

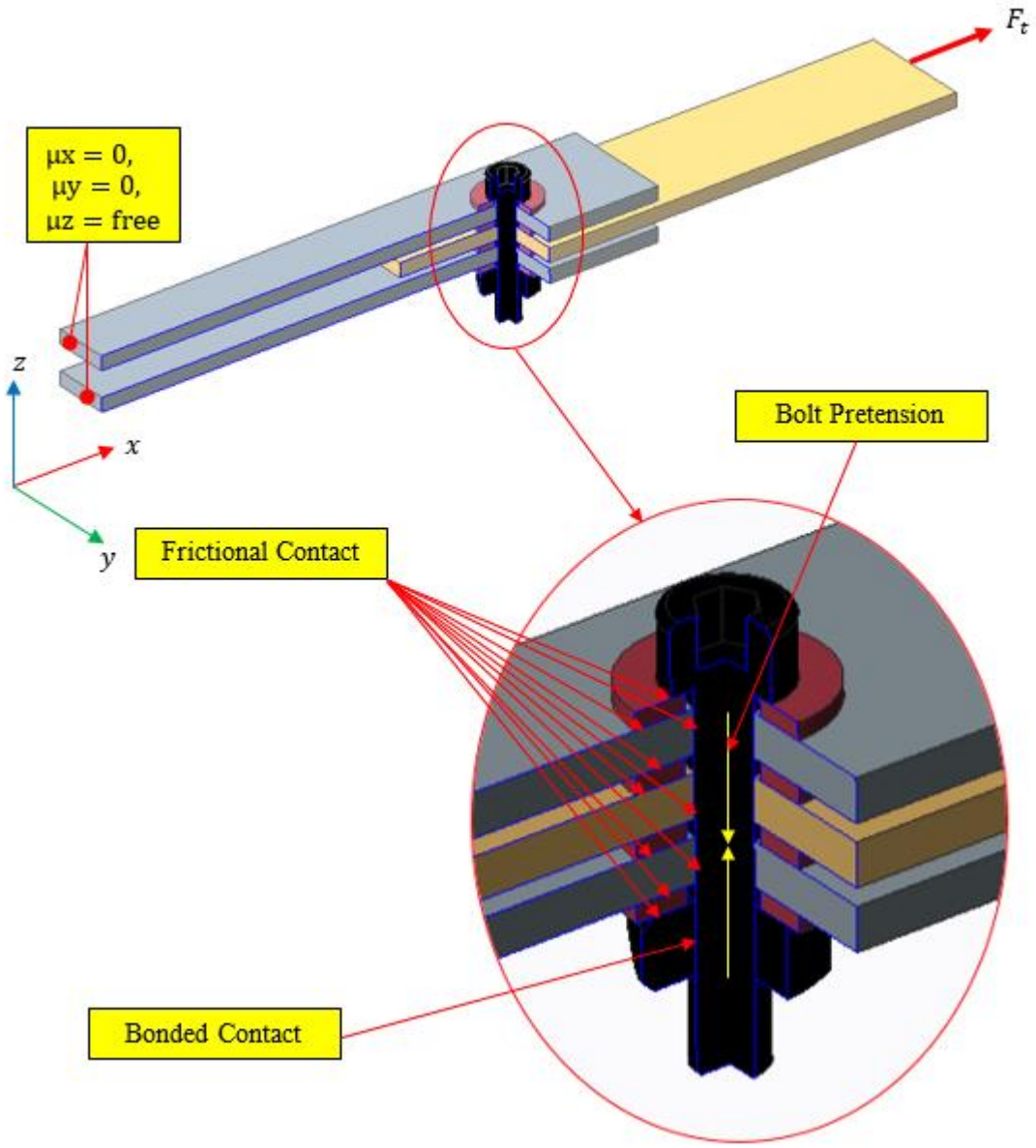

Fig. 6.22 Loads, boundary conditions and contacts set up in the numerical analysis of the joint

One side of the lap joint is fixed in *x*, *y* directions and is free in *z*-direction to allow bolt pretension to work, while on the other side of the joint an arbitrary tensile load, F_t is applied. Frictional contact behavior have been considered in all contact regions except the contact between nut and bolt which represents the locked condition and is taken as bonded. The friction coefficient was taken as constant in all joint configurations and it was assumed that there is no effect of aging on the friction coefficient. Complete mesh of the joint is shown in Fig. 6.23. Multizone mesh method with all Quad elements has been used. The used refined mesh along the characteristic curve is shown in Fig. 6.24. Analysis has been done in two steps. In the first step, bolt pre-tension is applied and in the second step, bolt pre-tension is locked and the tensile load is applied.

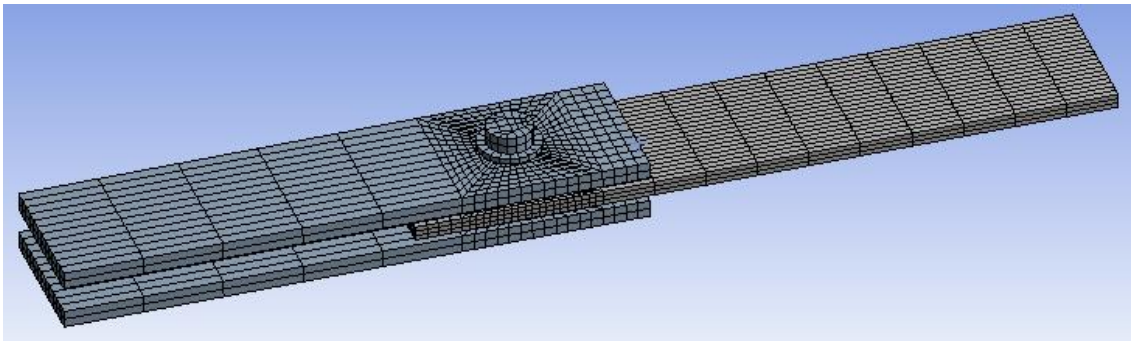

Fig. 6.23 Complete mesh of the double lap joint

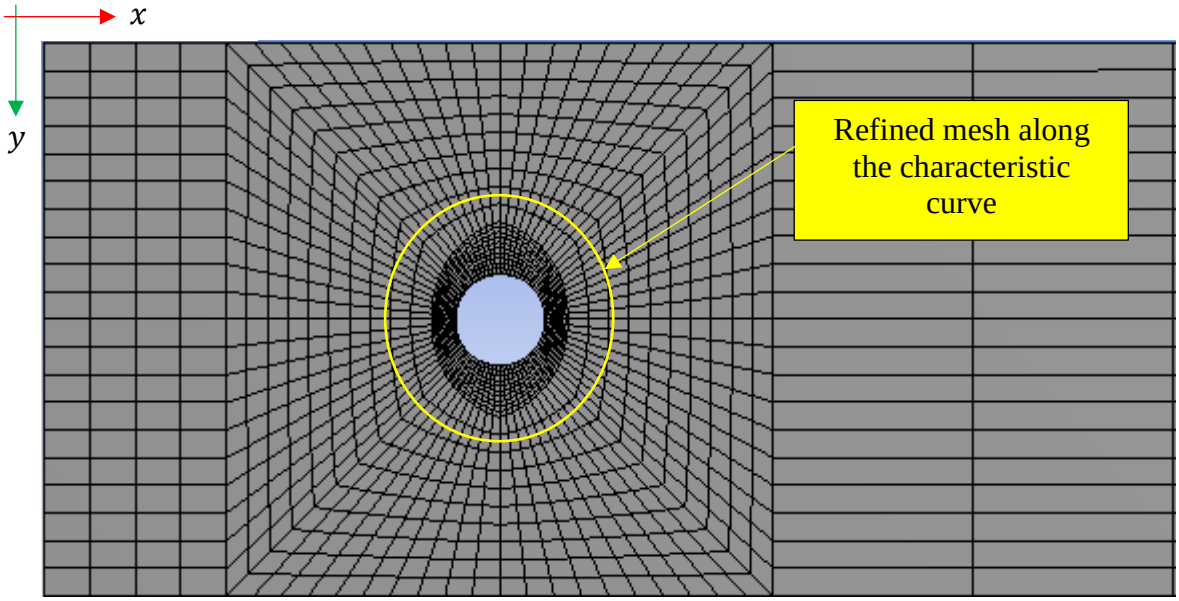

Fig. 6.24 Refined mesh around the hole in the composite joint

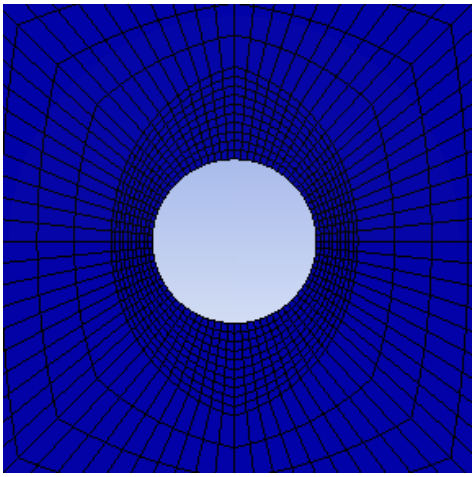

(a) 20% of applied load

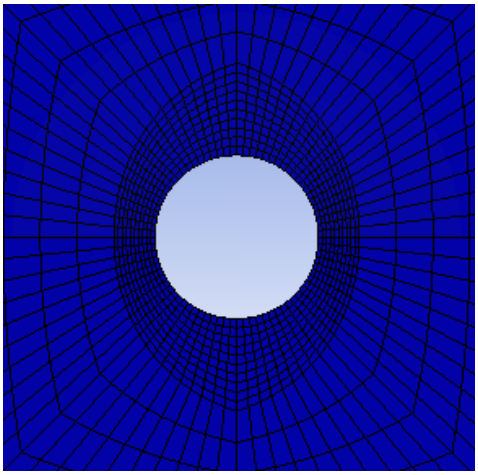

(b) 40% of applied load

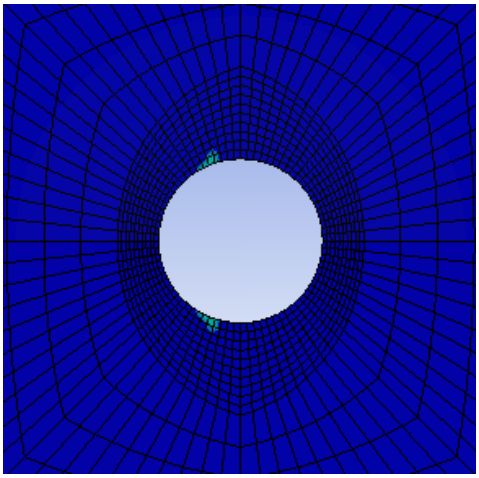

(c) 60% of applied load

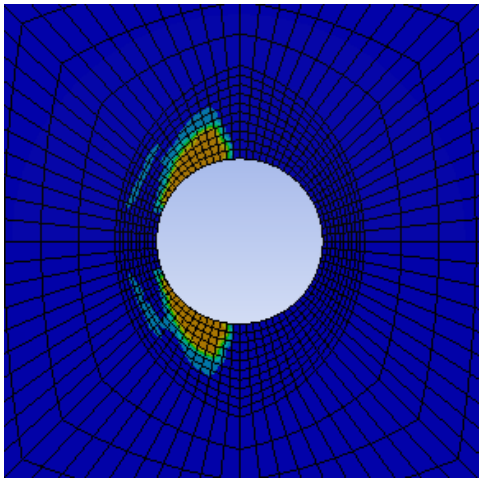

(d) 80% of applied load

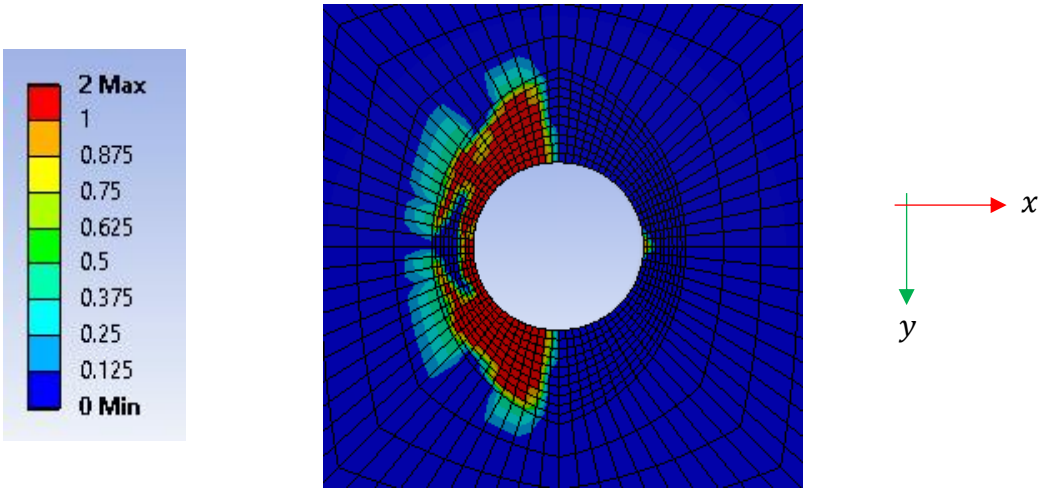

(e) 100% of applied load

Fig. 6.25 Damage progress in bolted joint with E/D = 5, W/D = 6, and a bolt torque of 2 Nm

The progressive damage contour plots of a particular joint configuration are shown in Fig. 6.25. As the load increases gradually, the damage initiates in the vicinity of the hole and progress radially towards the free edge of the specimen. The effect of bolt pretension can be clearly seen in the damage contour plots. Instead of going straight towards the free edge, the damage is distributed over area under compressive force applied through washer in the bolt joint. The failure of the bolted joint is considered when the damage status is unity on any point of the characteristic curve.

The failure loads predicted by the numerical analysis of the composite joint are shown in Table 6.11. The comparison of experimental and numerical results is shown in Fig. 6.26. A good agreement is observed between the numerical and the experimental results. It is observed from the Fig. 6.26 that the failure load of the composite joint is significantly hampered by the aging duration. Comparing the unaged, specimens aged for 250 and 500 hours, demonstrated lower load carrying capacity. On the other hand, the bolt torque has shown improvement in the ultimate failure load of the joint. Comparing the results of the neat and the nanocomposite joints, larger failure loads are taken by the nanocomposite joint.

Table 6.11 Failure loads predicted through numerical analysis

Sr. No.	Factor			Failure load (N)
	Material	Time (Hours)	Torque (Nm)	
1	Neat	0	0	5885
2	Neat	0	2	6215
3	Neat	0	4	6504
4	Neat	250	0	5666
5	Neat	250	2	5899
6	Neat	250	4	6092
7	Neat	500	0	5208
8	Neat	500	2	5407
9	Neat	500	4	5653
10	Nanoclay	0	0	6017
11	Nanoclay	0	2	6498
12	Nanoclay	0	4	7099
13	Nanoclay	250	0	5723
14	Nanoclay	250	2	6151
15	Nanoclay	250	4	6638
16	Nanoclay	500	0	5553
17	Nanoclay	500	2	5839
18	Nanoclay	500	4	5553

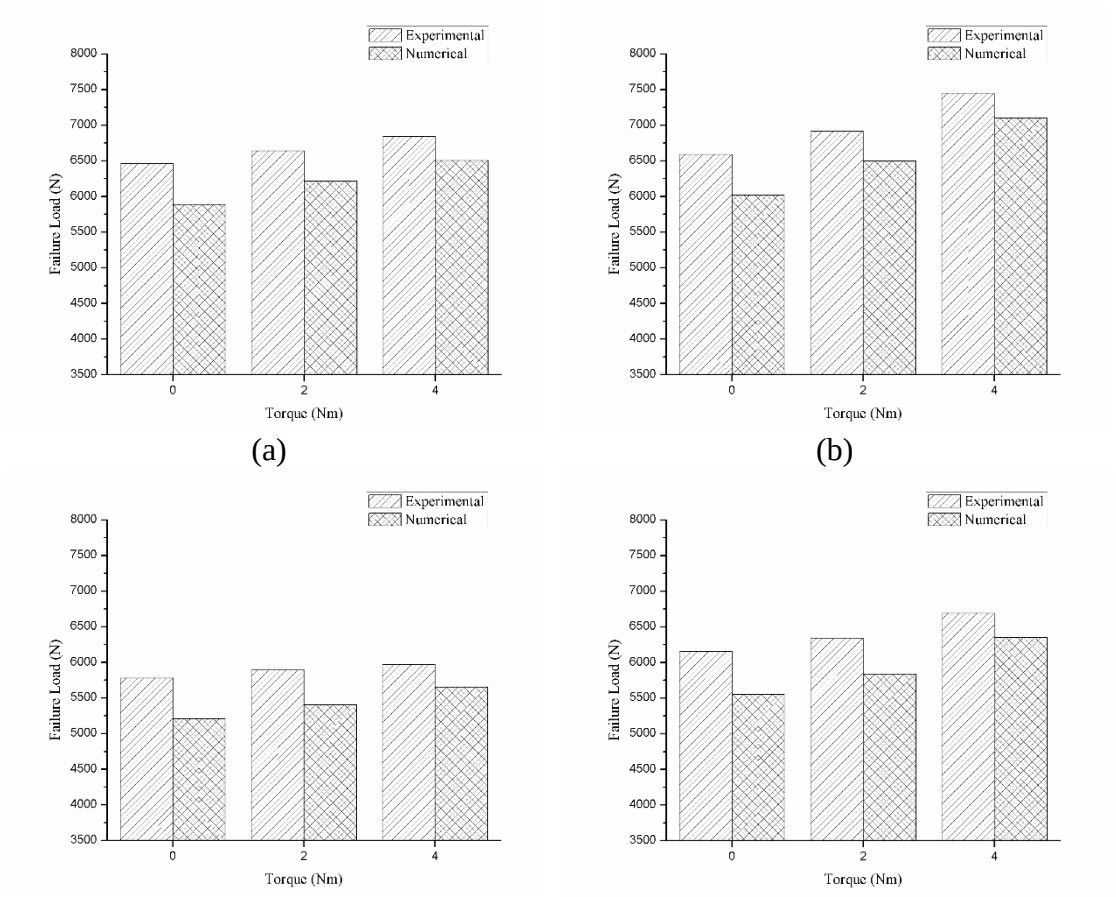

Fig. 6.26 Comparison of experimental and numerical results
(a) neat unaged, (b) nanocomposite unaged,
(c) neat aged for 500 hours, and (d) nanocomposite aged for 500 hours

6.6 Closure

The present chapter discussed about the aging of the bolted joints prepared using woven glass fiber reinforced composite laminates. Two different types of aging environments, *i.e.*, hygrothermal aging, and accelerated aging, were used in the present work. Nanoclay was used as nanofillers to improve the structural properties of the composite laminates. Effect of bolt torque was studied over a range of 0–4 Nm. Increasing the bolt torque facilitated to distribute the stresses over a wider area and increased the ultimate failure load as well as stiffness of the joint.

To estimate the effect of hygrothermal aging, parameters such as water temperature, and exposure time were considered in the range of 25–75°C, and 1–3 weeks, respectively. The specimens under combined attack of elevated temperature (50, and 75°C), and

moisture for 3 weeks experienced a significant degradation. However, at a lower temperature (25°C), no significant degradation was observed in the composite laminates. The tensile strength retention in the nanocomposite specimen was better than the neat composite specimens. A strong correlation between the water temperature, aging duration, and the ultimate failure load of the joint was observed. As the temperature and duration of exposure increases, the ultimate failure load of the bolt joint reduces. However, compared to the neat composite specimens, the joints made with nanoclay content had higher retention in the failure loads in different experimental conditions. Statistical analysis reported 'water temperature' as the most significant factor in the degradation of the material.

In case of accelerated aging of the bolted joints, a maximum of 500 hours of cyclical exposure to ultraviolet radiations, and moisture was given to the composite specimens. The duration of 500 hours of cyclical exposure to ultraviolet radiation and condensation significantly degraded the composite laminates which in turn diminished the load carrying capacity of the bolted joints. However, the strength retention in the nanocomposite specimen was better than the neat composite specimens. The statistical analysis reported 'aging duration' as the most significant factor to predict the failure load of the composite joints.

The next chapter gives the conclusions and recommendations for further direction to the present research work.

Chapter 7
Conclusions and Recommendations for Future Work

7.1 Conclusions

In the present work, the mechanical joints, *i.e.*, single pin joint, and single bolted joint were studied. Initially the mechanical properties of the composite laminate were maximized by optimizing the process parameters for the compression molding process using design of experiment. Selecting the optimized levels of mold pressure, temperature, and duration, the composite laminates were prepared. Then, to analyze the effect of nanoclay on the strength of the composite laminates, the nanoclay content was varied from 1 to 5 wt.%. Increasing the nanoclay concentration from 1 to 3 wt.% has increased the strength of the composite laminate. Further increase in nanoclay wt.% diminished the strength of the material. Incorporating 3 wt.% of nanoclay, an improvement of 20%, 21%, and 10% was observed in tensile, compressive and shear strengths of the composite laminates, respectively. The optimum strength was achieved with a pressure of 140 kN, temperature of 150°C and holding time of 30 minutes in the compression molding process.

The single hole pin joint were prepared from the glass fiber reinforced composite laminates. To reduce the effect of stress concentration around the hole, metal inserts were fitted in the hole drilled into the composite specimen, to increase the local stiffness around the hole edge. The combined effect of nanoclay and metal inserts was studied in the single hole pin joint. The study was further extended for bolted joint to analyze their durability in the different weathering conditions.

Metal inserts reduces stress concentration around the hole and redistribute the stresses around the pin/hole interface and significantly increase the failure load of the pin joint. Incorporating metal inserts increased the failure load of the pin joints. An increase of 68% to 90% and 67% to 71% was observed in the failure load of different geometric configurations of the pin joints made of unidirectional and bidirectional fiber reinforced composites, respectively. Using nanoclay showed a maximum of 26% and 31% improvement in the failure load of joints prepared with and without metal inserts, respectively. But the metal inserts are not recommended for joints having $W/D \leq 3$ and

E/D ≤ 2 as the failure mode in these joint configurations is net-tension or shear-out, which are the most undesired and catastrophic failure. Using metal inserts for the lower values of W/D and E/D ratios; reduces the margin between the hole boundary, the side edge of the composite laminate and the free edge of the laminate, which eventually lead to the net-tension or shear-out failure mode. E/D and W/D ratios as 4 is the critical value for using metal inserts into pin joints, which enables the designer to obtain the pure bearing mode of failure which have less serious consequences as compared to the net-tension and shear-out failure modes.

Failure load of the single bolt joint increases by increasing E/D and W/D ratios. However, for the low value of W/D ratio, *i.e.*, 2, there is no effect of E/D ratio on the joint failure load. Net-tension failure mode has been observed for W/D ratio to be 2 and 3. Bolted joints with W/D ratio as 5 failed in the pure bearing mode. For W/D ratio as 4, the initial failure mode was bearing followed by secondary bending leading to net-tension failure. Incorporating 3 wt.% of nanoclay has shown improvement in failure load of the bolted joints. A maximum of 21% improvement has been reported for joint configuration with W/D and E/D ratios as 3. Increasing bolt torque has shown an increase in the failure load and stiffness of the bolted joint. For joints without nanoclay, failure load has been improved by 19% and 37% having torque of 3 Nm and 5 Nm, respectively. Similarly, 21% and 35% improvement is observed for joints prepared with nanoclay having torque of 3 Nm and 5 Nm, respectively.

The duration of 500 hours of cyclical exposure to ultraviolet (UV) radiation and condensation significantly degraded the composite laminates. The tensile, compressive, and shear strength retentions of the neat composite specimens were 71.3%, 77.7%, and 81%, respectively. However, for the corresponding mechanical properties, the specimens made with 3 wt.% of nanoclay content demonstrated more strength retention of 79.5%, 85.3%, and 89.8%. The tortuosity of nanoclay helped to reduce the moisture absorption rate of the nanocomposite and maintained the interfacial bond between fiber and matrix, which in turn improved the strength retention of the nanocomposite laminates. Incorporating nanoclay as dispersed phase acted as a mechanical interlock between the matrix and the fiber, which eventually helped to improve the interfacial bond strength of the GFRP and its joints. The ultimate failure load of the bolted joint is significantly

affected by accelerated aging. A reduction of 10.5% to 12.7% has occurred in the ultimate failure load of neat joint configurations set to different torque levels. Whereas, joints made of nanocomposite material have shown a reduction of 6.6% to 10.2% in the ultimate failure loads of the joints set to different levels of torque. The thermal and swelling stresses are more in the severe conditions as compared to the ambient conditions which result in de-bonding of the neat epoxy and the glass fiber. The addition of nanoclay demonstrated a good adhesion between the fiber and the epoxy. Nanoclay also bridges the micro-cracks and limits their propagation which helps to delay the ultimate fracture. The bolt torque has shown a positive effect on the joint performance in all cases. Increasing the bolt torque facilitated to distribute the stresses over a wider area and increased the ultimate failure load as well as stiffness of the joint. However, the effect of bolt torque is more in unaged specimens compared to the aged specimen. A maximum of 5.8% and 13% improvement is observed in the failure load of the unaged joints made of neat and nanocomposite material, respectively. Accelerated aging duration showed less effect on the torque efficiency in the joints made of nanocomposite as compared to neat composite. The fiber matrix bonds loosened due to severe degradation of neat composite, as a result of which the applied torque could not maintain the joint stiffness and enhance the ultimate failure load of the joint. The addition of nanoclay reduced the moisture absorption rate of the nanocomposite which in turn helped to maintain the fiber-matrix interfacial bond and reduced structure property degradation due to accelerated aging in the nanocomposite. Joints with hand tightened conditions, *i.e.*, 0 Nm, experienced delamination and through-thickness expansion in the vicinity of the hole. This type of damage is undesired and hampers the joint performance. The joints having torque did not show any delamination. RSM analysis suggested the significance of all the control factors, *i.e.*, aging time, bolt torque, and material variation. The most significant factor for ultimate failure load prediction of the joint is duration of aging.

In case of joints exposed to hot water, the combined attack of elevated temperature, *i.e.*, 50°C and 75°C, and moisture for three weeks significantly degraded the composite laminates. However, at a lower temperature, *i.e.*, 25°C, no significant degradation is observed in the composite laminates. The tensile strength retentions of the neat composite specimens aged for 3 weeks at different temperatures, *i.e.*, 25°C, 50°C, and 75°C were

91.5%, 82.2%, and 70.7%, respectively. However, for the corresponding conditions, the specimens made with 3 wt.% of nanoclay content demonstrated more strength retention of 92.5%, 87.2%, and 80.9%. The tortuosity of nanoclay increased the length of the diffusion path and reduced the moisture absorption rate. Consequently, the degradation caused by the combined attack of moisture and temperature is less severe in the specimens made with the addition of nanoclay. A strong correlation between the water temperature, aging duration, and the ultimate failure load of the joint is observed. As the temperature and duration of exposure increases, the ultimate failure load of the bolted joint reduces. However, compared to the neat composite specimens, the joints made with nanoclay content had higher retention in the failure loads in different experimental conditions, which could be attributed to the ability of the nanoclay to hamper the water-polymer interaction through reduced moisture diffusion. Reduced moisture attack further controls the epoxy swelling, and fiber-matrix debonding at the interface, which leads to better retention in the performance of the bolted joints even under severe aging conditions. After 3 weeks of exposure to different temperatures, *i.e.*, 25°C, 50°C, and 75°C, a maximum of 2.3%, 18.7%, and 34.2% reduction occurred in the joint made of neat material, respectively. Whereas, for the similar conditions, joints made of nanocomposite material have shown the reduction of 1.3%, 14.5%, and 27.9%, respectively. The tortuosity of nanoclay reduced the moisture absorption rate of the nanocomposite which in turn helped to maintain the fiber-matrix interfacial bond and reduced structure property degradation due to accelerated aging. The bolt torque helped to distribute the stresses within the composite specimen and increase the ultimate failure load of the joint. An increase in joint stiffness is also observed by increasing the bolt torque. Compared to neat, the joints made of nanocomposite demonstrated higher torque efficiency in all conditions. Regression analysis suggested that the water temperature is the most significant factor in the degradation of the fiber reinforced polymer material.

Finite element method was used for numerical analysis of the mechanical joints. Characteristic curve method along with Hashin failure criteria was used to predict the failure loads and failure modes of the joints.

7.2 Recommendations for Future Work

The work can be extended in the following directions:

(i) Different methods can be used for the preparation of the composite laminates.

(ii) Different materials, *i.e.*, fiber and nanofillers can be used for the preparation of the composite laminates.

(iii) The analysis can be extended for different types of mechanical joints and loading types.

(iv) The durability of the mechanical joints can be tested in other different environmental conditions.

References

[1] Chen Y, Ma J, Han B, Zhang P, Hua H, Chen H, Su X. Emissions of automobiles fueled with alternative fuels based on engine technology: A review. Journal of Traffic and Transportation Engineering (English Edition). 2018;5:318–334.

[2] Ehsani M, Gao Y, Longo S, Ebrahimi K. Modern electric, hybrid electric, and fuel cell vehicles. Boca Raton, USA: CRC Press; 2018.

[3] Jacob A. Carbon fibre and cars – 2013 in review. Reinforced Plastics. 2014;58:18–19.

[4] Soutis C. Carbon fiber reinforced plastics in aircraft construction. Materials Science and Engineering: A. 2005;412:171–176.

[5] Mouritz AP, Gellert E, Burchill P, Challis K. Review of advanced composite structures for naval ships and submarines. Composite Structures. 2001;53:21–42.

[6] Al-saadi AU, Aravinthan T, Lokuge W. Structural applications of fibre reinforced polymer (FRP) composite tubes: A review of columns members. Composite Structures. 2018;204:513–524.

[7] Barbero E. Introduction to composite materials design. Boca Raton, USA CRC Press; 2018.

[8] Griffith AA. VI. The phenomena of rupture and flow in solids. Phil Trans R Soc Lond A. 1921;221:163–198.

[9] Mallick PK. Fiber-reinforced composites: materials, manufacturing, and design. Boca Raton, USA: CRC press; 2007.

[10] Guo F, Al-Saadi S, Singh Raman RK, Zhao XL. Durability of fiber reinforced polymer (FRP) in simulated seawater sea sand concrete (SWSSC) environment. Corrosion Science. 2018;141:1–13.

[11] Mouritz AP. Environmental durability of z-pinned carbon fibre–epoxy laminate exposed to water. Composites Science and Technology. 2012;72:1568–1574.

[12] Sharma B, Mahajan S, Chhibber R, Mehta R. Glass fiber reinforced polymer-clay nanocomposites: processing, structure and hygrothermal effects on mechanical properties. Procedia Chemistry. 2012;4:39–46.

[13] Soykok IF, Sayman O, Pasinli A. Effects of hot water aging on failure behavior of mechanically fastened glass fiber/epoxy composite joints. Composites Part B: Engineering. 2013;54:59–70.

[14] Firdosh S, Murthy HNN, Pal R, Angadi G, Raghavendra N, Krishna M. Durability of GFRP nanocomposites subjected to hygrothermal ageing. Composites Part B: Engineering. 2015;69:443–451.

[15] Zhang J, Qi D, Zhou L, Zhao L, Hu N. A progressive failure analysis model for composite structures in hygrothermal environments. Composite Structures. 2015;133:331–342.

[16] Kumar BG, Singh RP, Nakamura T. Degradation of carbon fiber-reinforced epoxy composites by ultraviolet radiation and condensation. Journal of Composite Materials. 2002;36:2713–2733.

[17] Maxwell A, Broughton W, Dean G, Sims G. Review of accelerated ageing methods and lifetime prediction techniques for polymeric materials. NPL Report DEPC MPR. 2005;16:22.

[18] Woo RSC, Chen Y, Zhu H, Li J, Kim J-K, Leung CKY. Environmental degradation of epoxy–organoclay nanocomposites due to UV exposure. Part I: Photo-degradation. Composites Science and Technology. 2007;67:3448–3456.
[19] Chang LN, Chow WS. Accelerated weathering on glass fiber/epoxy/organo-montmorillonite nanocomposites. Journal of Composite Materials. 2010;44:1421–1434.
[20] Soykok IF, Sayman O, Ozen M, Korkmaz B. Failure analysis of mechanically fastened glass fiber/epoxy composite joints under thermal effects. Composites Part B: Engineering. 2013;45:192–199.
[21] Xie Y, Hill CAS, Xiao Z, Militz H, Mai C. Silane coupling agents used for natural fiber/polymer composites: A review. Composites Part A: Applied Science and Manufacturing. 2010;41:806–819.
[22] Kornmann X, Rees M, Thomann Y, Necola A, Barbezat M, Thomann R. Epoxy-layered silicate nanocomposites as matrix in glass fibre-reinforced composites. Composites Science and Technology. 2005;65:2259–2268.
[23] Evans AG, Zok FW, Davis J. The role of interfaces in fiber-reinforced brittle matrix composites. Composites Science and Technology. 1991;42:3–24.
[24] Timmerman JF, Hayes BS, Seferis JC. Nanoclay reinforcement effects on the cryogenic microcracking of carbon fiber/epoxy composites. Composites Science and Technology. 2002;62:1249–1258.
[25] Haque A, Shamsuzzoha M, Hussain F, Dean D. S2-glass/epoxy polymer nanocomposites: manufacturing, structures, thermal and mechanical properties. Journal of Composite Materials. 2003;37:1821–1837.
[26] Chowdhury FH, Hosur MV, Jeelani S. Studies on the flexural and thermomechanical properties of woven carbon/nanoclay-epoxy laminates. Materials Science and Engineering: A. 2006;421:298–306.
[27] Lin L-Y, Lee J-H, Hong C-E, Yoo G-H, Advani SG. Preparation and characterization of layered silicate/glass fiber/epoxy hybrid nanocomposites via vacuum-assisted resin transfer molding (VARTM). Composites Science and Technology. 2006;66:2116–2125.
[28] Quaresimin M, Varley RJ. Understanding the effect of nano-modifier addition upon the properties of fibre reinforced laminates. Composites Science and Technology. 2008;68:718–726.
[29] Xu Y, Hoa SV. Mechanical properties of carbon fiber reinforced epoxy/clay nanocomposites. Composites Science and Technology. 2008;68:854–861.
[30] Singh SK, Singh S, Sharma S, Sharma V. Strength degradation of mechanical properties of unidirectional E-glass fiber epoxy resin nanoclay composites under hygrothermal loading conditions. Procedia Materials Science. 2014;5:1114–1119.
[31] Gibson R. Principles of composite material mechanics, 1994. New York: McGraw-Hall Inc.
[32] Ebewele RO. Polymer science and technology: CRC press; 2000.
[33] Harris CE, Starnes JH, Shuart MJ. Design and manufacturing of aerospace composite structures, state-of-the-art assessment. Journal of Aircraft. 2002;39:545–560.
[34] Agarwal BD, Broutman LJ, Chandrashekhara K. Analysis and performance of fiber composites: John Wiley & Sons; 2017.

[35] Bansemir H, Haider O. Fibre composite structures for space applications—recent and future developments. Cryogenics. 1998;38:51–59.
[36] Hollaway LC. The evolution of and the way forward for advanced polymer composites in the civil infrastructure. Construction and Building Materials. 2003;17:365–378.
[37] Karbhari VM. Fiber reinforced composite bridge systems—transition from the laboratory to the field. Composite Structures. 2004;66:5–16.
[38] Savage G. Composite materials in formula 1 racing. Metals and Materials. 1991;7:617–624.
[39] Beardmore P. Composite structures for automobiles. Composite Structures. 1986;5:163–176.
[40] Beardmore P, Johnson CF. The potential for composites in structural automotive applications. Composites Science and Technology. 1986;26:251–281.
[41] Chalmers DW. The Potential for the use of composite materials in marine structures. Marine Structures. 1994;7:441–456.
[42] Irisarri FX, Laurin F, Carrere N, Maire JF. Progressive damage and failure of mechanically fastened joints in CFRP laminates–Part I: refined finite element modelling of single-fastener joints. Composite Structures. 2012;94:2269–2277.
[43] Asgari Mehrabadi F. Experimental and numerical failure analysis of adhesive composite joints. International Journal of Aerospace Engineering. 2012;2012:1–10.
[44] Khashaba UA, Sebaey TA, Alnefaie KA. Failure and reliability analysis of pinned-joints composite laminates: Effects of stacking sequences. Composites Part B: Engineering. 2013;45:1694–1703.
[45] Karakuzu R, Çalışkan CR, Aktaş M, İçten BM. Failure behavior of laminated composite plates with two serial pin-loaded holes. Composite Structures. 2008;82:225–234.
[46] İçten BM, Karakuzu R, Toygar ME. Failure analysis of woven kevlar fiber reinforced epoxy composites pinned joints. Composite Structures. 2006;73:443–450.
[47] Li H-S, Xia S, Luo D-M. A probabilistic analysis for pin joint bearing strength in composite laminates using Subset Simulation. Composites Part B: Engineering. 2014;56:780–789.
[48] Pisano AA, Fuschi P, De Domenico D. A layered limit analysis of pinned-joints composite laminates: numerical versus experimental findings. Composites Part B: Engineering. 2012;43:940–952.
[49] Okutan B, Aslan Z, Karakuzu R. A study of the effects of various geometric parameters on the failure strength of pin-loaded woven-glass-fiber reinforced epoxy laminate. Composites Science and Technology. 2001;61:1491–1497.
[50] Asi O. Effect of different woven linear densities on the bearing strength behaviour of glass fiber reinforced epoxy composites pinned joints. Composite Structures. 2009;90:43–52.
[51] Öndürücü A, Esendemir Ü, Tunay RF. Progressive failure analysis of glass–epoxy laminated composite pinned-joints. Materials & Design (1980-2015). 2012;36:617–625.

[52] Kweon J-H, Ahn H-S, Choi J-H. A new method to determine the characteristic lengths of composite joints without testing. Composite Structures. 2004;66:305–315.
[53] Aktas A, Husnu Dirikolu M. An experimental and numerical investigation of strength characteristics of carbon-epoxy pinned-joint plates. Composites Science and Technology. 2004;64:1605–1611.
[54] Qin T, Zhao L, Zhang J. Fastener effects on mechanical behaviors of double-lap composite joints. Composite Structures. 2013;100:413–423.
[55] Ghorbel I, Valentin D. Hydrothermal effects on the physico-chemical properties of pure and glass fiber reinforced polyester and vinylester resins. Polymer Composites. 1993;14:324–334.
[56] Weitsman YJ, Elahi M. Effects of fluids on the deformation, strength and durability of polymeric composites–an overview. Mechanics of Time-Dependent Materials. 2000;4:107–126.
[57] Chen Y, Davalos JF, Ray I. Durability prediction for GFRP reinforcing bars using short-term data of accelerated aging tests. Journal of Composites for Construction. 2006;10:279–286.
[58] Aldajah S, Alawsi G, Rahmaan SA. Impact of sea and tap water exposure on the durability of GFRP laminates. Materials & Design. 2009;30:1835–1840.
[59] Camino G, Luda MP, Polishchuk AY, Revellino M, Blancon R, Merle G, Martinez-Vega JJ. Kinetic aspects of water sorption in polyester-resin/glass-fibre composites. Composites Science and Technology. 1997;57:1469–1482.
[60] Chin JW, Nguyen T, Aouadi K. Sorption and diffusion of water, salt water, and concrete pore solution in composite matrices. Journal of Applied Polymer Science. 1999;71:483–492.
[61] Roy S, Xu WX, Park SJ, Liechti KM. Anomalous moisture diffusion in viscoelastic polymers: modeling and testing. Journal of Applied Mechanics. 2000;67:391–396.
[62] Picard E, Vermogen A, Gérard J-F, Espuche E. Barrier properties of nylon 6-montmorillonite nanocomposite membranes prepared by melt blending: influence of the clay content and dispersion state: consequences on modelling. Journal of Membrane Science. 2007;292:133–144.
[63] Chow WS, Abu Bakar A, Mohd Ishak ZA. Water absorption and hygrothermal aging study on organomontmorillonite reinforced polyamide 6/polypropylene nanocomposites. Journal of Applied Polymer Science. 2005;98:780–790.
[64] Chow WS. Water absorption of epoxy/glass fiber/organo-montmorillonite nanocomposites. Express Polymer Letters. 2007;1:104–108.
[65] Chow WS, Teoh JK, Lim LY. Mechanical and hygrothermal aging study on polystyrene/organo-montmorillonite nanocomposites. Polymer-Plastics Technology and Engineering. 2008;47:1040–1045.
[66] Panwar A, Choudhary V, Sharma DK. Review: A review: polystyrene/clay nanocomposites. Journal of Reinforced Plastics and Composites. 2011;30:446–459.
[67] Ku H, Wang H, Pattarachaiyakoop N, Trada M. A review on the tensile properties of natural fiber reinforced polymer composites. Composites Part B: Engineering. 2011;42:856–873.
[68] Koo JH. Polymer nanocomposites: McGraw-Hill Professional Pub.; 2006.

[69] Chang F-K, Scott RA, Springer GS. Strength of mechanically fastened composite joints. Journal of Composite materials. 1982;16:470–494.
[70] İçten BM, Karakuzu R. Progressive failure analysis of pin-loaded carbon–epoxy woven composite plates. Composites Science and Technology. 2002;62:1259–1271.
[71] Okutan B, Karakuzu R. The strength of pinned joints in laminated composites. Composites Science and Technology. 2003;63:893–905.
[72] Okutan Baba B. Behavior of pin-loaded laminated composites. Experimental Mechanics. 2006;46:589–600.
[73] Tercan M, Asi O, Aktaş A. An experimental investigation of the bearing strength of weft-knitted 1× 1 rib glass fiber composites. Composite Structures. 2007;78:392–396.
[74] Atas C. Bearing strength of pinned joints in woven fabric composites with small weaving angles. Composite Structures. 2009;88:40–45.
[75] Aluko O. An analytical method for failure prediction of composite pinned joints. Proceedings of the World Congress on Engineering2011. p. 978–988.
[76] Ilić I, Petrovic Z, Maksimović M, Stupar S, Stamenković D. Computation method in failure analysis of mechanically fastened joints at layered composites. Strojniški vestnik-Journal of Mechanical Engineering. 2012;58:553–559.
[77] Turan K, Gur M, Kaman MO. Progressive failure analysis of pin-loaded unidirectional carbon-epoxy laminated composites. Mechanics of Advanced Materials and Structures. 2014;21:98–106.
[78] Zhang C, Curiel-Sosa JL, Bui TQ. Meso-scale progressive damage modeling and life prediction of 3D braided composites under fatigue tension loading. Composite Structures. 2018;201:62–71.
[79] Karakuzu R, Gülem T, İçten BM. Failure analysis of woven laminated glass–vinylester composites with pin-loaded hole. Composite Structures. 2006;72:27–32.
[80] Karakuzu R, Taylak N, İçten BM, Aktaş M. Effects of geometric parameters on failure behavior in laminated composite plates with two parallel pin-loaded holes. Composite Structures. 2008;85:1–9.
[81] Aktaş A, İmrek H, Cunedioğlu Y. Experimental and numerical failure analysis of pinned-joints in composite materials. Composite Structures. 2009;89:459–466.
[82] Aktaş A. Failure analysis of serial pinned joints in composite materials. Indian Journal of Engineering & Materials Sciences. 2011;18:102–110.
[83] Kishore AN, Malhotra SK, Prasad NS. Failure analysis of multi-pin joints in glass fibre/epoxy composite laminates. Composite Structures. 2009;91:266–277.
[84] Kishore AN, Malhotra SK, Prasad NS. Strength prediction in multi-pin joints from equivalent material properties in composite laminates. Mechanics of Advanced Materials and Structures. 2010;17:204–214.
[85] Karakuzu R, Demirgoren O, Icten BM, Deniz ME. Failure behavior of quasi-isotropic laminates with three-pin loaded holes. Materials & Design. 2010;31:3029–3032.
[86] Pisano AA, Fuschi P, De Domenico D. Failure modes prediction of multi-pin joints FRP laminates by limit analysis. Composites Part B: Engineering. 2013;46:197–206.

[87] Pisano AA, Fuschi P, De Domenico D. Peak load prediction of multi-pin joints FRP laminates by limit analysis. Composite Structures. 2013;96:763–772.
[88] Olmedo A, Santiuste C, Barbero E. An analytical model for predicting the stiffness and strength of pinned-joint composite laminates. Composites Science and Technology. 2014;90:67–73.
[89] Sen F, Pakdil M, Sayman O, Benli S. Experimental failure analysis of mechanically fastened joints with clearance in composite laminates under preload. Materials & Design. 2008;29:1159–1169.
[90] Ataş A, Soutis C. Strength prediction of bolted joints in CFRP composite laminates using cohesive zone elements. Composites Part B: Engineering. 2014;58:25–34.
[91] Zhang J, Liu F, Zhao L, Chen Y, Fei B. A progressive damage analysis based characteristic length method for multi-bolt composite joints. Composite Structures. 2014;108:915–923.
[92] Murthy AV, Dattaguru B, Narayana H, Rao A. Stress and strength analysis of pin joints in laminated anisotropic plates. Composite Structures. 1991;19:299–312.
[93] McCarthy M, McCarthy C, Lawlor V, Stanley W. Three-dimensional finite element analysis of single-bolt, single-lap composite bolted joints: part I—model development and validation. Composite Structures. 2005;71:140–158.
[94] Zhai Y, Li D, Li X, Wang L, Yin Y. An experimental study on the effect of bolt-hole clearance and bolt torque on single-lap, countersunk composite joints. Composite Structures. 2015;127:411–419.
[95] Esmaeili F, Chakherlou T. Investigation on the effect of tigthening torque on the stress distribution in double lap simple bolted and hybrid (bolted-bonded) Joints. Journal of Solid Mechanics. 2015;7:268–280.
[96] Asi O. An experimental study on the bearing strength behavior of Al_2O_3 particle filled glass fiber reinforced epoxy composites pinned joints. Composite Structures. 2010;92:354–363.
[97] Arun KV, Sujay Kumar D, Murugesh MC. Influence of bolt configuration and TiO_2/ZnS fillers content on the strength of composites fasteners. Materials & Design. 2014;53:51–57.
[98] Singh M, Bhunia H, Saini JS. Effect of ply orientation on strength and failure mode of pin jointed unidirectional glass-epoxy nanoclay laminates. Defence Science Journal. 2015;65:489–499.
[99] Singh IV, Shedbale A, Mishra B. Material property evaluation of particle reinforced composites using finite element approach. Journal of Composite Materials. 2016;50:2757–2771.
[100] Joshi RS, Singh H, Singh I. Modulation-assisted drilling of glass-fiber-reinforced plastics. Materials and Manufacturing Processes. 2014;29:370–378.
[101] Nilsson S. Increasing strength of graphite/epoxy bolted joints by introducing an adhesively bonded metallic insert. Journal of Composite Materials. 1989;23:642–650.
[102] Herrera-Franco PJ, Cloud GL. Strain-relief inserts for composite fasteners-an experimental study. Journal of Composite Materials. 1992;26:751–768.
[103] Camanho PP, Matthews FL. Bonded metallic inserts for bolted joints in composite laminates. Proceedings of the Institution of Mechanical Engineers, Part L: Journal of Materials Design and Applications. 2000;214:33–40.

[104] Camanho PP, Tavares CML, de Oliveira R, Marques AT, Ferreira AJM. Increasing the efficiency of composite single-shear lap joints using bonded inserts. Composites Part B: Engineering. 2005;36:372–383.
[105] Mara V, Haghani R, Al-Emrani M. Improving the performance of bolted joints in composite structures using metal inserts. Journal of Composite Materials. 2016;50:3001–3018.
[106] Liu W, Hoa SV, Pugh M. Fracture toughness and water uptake of high-performance epoxy/nanoclay nanocomposites. Composites Science and Technology. 2005;65:2364–2373.
[107] Olmos D, Lopez-Moron R, Gonzalez-Benito J. The nature of the glass fibre surface and its effect in the water absorption of glass fibre/epoxy composites. The use of fluorescence to obtain information at the interface. Composites Science and Technology. 2006;66:2758–2768.
[108] Liu W, Hoa SV, Pugh M. Water uptake of epoxy–clay nanocomposites: model development. Composites Science and Technology. 2008;68:156–163.
[109] Liu W, Hoa SV, Pugh M. Water uptake of epoxy–clay nanocomposites: experiments and model validation. Composites Science and Technology. 2008;68:2066–2072.
[110] Glaskova T, Aniskevich A. Moisture absorption by epoxy/montmorillonite nanocomposite. Composites Science and Technology. 2009;69:2711–2715.
[111] Lee JH, Rhee KY, Lee JH. Effects of moisture absorption and surface modification using 3-aminopropyltriethoxysilane on the tensile and fracture characteristics of MWCNT/epoxy nanocomposites. Applied Surface Science. 2010;256:7658–7667.
[112] Lo SH, Zhen W, Cheung YK, Wanji C. Hygrothermal effects on multilayered composite plates using a refined higher order theory. Composite Structures. 2010;92:633–646.
[113] Balakrishnan H, Hassan A, Imran M, Wahit MU. Aging of toughened polylactic acid nanocomposites: water absorption, hygrothermal degradation and soil burial analysis. Journal of Polymers and the Environment. 2011;19:863–875.
[114] Marin L, Trias D, Badallo P, Rus G, Mayugo JA. Optimization of composite stiffened panels under mechanical and hygrothermal loads using neural networks and genetic algorithms. Composite Structures. 2012;94:3321–3326.
[115] Starkova O, Chandrasekaran S, Prado LASA, Tölle F, Mülhaupt R, Schulte K. Hydrothermally resistant thermally reduced graphene oxide and multi-wall carbon nanotube based epoxy nanocomposites. Polymer Degradation and Stability. 2013;98:519–526.
[116] Jen Y-M, Huang C-Y. Combined temperature and moisture effect on the strength of carbon nanotube reinforced epoxy materials. Transactions of the Canadian Society for Mechanical Engineering. 2013;37:755–763.
[117] Hamim SU, Singh RP. Effect of hygrothermal aging on the mechanical properties of fluorinated and nonfluorinated clay-epoxy nanocomposites. International Scholarly Research Notices. 2014;2014:489453(1-13).
[118] Park H, Kim H. Damage resistance of single lap adhesive composite joints by transverse ice impact. International Journal of Impact Engineering. 2010;37:177–184.

[119] Zhang J, Rowland J. Damage modeling of carbon-fiber reinforced polymer composite pin-joints at extreme temperatures. Composite Structures. 2012;94:2314–2325.
[120] Kapidžić Z, Ansell H, Schön J, Simonsson K. Quasi-static bearing failure of CFRP composite in biaxially loaded bolted joints. Composite Structures. 2015;125:60–71.
[121] Woo RSC, Zhu H, Leung CKY, Kim J-K. Environmental degradation of epoxy-organoclay nanocomposites due to UV exposure: Part II residual mechanical properties. Composites Science and Technology. 2008;68:2149–2155.
[122] Mouzakis DE, Zoga H, Galiotis C. Accelerated environmental ageing study of polyester/glass fiber reinforced composites (GFRPCs). Composites Part B: Engineering. 2008;39:467–475.
[123] Boubakri A, Guermazi N, Elleuch K, Ayedi HF. Study of UV-aging of thermoplastic polyurethane material. Materials Science and Engineering: A. 2010;527:1649–1654.
[124] de Souza Rios A, de Amorim WF, de Moura EP, de Deus EP, de Andrade Feitosa JP. Effects of accelerated aging on mechanical, thermal and morphological behavior of polyurethane/epoxy/fiberglass composites. Polymer Testing. 2016;50:152–163.
[125] Nicholas J, Mohamed M, Dhaliwal GS, Anandan S, Chandrashekhara K. Effects of accelerated environmental aging on glass fiber reinforced thermoset polyurethane composites. Composites Part B: Engineering. 2016;94:370–378.
[126] Barbosa APC, Fulco APP, Guerra ES, Arakaki FK, Tosatto M, Costa MCB, Melo JDD. Accelerated aging effects on carbon fiber/epoxy composites. Composites Part B: Engineering. 2017;110:298-306.
[127] Liu L, Zhang BM, Wang DF, Wu ZJ. Effects of cure cycles on void content and mechanical properties of composite laminates. Composite Structures. 2006;73:303–309.
[128] Singh M, Saini JS, Bhunia H, Singh P. Application of Taguchi method in the optimization of geometric parameters for double pin joint configurations made from glass–epoxy nanoclay laminates. Journal of Composite Materials. 2017;51:2689–2706.
[129] Pandey RK, Panda SS. Multi-performance optimization of bone drilling using Taguchi method based on membership function. Measurement. 2015;59:9–13.
[130] Ghani JA, Choudhury I, Hassan H. Application of Taguchi method in the optimization of end milling parameters. Journal of Materials Processing Technology. 2004;145:84–92.
[131] Nalbant M, Gokkaya H, Sur G. Application of Taguchi method in the optimization of cutting parameters for surface roughness in turning. Materials & Design. 2007;28:1379–1385.
[132] Anawa E, Olabi A, Hashmi M. Application of Taguchi method to optimise dissimilar laser welded components. International Journal of Manufacturing Technology and Management. 2008;15:219–227.
[133] Ghaffari M, Ehsani M, Khonakdar HA, Van Assche G, Terryn H. The kinetic analysis of isothermal curing reaction of an epoxy resin-glassflake nanocomposite. Thermochimica Acta. 2012;549:81–86.

[134] Ghaemy M, Riahy M. Kinetics of anhydride and polyamide curing of bisphenol A-based diglycidyl ether using DSC. European Polymer Journal. 1996;32:1207–1212.
[135] Zhang S, Li L, Kumar A. Materials characterization techniques. Boca Raton, USA: CRC press; 2008.
[136] Ahmad Z, Sarwar MI, Mark JE. Dynamic-mechanical thermal analysis of aramid-silica hybrid composites prepared in a sol-gel process. Journal of Applied Polymer Science. 1997;63:1345–1352.
[137] Hashin Z. Failure criteria for unidirectional fiber composite. Journal of Applied Mechanics. 1980;47:329–334.
[138] Rahmani H, Najafi SHM, Saffarzadeh-Matin S, Ashori A. Mechanical properties of carbon fiber/epoxy composites: Effects of number of plies, fiber contents, and angle-ply layers. Polymer Engineering & Science. 2014;54:2676–2682.
[139] Sethi S, Ray BC. Environmental effects on fibre reinforced polymeric composites: evolving reasons and remarks on interfacial strength and stability. Advances in Colloid and Interface Science. 2015;217:43–67.
[140] Joliff Y, Rekik W, Belec L, Chailan JF. Study of the moisture/stress effects on glass fibre/epoxy composite and the impact of the interphase area. Composite Structures. 2014;108:876–885.
[141] Singh M, Saini JS, Bhunia H. Investigation on failure modes for pin joints made from unidirectional glass-epoxy nanoclay laminates. Fatigue & Fracture of Engineering Materials & Structures. 2016;39:320–334.
[142] Tjandraatmadja GF, Burn LS, Jollands MC. Evaluation of commercial polycarbonate optical properties after QUV-A radiation–the role of humidity in photodegradation. Polymer Degradation and Stability. 2002;78:435–448.
[143] Gunst RF. Response surface methodology: process and product optimization using designed experiments. Technometrics. 1996;38:284–286.
[144] Walpole RE, Myers RH, Myers SL, Ye K. Probability and statistics for engineers and scientists: Pearson London; 2014.

List of Publications

Published in peer reviewed (SCI) journals

1. **Kulwinder Singh**, J. S. Saini, H. Bhunia and S. R. Chowdhury, "Hygrothermal Effects on Mechanical Joints Prepared from Fiber Reinforced Plastic Nanocomposites", *Journal of Composite Materials* (impact factor 1.613) (accepted)

2. **Kulwinder Singh**, J. S. Saini and H. Bhunia,"Effect of Nanoclay and Bolt Preloads on the Strength of Bolted Joints in Glass Epoxy Nanocomposites", *Journal of the Brazilian Society of Mechanical Sciences and Engineering* 2018, 40, pp. 184. (impact factor: 1.627)

3. **Kulwinder Singh Chani**, J. S. Saini and H. Bhunia, "Accelerated Weathering of Bolted Joints Prepared from Woven Glass Fiber Reinforced Nanocomposites", *Proceedings of the Institution of Mechanical Engineers, Part L: Journal of Materials: Design and Applications,* DOI: 10.1177/1464420719828155 (impact factor 1.281)

4. **Kulwinder Singh**, J. S. Saini, H. Bhunia and Jaspreet Singh, "Investigations to increase the failure load for joints in glass epoxy composites", *Proceedings of the Institution of Mechanical Engineers, Part C: Journal of Mechanical Engineering Science* 2019, 233, 2074-2090. (impact factor 1.0)

5. **Kulwinder Singh**, J. S. Saini and H. Bhunia, "Effect of Metallic Inserts on the Strength of Pin Joints Prepared from Glass Fiber Reinforced Composites", *Defence Science Journal* 2017, 67, 592-600. (impact factor: 0.5)